INFORMATION TO USERS

This manuscript has been reproduced from the microfilm master. UMI films the text directly from the original or copy submitted. Thus, some thesis and dissertation copies are in typewriter face, while others may be from any type of computer printer.

The quality of this reproduction is dependent upon the quality of the copy submitted. Broken or indistinct print, colored or poor quality illustrations and photographs, print bleedthrough, substandard margins, and improper alignment can adversely affect reproduction.

In the unlikely event that the author did not send UMI a complete manuscript and there are missing pages, these will be noted. Also, if unauthorized copyright material had to be removed, a note will indicate the deletion.

Oversize materials (e.g., maps, drawings, charts) are reproduced by sectioning the original, beginning at the upper left-hand corner and continuing from left to right in equal sections with small overlaps.

ProQuest Information and Learning
300 North Zeeb Road, Ann Arbor, MI 48106-1346 USA
800-521-0600

NANOSTRUCTURED ELECTRODE MATERIALS FOR LITHIUM ION BATTERIES

by

Mark Nikolas Obrovac
B.Sc. (Hon.), Simon Fraser University, Burnaby, British Columbia, Canada 1995
M.Sc., Dalhousie University, Halifax, Nova Scotia, Canada 1997

Submitted in partial fulfillment of the requirements
for the degree of Doctor of Philosophy

in the Department of Physics
Dalhousie University
Halifax, Nova Scotia, Canada
May 11, 2001

DALHOUSIE UNIVERSITY

DATE: 10 May 2001

AUTHOR: Mark Nikolas Obrovac

TITLE: Nanostructured Electrode Materials for Lithium Ion Batteries

DEPARTMENT OR SCHOOL: Physics

DEGREE: Ph.D. CONVOCATION: October Year: 2001

Permission is herewith granted to Dalhousie University to circulate and have copies for non-commercial purposes, at its discretion, the above title upon the request of individuals or institutions.

[redacted]

Signature of Author

TABLE OF CONTENTS

LIST OF FIGURES

LIST OF TABLES

ABSTRACT

This thesis discusses two aspects of nanograined electrode materials for lithium batteries. Firstly the size and surface effects in nanosized lithium intercalation materials is explored. Nanosized intercalation materials are modelled using Monte Carlo simulations of finite sized lattice gases. This study shows that finite size intercalation materials can have marked differences in their voltage-composition behaviour compared to their bulk counterparts. The finite size of the lattices tends to cause a rounding-off of voltage plateaus, while surface effects cause extra plateaus to appear in voltage curves and can also cause phase transitions to occur at different voltages than they do in the bulk. Attempts at making real nanosized intercalation materials proved difficult by standard laboratory methods. A nanograined lithium manganese oxide was prepared in aqueous solution, however. This material has an interesting microstructure, being composed of 7 nm grains which self-assemble into 50 nm squares and rectangles. The voltage behaviour of this material is similar to that of lithium rich $LiMn_2O_4$ spinel, but has capacity between 3.3 V and 3.8 V, where no capacity exists in bulk $LiMn_2O_4$. The voltage plateaus of this material are also sloped and rounded off. It is unclear if these effects are caused by surface and size effects or by lattice defects in the structure.

The second focus of the thesis explores the mechanism and applications of displacement electrodes for secondary lithium cells. Such electrodes do not intercalate lithium, but undergo a reversible displacement reaction during cycling. It was found that non-intercalating transition metal oxide electrodes are displaced by lithium on the first discharge to form a nanocomposite of lithia and reduced transition metal. During charge lithium is removed from this composite, while concurrently the transition metal enters the oxygen lattice of the lithia. This process is thought to resemble an ion-exchange mechanism. It is also shown that a nanocomposite of lithia and transition metal made by ball-milling contains electrochemically active lithium. Such materials have a huge capacity (~500 mAh/g) compared to conventional intercalation cathodes. These composites might find application in lithium batteries as high capacity cathode materials or as an additive to provide a source of lithium for conventional anodes which suffer from irreversible capacity or for cathodes that can uptake more lithium than they contain as made. Finally, the ion-exchange mechanism discussed for displacement type electrodes was attempted outside of the cell by reacting Li_2O with transition metal ions in nonaqueous solvents. Although a reaction occurred, it was difficult to tell if an ion exchange type reaction took place or if a water impurity was the cause of the reaction. Nevertheless such a reaction was shown to take place very slowly in solution, if it occurs at all. Because of this, binary lithium compounds other than Li_2O in which the reaction does take place more quickly, such as Li_2S, are suggested as better candidates for electrochemical displacement type electrodes.

LIST OF SYMBOLS

Chapter 1

e	electronic charge
V_{cell}	cell voltage
μ	chemical potential

Chapter 2

a	in-plane lattice constant
b	magnitude of the in-plane reciprocal lattice vectors
$\mathbf{a}_i$	unit cell vectors
$B(2\theta)$	full width half maximum in radians
c	speed of light
C	proportionality constant
D_q	x-ray shape function
d_{002}	inter-layer spacing
E_Q	electric quadrupole interaction energy
E_γ	gamma-ray energy
E_m	energy of the magnetic dipole interaction
E_D	magnitude of the Doppler shift of a gamma ray emitted from a moving source
f	atomic form factor
F_k	structure factor
f_r	recoil-free fraction
g_N	nuclear Landé splitting factor
$g(\mathbf{R})$	crystal shape function
$G(\mathbf{q})$	crystal modulation function
G_{ik}	normalised peak profile pseudo-Voigt function

g	fraction of low strained layers
h,k,l	Miller indices
H	magnetic field magnitude
I	nuclear spin
I_{qc}	calculated integrated x-ray intensity of the Bragg reflection q
I_{qo}	observed integrated x-ray intensity of the Bragg reflection q
I_q	intensity of the Bragg reflection q
I_o	incident intensity
$\mathbf{k_o}$	incident wavevector
$\mathbf{k}$	scattered wavevector
k_B	Boltzmann constant
L	linear dimension of a crystallite
L_q	Lorentz polarisation factor
L_a	lateral extent of single layer sheets
m	magnetic moment per atom
M	number of layers in a powder grain
M_o	the average number of layers in a powder grain
M_q	multiplicity
m_I	magnetic quantum number
m_e	electron mass
M_{grain}	magnetic moment per grain
n	diffraction order
N	number of collected x-ray data points
N_{grain}	number of atoms per grain
P	probability of random stacking
P_q	polarisation factor
$p(\mathbf{q})$	inter-plane strain distribution
Q	nuclear quadrupole moment
$\mathbf{q}$	scattering wave vector
r	radial distance
R_B	Bragg R factor

R	goniometer radius
R_{nuc}	ground state nuclear radius
$\mathbf{R}$	Bravais lattice vector
S	scale factor
T	temperature
T_B	blocking temperature
$\mathbf{v}_i$	atom co-ordinates within a unit cell
V_{ZZ}	z-component of the electric field gradient tensor
W_q	Debye-Waller temperature factor
x_n, y_n, z_n	fractional atomic coordinates
$\langle x^2 \rangle$	mean square vibrational amplitude of a resonating atom
Y_{ic}	net x-ray intensity calculated at the point i
Y_{ib}	background x-ray intensity at the point i
Y_{io}	x-ray intensity observed at the point i
β_N	Bohr magneton
χ^2	goodness of fit
δ_D	Dirac delta function
$\sqrt{\langle \delta \rangle^2}$	fluctuation in spacing between adjacent layers
δ_{ij}	Kroneker delta
δ	isomer shift
$\varepsilon_1, \varepsilon_2$	small deviation of the scattering vector away from the Bragg rod
$\lvert\varepsilon\rvert$	$b\sqrt{\varepsilon_1^2 + \varepsilon_2^2 + \varepsilon_1\varepsilon_2}$
Φ	scattering amplitude
ϕ	single-layer scattering amplitude
$\eta(q)$	Fourier transform of the layer shape function
η	asymmetry parameter of the electric field gradient tensor
λ	wavelength
μ	nuclear magnetic dipole moment

v	velocity of Mössbauer source
2θ	scattering angle
θ	diffraction angle
$\rho_m(r)$	radial probability density of the m^{th} electron
ω	reciprocal decay length of the scattering amplitude away from a Bragg rod
$\lvert\Psi(0)\rvert_A^2$	electron charge density about an absorber nucleus
ζ	dimensionless in-plane strain parameter
$\Im$	layer structure factor

Chapter 3

A	total energy of a finite lattice gas
$A_{(\infty)}$	total energy for a infinite lattice gas
$A_{m(\infty)}$	total energy of an infinite Ising lattice
$A(x_s x_b)$	the ground state energy of a configuration with occupations x_s and x_b
d	dimension of lattice gas
E	lattice site energy
E_{mo}	constant in the expression of the Ising lattice energy
E_l	excess surface lattice binding energy
H	external magnetic field
H_l	surface magnetic field
J	spin-spin interaction energy
J_s	surface spin-spin interaction energy
L	linear dimension of lattice gas
m	magnetisation per spin
n	number of moles of lithium
n_i	lattice site occupation
N	number of lattice sites

$P(\mathbf{x})$	the probability for a system to be in a state **x**
r	a random number
T_o	298.15 K
U	nearest neighbour interaction energy
U_s	surface nearest neighbour interaction
V_s	size dependent shift in voltage of a phase transition
V_{max}	the voltage at which the maximum in the differential capacity peak occurs near a first order phase transition
ΔV_{max}	difference in voltage between a first order phase transition in a finite and infinite system
W^i	wetting critical point
$W(\mathbf{x},\mathbf{x}')$	the transition probability between the states **x** and **x'**
x	lithium mole fraction
x	a vector describing the state of a system
x_s	surface occupation number
x_b	bulk occupation number
$(-dx/dV)_{max}$	maximum value of the differential capacity peak near a first order phase transiton
γ	number of nearest neighbours
μ	chemical potential
$\mu_{(x_s x_b)(x_s' x_b')}$	the chemical potential at the transition between the states $(x_s x_b)$ and $(x_s' x_b')$
ν	$\tanh(U/k_B T)$
σ_i	spin

Chapter 4

A	number of moles of Mn^{4+}
B	number of moles of Mn^{3+}
W	sample molecular weight

W_{MnO_2}	molecular weight of MnO_2
W_{Mn}	molecular weight of Mn
χ^2	goodness of fit

Chapter 6

Z	number of formula units per unit cell
χ^2	goodness of fit

Chapter 7

$a_{M^{n+}}$	the activity of the M^{n+} ion in solution
a	in plane cell constant (Å)
g	fraction of organized layers
ΔG_{el}	the electrolytic free energy of formation
ΔG_{el}^{o}	electrolytic free energy of formation with all ions at unit activity
ΔG_{f}^{o}	the standard free energy of formation
$\Delta \overline{G}_{el}^{o}$	*the standard electrolytic free energy of formation per equivalent*
L_a	layer extent (Å)
M	total number of layers
P	probability of random stacking
R	the ideal gas constant
$\sqrt{\langle \delta \rangle}$	inter plane strain
σ_M	width of M distribution
ζ	in plane strain

ACKNOWLEDGEMENTS

I would like to firstly thank my supervisor, Dr. Jeff Dahn, for his invaluable guidance and insight. I have learned a lot from Jeff. I am certain that I couldn't have had a better supervisor. I would also like to acknowledge all my fellow lab members, past and present. Let me see, there was Monique Richard, Ian Courtney, Ed Buiel, David Stevens, Jennifer Seel, Tao Zheng, Weibing Xing, Yuan Gao, Kevin Hewitt, Shane Beattie, Luc Beaulieu, Jason Mueller-Neuhaus, Dean MacNeil (thanks for sealing my stainless tubes, Dean!), Tim Hatchard, Zhonghua Lu, Jens Paulsen, Dominic Larcher, Ou Mao, Aaron Davis, Arman Bonadarpour, Zonghai Chen, Zhaohui Chen and Hubert Fortier. Hopefully I haven't forgotten anyone. Working in the lab was always enjoyable. Finally, I would like to thank my partner Mélanie Fredette and my family for their unwavering love and support.

Chapter 1

Introduction

1.1 CURRENT LITHIUM ION BATTERY TECHNOLOGY

Lithium ion batteries are the highest energy density secondary batteries on the market today [1]. They fill an important niche in the marketplace, providing power to laptops, cell phones, palmtops, portable GPS systems and other consumer devices, which require portability. The large energy density of these devices comes from the low atomic weight of lithium coupled with its low electronegativity. This results in a high gravimetric energy for the reaction of lithium with materials with high electronegativity, such as oxides. However, lithium metal is too unsafe to be used as an electrode in a rechargeable battery. After many charge/discharge cycles the lithium anode surface becomes rough. The high surface area lithium produced is very reactive and can lead to

self-heating chemical reactions, causing eventual cell failure and even the possibility of an explosion [1].

The solution of this problem is the lithium ion cell, which contains no lithium metal [1]. The cell is shown schematically in figure 1.1 and consists of a cathode, an anode and a lithium-ion-conducting electrolyte. Generally cathode materials are a metal oxide or phosphate, in which lithium has a low chemical potential. The cathode already contains lithium when it is synthesized, and so is generally relatively inert as made. The anode of the cell is made from a material in which lithium has a high chemical potential. Chiefly the material of choice for the anode is graphitic carbon. As constructed the cell is in its discharged state. During charge a potential difference is applied across the cell resulting in the flow of lithium ions from the cathode across the electrolyte to the anode as shown in figure 1.1. The potential difference required to move the lithium ions and electrons from the cathode to the anode is proportional to the chemical potential

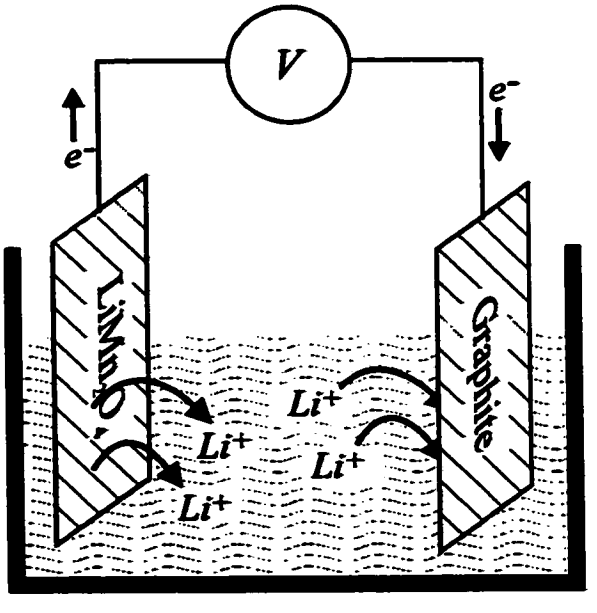

Figure 1.1 Schematic diagram of a $LiMn_2O_4$ (cathode) vs graphite (anode) lithium ion cell showing the direction of the lithium ion and electron flow during the charging process

$$V_{cell} = -\frac{1}{e}\left[\left(\mu_{Li^+}^{anode} - \mu_{Li^+}^{cathode}\right) + \left(\mu_{e^-}^{anode} - \mu_{e^-}^{cathode}\right)\right] \quad (1.1)$$

where V_{cell} is the cell voltage, e is the electronic charge and μ is the chemical potential of a lithium ion or electron in the cathode or anode as indicated. Since lithium is in a state of higher chemical potential in the anode than the cathode, energy is required to move a lithium ion and electron from the cathode to the anode and charge the cell. During discharge the direction of electron and lithium ion flow is reversed and useful work can be done by the cell.

The choice of appropriate anode and cathode materials not only depends upon the difference in the chemical potential of lithium between the two, but also their volumetric energy density, specific energy density, safety at various states of charge and cycleability. All cathode materials for lithium ion batteries on the market today are based on lithium transition metal oxides such as $LiCoO_2$, $LiMn_2O_4$ and doped variants of these. As mentioned previously, anodes are almost exclusively made from graphitic carbons. All of these electrode systems are based on layered or tunnel structures in which the lithium can be inserted or removed without changing the structure of the host material. This process is known as intercalation when the lithium is added or de-intercalation when it is removed.

1.2 RECENT RESEARCH ON NANOSTRUCTURED MATERIALS FOR LITHIUM ION BATTERIES

Much of the current research on lithium batteries, specifically for anode materials, is based on materials that are not intercalation compounds. For instance some materials can

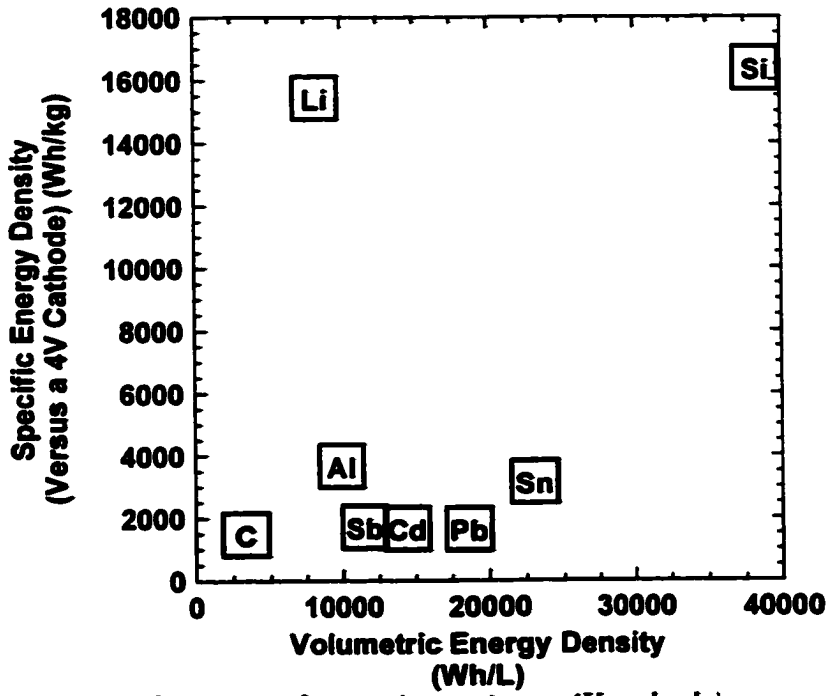

Figure 1.2 The specific energy density (assuming a 4V cathode) versus the volumetric energy density of various materials that alloy with lithium. Graphite is included in the figure for comparison.

electrochemically alloy with lithium such as silicon or tin. Unlike intercalation, in the alloying process the structure of the host material is changed when lithium is inserted. These materials can have significantly higher specific and volumetric energy densities than graphite as shown in figure 1.2. However the large volume changes associated with the two-phase regions during lithium insertion or removal in these alloys can cause structural failure in the material, causing them to crack. This can cause a significant fraction of the material to become electrically disconnected from the rest of the electrode and useless for further cycling [2].

The large volume changes associated with the alloying process are tolerated by nano-grained systems much better than by bulk materials [3]. This is because the nano-grained material does not pass through the two phase regions that the bulk material does during lithium insertion. Most current studies are based on systems in which nano-

grained materials are formed as the result of the discharging process. For instance tin oxides have been suggested as possible anode materials. During the first discharge of a lithium cell, lithium reacts with the tin oxides to make nano-grained lithia and tin metal. Further inserted lithium then alloys with the nano-grained tin metal. These reactions can be summarized as follows for SnO [2,3]:

$$SnO + 2Li \rightarrow Li_2O + Sn \tag{1.2}$$

$$4.4Li + Sn \rightleftharpoons Li_{4.4}Sn. \tag{1.3}$$

Unfortunately, reaction (1.2) is not significantly reversible at low voltages and so an appreciable amount of lithium is sequestered in the form of Li_2O. This results in a large irreversibly capacity. Furthermore repeated cycling of the nano-grained tin according to equation (1.3) leads to the aggregation of the tin into larger clusters, which eventually leads to cracking [2,3]. Other approaches to this problem include making intermetallic alloys, such as Sn_2Fe [4], to avoid the large irreversible capacity problem found with the oxide materials. However these materials still suffer from cycling induced grain aggregation [4].

Another approach to make high capacity anodes has come from oxides for which the displacement reaction in equation (1.2) is significantly reversible. At room temperature this seems to be generally the case for transition metal oxides [5-8]. Such reactions have been studied in high temperature systems decades ago [9]. In this case the displacement reactions with lithium progress through distinct phases which are in thermodynamic equilibrium [9]. This is unlikely to occur at room temperature. Indeed, most room temperature studies have reported an uptake of lithium greater than that predicted from a simple reduction of the metal [5-8], which has created an impetus for

further studies. Although these anodes operate at rather high voltages and suffer from a large polarization effect (a large voltage difference between charge and discharge) they are attractive because of their potentially large capacities compared with graphitic carbon anodes. For instance graphite can accommodate one lithium for every six carbon atoms giving a capacity of 370mAh/g while one can expect a capacity of 750mAh/g for the lithium reduction of a typical transition metal (II) oxide or 1000mAh/g for a transition metal (III) oxide. Thus far relatively few studies have been conducted on these oxide systems and they are generally not well understood. For instance reaction (1.2) is not even widely accepted as the mechanism for the reaction [5-7].

There is no fundamental reason why such reactions cannot be also applied to cathode systems, which generally do not have capacities exceeding 200mAh/g. Indeed such cathode materials have been suggested over thirty years ago [10-13], but have been overlooked by the modern battery community. The possible gains in energy density are huge as shown in figure 1.3. Here many possible battery couples are plotted according to their specific energy density and equivalent weight. Solid lines in the figures represent the voltages of the couples as indicated. The limit of current intercalation technology is represented by a hypothetical 4V $Li/LiCoO_2$ couple based on the capacity of $LiCoO_2$ if all the lithium could be removed. In reality only half the lithium can be removed from this material, otherwise structural failure results. This is represented by the $Li/Li_{0.5}CoO_2$ couple in the figure. Although $LiCoO_2$ is a high voltage material, it has a relatively low energy density due to its high equivalent weight. On the other hand couples such as Li/NiF_2 and Li/CuF_2, which are based on displacement reactions with lithium, have a

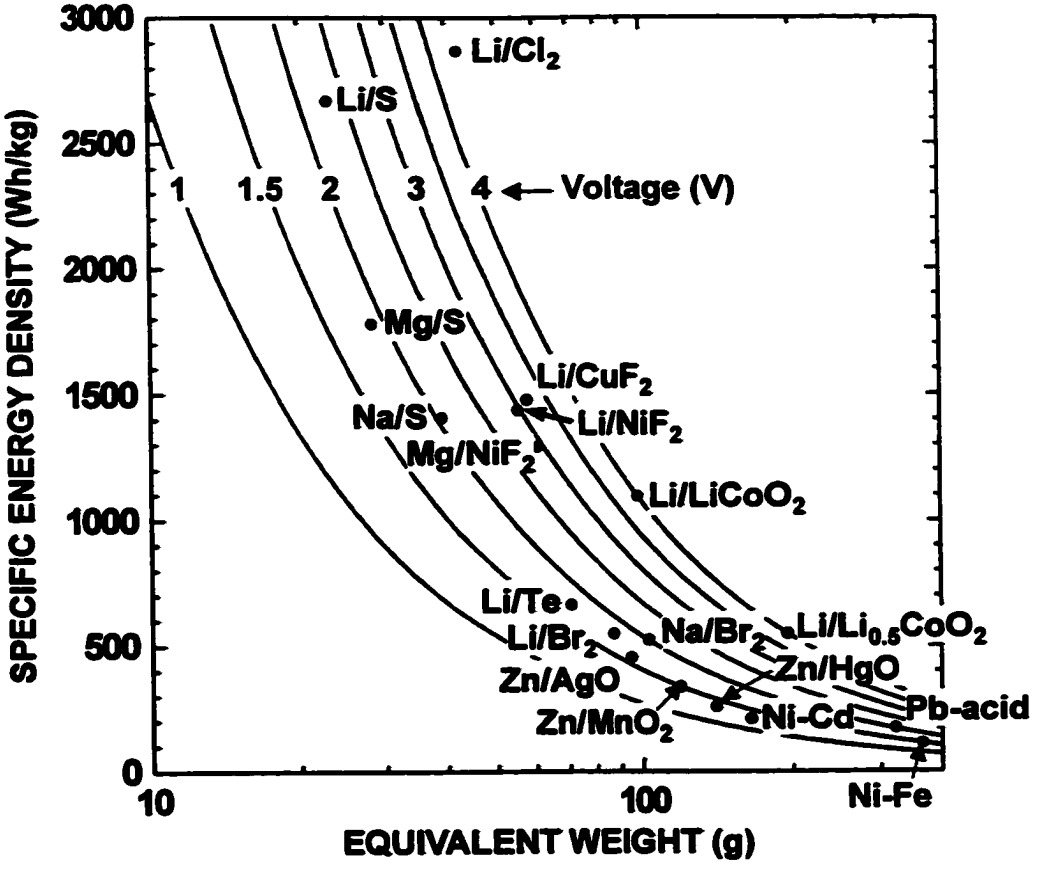

Figure 1.3 The specific energy density versus the equivalent weight (per electron transferred in the electrochemical reaction) of a number of couples proposed for high energy density batteries. Lines of constant voltage are also shown in the figure. The theoretical limit of lithium intercalation technology is represented by the $Li/LiCoO_2$ couple where it is assumed that all the lithium can be removed at 4V. In reality only about half of the lithium can be removed from $LiCoO_2$. This is represented by the $Li/Li_{0.5}CoO_2$ couple.

low theoretical voltage, but their energy density is about one and a half times as much as the hypothetical $LiCoO_2$ material (or three times as much as the current technology). This is because these materials have low equivalent weights. The problem with such couples is that no lithium is stored in a cathode material such as NiF_2. Thus a lithium anode must be used, along with its associated problems.

1.3 AIMS OF THIS THESIS

This thesis focuses on two areas of nanostructured materials. The first is intercalation based nanostructured electrode materials. Here the consequences of making existing intercalation materials nano-grained will be explored. This will be first done on a purely theoretical basis, extending the current lattice gas theory for bulk intercalation materials to nano-grained materials in which boundary effects play a significant role. Real nano-grained intercalation materials will then be studied. A number of methods of synthesis will be explored which will show the inherent difficulty in making nano-grained intercalation materials. Finally the electrochemistry of nano-grained lithium manganese oxide will be investigated and compared to the theoretical results.

The second area of focus is nanostructured materials from electrochemical displacement reactions with lithium. Here a careful examination of the displacement reaction by in-situ methods will be presented. This will lead to a completely new understanding of how these materials work. With the principles learned from these studies, possible new materials for novel high capacity cathodes based on displacement reactions will be discussed. Unlike previous such cathodes, which do not contain lithium and require a lithium anode as previously discussed, these materials use lithia as a novel lithium source and are compatible with lithium ion technology. The electrochemical performance of prototype new materials based on these premises will be examined. Finally, the mechanisms found for these displacement reactions suggest that room temperature ion-exchange of transition metal ions with lithium oxide might be possible in nonaqueous solvents. The results of preliminary investigations of this possibility will be presented.

Chapter 2

Characterisation of Nanostructured Electrode Materials

2.1 ELECTROCHEMICAL CHARACTERIZATION

Figure 2.1 shows an exploded view of a lithium coin cell of the type used for electrochemical characterisation of electrode materials. Such cells are convenient for use in a research environment since the amount of electrode material they require is small (about 10mg) and their assembly is relatively quick. The cell stack consists of a cathode (the electrode being evaluated), a microporous polypropylene separator (Celgard 2502) soaked with electrolyte (1M $LiPF_6$ in a 33:67 solution by weight of ethylene carbonate (EC)/ diethylcarbonate (DEC)) and a lithium metal anode. The separator keeps the cathode and anode from electrically shorting, while allowing for lithium ion conduction

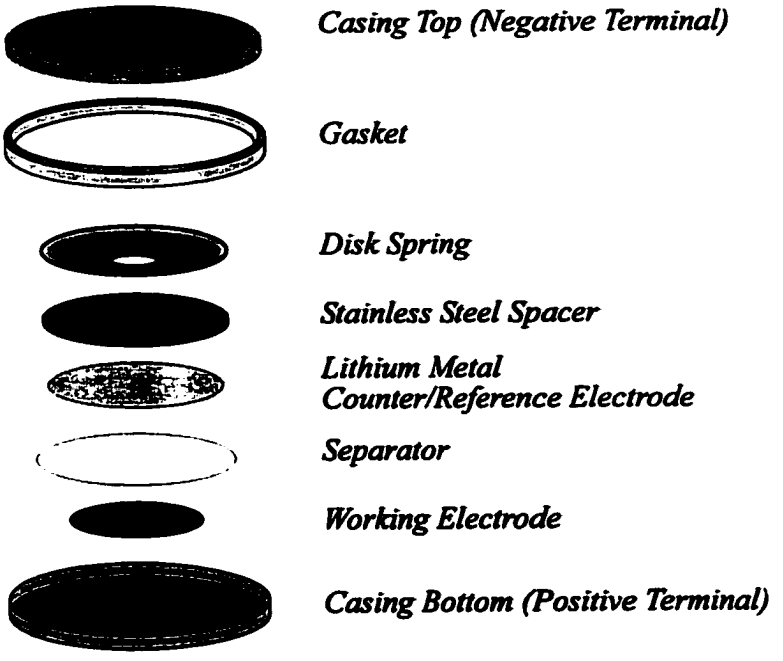

Figure 2.1 An exploded view of a coin type test cell.

through the electrolyte contained in its pores. A lithium metal anode is used for testing purposes, since it also doubles as a convenient reference electrode. All voltages quoted in this thesis are made with reference to a lithium metal electrode. The cell stack is held in place with a spacer and a spring, which apply even pressure to the stack. The whole assembly is held between the cell can and top, which are crimp-sealed together. All cell assembly was performed in an argon-filled glovebox, since lithium is not air stable.

Electrodes were made by one of two ways, depending on if the active material is air sensitive or not. For air-stable materials a method based on the Bellcore plastic electrode technology was used [14]. This method will be referred to as the "Bellcore method". A slurry was prepared containing 300 mg of the electrode material to be evaluated, 38 mg of Super S carbon black (Chemetals Inc.), which makes the electrode with electrically conductive, 151 mg polyvinylidene difluoride (PVDF)/hexafluoro-

propylene (HFP) (88/12 by weight) binder (Kynar Flex 2801), 262 mg dibutylpthalate (DBP) plasticizing agent, and 1800 mg acetone (in which the binder and DBP are soluble). The slurry was mixed for four hours by agitating on a bench-top agitator with a ceramic bead (this way problems with magnetic active materials are avoided) until the PVDF binder was dissolved. Then the slurry was immediately spread by means of a doctor blade with a 0.025" gap onto a glass plate. After the acetone evaporated, the cathodes were cut into 1.2cm diameter disks with a punch. Before use in cells, the cathodes were placed in anhydrous diethyl ether three times for fifteen minutes each to extract the EC/PC plasticizer. The resulting cathodes consisted of 61.3% active material, 7.7% carbon black and 30.9% binder by weight. During cell assembly, electrolyte added to the cell is drawn into the voids left by the plasticizer, providing ionic conduction within the electrode.

For active materials which are not air stable a different method was developed in which the electrode fabrication could be carried out in a glovebox (the acetone used in the method above is not compatible with our gloveboxes which contain lithium metal). This method will be referred to as the "method employed to make air-sensitive electrodes". All the steps described below were performed in a helium filled glovebox. In this method a slurry was made of 200 mg of active material with 25 mg of Super S carbon black and 260 mg of a 10% solution of PVDF in n-methyl pyrrolidinone (NMP) (National Research Council of Canada). An additional 600 mg of NMP was added to make the slurry less viscous. Although NMP does react with lithium, it can be used (with appropriate care to keep the solvent levels in the glovebox to a minimum) in a lithium-containing glovebox since its vapour pressure is low.

The above slurry was mixed thoroughly (with a brass rod), spread on copper foil or a glass plate with a doctor blade with a 0.43 mm gap and placed in the glovebox anti-chamber. The anti-chamber was then partially evacuated to 44 kPa of He and was left for 12 hours to allow for slow evaporation of the NMP. For regular electrochemical cells, electrode disks were then cut from the copper foil. For in-situ studies, which will be described later, the electrodes were dried on a glass plate, scraped off, ground with a mortar and pestle and pressed into electrode pellets which were 1.3cm in diameter, about half a millimetre thick and typically 50mg in mass. The resulting electrodes consisted of 80% active material, 10% carbon black and 10% binder.

The assembled electrochemical cells were charged and discharged under thermostatic conditions at 30°C using constant current cyclers with ±1% current stability. Typically cells were cycled at C/60 rate where C-rate is defined as the current required to fully charge/discharge a cell in one hour.

2.2. POWDER X-RAY DIFFRACTION AND IN-SITU X-RAY DIFFRACTION

2.2.1 Theory of X-ray Diffraction

Powder X-ray Diffraction (XRD) is a powerful way of determining crystal structures, phase compositions and grain sizes. It is based on the same principle as the diffraction of light from a grating, except in this case the grating is three dimensional, being the electrons of the atoms in a solid. The most simplified view of this effect is given by the well-known Bragg law, which assumes that the x-rays are reflected by planes made up of the atoms in the crystal lattice. With this view constructive

interference from a family of lattice planes will occur when:

$$n\lambda = 2d\sin\theta \tag{2.1}$$

where n is an integer, λ is the wavelength of the incident radiation, d is the plane spacing, and θ is the angle between the lattice planes and the incident wavevector. A more rigorous treatment of the diffraction of x-rays by a crystal can be built up from three steps: the scattering of x-rays from a single electron, scattering from a group of electrons in an atom, and diffraction from the collection of atoms which make up a crystal. The scattering of x-rays from a single electron can be derived from simple electromagnetic theory. The intensity, I_q, of the scattered radiation is given by the Thomson scattering equation [15]:

$$I_q = I_o \frac{e^4}{m_e^2 c^4 R^2}\left(\frac{1+\cos^2 2\theta}{2}\right) = I_o S P_q;\ S = \frac{e^4}{m_e^2 c^4 R^2};\ P_q = \left(\frac{1+\cos^2 2\theta}{2}\right) \tag{2.2}$$

where I_o is the incident intensity and R is the distance from the electron to the point of observation. P_q is known as the polarization factor.

X-ray scattering from an ion or atom can then be calculated by simply summing the scattered radiation from each electron. Usually, an approximation is used which assumes each electron is smeared over a spherical distribution. The result adds an extra multiplicative factor to equation (2.2) known as the atomic form factor [15]:

$$f_n = \sum_m \int_0^\infty 4\pi r^2 \rho_m(r) \frac{\sin qr}{qr} dr \tag{2.3}$$

where f_n is the atomic form factor of the n^{th} atom, $\rho_m(r)$ is the probability density of the m^{th} electron at the radial distance r, q is the magnitude of the scattering wavevector: $\mathbf{q} = \mathbf{k} - \mathbf{k_o}$ where $\mathbf{k_o}$ an $\mathbf{k}$ are the incident and scattered wavevectors, and the sum is over

all the electrons in the atom. The scattering wave vector is related to the scattering angle by $q = 4\pi\sin\theta/\lambda$.

Summing over the scattering amplitudes of all the ions in a crystal yields the total scattering amplitude [15]:

$$\Phi(\mathbf{q}) = F_k \prod_{i=1}^{3} \frac{e^{iN_i \mathbf{q}\cdot\mathbf{a}_i} - 1}{e^{i\mathbf{q}\cdot\mathbf{a}_i} - 1} \tag{2.4}$$

where $\mathbf{a}_i$ are the unit cell vectors and N_i are the crystallite dimensions in terms of the unit cell vectors. F_q is the structure factor [15]:

$$F_q = \sum_n f_n e^{2\pi i(hx_n + ky_n + lz_n)} \tag{2.5}$$

where the sum is over all the atoms in the unit cell, h, k, l are the components of the scattering vector, $\mathbf{q}$, in the reciprocal lattice space and x_n, y_n, z_n are the fractional atomic co-ordinates. Since for reciprocal lattice vectors: $\mathbf{a}_i \cdot \mathbf{b}_j = 2\pi\delta_{ij}$ where δ_{ij} is the Kroneker delta, equation (2.4) indicates that there will be sharp diffraction peaks when the scattering vector is a reciprocal lattice vector. However this will only occur on the condition that the reflection is allowed by the structure factor in equation (2.5). Squaring equation (2.4) and including the polarisation factor gives the total scattered intensity [15]:

$$I_q = SP_q |F_q|^2 D_q(N_i) \tag{2.6}$$

where:

$$D_q = \prod_{i=1}^{3} \frac{\sin^2(\mathbf{q}\cdot N_i\mathbf{a}_i/2)}{\sin^2(\mathbf{q}\cdot\mathbf{a}_i/2)}. \tag{2.7}$$

is a function that depends on the crystallite size.

The Scherrer equation, which gives the peak width as a function of the crystallite size, can be derived from equation (2.7) if one assumes that each term in the product can

be approximated by Gaussian functions [15]:

$$B(2\theta)=\frac{0.94\lambda}{L\cos\theta}. \tag{2.8}$$

Here $B(2\theta)$ is the full width at half maximum (FWHM) in radians of the powder pattern peak, L is the length of the edge of the crystallite cube and *0.94* is the shape factor constant for a three dimensional crystal.

Ideal powder diffraction samples consist of an enormous number of small ($<10^{-3}$cm) crystalline grains with completely random orientations. Thus, for a set of planes with spacing d, there will be many crystals oriented so that their *hkl*-planes make the correct Bragg law angle, θ, with the incident beam and detector. To take into account the number of equivalent orientations of each lattice plane another factor, M_q, called the multiplicity is included in the expression for the intensity.

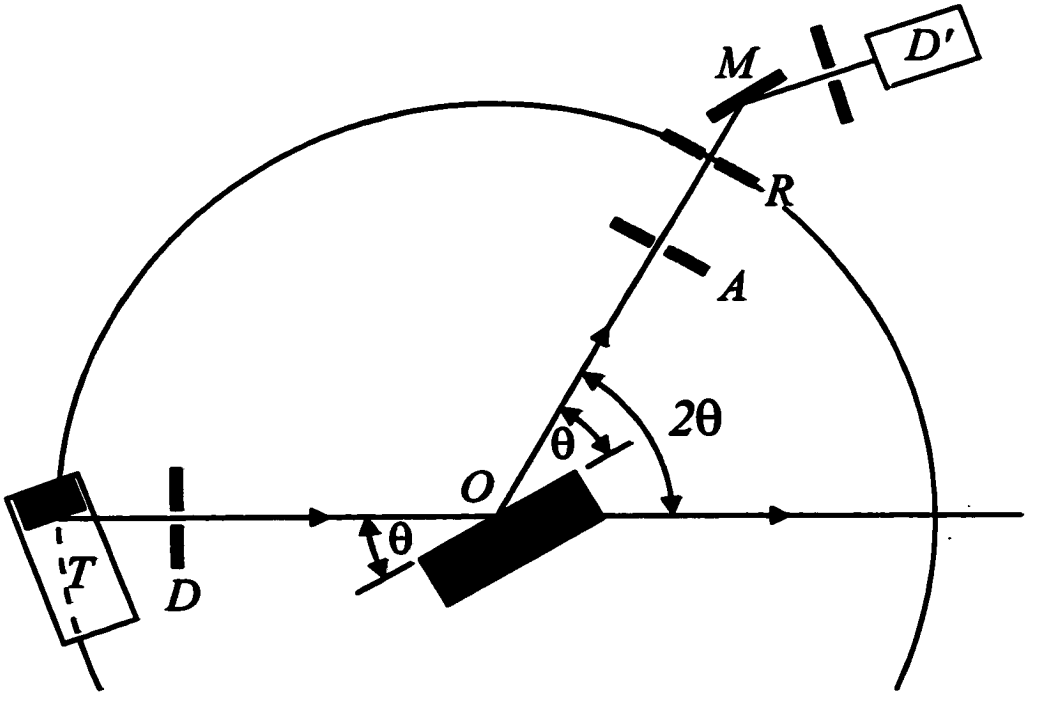

Figure 2.2 The x-ray measurement geometry: T = x-ray tube; D = Divergence Slits; A = Anti-scatter Slits; R = Receiving Slits; M = Monochromator; D' = Detector.

In an XRD measurement the diffraction angle, 2θ, and the intensity are recorded as θ is varied by changing the orientation of the source and the detector. This is illustrated in figure 2.2, which shows the orientation of the x-ray source, the sample, and the detector for the Siemens D5000 powder diffractometer that was used for x-ray measurements. Since the crystallites in a powder sample have all orientations about the incident beam, the diffracted radiation forms a cone of half apex angle 2θ. To take into account that the detector only measures the intensity of a section of the diffraction cone, an extra factor must be added to the expression of the intensity. It is usually combined with the polarisation factor to give the Lorentz polarisation factor [15]:

$$L_q = \left(\frac{1 + \cos^2 2\theta}{\sin\theta \sin 2\theta} \right). \tag{2.9}$$

There are other factors that affect the x-ray diffraction pattern which result from the measurement of real, non-ideal samples at ambient temperatures with a non-ideal spectrometer. The effects of lattice defects in the form of stacking faults will be discussed in the next section. Other effects which will only be mentioned here include lattice vibrations which tend to decrease intensities and finite incident beam width, internal strain in the sample and finite detector resolution which tend to broaden peaks.

2.2.2 XRD Theory of Stacking Faults

Crystalline materials with layered structures are ideally made up of two-dimensional sheets infinitely stacked with recursive ordering, such as the ABCABC... stacking sequence for cubic-close-packed systems. A common defect in layered systems is disorder in the arrangement of the layers, while order is maintained in the in-layer

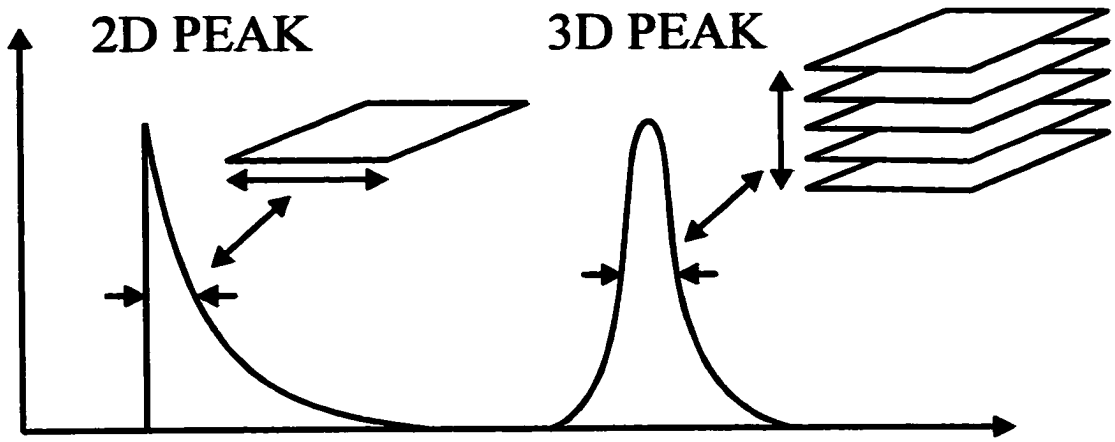

Figure 2.3 A comparison between 2D and 3D peaks. In the 2D peak the layer dimension is reflected in the width of the asymmetric peak. For the 3D peak the number of stacked layers is reflected in the peak width..

plane. Defects of this type include stacking faults (e.g. ...ABCABCACABCABC...) and twinning (e.g. ABCABC|BACBA...). A random collection of stacking faults that persists throughout the crystal is termed turbostratic disorder. A famous paper by Warren in 1941 [16] studied the XRD spectra of turbostratically disordered graphitic carbon. The results are summarised qualitatively in figure 2.3. While the 3D peaks in the pattern retain their symmetry, the in-plane (2D) peaks are strongly asymmetric and look like a triangular spike with a long tail towards large scattering angles (a "Warren tail") [16].

Since Warren's analysis there have been more detailed treatments of XRD from stack-faulted materials [17,18,19]. These methods were consolidated by Shi, Reimers and Dahn to create a structure refinement program for disordered carbons [20]. The theory that follows closely follows Shi's formalism, which was developed for carbons, but applies equally well to any material consisting of layers of two-dimensional sheets. It is convenient to redefine the scattering amplitude as the sum of the amplitudes of the single layers in the lattice. The single layer scattering amplitude is defined as:

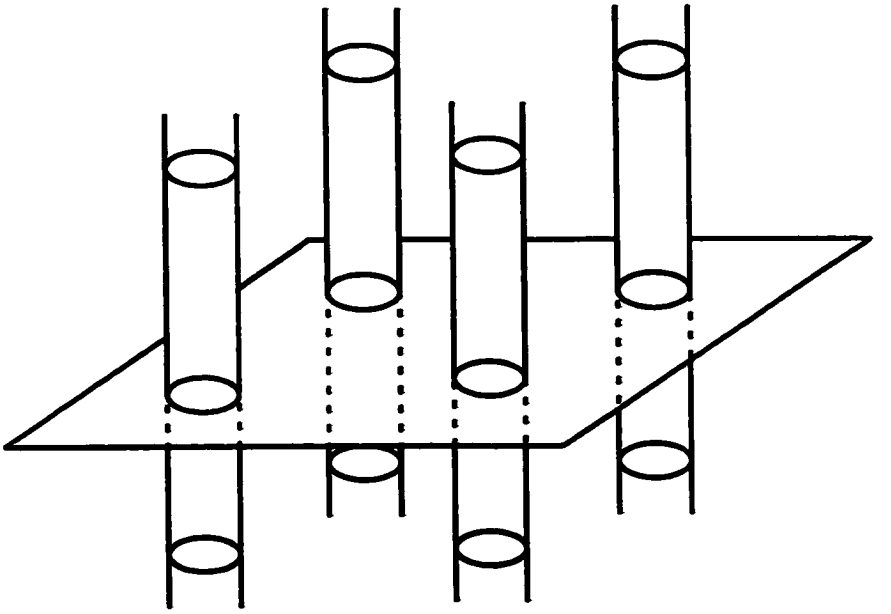

Figure 2.4 The reciprocal lattice of a real triangular lattice: an array of infinite rods.

$$\phi(\mathbf{q}) = f(\mathbf{q}) \sum_{\mathbf{R},\mathbf{v}} e^{2\pi i \mathbf{q}\cdot(\mathbf{R}+\mathbf{v})} g(\mathbf{R}) = \Im(\mathbf{q})\eta(\mathbf{q}) \tag{2.10}$$

where $\mathbf{R} = n_1\mathbf{a}_1 + n_2\mathbf{a}_2 + n_3\mathbf{a}_3$ is a Bravais lattice vector, $\mathbf{v}_i = x_i\mathbf{a}_1 + y_i\mathbf{a}_2$ are the atom positions in the planar unit cell and $g(\mathbf{R})$ is the shape function of the crystal, which is equal to 1 in the crystal and 0 outside. $\Im(\mathbf{q})$ is the structure factor function now defined for a single layer:

$$\Im(\mathbf{q}) = f(\mathbf{q}) \sum_{\mathbf{q}} e^{2\pi i \mathbf{v}\cdot\mathbf{q}} . \tag{2.11}$$

and $\eta(\mathbf{q})$ is the Fourier transform of the shape function for a single layer:

$$\eta(\mathbf{q}) = \sum_{\mathbf{R}} g(\mathbf{R}) e^{2\pi i \mathbf{v}\cdot\mathbf{R}} . \tag{2.12}$$

Figure 2.4 shows the reciprocal lattice as defined by equation (2.11) of a real triangular lattice. The lattice consists of an array of infinite rods. The transverse decay

of the scattering away from the rods is determined by $\eta(\mathbf{q})$. $\eta(\mathbf{q})$ is sharply peaked at reciprocal lattice points. If ε_1 and ε_2 are the deviations away from a reciprocal lattice point in the hk plane then $\eta(\varepsilon_1, \varepsilon_2)$ can be written as:

$$\eta(\varepsilon_1,\varepsilon_2)=\sum_{\mathbf{R}} g(\mathbf{R})e^{2\pi i\varepsilon\cdot\mathbf{R}} \approx \frac{sin^2\left(\frac{\sqrt{3}\pi}{2}(L_a+a)|\varepsilon|\right)}{sin^2\left(\frac{\sqrt{3}\pi}{2}a|\varepsilon|\right)}, \tag{2.13}$$

where L_a is the dimension of the layer and $|\varepsilon| = b\sqrt{\varepsilon_1^2+\varepsilon_2^2+\varepsilon_1\varepsilon_2}$ where $b=\frac{2}{\sqrt{3}a}$. This function can be closely approximated by a equal area Gaussian function:

$$\eta(\varepsilon)\approx\frac{L_a^2}{a^2}e^{-|\varepsilon|^2/\omega^2} \tag{2.14}$$

where $\omega = 2/\left(L_a\sqrt{3\pi}\right)$ determines the transverse decay from the rod. To include the effect of layer strain, ω is modified to include a dimensionless parameter ζ, so that $\omega = \omega + \zeta q_o$. Thus now the rod radius depends on hk through q_o:

$$\eta(\varepsilon)\rightarrow\frac{L_a^2}{a^2}\frac{\omega}{\omega+\zeta q_o}e^{-|\varepsilon|^2/(\omega+\zeta q_o)^2}. \tag{2.15}$$

The scattering intensity from a stack of identical layers will simply be the sum of the squares of the scattering amplitudes for each layer. Assuming the position of neighboring layers is uncorrelated the result is:

$$I(\mathbf{q})=M|\phi(\mathbf{q})|^2G(\mathbf{q}) \tag{2.16}$$

where M is the number of layers in the crystal and $G(\mathbf{q})$ is called the modulation function for the crystal which contains all the stacking information and is sharply peaked at 00l reciprocal lattice points [20]. This will cause the scattering to decay in a direction

parallel to the axis of the rods in reciprocal space. Because a powder sample contains a distribution of grain sizes, $G(\mathbf{q})$ is averaged over a Gaussian distribution of stacking size centered at M_o with a distribution width of σ_m. $G(\mathbf{q})$ is further modified by inter-plane strain. This can be described by a simple strain distribution [20]:

$$p(\delta) = g\delta_D(\delta) + (1-g)\frac{1}{\sqrt{2\pi\langle\delta^2\rangle}} e^{\frac{\delta^2}{2\langle\delta^2\rangle}} \tag{2.17}$$

where $\sqrt{\langle\delta\rangle^2}$ is the fluctuation in spacing between adjacent layers, g is the fraction of low strained layers and δ_D is the Dirac delta function. Inter-plane strain and only having finite layer stacking both cause broadening of the 00*l* reflections.

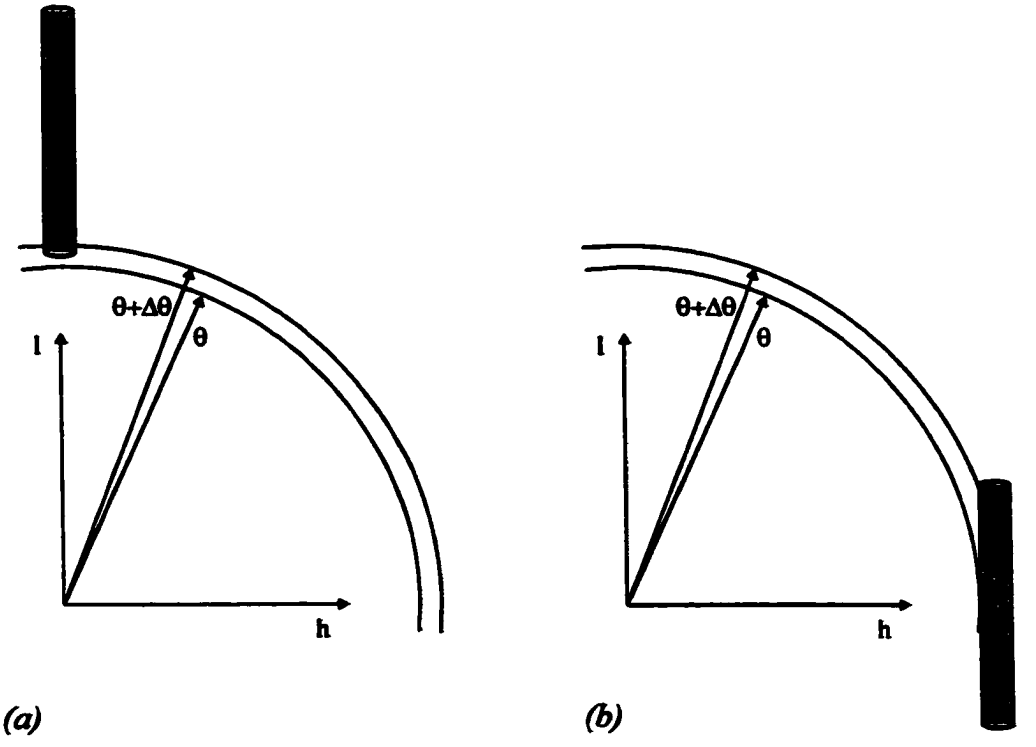

Figure 2.5 (a) Intersection of a rod by the Ewald sphere for a 00l reflection, giving rise to a symmetric peak. (b) Intersection of a rod by the Ewald sphere for a h00 reflection, giving rise to an asymmetric peak.

Figure 2.5 shows the effects of inter-plane and in-plane broadening on the XRD pattern of a sample. For a *00l* reflection the Ewald sphere will intercept a shape-broadened peak perpendicularly as shown in figure 2.5(c), giving rise to a symmetrically broadened peak. For *hk0* reflections, the sphere will be tangential to the rod as shown in figure 2.5(b). This produces an asymmetrical peak with a sharp onset and a long Warren tail. In the structural refinement program by Shi, Reimers and Dahn the Ewald sphere is replaced by a cylinder to make the numerical integrals for the intensity more manageable [20]. This is known as the tangent cylinder approximation [21].

The parameters used in the refinement program by Shi, Reimers and Dahn are summarised in the table below.

Parameter	*Description*
a	*In plane Cell constant (Å)*
d_{002}	*Interlayer Spacing (Å)*
L_a	*Layer Extent (Å)*
M	*Total Number of Layers*
σ_M	*Width of M Distribution*
ζ	*In plane strain*
$\sqrt{\langle\delta\rangle}$	*Inter Plane Strain (Å)*
P	*Probability of Random Stacking*
g	*Fraction of Organized Carbon,*

Table 2.1 Parameters used in the structure-refinement program for disordered carbons by Shi, Reimers and Dahn [20].

Most of these parameters have already been defined. The probability of random stacking is defined in terms of a hexagonal lattice. P is the probability of a random shift between adjacent layers while the probabilities for a registered shift to a B or C layer are both

equal to *(1-P)/2*.

2.2.3 The Rietveld Refinement Method

In order to obtain quantitative information about the crystal structure, a program based on the Rietveld method for crystal structure refinement [22,23] was used. The method is based on fitting intensities obtained from step-scanning measurements of powder samples to the equation:

$$Y_{ic} = Y_{ib} + \sum_q G_{iq} I_q \tag{2.18}$$

where Y_{ic} is the net intensity calculated at the point i in the pattern, Y_{ib} is the background intensity, G_{iq} is a normalised peak profile pseudo-Voigt function, I_q is the intensity of the q^{th} Bragg reflection, and q is summed over all reflections contributing to the intensity at the point i. The intensity, I_q, is given by the expression:

$$I_q = SM_q L_q |F_q|^2 W_q \tag{2.19}$$

where M_q is the multiplicity and W_q takes into account the decrease in intensity caused by thermal vibrations, and is called the Debye-Waller temperature factor. It is assumed here that W_q is the same for all the atoms in the crystal.

The goodness of the fit was measured by two parameters:

(i) the Bragg R_B: $$R_B = \frac{\sum |I_{qo} - I_{qc}|}{\sum I_{qo}} \tag{2.20}$$

(ii) the "goodness of fit" (GOF): $$\chi^2 = \sum \left[\frac{(Y_{io} - Y_{ic})^2}{Y_{ic}} \right] \frac{1}{N} \tag{2.21}$$

where N is the number of data points and I_{qo} is the 'observed' integrated intensity of reflection q calculated at the end of the refinement after apportioning each Y_{io} between

the contributing peaks and background according to the calculated intensities I_{qc}.

2.2.4 XRD Sample Measurement and the In-situ Technique

Powder XRD measurements were made with a Siemens D5000 powder diffractometer equipped with a Cu target x-ray tube and a diffracted-beam monochromator. Since many of the materials in this study are air-sensitive, a special XRD sample stage was designed to fit in the D5000. The stage, shown in figure 2.6, consists of a base with a well to contain the powder sample and a cover, which has an aluminized Mylar window in the shape of an arc. The base and cover were secured together by screws and sealed by means of an o-ring which sat in the grove in the sample stage's base. Since the Mylar window is so far removed from the scattering axis it does

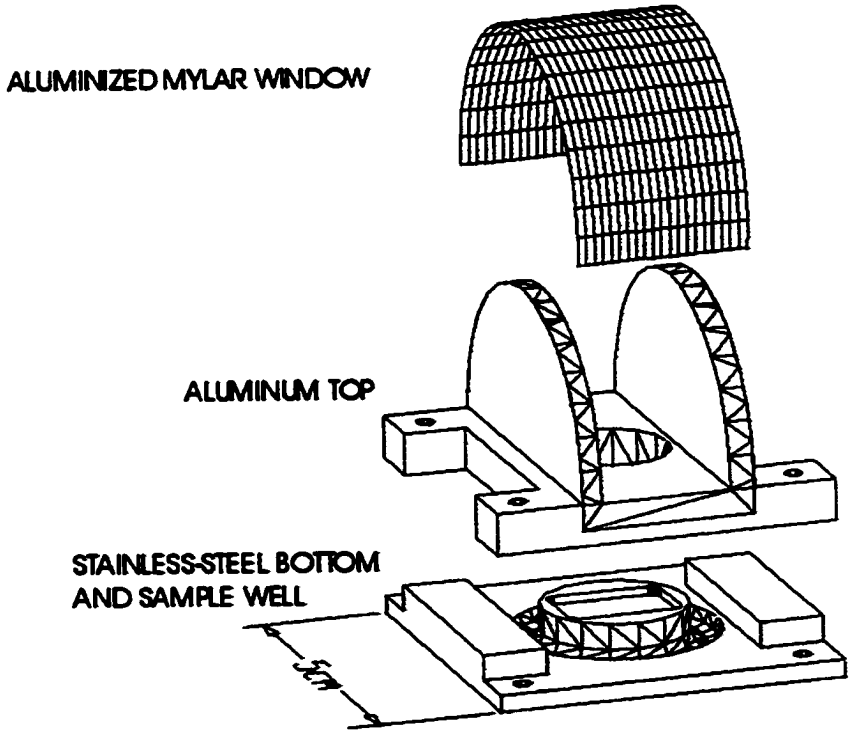

Figure 2.6 Air sensitive sample XRD stage.

not contribute to the x-ray pattern. Furthermore, because it is always at right angles to the beam, the beam attenuation by the window is constant and was found to be about 5%. To further improve the beam intensity, the samples were loaded in a helium-filled glovebox. A sample stage designed by Aaron Davis [24] similar to the stage described above, but equipped with a heater, was also used. This stage could heat samples at temperatures up to 600°C with an accuracy of ±1°C while XRD spectra were collected. The atmosphere in the sample stage was kept pure by a constant flow of helium.

To understand the processes occurring during the cycling of a cell, in-situ XRD measurements were made on working cells. To do this a hole was made in the stainless steel cell can of the coin cell in which was fit a Beryllium window. The window was fixed in place, and thereby the cell was also sealed, with epoxy (Varian Torr-Seal). A special holder kept the cell in place in the x-ray spectrometer while both XRD measurements and cycling occurred simultaneously. Further details of the in-situ XRD technique can be found in reference [25].

2.3 THE MÖSSBAUER EFFECT AND IN-SITU MÖSSBAUER MEASUREMENT

2.3.1 Theory of the Mössbauer Effect

Mössbauer spectroscopy is based on measuring the absorption of gamma rays by nuclear transitions. This statement immediately implies the necessity of three things: a source of tuneable gamma rays in the range of the nuclear transition, a reference or standard from which to measure the absorption with respect to and a suitable detector. It turns out that the requirement of a tuneable source is rather subtle and probably is

responsible for the delay in the appearance of the technique until the late 1950's. For instance suppose a nuclear absorption in a certain element, X, is to be measured. The obvious source of radiation for the experiment is to excite the nuclei of another sample of X or to create an atom of X in its excited state (by nuclear decay) and use the emitted radiation for the experiment. However, the radiation emitted will cause the nucleus of the emitting atom to recoil with the same momentum as the emitted photon. This will cause the excitation of optical phonon modes in the crystal lattice. The resulting motion will Doppler-shift the radiation. A similar effect will happen at the absorber. The measured absorption spectrum, then, will be a low-intensity broad peak, which represents the overlap of the distributions of the Doppler-shifted absorption and emission energies.

This problem is solved by selecting elements such that their recoil energy is less than the minimum energy required to excite an optical phonon mode (the Einstein energy). The probability of exciting a phonon will now be low and recoil-free transitions can occur in the source and absorber in which the recoil is taken up by the whole crystal without exciting phonons. The probability of a recoil-free event is given by the "recoil-free fraction", f_r, which is related to the magnitude of the incident photon wavevector, k, and the mean square vibrational amplitude of the resonating atom [26]:

$$f_r = exp(-k^2 \langle x^2 \rangle) \tag{2.22}$$

A rough approximation for $\langle x^2 \rangle$ can be made using the Debye model. This leads to the following expression for f_r [26]:

$$f_r = exp\left[\frac{-6E_R}{k_B\theta_D}\left\{\frac{1}{4}+\left(\frac{T}{\theta_D}\right)^2\left(\int_0^{\theta_D/T}\frac{x\,dx}{e^x-1}\right)\right\}\right] \tag{2.23}$$

where E_R is the recoil energy and θ_D is the Debye temperature. In the high temperature

limit equation (2.23) can be approximated as:

$$f_r \approx exp\left[\frac{-6E_R\hbar c}{k_B\theta_D{}^2 E_\gamma}\right]; \qquad T > \theta_D/2 \tag{2.24}$$

where E_γ is the incident photon energy. Substituting E_R = 1.957×10^{-3} eV, θ_D = 440K, T = 298 K and E_γ = 14.41 keV for ^{57}Fe [26] gives an approximate value for f_r of about $e^{-10^{-14}} \approx 1$.

The source energy is tuned by employing the Doppler effect. The emitted energy, E_γ, from a moving source is shifted given by an amount [26]:

$$E_D = \frac{v}{c}E_\gamma. \tag{2.25}$$

At zero temperature the width of the transition will be limited only by Heisenberg's uncertainty principle. For ^{57}Fe this line width is about 10^{-8} eV which is exceedingly small when compared to the energy of the Mössbauer transition in ^{57}Fe of about 10^4 eV. Thus a velocity of just ±3 mm/s will shift the emitted energy of the source by ±10^{-7} eV which is ten times the natural line width!

2.3.2 The ^{57}Co Source and Nuclear Transitions in Iron

To continue the theory about the Mössbauer it is necessary to specify the source and absorber atoms. In this thesis ^{57}Fe Mössbauer spectroscopy is used. The radiation source is ^{57}Co which decays by electron capture to ^{57}Fe thereby emitting a 14.41 keV and 136.46 keV γ-rays [26]. The decay scheme is shown in figure 2.7. The 14.41 keV line is the one used here for Mössbauer measurements. This line corresponds to the transition between the ground state for ^{57}Fe which has a nuclear spin of I =1/2 and the 14.41 keV

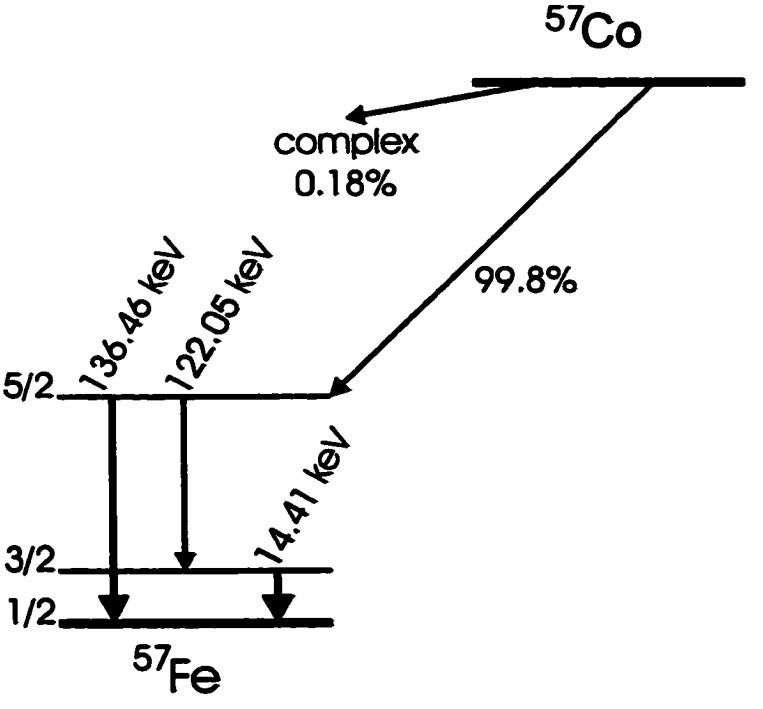

Figure 2.7 The decay scheme of ^{57}Co. The heavy arrows indicate Mössbauer lines for ^{57}Fe. The 14.41 keV line was used in this thesis.

first excited state which has $I = 3/2$.

2.3.3 Hyperfine Interactions

The hyperfine interactions result from the interaction between the nucleus and an electronic or atomic property. The interpretation of these interactions yields information on the electron density and its distribution around the iron nucleus. In short they reveal the chemical environment around the iron nuclei in the sample. The three main types of hyperfine interactions are the electric monopole interaction (the isomer shift), the magnetic dipole interaction (the nuclear Zeeman effect) and the electric quadrupole interaction (quadrupole splitting). Each will be discussed in its own subsection below.

2.3.3.1 The Isomer Shift

The isomer (or chemical) shift results from the Coulomb interaction between the nuclear charge distribution and the electronic charge distribution at the nucleus, which is from the s-orbitals. The shift is measured from a standard scale, which is usually zeroed at the 14.41 keV line in ^{57}Fe. For a given source the isomer shift, δ, measured from some standard is a linear function of the electron charge density $|\Psi(0)|^2_A$ at the nucleus of the absorber [26]:

$$\delta = const\left(\delta R_{nuc}/R_{nuc}\right)\left[|\Psi(0)|^2_A - C\right] \tag{2.26}$$

where R_{nuc} is the ground state radius of the nucleus, δR_{nuc} is the change in the nuclear radius upon going from the exited state to the ground state and C is a constant, depending on the measurement standard. For ^{57}Fe δR is negative, meaning that a reduction in the charge density around the iron nucleus results in a positive isomer shift [26].

Changes in the s-orbital charge density around the nucleus are mostly affected by the valence s-orbitals, or indirectly by the valence d- and p-orbitals which screen the inner s-orbitals. By measuring a number of different iron compounds it becomes clear that δ is greatly affected by the valence of the iron as shown in figure 2.8. Fortunately the assignment of the valence-state for ionic (high-spin) iron compounds is unambiguous. For low-spin compounds it is more difficult, but is aided by the fact that low spin iron (II) compounds have a small quadrupole splitting ($0 \leq \Delta \leq \sim 0.8$ mm/sec) while the splitting is larger in low spin iron (III) compounds ($\sim 0.7 \leq \Delta \leq \sim 1.7$ mm/sec) [26].

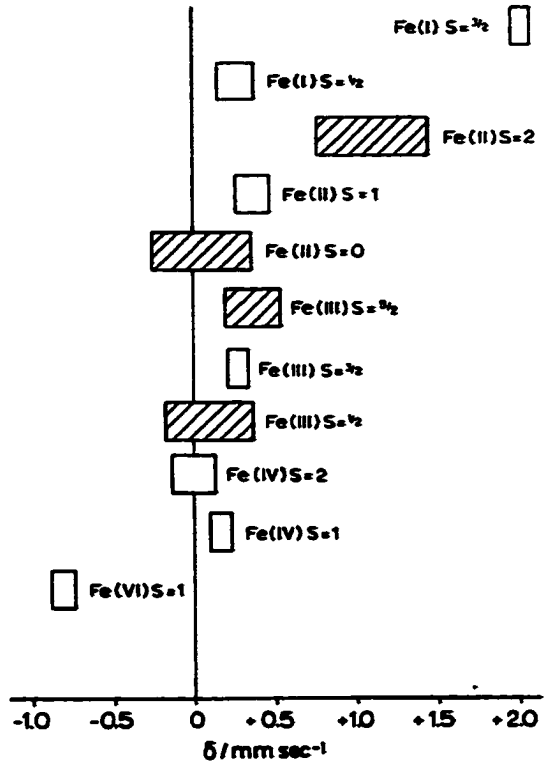

Figure 2.8 Approximate ranges of isomer shifts observed in iron compounds (relative to metallic iron at room temperature). Shadowed regions belong to more frequently met configurations. From reference [26].

2.3.3.2 Quadrupole Splitting

The electronic distribution around the nucleus is described by the electric field gradient (EFG). If this field is inhomogeneous the EFG can interact with the quadrupole moment of the nucleus. Any nuclei with $I > ½$ (such as the first excited state of ^{57}Fe) will have a non-zero quadrupole moment. The interaction of the EFG with the nuclear quadrupole moment will split the nuclear levels, giving rise to the electric quadrupole interaction. The energy of the interaction is given by [26]:

$$E_Q = \frac{eQV_{zz}}{4I(2I-1)}\left[3m_I^2 - I(I+1)\right]\left(1+\eta^2/3\right)^{1/2} \qquad (2.27)$$

where m_I is the magnetic quantum number with values $m_I = I, I\text{-}1, \ldots -I$, Q is the quadrupole moment at the nucleus, V_{ZZ} is the z-component of the EFG tensor and η is a parameter that measures the asymmetry of the EFG (for cubic symmetry about the Mössbauer nucleus η=0). Since only the square of m_I appears in (2.27), the $I = 3/2$ state for ^{57}Fe will be split into two substates which will be centred around the energy of the unsplit level. The resulting Mössbauer spectrum will thus be a doublet. The centre of the doublet corresponding to the centre shift energy discussed in the previous section and the difference in energy between the two peaks corresponding to the difference in energy between the split $I = 3/2$ energy level. As mentioned in the previous section, low spin iron (II) compounds typically have a small quadrupole splitting of $0 \leq \Delta \leq \sim 0.8$ mm/sec ($0\text{-}4\times10^{-8}$ eV), while the splitting is larger in low spin iron (III) compounds and is typically $\sim 0.7 \leq \Delta \leq \sim 1.7$ mm/sec (3×10^{-8} - 8×10^{-8} eV) [26].

2.3.3.3 The Nuclear Zeeman Effect

Just as in the Zeeman effect for electrons, the nuclear levels split when a magnetic field is applied. In the nuclear Zeeman effect the interaction of the nuclear magnetic dipole moment, μ, with a magnetic field, H, at the site of the nucleus, splits the nuclear state with spin $I(I>0)$ into $(2I+1)$ sublevels with the eigenvalues [26]:

$$E_m = \frac{-\mu H m_I}{I} = -g_N \beta_N H m_I, \tag{2.28}$$

The nuclear magnetic moment is related to the nuclear Bohr magneton, β_N, (3.151×10^{-12} eV/Oe), by the nuclear Landé splitting factor, g_N:

$$\mu = g_N \beta_N I. \tag{2.29}$$

The selection rule for transitions between the levels is given by $\Delta m_I = 0, \pm 1$, thus giving

rise to six allowed transitions as shown in figure 2.9. This will result in a six-line Mössbauer absorption spectrum.

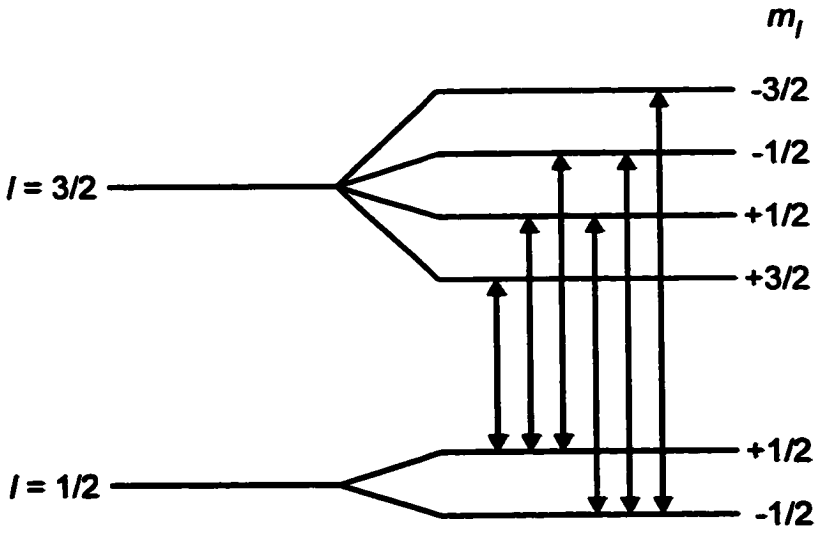

Figure 2.9 The six allowed transitions between the magnetically split I = 3/2 and I = 1/2 levels in ^{57}Fe which give rise to a six line Mössbauer spectrum.

The six-line spectrum will also arise if the absorber has an internal magnetic field, as is often the case for iron and iron compounds. As an example, iron metal has an internal magnetic field of 330 kOe. The values of the nuclear magnetic moment of the iron nucleus are 0.0903±0.0007 nuclear magnetons (n.m.) and -0.1549±0.0013 n.m. in the $I = 1/2$ and $I = 2/3$ states respectively [26]. Substitution into (2.28) yields a splitting of 9.391×10^{-8} eV (~1.96 mm/s) for the $I = 1/2$, $m_I = 1/2$ level and -1.611×10^{-7} eV (~3.36 mm/s) for the $I = 3/2$, $m_I = 3/2$ level. Thus the transition energy between these two states will be shifted from the unsplit 14.41 keV ^{57}Fe line by -2.550×10^{-7} eV (~ -5.31 mm/s). This line will be the leftmost in the sextet.

The magnetic ordering of the sample, which is signified by a sextet in the Mössbauer spectrum, can be used to measure the sample grain size. If m is defined as the magnetic moment per iron atom and N_{grain} is the number of atoms per grain then

$M_{grain} = mN_{grain}$ will be the magnetic moment per grain. The required energy to rotate M_{grain} off the easy axis of the grain will then be:

$$E_H = HM_{grain} = HmN_{grain} \tag{2.30}$$

where H is the applied magnetic field. If E_H is of the order or smaller than k_BT then the

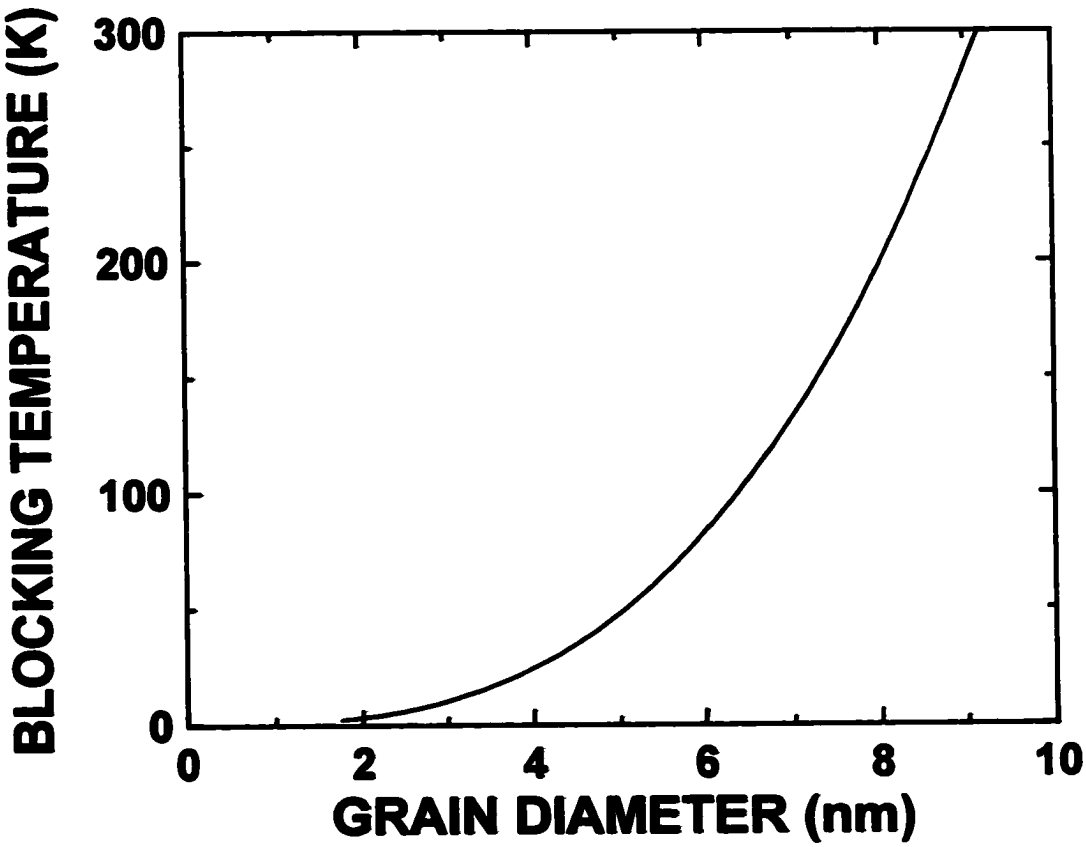

Figure 2.10 The relationship between the blocking temperature and the grain diameter for iron. From reference [28].

internal magnetic field will rotate spontaneously and the average field at the nuclear site will be zero. The temperature at which this occurs is called the blocking temperature, T_B [27,28]. From equation (2.30) T_B is highly dependent on the grain size. Figure 2.10 shows the relation between T_B and grain size for iron.

2.3.4 Mössbauer Sample Measurement and the In-situ Technique

^{57}Fe Mössbauer spectra were measured using a Wissel System II constant acceleration spectrometer. The source was ^{57}Co embedded in a palladium matrix. Data were collected using an Ortec ACE multichannel scaling board. The source/spectrometer had an intrinsic line width of 0.22 mm s^{-1}. The centre-shift and splitting parameters were calibrated using α-Fe. To understand the processes occurring during the cycling of a cell, in-situ Mössbauer measurements were made on working cells. The in-situ Mössbauer cells were similar to the XRD in-situ cells except a hole was made in the stainless steel cell can and in the cell top in which was fit Beryllium windows. The Be window in the cell top was made thick so as to fill up the volume of the steel spring and spacer which were excluded from the cell for obvious reasons. Figure 2.11 shows a diagram of the Mössbauer in-situ cell. Steel tabs were welded to the edges of the cell can and top for

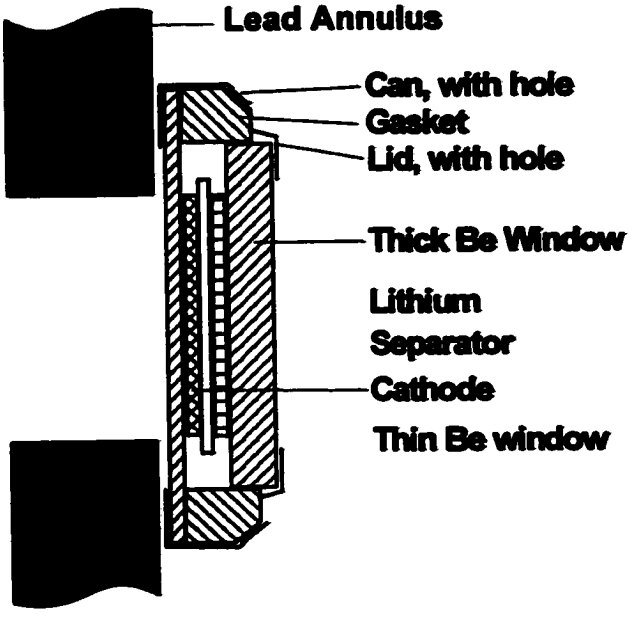

Figure 2.11 The in-situ Mössbauer cell showing also the position of the lead shielding.

electrical connections to the cell cycler. A 4 mm thick annulus of lead was taped to the cell to shield the source radiation from the cell can and top, but allowing it to pass through the beryllium window as shown in the figure.

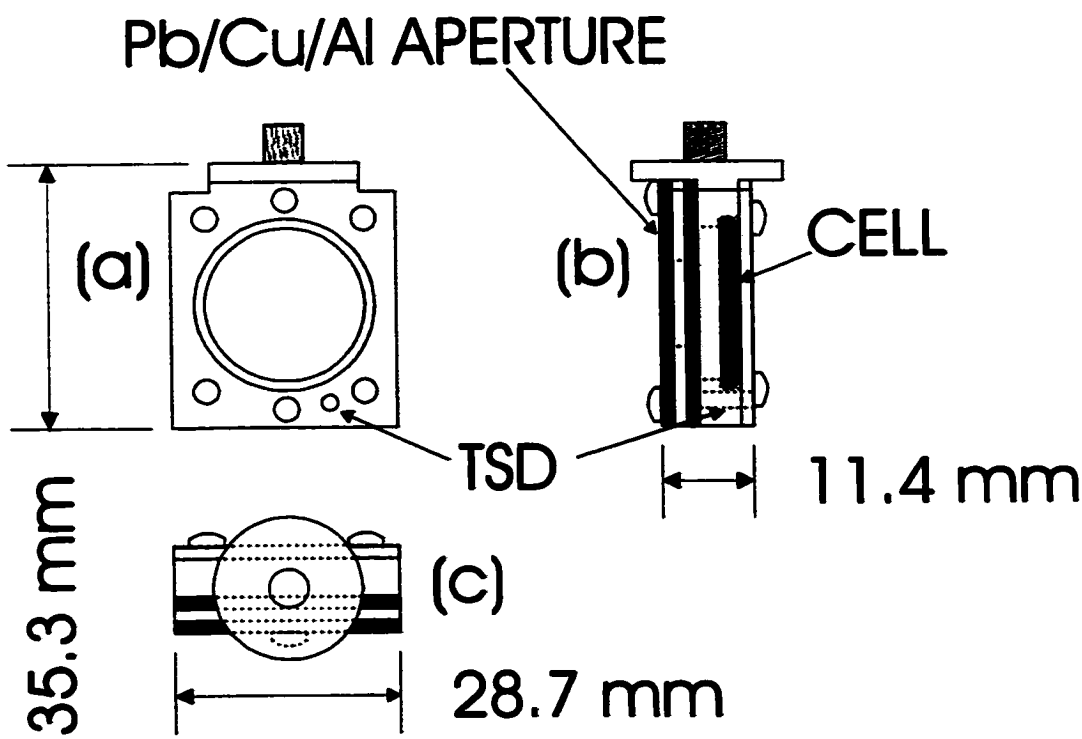

Figure 2.12 The cold-finger cell sample mount. (a) Copper main block with hole for TSD. (b) Side view of assembled sample mount with cell. (c) Top view of assembled sample mount.

Low temperature studies were carried out using a DMX-20 cold-finger interface (APD Cryogenics Inc.). Cryogenic helium was supplied to the cold finger via a vibration free coupling to a two-stage helium expander (Displex DE-202 (APD)) and a helium compressor (APD model HC-2D-1). The system was fitted with a thermostatically controlled heater (Lakeshore Cryogenics Inc. model DRC 80C) which could keep constant temperature to within ±0.1K. A special attachment, shown in figure 2.12, was made to mount cells to the cold-finger. It consisted of a copper block that screwed into

the cold-finger, a copper plate to hold the coin-cell in place and Pb/Cu/Al shielding with vacuum grease in a small hole in the copper block. Coin cells with beryllium windows were cycled to the desired state of charge at room temperature and then cooled at open circuit in the sample mount before obtaining the low temperature Mössbauer spectra. Cells not measured at 0 V were insulated from shorting by covering one side of the cell with electrical tape.

2.4 TRANSMISSION ELECTRON MICROSCOPY

2.4.1 Theory of Transmission Electron Microscopy

Figure 2.13 shows a diagram of a transmission electron microscope (TEM). The TEM consists of an electron gun which emits electrons (typically between 60-150 keV) through a series of condenser magnetic lenses. The beam then interacts with the specimen before passing through a series of focusing lenses and apertures. The beam is finally imaged on a fluorescent screen or is energy analysed with a electron energy-loss spectrometer (EELS). Because electrons interact strongly with atoms by elastic and inelastic scattering, samples have to be very thin (on the order of 5 nm-0.5 μm). Ideally samples should also be conducting to avoid charging effects. TEM can provide high resolution (tenths of nanometers) since the elastic scattering process is highly localised to the region occupied by the screened Coulomb potential of an atomic nucleus [29].

In general two imaging modes are used with the TEM. In the *bright-field mode* the objective aperture is centred along the optical axis and is made small so only the primary electron beam can pass through. This mode produces high-resolution images of the sample which are focused on a fluorescent screen or a CCD camera. In the *dark-field*

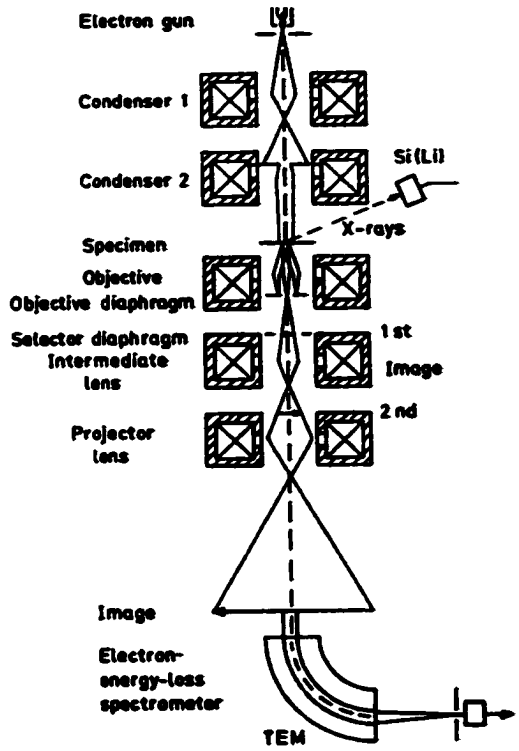

Figure 2.13 Schematic of a TEM equipped for x-ray and electron energy loss spectroscopy. From reference [29]

mode the objective diaphragm is positioned so that only selected scattered electrons from the sample can pass through. The resulting image shows only the grains in the sample which are oriented to diffract the electrons through the spot selected by the objective diaphragm.

2.4.2 TEM Sample Preparation and Measurement

TEM samples were prepared on copper grids by ultrasonically suspending the sample particles in acetone and then placing a drop of this suspension on the grid and letting the acetone evaporate. Samples were measured with a Hitachi H9000 TEM equipped with a Gatan Parallel EELS CCD Camera, both interfaced to computers. Routinely the instrument resolves at about 0.18 nm for bulk lattice spacings and atomic structure of surfaces at about 0.25 nm.

Chapter 3

Implications of Finite Size Effects in Intercalation Materials

3.1 BACKGROUND

As in other fields of materials science, nano-sized materials are finding applications in lithium ion batteries. Carbons containing nano-sized pores have been considered as high capacity anode materials [30]. It has also been shown that Sn anodes can be cycled reversibly if the Sn is made a nano-sized component of a composite material [31]. Nano-crystalline cathode materials are also presently being studied [32,33,34]. All the above materials have the common property that features in the voltage curves become rounded-off as the grain size becomes smaller. This is a well-known property of systems with finite-size [35,36,37]. In addition, the chemical potential

for intercalation or for alloying in the above systems changes with the grain-size. This is consistent with surface effects that can change the chemical potential of phase transitions in the bulk [38]. As the grain-size becomes smaller these surface effects ought to have greater importance. Here a lattice gas model is used to study the consequences of surface and size effects in lithium intercalation materials [39]. However the theory can equally be applied to other finite sized systems which are described well in the bulk by a lattice gas, such as gas adsorption on finite sized surfaces.

3.2 THE LATTICE GAS DESCRIPTION OF INTERCALATION

Equation (1.1) relates the voltage of a lithium ion cell to the chemical potential of lithium and its associated valence electron in the cathode and in the anode. In a lithium test cell the anode is lithium metal and the chemical potentials associated with the anode will not change during cycling and by convention are taken to be zero. Thus (1.1) reduces to $V = -\mu/e$ where $\mu = \mu_{Li^+}^{cathode} + \mu_{e^-}^{cathode}$ is the chemical potential of lithium in the cathode. The problem of modelling voltage curves then is equivalent to calculating the chemical potential as a function of lithium concentration. The lattice gas model is well suited to this purpose since lithium intercalation materials have large diffusion coefficients and are in quasi-equilibrium at room temperature, the host lattice is not changed appreciably during the intercalation process and because the Li-Li interactions in these materials are short-range [40]. Usually a rigid band approximation for the electronic contribution to the chemical potential is made in these models. The approximation is described in figure 3.1. When electrons are removed from the band structure of an intercalation material during charge the Fermi level will tend to decrease

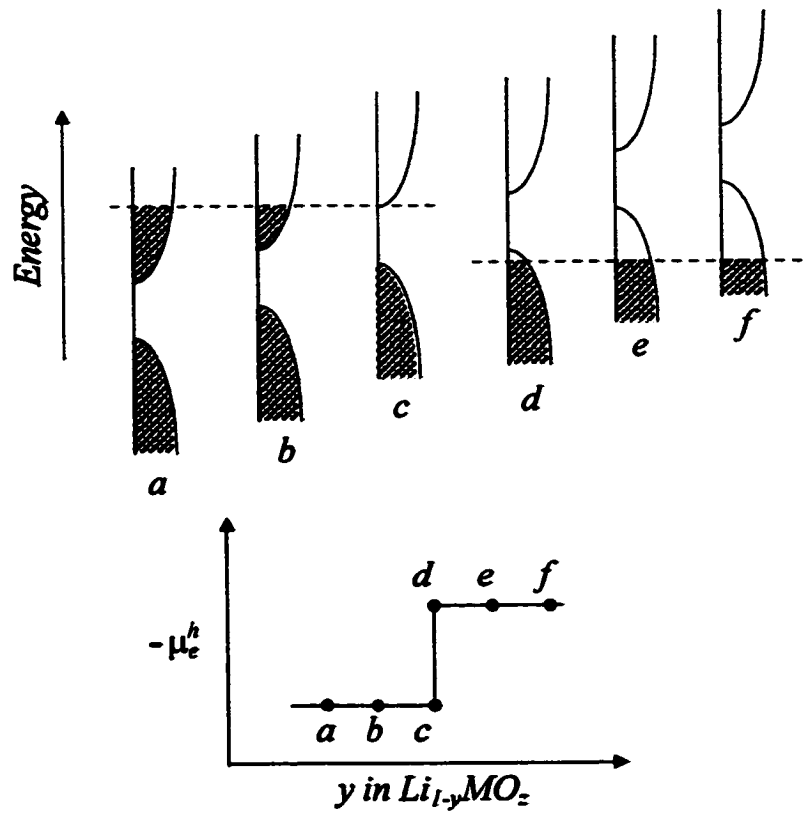

Figure 3.1 The rigid band picture of intercalation. As electrons are removed from the cathode, lithium ions are removed at the same time. The removal of the lithium ions tends to shift the entire band structure to higher energy. The combination of the emptying of the band and the shift caused by lithium removal causes the Fermi energy to remain roughly constant during the intercalation process as shown in the bottom panel from points 'a' to 'c'. At point 'c' a band gap is encountered, which causes the Fermi level to drop abruptly in energy.

in energy as electrons from high-energy bands are removed. However the lithium ions that are removed at the same time during the charge will decrease the cation concentration in the cathode and will tend to shift the band structure to higher energy. The same effects will happen in reverse during discharge. To a first approximation both effects cancel each other and the Fermi energy can be regarded as a constant. The approximation will not hold when a band gap is encountered during an intercalation

process. When this happens the Fermi energy can change by as much as an electron volt with a corresponding rise in the cell voltage [41,43]. In this case the electronic contribution to the chemical potential must be included in the lattice gas calculation [43].

The derivation of the lattice gas model starts with a lattice of sites. To each site an occupation number, n_i, is assigned which is equal to 0 if the site is empty and 1 if it contains a lithium atom. Each site may also have a site energy associated with it for filling the site. As a simple example suppose that an infinite one-dimensional lattice with only nearest neighbour Li-Li interactions and a uniform site energy is to be modelled. The total energy for the infinite lattice gas is:

$$A_{(\infty)} = U \sum_{<i,j>} n_i n_j + (E - \mu) \sum_i n_i \tag{3.1}$$

where U is the nearest neighbour interaction energy, $<i,j>$ represents a sum over nearest neighbour sites and E is site energy. Infinite lattices are modelled by the use of periodic boundary conditions (PBC's). The lithium concentration can then be defined as:

$$x = \frac{1}{N} \sum_i n_i = \frac{n}{N} \tag{3.2}$$

where N is the number of lattice sites and n is the total lattice occupation.

Equation (3.1) can be shown to be equivalent to the Ising model, which has been extensively used to study magnetic systems. In the Ising model, each lattice site is assigned with a spin σ_i which can be either up (+1) or down (-1). Then if parallel (anti-parallel) sites have an interaction energy $-J$ ($+J$) the energy of an infinite Ising lattice in an upward magnetic field H will be:

$$A_{m(\infty)} = -J \sum_{<i,j>b} \sigma_i \sigma_j - H \sum_i \sigma_i + E_{mo} \tag{3.3}$$

where E_{mo} is some additive constant. Then, defining the magnetization per spin as:

$$m = \frac{1}{N}\sum_i \sigma_i \,, \tag{3.4}$$

the following relations can be made upon comparing (3.1) and (3.3) [40]:

$$A_{m(\infty)} = A_{(\infty)} - \mu n \tag{3.5}$$

$$m = 2x - 1 \tag{3.6}$$

$$J = -U/4 \tag{3.7}$$

$$H = \tfrac{1}{2}(\mu - E - \gamma U/2) \tag{3.8}$$

$$E_{mo} = \frac{N}{2}(\mu - E) - \frac{N\gamma U}{8} \tag{3.9}$$

where γ is the number of nearest neighbours in the lattice. In a famous paper by Onsager, equation (3.3) was solved in closed form for a one-dimensional lattice giving the magnetisation as a function of field and temperature [44]:

$$m = \frac{\sinh(H/k_BT)}{\left(\sinh^2(H/k_BT) + e^{-4J/k_BT}\right)^{1/2}}. \tag{3.10}$$

In the language of the lattice gas this then becomes:

$$x = \frac{1}{2}\left\{1 + \frac{\sinh[(\mu - U - E)/2k_BT]}{\left(\sinh^2[(\mu - U - E)/2k_BT] + e^{U/k_BT}\right)^{1/2}}\right\}. \tag{3.11}$$

Equation (3.11) gives the relation between the lithium composition and the voltage (chemical potential) and is plotted in figure 3.2 for a lattice with repulsive nearest-neighbour interactions ($U = 10k_BT$).

To illustrate the usefulness and limitations of the lattice gas model it is instructive to review some past results. Although such models are usually only semi-qualitative they

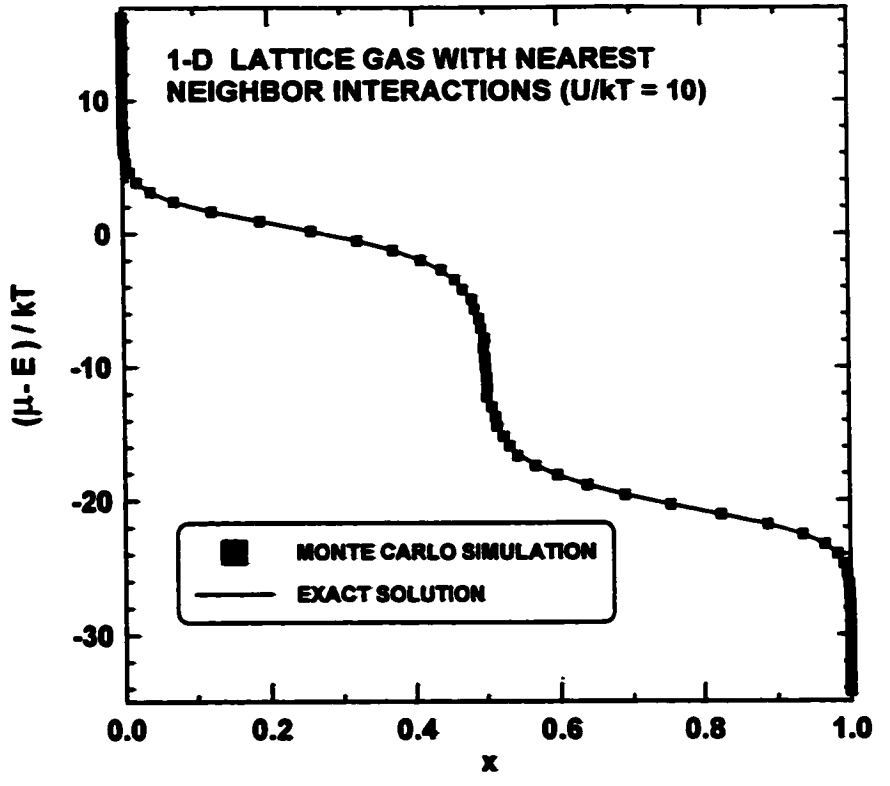

Figure 3.2 The exact solution and a Monte Carlo simulation of the chemical potential versus the composition plotted for a 1-D lattice-gas with a repulsive nearest-neighbour Li-Li interaction of $U = 10k_BT$.

are an important tool to help understand the fundamental processes that occur during intercalation. One of the first such studies used a lattice gas model to describe the intercalation of lithium into Mo_6Se_8 [45]. It was found that a lattice gas model with a mean field attractive Li-Li interaction accurately predicts the temperature dependence of the differential capacity curves of the intercalation process, as shown in figure 3.3. A model with nearest neighbour interactions poorly reproduced the data. This implies long range Li-Li interactions, which is consistent with an elastic mediated interaction caused by lattice expansion during intercalation [45]. The simplicity of the interaction resulted in the lattice gas model having excellent agreement with the experiment.

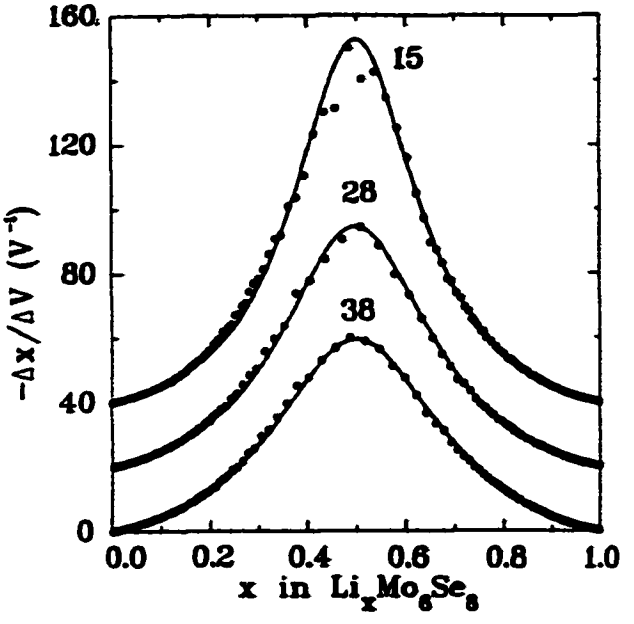

Figure 3.3 Derivative curves, -dx/dV vs V, for $Li/Li_xMo_6Se_8$ cells cycled at different temperatures (o) as indicated (in °C). The solid lines are calculations from a mean field lattice gas model. The data and calculations for 28°C and 15°C have been offset by 20 V^{-1} and 40 V^{-1}, respectively, for clarity. From reference [44].

A more complicated interaction was found for the intercalation of lithium into the layers of TaS_2 [46]. Figure 3.4(a) shows the differential capacity curves of lithium intercalation in Li_xTaS_2 at different temperatures near x = 2/3. Similar behaviour occurs near x = 1/3. The features in the curves are consistent with sub-lattice order-disorder

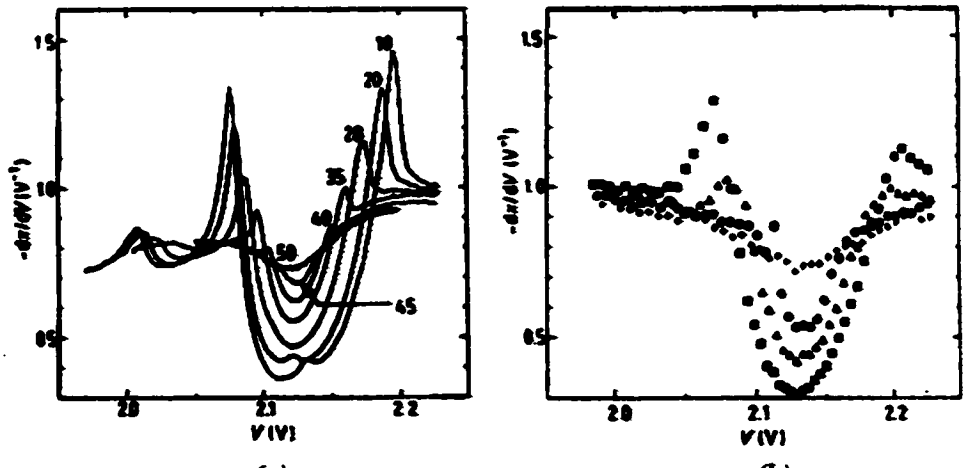

(a) *(b)*

Figure 3.4 (a) Derivative curves, -dx/dV vs V, for a series of discharges of Li_xTaS_2 near x = 2/3. Temperatures are in °C. (b) Derivative curves calculated from a lattice gas model for Li_xTaS_2 described in the text. The calculations correspond to the following temperatures: □, 9.8°C; △, 28.0°C; ●, 38.0°C; +, 60.3°C. From reference [46].

transitions on a two dimensional triangular lattice [46]. The results of a calculation of a triangular lattice gas near x = 2/3 are shown in figure 3.4(b). For this calculation it was found that the short range Li-Li interactions were significant and a combination of repulsive short-range and elastically mediated interactions from inter-layer expansion were used to reproduce the data [46]. Although in this case the agreement between the differential capacity curves with experiment was only qualitative, the physics of the intercalation process was adequately described. This is illustrated by the good agreement obtained for the temperature dependence of the order-disorder transition shown in the phase diagram in figure 3.5.

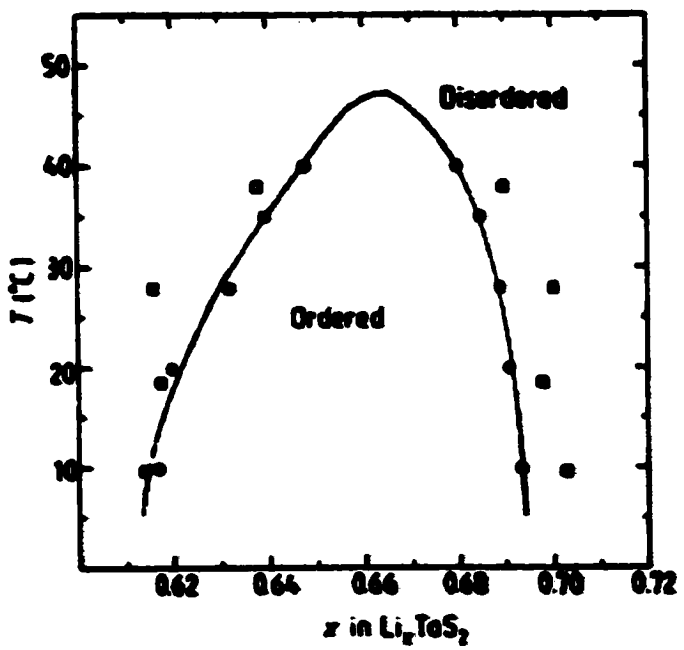

Figure 3.5 A phase diagram (T versus x) for the lithium order-disorder transition near x = 2/3 in 2H-Li_xTaS_2. The full curve through the data (O) is a guide to the eye. Results of the lattice gas calculation described in the text are also shown (□). From reference [46].

As a final example of the lattice gas model for an intercalation material, the intercalation of lithium in $LiNi_xMn_{2-x}O_4$ is a case where a large change in the electronic density of states encountered and the electronic structure of the material must be taken into account [41,43]. Figure 3.6 shows the voltage curves and the corresponding differential capacity curves of $LiNi_xMn_{2-x}O_4$ with different nickel contents. The

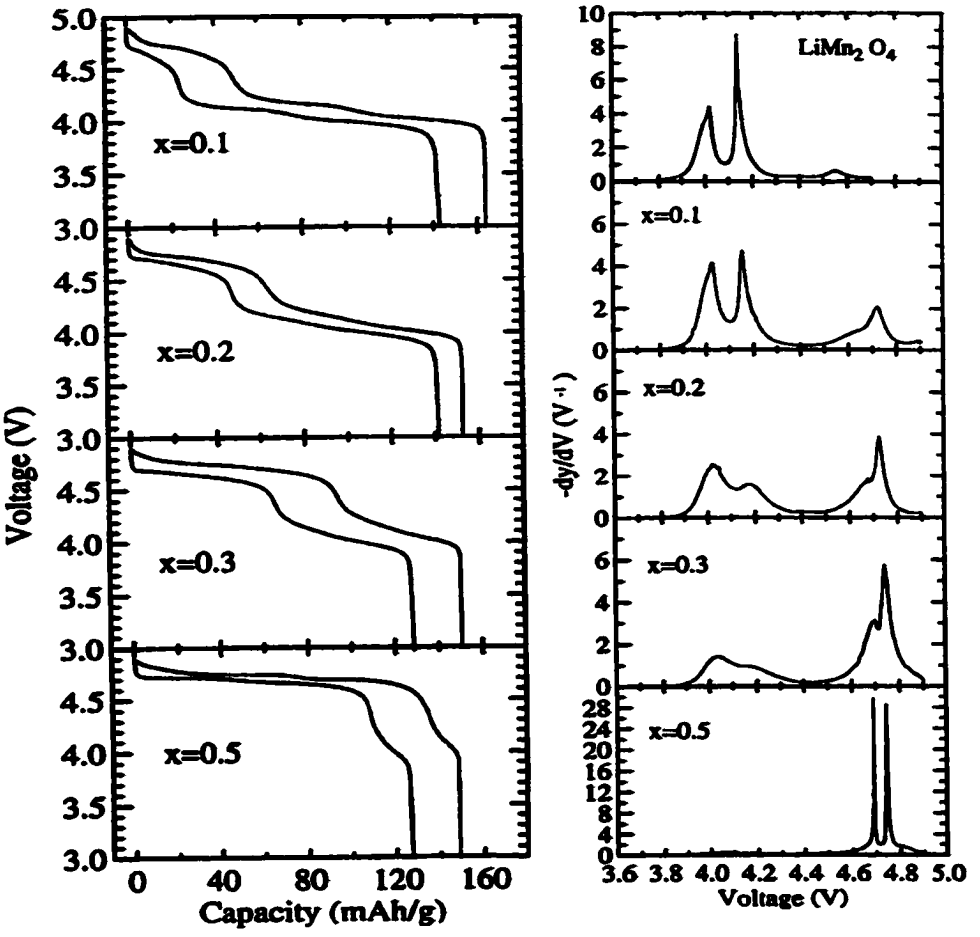

Figure 3.6 The voltage profiles and derivative curves, -dy/dV vs V, for $Li_yNi_xMn_{2-x}O_4/Li$ cells with different Ni content. From reference [43].

appearance of two plateaus in the voltage curve can be explained by supposing that only the manganese is oxidised during charging on the 4.1V plateau:

$$Li^+ Ni_x^{2+} Mn_{1-2x}^{3+} Mn_{1+x}^{4+} O_4^{2-} \rightarrow Li_{2x}^+ Ni_x^{2+} Mn_{2-x}^{4+} O_4^{2-} + (1-2x)Li^+ + (1-2x)e^- \quad (3.12)$$

while the 4.7 V plateau is due to the oxidation of the nickel:

$$Li_{2x}^+ Ni_x^{2+} Mn_{2-x}^{4+} O_4^{2-} \rightarrow Ni_x^{4+} Mn_{2-x}^{4+} O_4^{2-} + 2xLi^+ + 2xe^- \text{ [41]}. \quad (3.13)$$

To reproduce this behaviour it was assumed that the binding energy of lithium on the lattice was greater during the Ni^{2+} oxidation than during the oxidation of Mn^{3+} [43].

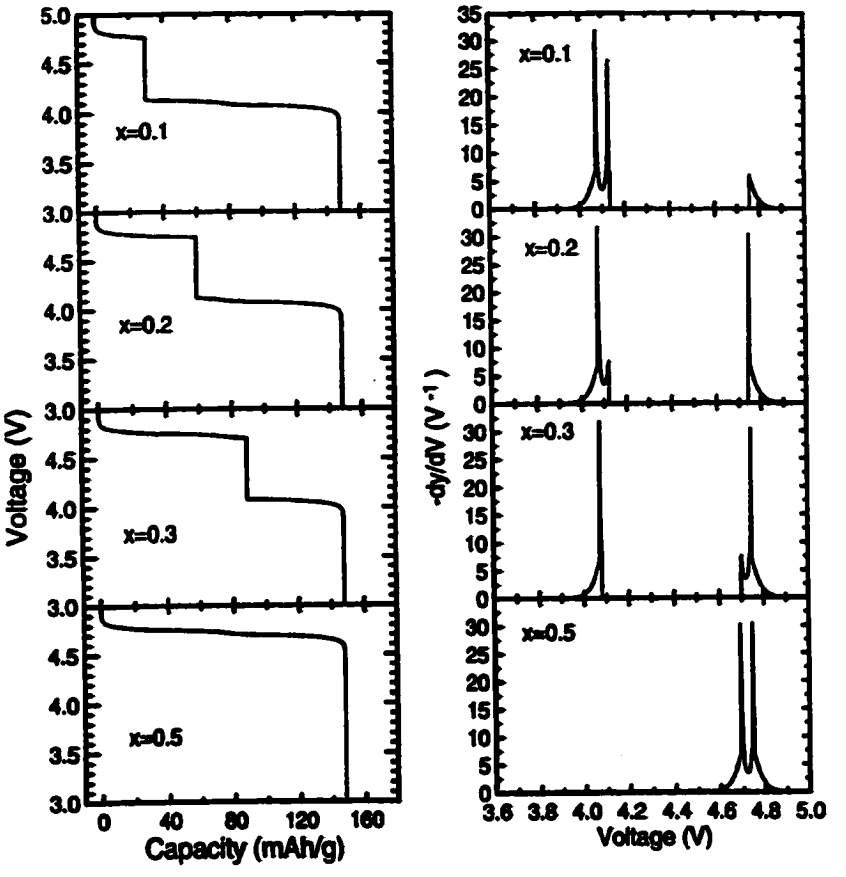

Figure 3.7 Voltage profiles and derivative curves, -dy/dV vs V, from a lattice gas calculation of lithium intercalation in $Li_yNi_xMn_{2-x}O_4$. The model assumes that the binding energy for Li changes abruptly at y = 1-2x. From reference [43].

Otherwise the model was identical to the lattice gas description of $LiMn_2O_4$ [47]. Two scenarios to model the deintercalation were considered: that the lithium has different binding energies whether it is being removed from near a nickel atom or a manganese atom, or that the binding energies of all the lithium atoms will be the same, but the binding energy will uniformly increase when the nickel is oxidised. Only the second scenario gave satisfactory results [43]. These are shown in figure 3.7. Although the results are again only qualitative, they give important information about the delocalisation of charge in this material which results in the lithium having little preference for sites near manganese or nickel atoms.

3.3 THE FINITE LATTICE GAS MODEL OF A NANOCRYSTALLINE INTERCALATION MATERIAL

Up until now lattice gas models have only been used to study lithium intercalation materials that can be described with infinite lattices. In order to model finite systems, such as a nanocrystalline intercalation material, a finite size lattice that reflects the number of sites in the grains must be used. Although there have been many previous studies on other finite-size systems and associated surface effects [35-37,48-53], notably in magnetic lattices, these studies have mostly concentrated on the temperature dependence of phase transitions at zero magnetic field whereas here we are interested in changes in the composition with the chemical potential (or in magnetic terminology the isothermal magnetization as a function of field). Furthermore, previous studies usually separate finite-size and surface effects by using periodic boundary conditions or semi-infinite lattices respectively [49]. Studies that emulate real materials with all boundaries free are few and such studies on antiferromagnetic systems are even fewer [50]. To complicate matters, usually lattice gas models are transformed into an Ising lattice to take advantage of its symmetry. Unfortunately, the two models are not equivalent on lattices with all boundaries free as they are for an infinite lattice. In fact the lattice gas model with free boundaries is equivalent to the Ising model surrounded by spins that are all "pinned" in a particular direction [51].

Some general features of a lattice gas with free boundaries can be extracted from the literature. Because of the finite size of the lattice no singularities can occur during phase transitions and a rounding of the peak in the differential capacity (the susceptibility in the language of magnetism) may be expected [52]. In a finite system with periodic boundary conditions the maximum differential capacity peak height is related to the

system size by

$$(-dx/dV)_{max} \sim L^d \tag{3.14}$$

where L is the linear dimension of the lattice of dimension d [52]. There should also be a shift in the voltage of a phase transition which is size dependent [52]: $V_s \sim L^{-1}$. Wetting transitions on the lattice boundaries should also occur, as is observed in the well-studied case of an Ising lattice with free boundaries [49,53]. As the grain size of active materials becomes smaller these effects will increase in importance.

To model a nano-sized intercalation material a L×L square lattice gas with free boundaries was used. Since many lithium intercalation compounds are layered, the choice of a two dimensional model is not unreasonable for these systems. For simplicity, only nearest neighbour interactions are considered here. The $d = 2$ square lattice gas with only nearest neighbour interactions on an infinite lattice is well understood. For attractive nearest neighbour interactions it undergoes a first order phase transition when $v = \tanh(U/kT) < v_c = -0.44068\cdots$ and $\mu = 2U + E$ [54]. For repulsive interactions when $v > -v_c$ an ordered state with $x = ½$ is formed when $\mu > E$ and the lattice completely fills when $\mu > 4U + E$ [54].

For a finite model with free boundaries it must be further considered that the interaction energy and the lattice binding energy in nano-sized materials will most likely be different on the surface than in the bulk. As an approximation the excess surface and binding energies are restricted only to sites on the first layer. The energy of the model is then [39]:

$$A = U \sum_{<i,j>b} n_i n_j + U_s \sum_{<i,j>s} n_i n_j + (E - \mu) \sum_i n_i + E_1 \sum_{surface} n_i \tag{3.15}$$

where $<i,j>b$ and $<i,j>s$ are sums over nearest neighbour bulk and surface sites

respectively, U and U_s are the interaction energies between bulk and surface lithium atoms respectively and E_l is the excess surface lattice binding energy. Equation (3.15) can be written equivalently in the form of an Ising model surrounded completely by spins pinned downward [39]:

$$A = -J \sum_{<i,j>b} \sigma_i \sigma_j - J_s \sum_{<i,j>s} \sigma_i \sigma_j - H \sum_i \sigma_i - H_1 \sum_{surface} \sigma_i + J \sum_{surface} \sigma_i + J \sum_{corners} \sigma_i \quad (3.16)$$
$$+ E_{mo}$$

where the interaction energy between the boundary sites and the surrounding pinned sites is equal to the bulk interaction energy J. By making the substitution $\sigma_i = 2n_i + 1$ the last two sums in equation (3.16) disappear and equations (3.15) and (3.16) can be compared directly giving [39]:

$$J = -\frac{U}{4}, \quad J_s = -\frac{U_s}{4}, \quad H = (\mu - E)/2 - U, \quad H_1 = [(U - U_s) - E_1]/2, \quad (3.17)$$

$$E_{mo} = 2J[L(L-1)+] + 4J_s(L-1) - HL^2 - 4H_1(L-1).$$

In this study only the effects of different surface and bulk lattice binding energies are considered while the nearest neighbour interaction energy is made constant throughout. Thus U is set equal to U_s.

Equation (3.15) can be used to create μ-E_1 ground-state phase diagrams by comparing the free energies of lattices in a finite set of probable ground-state configurations. The phase behaviour of the ground state can be useful to understand phase changes that occur at finite temperatures. All diagrams made in this manner were found to almost have centre of inversion symmetry. Why this is so can be seen from equation (3.16) which is symmetric about $H = 0$ and $H_l = J$, excepting the sum over the corners, when $J = J_s$. Thus except for this term equation (3.16) is almost symmetric with respect to inversion about the point $\mu = 2U + E$, $E_l = U/2$ (the centre of inversion only

diverges from this point by a factor on the order of L/(L-1) for most lines in the diagrams).

3.4 MONTE-CARLO SIMULATION

Given the expression for the energy of a system, such as equation (3.15) it is straightforward to calculate the partition function from which the probability of any given configuration of the system can be derived under any conditions specified by the intensive variables. In principle this is all that is needed to construct a voltage curve, say, of the system. However this would require the calculation of the probability of every configuration for each point on the voltage curve. For systems with a large number of configurations this is not practical. On the other hand, most of the configurations will have a low probability of occurring anyway. For instance, if a system has strong repulsive interactions, a configuration with all the lithium clumped together is unlikely. If only likely configurations were included then the amount of calculations required to find average quantities (such as the lithium concentration at a given voltage) would be reduced significantly. Furthermore if the quantity was averaged over a million or so of these likely configurations, this ought to be a good estimate of the quantity in question. This is in essence the Monte Carlo method.

The way to choose "likely configurations" requires the choice of some artificial dynamics for the system. According to the Ergodic theorem the equilibrium state doesn't depend on the path taken. Thus any reasonable dynamics which lead to equilibrium will be acceptable. Note that since the dynamics are artificial, Monte Carlo simulations cannot tell us anything about kinetics.

The simplest dynamics are Markov processes, in which the state of the system

does not depend on its past history. This adequately describes most systems, except those that exhibit hysteresis, which is forbidden in a Markov process. If the probability for a system to be in a state **x** is $P(\mathbf{x})$ and the transition probability between the states **x** and **x'** is $W(\mathbf{x},\mathbf{x}')$ then for a system in equilibrium which follows a Markov process [55]:

$$W(\mathbf{x},\mathbf{x}')P(\mathbf{x}') = W(\mathbf{x}',\mathbf{x})P(\mathbf{x}). \tag{3.18}$$

Since lithium intercalation is described by a grand canonical description, $P(\mathbf{x})$ is given by:

$$P(\mathbf{x}) = \frac{e^{-(A-n\mu)/k_BT}}{Z};\ Z = \sum_{\mathbf{x}} e^{-(A-n\mu)/k_BT} \tag{3.19}$$

where Z is the grand canonical partition function. Choosing the simplest form of $W(\mathbf{x},\mathbf{x}')$, namely $W(\mathbf{x},\mathbf{x}') = 1$, then $W(\mathbf{x}',\mathbf{x}) = e^{-\Delta(A-n\mu)/k_BT}$ where $\Delta(A\text{-}n\mu) = (A\text{-}n\mu) - (A'\text{-}n'\mu)$. This implies a simple formula for making transitions between states: The transition should be made with the probability $e^{-\Delta(A-n\mu)/k_BT}$ if $\Delta(A\text{-}n\mu) > 0$, and with a probability of 1 if $\Delta(A\text{-}n\mu) < 0$ [55].

The simplest way of implementing the Monte Carlo method is the scheme used originally by Metropolis [56]. In the language of the lithium lattice gas the algorithm would be:

1. Select one site for consideration.
2. If the site is empty (full) then calculate the change in energy, $\Delta(A\text{-}n\mu)$, associated with filling (emptying) the site.
3. If $\Delta(A\text{-}n\mu)$ is less than zero then fill (empty) the site. Otherwise, calculate a random number, r, between zero and unity. If $r < e^{-\Delta(A-n\mu)/k_BT}$ flip the spin, otherwise do not flip.

4. Return to step 1 and repeat.

Each cycle of the above algorithm is known as a Monte-Carlo step (MCS). Usually many MCS are performed to bring a system to equilibrium before any calculations are made. These initialising steps will be called IMCS in this thesis. Since the algorithm follows a Markov process, a good test to ensure that enough MCS and IMCS were used to bring the system to equilibrium is to check for hysteresis.

Figure 3.2 shows the results of a Monte-Carlo simulation of a one-dimensional lattice-gas with a repulsive nearest neighbour interaction of $10k_BT$. The simulation is in excellent agreement with the exact solution. For this simulation a one-dimensional 100-site lattice was used with PBC's. At a given chemical potential five thousand MCS were used to initialise the lattice before the lithium occupation number was averaged over another five thousand MCS.

3.5 FINITE LATTICE-GAS WITH ATTRACTIVE INTERACTIONS

3.5.1 Ground State Properties

A finite set of four ground states was used for lattices with attractive interactions. The energies of the possible transitions between the states are given below where the states are labelled by the occupation number on their surface and bulk, (x_s,x_b) [39]:

$$A_{(00)} = 0 \tag{3.20a}$$

$$A_{(10)} = 4(L-1)(U+E-\mu+E_1) \tag{3.20b}$$

$$A_{(01)} = (L-2)[(L-2)(2U+E-\mu)-2U] \tag{3.20c}$$

$$A_{(11)} = L[2(L-1)(U+4E_1)+E-\mu] \tag{3.20d}$$

The chemical potentials at the transitions between configurations are given by [39]:

$$\mu_{(00)(10)} = U + E + E_1 \tag{3.21a}$$

$$\mu_{(00)(01)} = E + 2U\left[1-(L-2)^{-1}\right] \tag{3.21b}$$

$$\mu_{(00)(11)} = E + 2U(1-L^{-1}) + 4E_1(L-1)/L^2 \tag{3.21c}$$

$$\mu_{(01)(10)} = E + 2U + 4\left(L^2 - 8K + 8\right)^{-1}\left[2LU - (L-1)E_1\right] \tag{3.21d}$$

$$\mu_{(01)(11)} = E + U\left[2-(L-1)^{-1}\right] + E_1 \tag{3.21e}$$

$$\mu_{(10)(11)} = E + 2U\left[1+(L-2)^{-1}\right] \tag{3.21f}$$

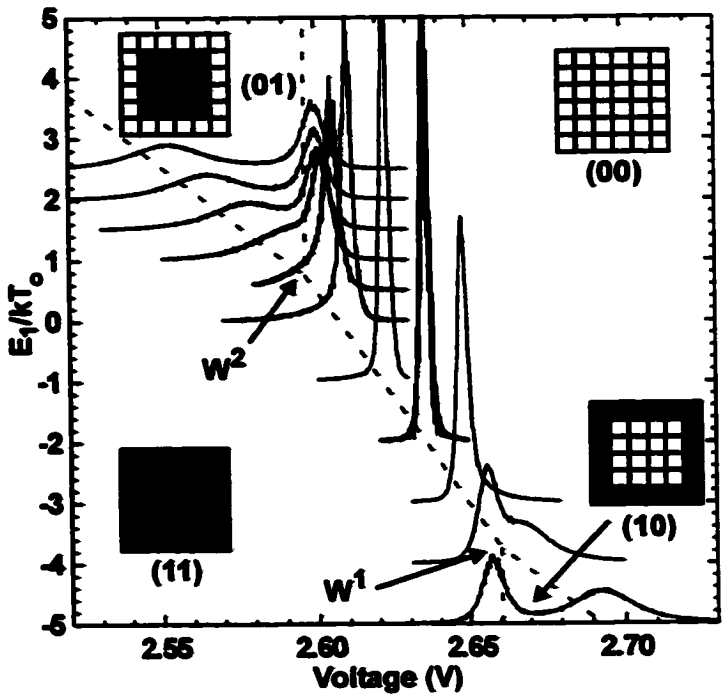

Figure 3.8 The μ-E_1 ground state phase diagram of a 6x6 lattice with attractive interactions. W^1 and W^2 are points of critical wetting. Differential capacity versus voltage curves obtained by Monte Carlo simulation are superimposed on the figure for comparison. All the differential capacity curves are plotted on the same scale, which is not shown in the figure, and are shifted in the vertical axis by E_1. ($U = -2.5kT_0$, $E = -2.5eV$)

Figure 3.8 shows the resulting μ-E_1 phase diagram for a 6×6 lattice. In order to compare with calculations of the lattice at room temperature the interaction energies are given in units of kT_0 where T_0 = 298.15 K. In this case an interaction energy of $U = -2.5kT_0$ was used. In the language of wetting phenomena the lines (00)(10) and (01)(11) correspond to prewetting transitions, (10)(11) and (00)(01) correspond to extraordinary transitions and the (00)(11) line is the ordinary transition [49,53]. The intersection of the (00)(10) and (10)(11) lines and the (01)(11) and (00)(01) lines correspond to critical wetting transitions (labelled W^1 and W^2 respectively) and these occur at [39]:

$$W^1 : E_1 = U\left[1+2(L-2)^{-1}\right] \tag{3.22a}$$

$$W^2 : E_1 = U\left[(L-1)^{-1} - 2(L-2)^{-1}\right] \tag{3.22b}$$

Because of the finite lattice size and the interaction between the bulk and surface atoms the chemical potential of the ordinary transition is dependent on E_1 and on L and the two wetting transitions do not occur at the same chemical potential as they do in a semi-infinite system [53]. The behaviour of the infinite system is recovered in the limit $L\rightarrow\infty$ where both extraordinary transitions and the ordinary transition occur on the line $\mu = E + 2U$ [39].

3.5.2 Monte Carlo Simulations of Finite Lattices with Attractive Interactions

Figure 3.9 shows the voltage profiles for lattices with $L = 6$ and $U = -2.5k_BT$ and different values of E_1 calculated by Monte Carlo simulation. The differential capacity plots are shown in the figure 3.8 shifted by E_1 in the vertical direction. There is good agreement between the simulations and the ground state phase diagram, which is drawn

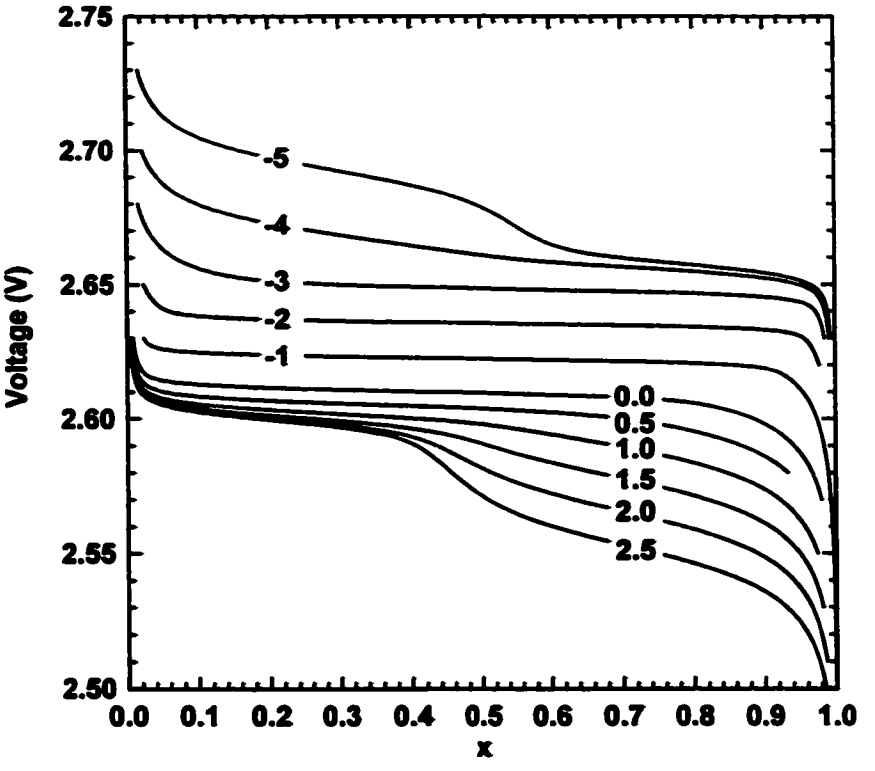

Figure 3.9 Monte Carlo simulations of the voltage profiles of 6×6 lattices with attractive neighbour interactions and different values of the boundary energy, E_l (in units of k_BT) ($U = -2.5k_BT$, $E = -2.5eV$).

with dotted lines in the figure, however the peaks on the ordinary transition are asymmetric. This asymmetry is caused by the surface sums in equation (3.16) and thus is strictly a surface effect. Qualitatively it can be described as thermal fluctuations between the (00) and (10) states or the (11) and (01) states. From equation (3.16) the curves should be symmetric (excepting the sum over the corners) when $E_l = U/2$.

Figure 3.10 shows the differential capacity plots of lattices with $U = -2.5k_BT$, $E_l=0$ for different values of L. As predicted by equation (3.21c), the first order phase transition occurs at different voltages for different lattice sizes. The curves are also asymmetric, having a tail towards lower voltages (towards the (10) state) as discussed above. This rounding becomes larger as the lattice size becomes smaller and the number

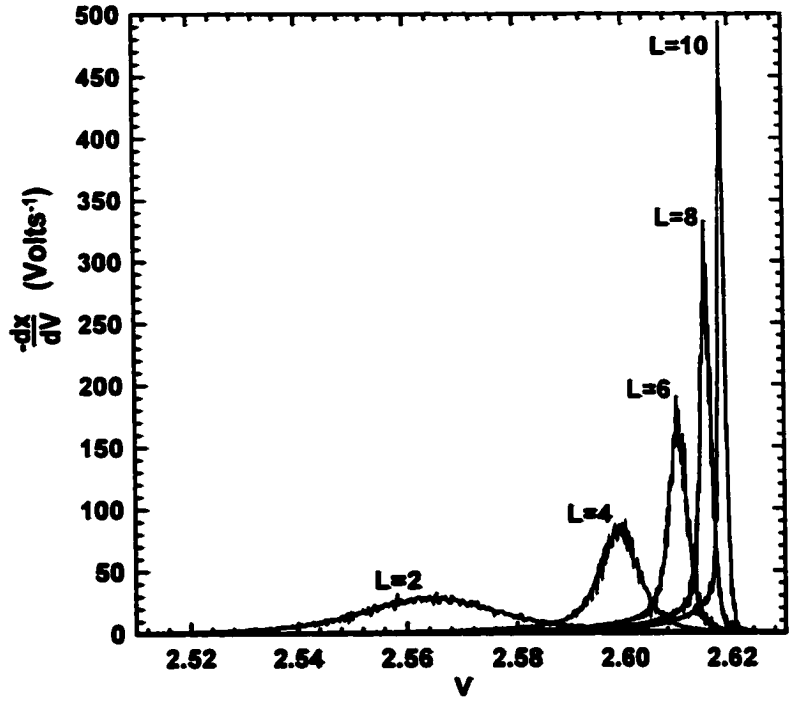

Figure 3.10 Differential capacity versus voltage obtained by Monte Carlo simulation for different sized lattices with attractive neighbour interactions ($U = -2.5k_B T$, $E_1=0$).

of surface sites becomes comparable to the bulk. The voltage profile is symmetric for $L = 2$ since all the sites are on the surface. Figure 3.11 shows the dependence of the peak height, $(-dx/dV)_{max}$, and position, V_{max}, on the lattice size. Equation (3.21c) predicts a linear relationship between L and LV_{max}. There is excellent agreement with this prediction in the figure. From equation (3.21c) the slope and intercept of the line should be $-(E+2U) = 2.551$eV and $2U = -0.1285$eV respectively which are close to those values in the figure. Although equation (3.14) was derived for systems with periodic boundary conditions, $L^{-1}(-dx/dV)_{max}$ still appears to have a linear dependence on L for our system with fixed boundaries, but has a finite intercept at $L = 0$.

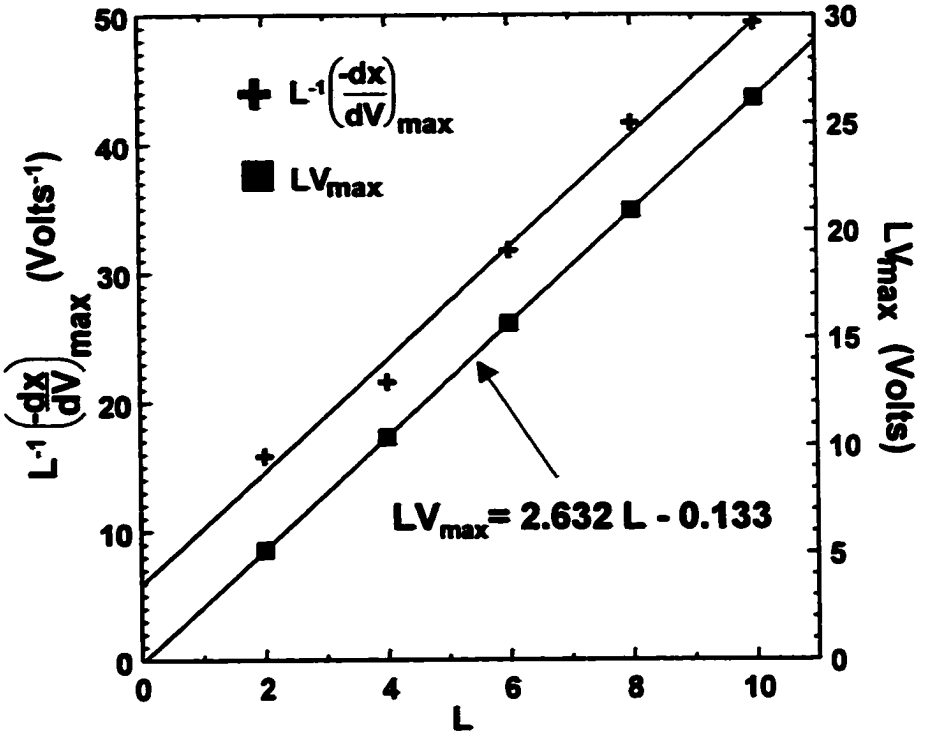

Figure 3.11 $L^{-1}(-dx/dV)_{max}$ *and* LV_{max} *versus L for lattices with attractive interactions* ($U = -2.5k_BT$, $E_1=0$).

3.6 FINITE LATTICE GAS WITH REPULSIVE INTERACTIONS

3.6.1 Ground State Properties

The ground state properties of the finite lattice with repulsive interactions are more difficult to derive than in the case of attractive interactions since a larger number of ground states are possible. To model the ground state properties an 8×8 lattice was chosen with $U = 10k_BT_0$ and $E = -2.5$ eV. The lattice was separated into three regions: the surface layer, the sub-surface layer and the remainder of the sites being the core. These three regions could either be independently empty, full, or in the half-full ordered state. In addition the corners of all three regions could all be independently full or empty. A computer program was used to determine the lowest energy-state from all the

permutations of possible configurations while the voltage was scanned. The resulting phase diagram is shown in figure 3.12.

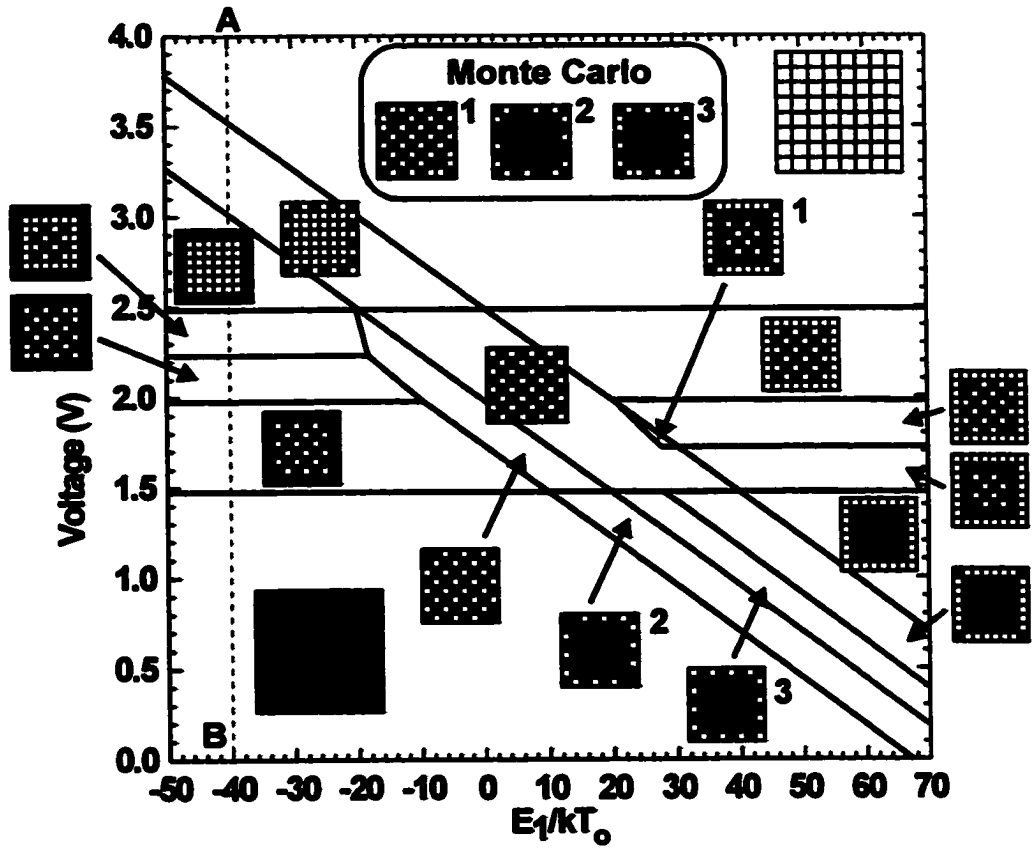

Figure 3.12 Ground-state μ-E_1 phase diagram of an 8×8 lattice with repulsive neighbor interactions ($U = 10k_BT_0$, $E = -2.5eV$). The numbered phases did not occur in the Monte Carlo simulations. This is because of the limited set of lattices used to calculate the ground-state phase diagram. Phases obtained by Monte Carlo simulation at regions near the numbered phases are shown in the inset.

Although the diagram appears complicated, the phase changes are intuitive. For example, going from point A to point B at the large attractive boundary potential of $E_1 = -40k_BT_o$, the lattice first becomes alternately filled on the surface which has a higher binding energy than the bulk. The sites are filled alternately to avoid repulsive neighbour interactions. As the voltage is lowered the remaining surface sites all become filled and then the core sites are alternately filled. The sub-surface layer remains empty because of

the repulsive interactions from the filled surface sites. As the voltage is further lowered the sub-surface layer alternately fills, save two corner sites which remain empty since they have two filled nearest neighbour surface sites as opposed to the other sub-surface sites which only have one each. The sub-surface corners fill as the voltage is lowered below two volts. Now all the sites have four nearest neighbours and are equivalent, so the next phase has all sites filled. Similar arguments as the above can be used to explain all the phases in the diagram. The phases labelled 1,2 and 3 were not observed in the Monte Carlo simulations. Instead phases with a frustrated surface layer were observed near the regions of phases 1,2 and 3 which were not included in the limited set used to calculate the ground states. These phases are shown in the inset in figure 3.12.

3.6.2 Monte Carlo Simulations of Finite Lattices with Repulsive Interactions

Figures 3.13 (a) and (b) show the voltage profiles for lattices with $L = 6$, $U = 10k_BT$ and different values of E_l calculated by Monte Carlo simulation. As predicted by the ground state phase diagram, the voltage profiles of lattices with finite size have a number of plateaus corresponding to the different phase regions. Figure 3.14 shows the differential capacity curves of these lattices superimposed on the ground state phase diagram. The results are in good agreement, even at large values of E_l where phases appear that were not included in the set of lattices used in the ground state calculation. In figure 3.15, the voltage profiles for lattices with $L = 6$ and a smaller repulsive interaction of 5 eV is plotted for different values of E_l. The plateaus in this plot are more rounded and less defined than in figure 3.15. Despite this the surface lattice energy still has a pronounced effect on the voltage curves.

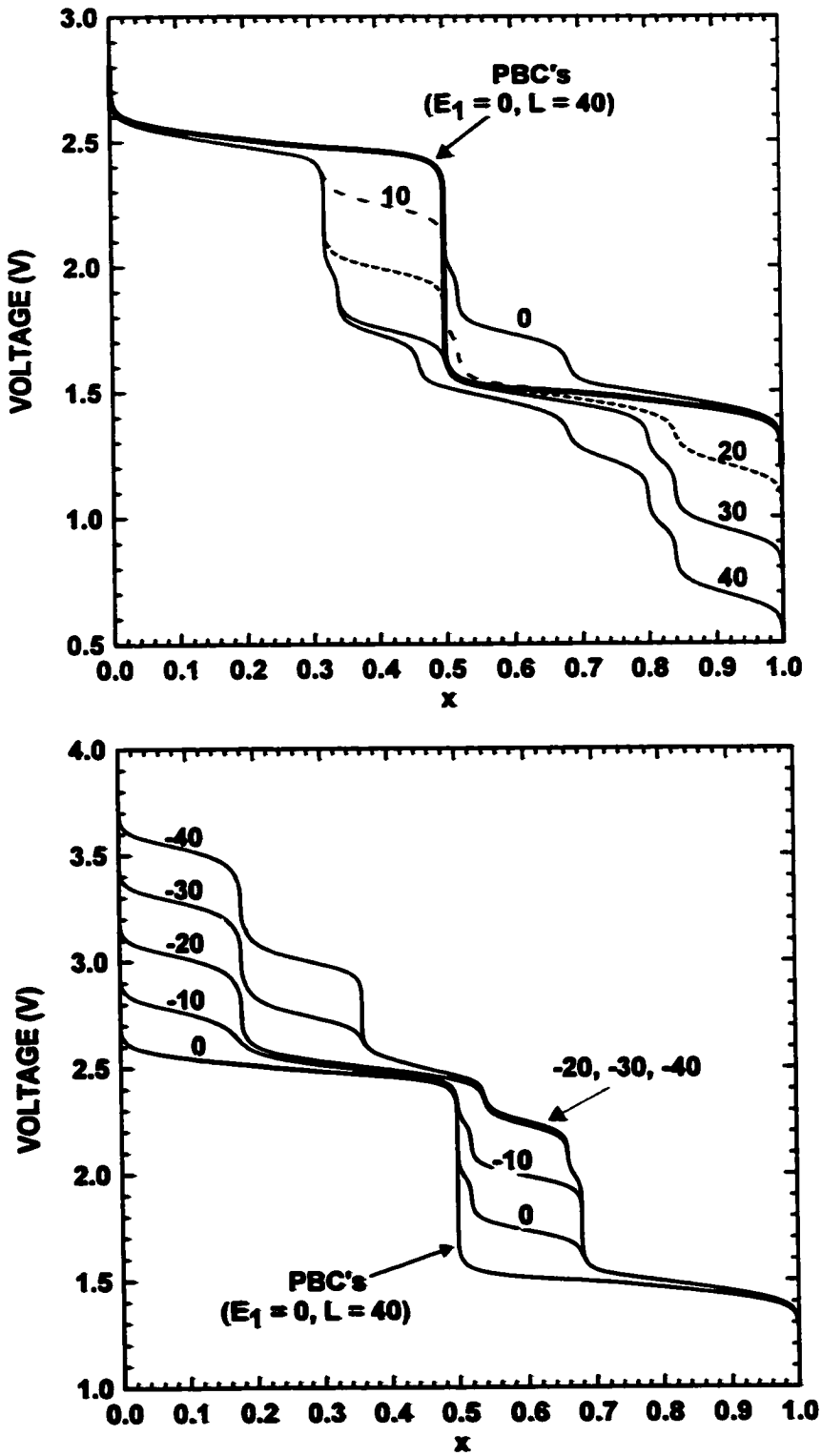

Figure 3.13 Voltage profiles obtained by Monte Carlo simulation for 10×10 lattices with repulsive neighbour interactions and with (a) positive and (b) negative values of the surface lattice energy E_l ($U = 10k_BT$, E=-2.5eV). For comparison the voltage curve of a 40×40 lattice with periodic boundary conditions is also shown

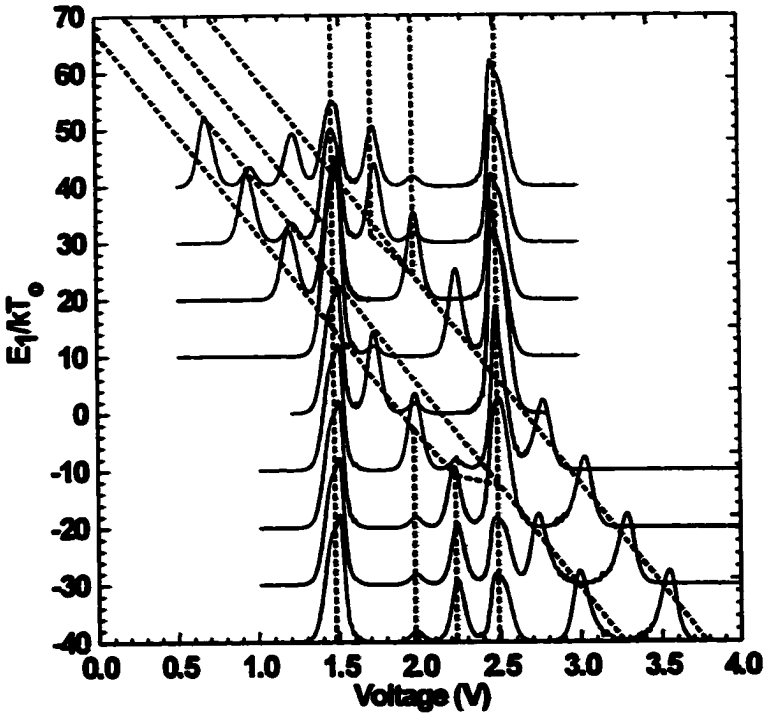

Figure 3.14 Differential capacity versus voltage obtained by Monte Carlo simulation for 10×10 lattices with repulsive interactions and different values of E_l. The curves are all plotted on the same scale (not shown in the figure), but are shifted in the vertical axis by E_l. The ground-state phase diagram (figure 5) is superimposed on the figure for comparison ($U = 10k_BT_0$, E =-2.5eV).

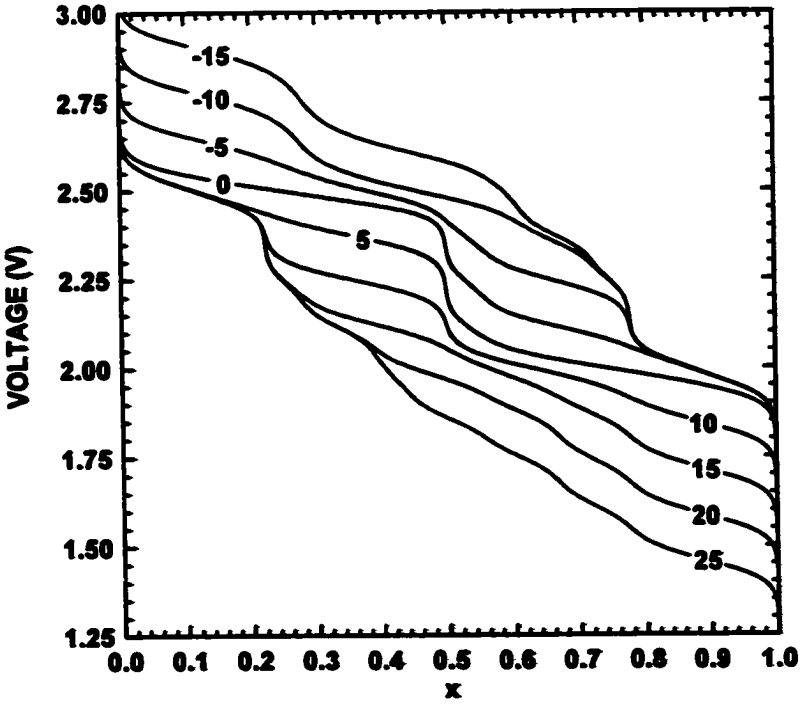

Figure 3.15 Voltage profiles obtained by Monte Carlo simulation for 10×10 lattices with repulsive neighbour interactions and different values of the surface lattice energy E_l ($U = 5k_BT$, E = -2.5).

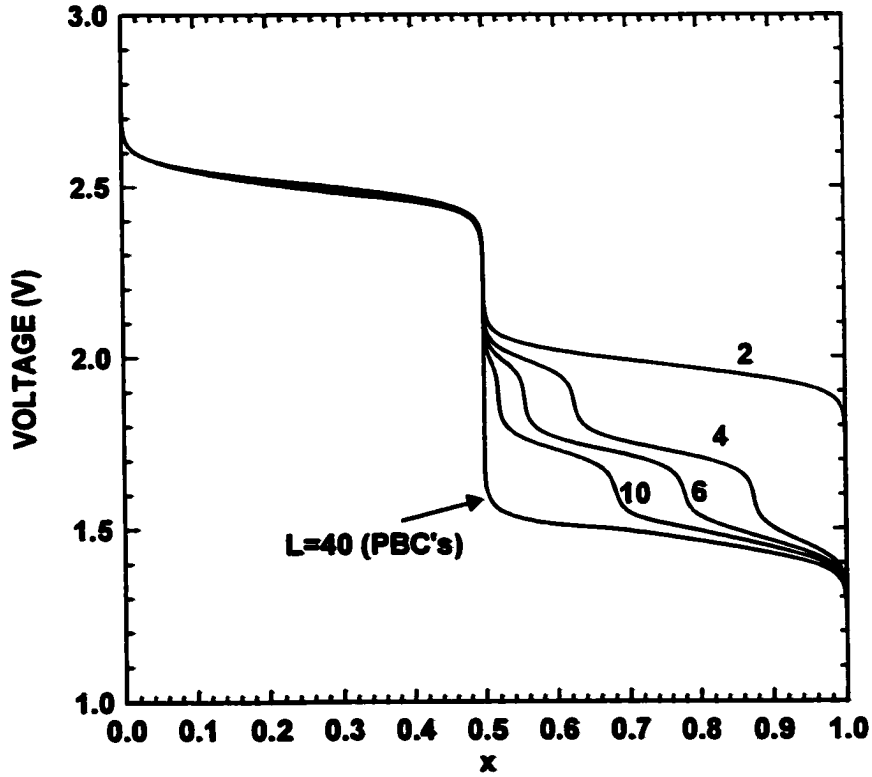

Figure 3.16 Voltage profiles obtained by Monte Carlo simulation for different sized lattices with repulsive neighbour interactions and a negative surface energy of $E_l = 0k_BT$ ($U = 10k_BT$, E=-2.5eV). For comparison, the voltage curve of a 40×40 lattice with periodic boundary conditions is also shown.

Figure 3.16 shows voltage profiles of different size lattices with $U = 10k_BT$ and $E_l = 0k_BT$. The plateaus due to the various transitions change in capacity as the number of surface sites becomes comparable to the bulk. As with the case of attractive interactions there is also a change in the voltage of the various plateaus with the lattice size, although it is difficult to see on the scale of the figure. Figure 3.17 shows the differential capacity versus voltage for the order-disorder transition near 2.5V. As the lattice size decreases the peak in the second order transition becomes smaller and disappears for $L = 2$. To explain this behaviour we note that the broad peak for the $L = 2$ lattice corresponds to the filling of a non-interacting lattice gas whereas in the infinite

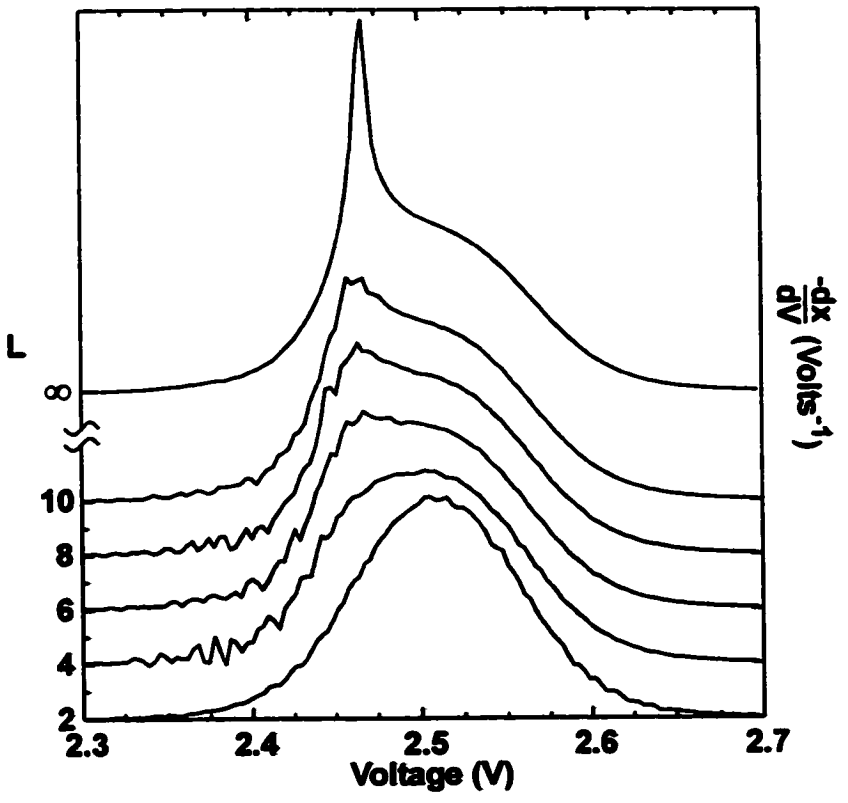

Figure 3.17 Differential capacity versus voltage obtained by Monte Carlo simulation for lattices with repulsive interactions and different lattice size. The plots are shifted on the vertical axis by L. The infinite lattice is approximated by a 40×40 lattice with periodic boundary conditions. ($U = 10k_BT$, $E = -2.5eV$, $E_l = 0k_BT$)

case there is frustration during the filling of the lattice which is released at the second order transition. Finite lattices with $L > 2$ represent an intermediate case. These lattices have a large fraction of surface sites that have less nearest neighbours than those in the bulk. This means the probability for frustration is less in these lattices, making the second order peak smaller than for the infinite case.

3.7 IMPLICATIONS FOR REAL FINITE SIZE LITHIUM INTERCALATION ELECTRODES

There are presently very few examples of nano-size storage materials that can be

compared to the above model. This is bound to change since more nano-sized storage materials are starting to appear in the literature [30-35]. The above results can be used to predict the behaviour of future materials, keeping in mind that real materials will probably have a rough surface with a distribution of grain sizes, interaction energies and site energies. Conceivably, independent adjustment of both L and E_1 could be possible in real materials and could be used to effectively tune the voltage profile of the material. L is simply controlled by modification of the grain size while E_1 could be modified by encapsulating the grains in different matrix materials or by chemically treating the surface of the grains.

For systems with attractive interactions and without surface wetting, equation (3.21c) predicts that the difference in voltage between the phase transition in the finite size system and the first order phase transition in a system of infinite size will be:

$$\Delta V_{max} = \frac{2U}{L} + 4E_1 \frac{(L-1)}{L^2} . \qquad (3.23)$$

Typically, the voltage of a lithium test cell is measured to within a microvolt during cycling. However because of diffusion, kinetic and ohmic effects only changes of about a millivolt are observable in practice. Thus, assuming U is on the order of $k_B T_o$, $E_1 = 0$ and the Li-Li nearest neighbour distance is about 0.2 nm, finite size effects can be observed for grain sizes below 10 nm. However these effects would be very small. In order to change the voltage of the (00)(11) phase transition significantly (by tenths of a volt) materials would have to have grain sizes less than 1 nm and $|U|$ or $|E_1|$ on the order of $10k_B T_o$. Larger effects could be expected for the prewetting transitions. For example the (00)(10) transition occurs at $-(U+E_1)/e$ volts above the bulk transition voltage regardless of the system size. This transition will become observable when the capacity

of the surface sites becomes measurable.

For systems with repulsive interactions the change in the voltages of the phase transitions caused by lattice size is also small. However the surface transitions should occur at significantly different voltages than in the bulk and should be observable when the capacity of the surface and sub-surface sites becomes measurable. For instance in the present model of a square lattice if a site on the surface is surrounded by n filled neighbours it will be filled when the voltage is approximately $-(nU+E+E_1)/e$ whereas the bulk will have two plateaus at $-E/e$ and $-(E+4U)/e$ volts.

Although, as previously mentioned, there are presently no suitible measurements of the voltage composition behaviour of nano-sized intercalation systems to compare with the model presented here, lithium intercalation into certain hydrogen-containing carbons provides an example in which finite-size effects can be observed [30]. However the lithium interactions are slightly different than those used in the present model [57]. These carbons are made up of graphene sheets about 30Å across with hydrogen atoms bonded to the carbons at the edges of the sheets [30]. When lithium is intercalated in this material it can either reside in the middle of a carbon hexagon in the bulk of the sheet where the Li-Li interaction is repulsive or bind to an edge carbon atom [57]. The binding energy of lithium to the edge carbons is greater than the sites in the bulk of the sheet by about 0.23 eV [30]. This corresponds to the case where $E_1 < 0$ and $U > 0$. However the surface-surface, surface-bulk and bulk-bulk lithium neighbour interactions are probably quite different from each other. The surface-surface interaction may even be attractive [57]. Nevertheless the contributions to the voltage curve from the edge and bulk sites can easily be differentiated.

Chapter 4

Synthesis and Electrochemistry of Nanostructured Intercalation Materials

4.1 INHERENT DIFFICULTIES IN MAKING NANOSTRUCTURED INTERCALATION MATERIALS

In chapter three it was found that finite size and surface effects should be observable in nanostructured intercalation materials. However, as it was pointed out in that chapter, there are few examples of nanostructured lithium intercalation materials in the literature. An inherent difficulty in making these materials seems to exist, namely that to make the correct structures for lithium intercalating oxides and sulphides high

temperatures are required, which favours the formation of large crystallites. Just recently the synthesis of $Li_{1+y}Mn_{2-y}O_4$ spinel and layered $LiNi_{1-y}Co_yO_2$ by means of laser assisted chemical vapour deposition was reported [58]. It was claimed that these materials do show size dependent features in their voltage curves, but the electrochemical data has not yet been published. In this chapter attempts to make nanostructured intercalation materials by less exotic means will be described. Although most of these attempts turned out to be fruitless, fascinating things were learned on the way. Because much of this chapter deals with $LiMn_2O_4$ a brief introduction to this material is given in the next section before proceeding further.

4.2 A REVIEW OF THE STRUCTURE, PHASE BEHAVIOUR AND ELECTROCHEMISTRY OF $LiMn_2O_4$

The spinel phase of $LiMn_2O_4$ is an important lithium intercalation material that is currently used as a cathode in commercial lithium ion cells. Stoichiometric $LiMn_2O_4$ spinel has the cubic space group $Fd\bar{3}m$ with a lattice constant of 8.240 Å [59]. The

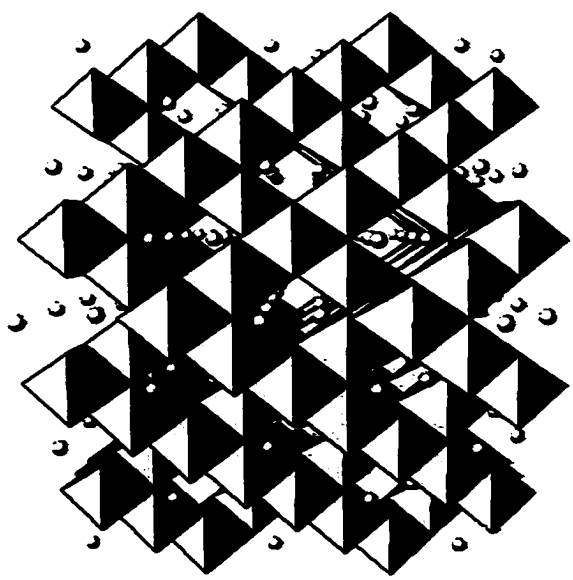

Figure 4.1 The structure of the spinel phase of $LiMn_2O_4$ viewed along the 110 direction. The lithium atoms are represented as small spheres and the manganese atoms are at the centres of the oxygen octahedra. In this orientation the tunnel structure is clearly visible.

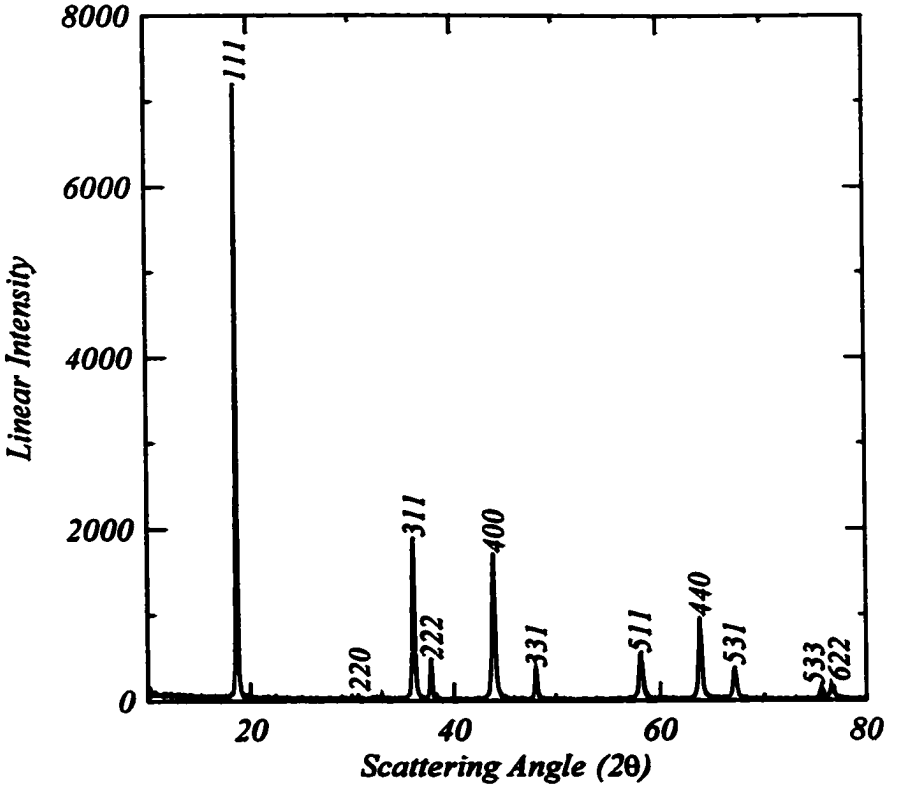

Figure 4.2 Powder x-ray diffraction pattern of the spinel phase of $LiMn_2O_4$..

oxygen atoms of $LiMn_2O_4$ fill the 32e sites of the structure and form an fcc lattice. The manganese atoms occupy 16d sites, which account for half of the octahedral holes in the oxygen lattice. The lithium atoms occupy the 8a sites, which account for half of the tetrahedral holes. A representation of the structure is shown in figure 4.1. The lithium sites are arranged in a series of rows in the lattice, facilitating easy lithium intercalation and fast internal diffusion. The XRD pattern of a crystalline sample of $LiMn_2O_4$ (Chemetals T2O2) is shown in figure 4.2. Figure 4.3(a) shows a TEM image of the same sample of $LiMn_2O_4$. The sample consists mostly of approximately 80 nm grains. The sample also contains larger grains. The large grain size of this sample is a result of the high temperatures (~800°C) used in its preparation. Figure 4.3(b) shows a TEM image of the sample at higher magnification. A fringe pattern is clearly visible in the figure. The

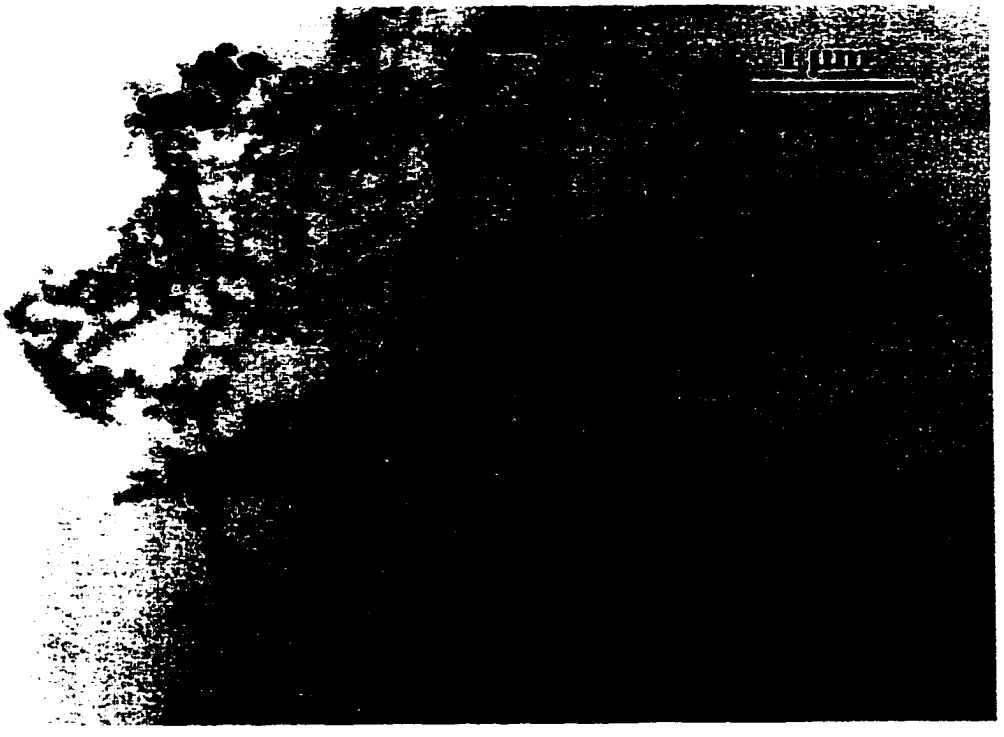

(a)

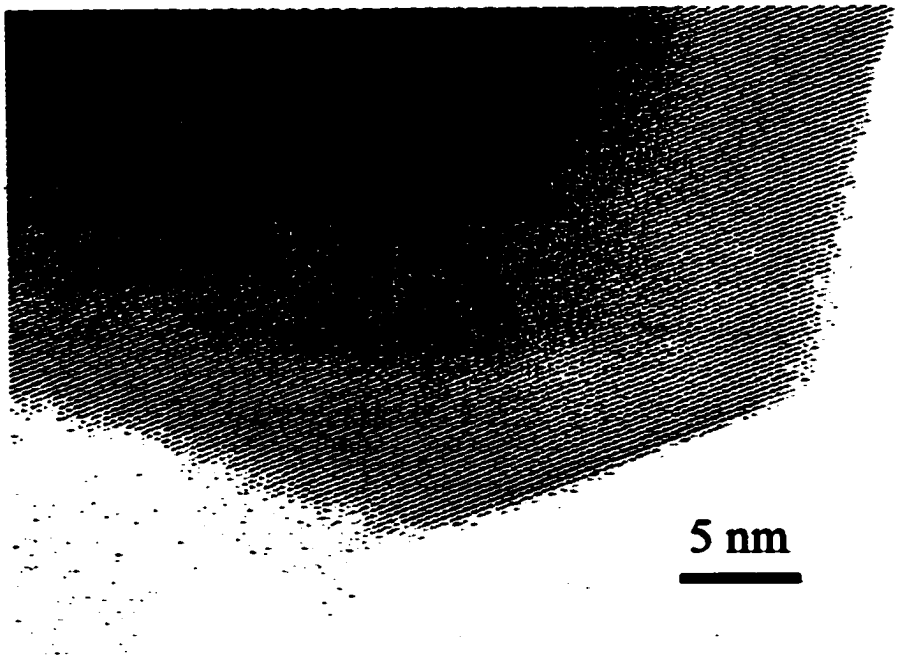

(b)

Figure 4.3 TEM images of $LiMn_2O_4$ prepared at high temperatures (Chemetals T202).

spacing of the fringes is about 4.58 Å. This is close to the value of the spacing between 111 planes in $LiMn_2O_4$, which is 4.757 Å. The 4 % discrepancy between the values may be due to a slight miscalibration in the TEM at this magnification.

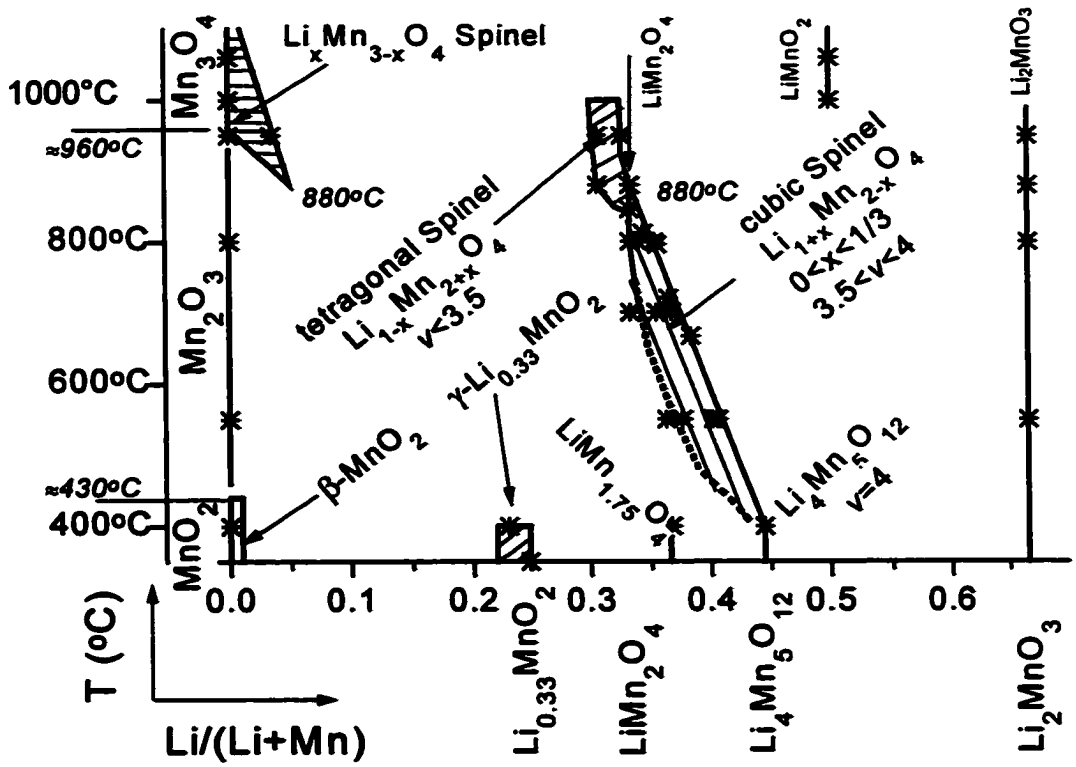

Figure 4.4 Phase diagram (of the second kind) of the system Li-Mn-O in air between 350°C and 1060°C. From reference [60].

Figure 4.4 shows the phase diagram of $LiMn_2O_4$ spinel in air. At 800°C, if the Mn/Li ratio is greater than two, a Li-Mn-oxide in air will be in a two phase region consisting of stoichiometric $LiMn_2O_4$ spinel and Mn_2O_3 [60]. On the other hand, if the sample is lithium rich, then above 400°C there exists a two-phase region between $Li_{1+x}Mn_{2-x}O_4$ and Li_2MnO_3 which culminates at 880°C when stoichiometric spinel and Li_2MnO_3 are in equilibrium [60]. In $Li_{1+x}Mn_{2-x}O_4$ the additional lithium replaces the manganese in the 16d sites and the formula for this material may be written as

$Li^{+}[Li_x^{+}Mn_{1-3x}^{3+}Mn_{1+2x}^{4+}]O_2$ [61]. The lithium atoms residing in the manganese sites are not electrochemically active.

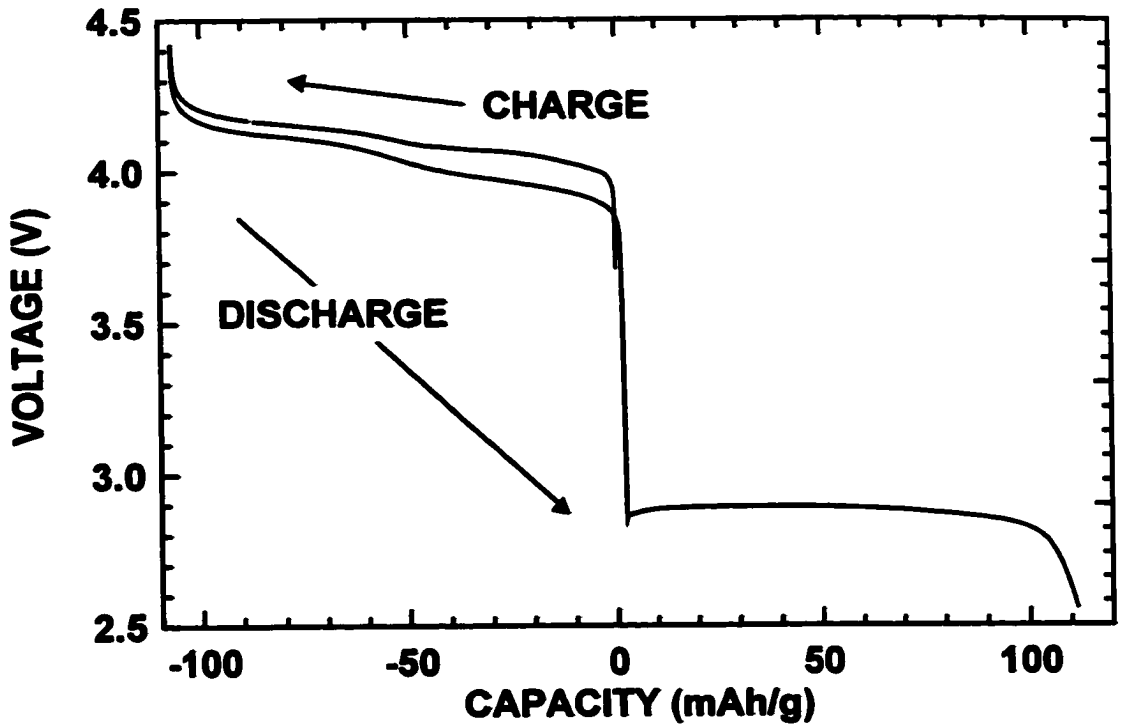

Figure 4.5 The voltage curve of crystalline $LiMn_2O_4$ spinel (Chemetals T202).

Figure 4.5 shows a voltage curve of crystalline $LiMn_2O_4$ spinel. There are two distinct voltage plateaus, one at about 4 V and one at about 3 V. In lithium ion batteries $LiMn_2O_4$ is cycled on the 4 V plateau. On this plateau the stoichiometry of the cathode varies from $LiMn_2O_4$ to the fully delithiated species Mn_2O_4 at the top of charge. Thus the valence of manganese changes from 3.5+ to 4+ on this plateau. The 4 V plateau actually consists of two plateaus with slightly different voltages due to Li ordering in the tetrahedral sites at the composition $Li_{\frac{1}{2}}Mn_2O_4$ [62]. The 3 V plateau corresponds to a two-phase region between $LiMn_2O_4$ and $Li_2Mn_2O_4$ [63]. In $Li_2Mn_2O_4$ all the lithium resides in octahedral sites and the overall structure is tetragonal owing to a co-operative

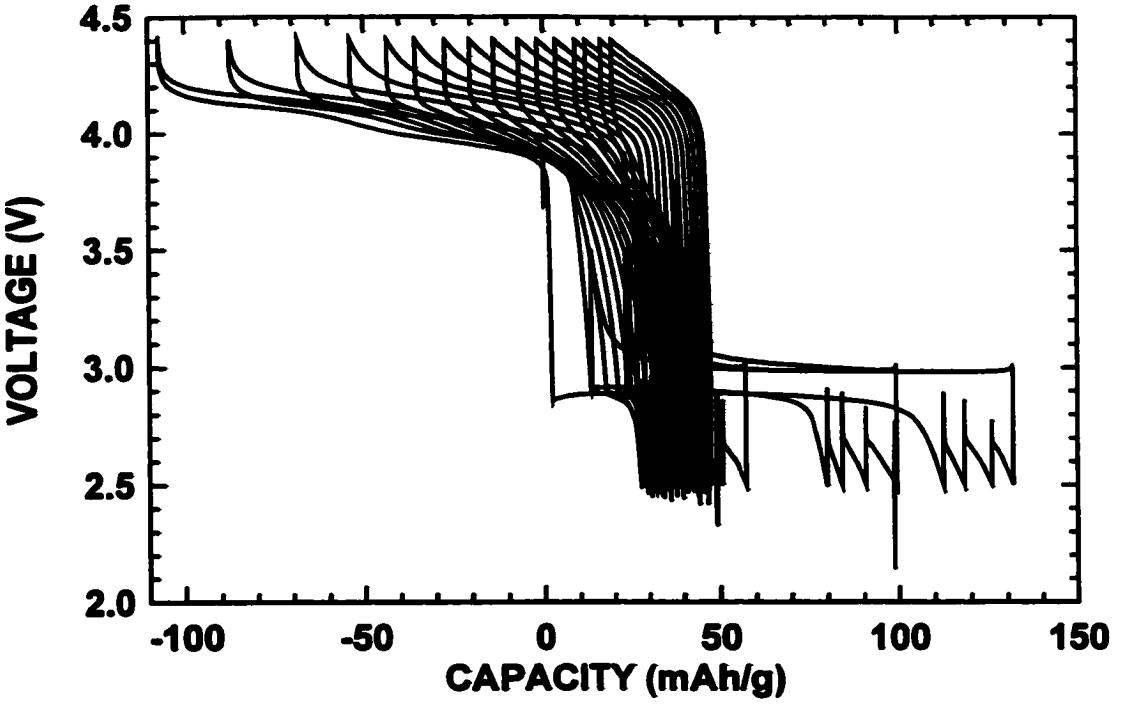

Figure 4.6 The voltage curve of crystalline $LiMn_2O_4$ spinel (Chemetals T202) cycled repeatedly over both the 4 V and 3 V plateaus.

Jahn-Teller distortion of the Mn^{3+} ions [63].

The anisotropic volume change associated with converting $LiMn_2O_4$ to $Li_2Mn_2O_4$ is thought to cause internal stresses and cracking which leads to the capacity fading observed during cycling on the 3 V plateau [63]. However this point is still under some debate and is unlikely to be at least the sole cause of capacity fading in $LiMn_2O_4$ [64]. For instance figure 4.6 shows the voltage curve of ChemetalsT202 $LiMn_2O_4$ spinel cycled on both plateaus.* During cycling the capacity fades much more quickly on the 3 V plateau than it does on the 4 V plateau. Furthermore, a large polarization develops

---

* After the low voltage trip point was reached during discharge the cell was allowed to relax for 15 minutes, then the cell was discharged at a rate of 50% of the previous discharge current. This was repeated three times at the end of each discharge cycle and is the reason for the "saw-tooth" appearance of the discharge curves. This is known as a signature discharge [65] and helps ensure that the cell has completely discharged to the prescribed voltage.

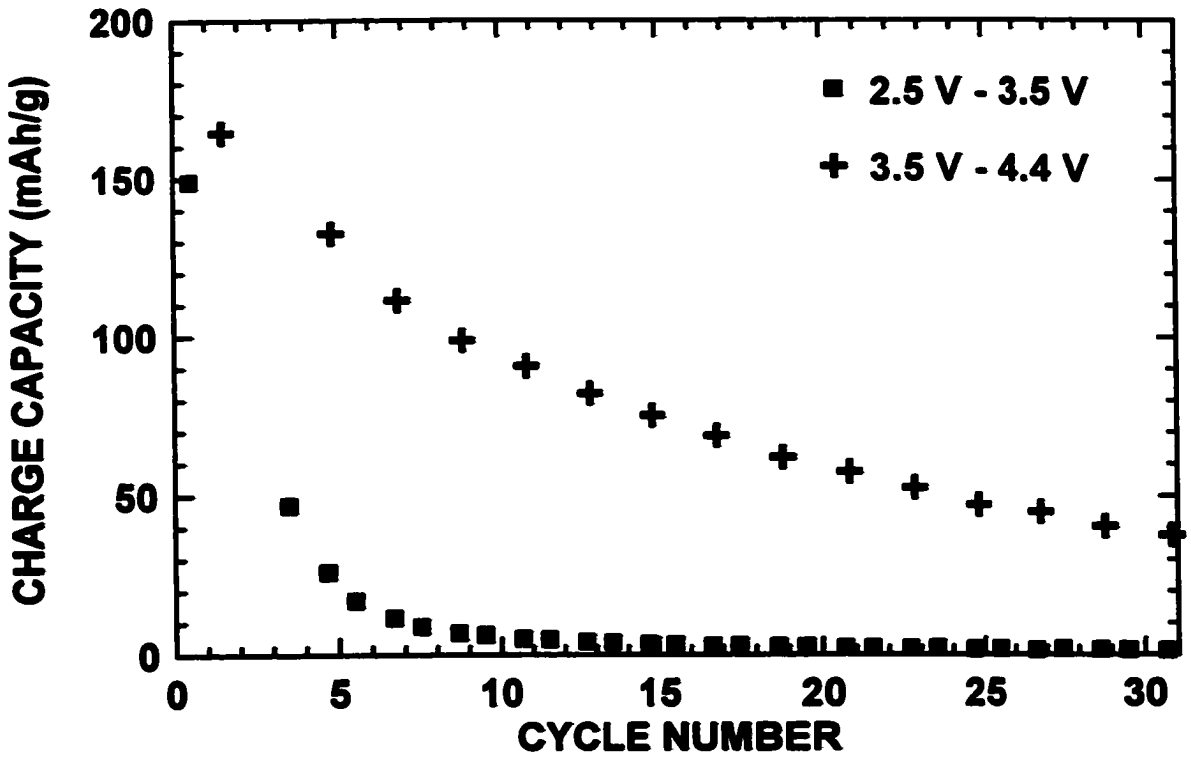

Figure 4.7 The charge capacity versus cycle number of the 4 V and 3 V plateaus of Chemetals T202 $LiMn_2O_4$ spinel, corresponding to the voltage curves in figure 4.6.

on the 4 V plateau. The capacity fading can be more clearly seen in figure 4.7, which shows the charge capacity on both plateaus as a function of cycle number. If the capacity fading is solely due to particle cracking, then both plateaus should fade at the same rate. Clearly this is not the case. One explanation of this behaviour may be that the tetragonal-cubic interface mobility becomes reduced during cycling [64]. This would cause the 3 V plateau to disappear, as the mobility is progressively worsened. In the 4 V range, there is no tetragonal-cubic interface, so the Li^+ ions can move freely throughout the volume of the particles [64]. This explanation does not explain the increased polarization on the 4 V plateau during cycling , however.

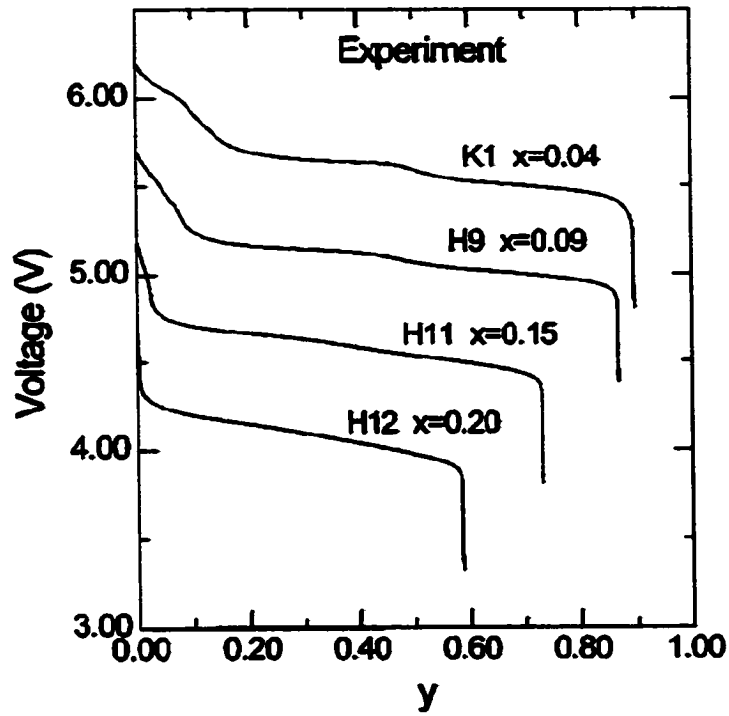

Figure 4.8 The voltage curves of $Li_{1+x}Mn_{2-x}O_4$ samples with different values of x. The horizontal scale represents the amount of lithium per formula unit inserted into the material during the first discharge. The voltage curves of samples H11, H9, and K1 are sequentially shifted up to 0.5 V for clarity. From reference [5].

Figure 4.8 shows the 4 V plateau of the voltage curve of a lithium substituted spinel with different values of x in $Li_{1+x}Mn_{2-x}O_4$ [62]. The capacity of the 4 V plateau decreases with increasing x since the amount of Mn^{3+} also decreases with x. Also, for increasing x, the order-disorder transition becomes less distinct because of an interaction between the intercalating lithium atoms and those in the 16c sites. This causes the voltage curve to have a gradual slope, rather than two distinct horizontal plateaus [62]. The 3 V plateau is limited by the number of lithium-containing octahedral sites in the tetragonal phase, $Li_2[Li_xMn_{2-x}]O_4$, and thus is not dependent on the value of x [64].

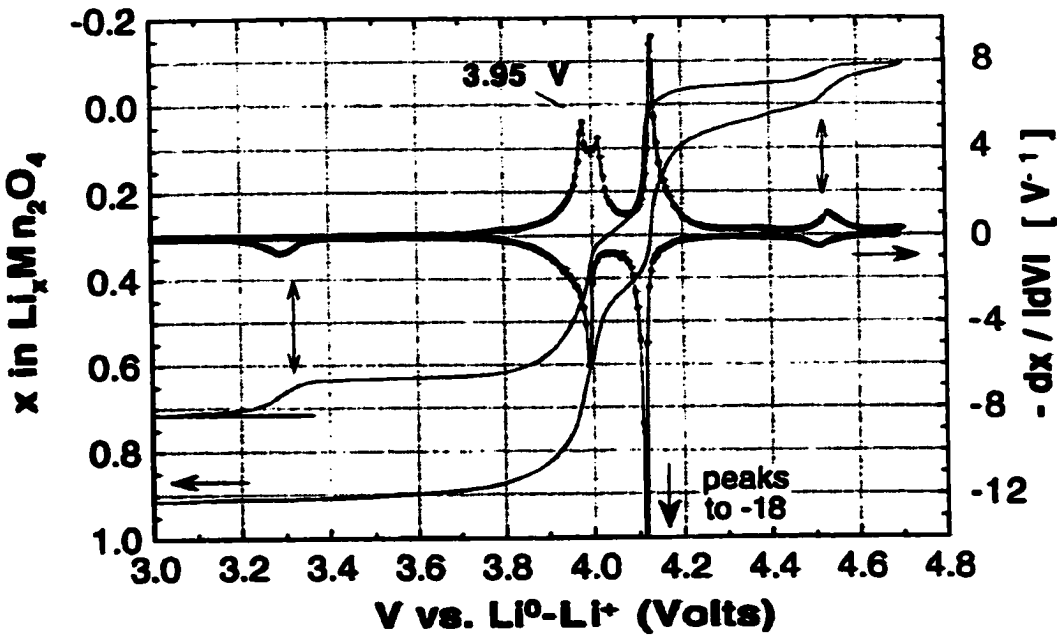

Figure 4.9 Differential capacity curve of a spinel sample showing large 3.3 V and 4.5 V plateaus [66].

Another electrochemical property of $LiMn_2O_4$ spinel which has only recently been explained is the appearance of additional peaks in the differential capacity curves of some samples, as shown in figure 4.9 [66]. These additional peaks are observed near 4.5 V and 3.3 V and have identical capacities. Furthermore the capacity obtained from these peaks are at the expense of the 4 V plateau capacity. It has been noticed that these peaks tend to occur in spinel samples that contain defects and vacancies and consequently have a lattice constant larger than that which is nominal for its composition [66]. The explanation for the occurrence of these features has been linked to the migration of some of the manganese atoms into 16c sites which are near to 8a sites that are vacated by lithium during charging. This possibly occurs near defect sites in the spinel structure. Eventually the migration of the manganese leads to the formation of "double

hexagonally" layered domains in the spinel structure. In these domains it is supposed that lithium has a higher binding energy, thus leading to the high voltage peaks in the differential capacity curve [66]. During discharge the lithium fills all of the 8a sites which are not near the 16c sites that are occupied by manganese. After all these 8a sites are filled, the manganese in the 16c sites must migrate back to the 16d sites to allow more lithium insertion. This causes the low voltage plateau on discharge.

4.3 $LiMn_2O_4/Mn_2O_3$ COMPOSITE FROM A SOL-GEL PROCESS

As mentioned above, the high temperatures required to form metal oxides conflicts with the conditions needed to make nanograined materials. However, if ion mobility is low, a composite material can be made in which a matrix material may constrain a metal oxide component in nanometer sized regions during high temperature synthesis. One of these methods, for instance, is to impregnate a templating material, such as a nano-porous membrane, with a solvent containing metal salts [67]. Upon heating in air the solvent evaporates and the metal salts decompose, leaving nanograined metal oxides in the voids of the template. Here an attempt was made to make a $LiMn_2O_4/Mn_2O_3$ nanocomposite by taking advantage of the $LiMn_2O_4$ phase diagram in air.

Above 3V Mn_2O_3 is electrochemically inactive towards lithium, making it an ideal inert matrix material. A composite of $LiMn_2O_4$ and Mn_2O_3 with a low spinel concentration was made by the sol-gel method as follows [68]. 4.902g of manganese acetate tetrahydrate and 0.102g lithium acetate were dissolved in 350ml of ethanol. This corresponds to a Mn/Li ratio of 20:1 or a $LiMn_2O_4/Mn_2O_3$ ratio of 1:9. 2.251g of tartartic acid were dissolved separately in 50ml of ethanol. The tartaric acid solution was then

added dropwise to the metal salt solution. The gel was aged at 60°C for one week after which it was ground and then heated at 300°C in air for one hour and finally at 800°C in air for 30 minutes.

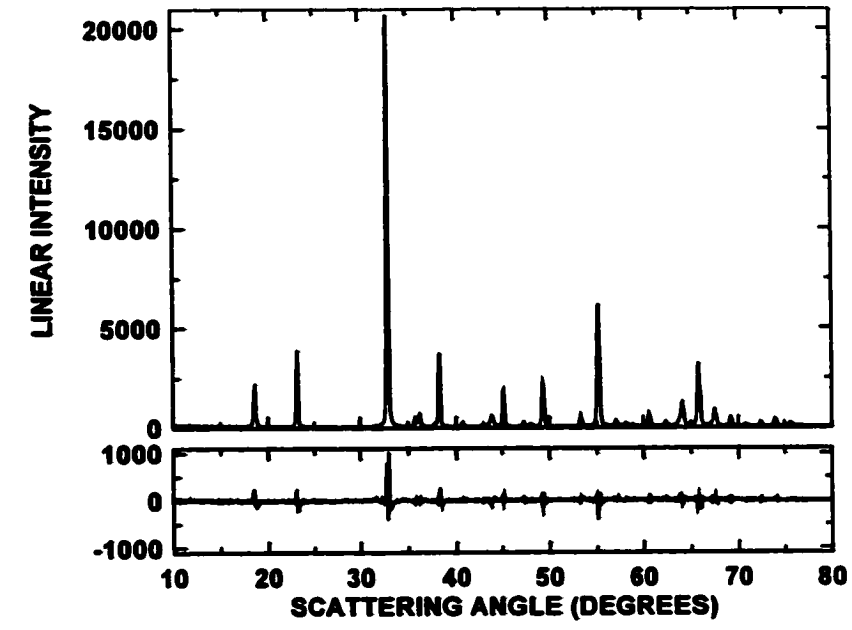

(a)

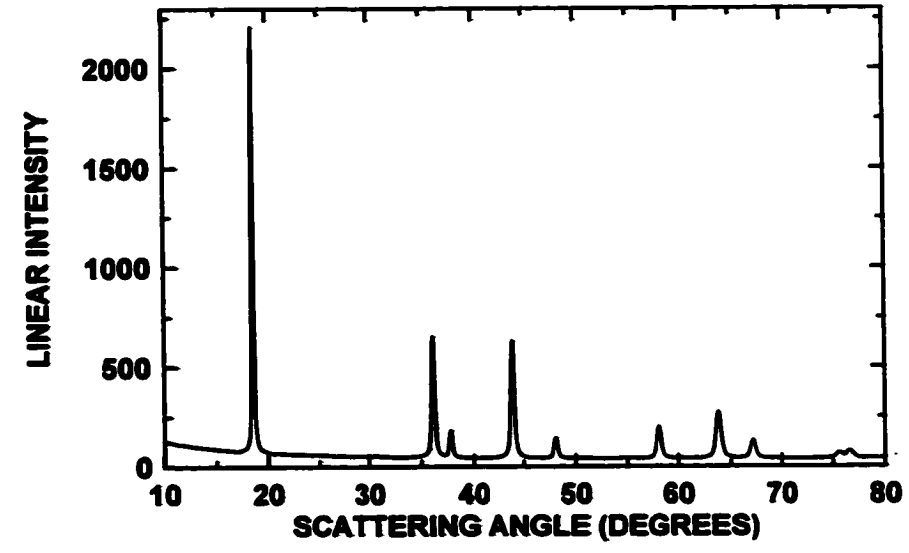

(b)

***Figure 4.10** (a) Rietveld refinement of the XRD pattern of the $LiMn_2O_4/Mn_2O_3$ composite prepared by the sol-gel method. Also shown, in the bottom panel, is the difference between the data and the refinement. (b) The $LiMn_2O_4$ spinel component of the refinement.*

Figure 4.10(a) shows the powder x-ray diffraction pattern of the resulting product and also the Rietveld refinement of the pattern. The refinement was based on a two phase mixture of $LiMn_2O_4$ and Mn_2O_3 and gave a Bragg R factor of $R_B = 2.13$ for the Mn_2O_3 phase, $R_B = 4.32$ for the spinel phase and an overall GOF of 3.22 indicating good agreement with the model. The spinel component of the refinement is shown in figure 4.10(b). From the 111 $LiMn_2O_4$ peak, which is not coincident with any of the Mn_2O_3 peaks, the Scherrer equation predicts a grain size of 800 Å. Although lower concentrations of lithium may have eventually produced $LiMn_2O_4$ with smaller grains, concentrations much lower than made here would be difficult to test electrochemically. For this reason this approach was not pursued further.

Another approach to this problem may be to work in the lithium rich region of the phase diagram in figure 4.5 where there is a two-phase co-existence between $Li_{1+x}Mn_{2-x}O_4$ and Li_2MnO_3. At 880°C $x = 0$ and stoichiometric $LiMn_2O_4$ is in equilibrium with Li_2MnO_3. Like Mn_2O_3, Li_2MnO_3 is electrochemically inert. Moreover at high temperatures the peaks of Li_2MnO_3 remain broad in a two-phase mixture with $LiMn_2O_4$ [60], indicating that small grains of Li_2MnO_3 are well dispersed in a $LiMn_2O_4$ matrix. This may indicate a compatibility between the two lattices and that, possibly, $LiMn_2O_4$ would also not aggregate in a matrix of Li_2MnO_3. The exploration of the lithium rich region of the phase diagram may be a worthwhile approach if future work is to be done on this topic.

4.4 STRUCTURE AND ELECTROCHEMISTRY OF $LiMO_2$ (M = Ti, Mn, Fe, Co, Ni) PREPARED BY MECHANOCHEMICAL SYNTHESIS

A great proportion of lithium intercalating materials are based on lithium transition metal oxides of the formula $LiMO_2$, where M is a 3d transition metal Generally, the structures of these materials are based on the sodium chloride lattice with the oxygen atoms in the close packed fcc sites and the cations filling all the octahedral interstices [69]. In α-$LiFeO_2$ and $LiTiO_2$ prepared at high temperature the cations adopt a random arrangement [69], the compounds do not de-intercalate lithium and thus are inactive as cathodes in lithium ion cells. However, high temperature preparation of the other $LiMO_2$ oxides results in ordered superstructure arrangements of the cations which can provide tunnels that allow the de-intercalation and re-intercalation of lithium [70]. All known active $LiMO_2$ cathode materials have an ordered cation structure. The structure and properties of $LiMO_2$ compounds have been reviewed by Hewston and Chamberland [69].

Because the high temperature preparation of these oxides is incompatible with nanograined materials, it was attempted to make $LiMO_2$ phases by means of room temperature ball milling [71]. In recent years ball milling (also referred to as reactive milling, mechanochemical synthesis and mechanical alloying etc.) has been demonstrated to be a powerful technique to synthesize new alloys and complex oxides with new structures and novel properties. Furthermore the products of mechanochemical syntheses are usually on the nanometer scale and when used in solid state reactions can react at significantly lower temperatures than they would normally. The method also has the advantage of allowing precise control of stoichiometry. Relatively few papers exist in the

literature which report the preparation of complex oxides by mechanochemical synthesis and the mechanisms involved are not well understood.

Fernandez-Rodriguez et al. have found that α-$LiFeO_2$ and $LiCoO_2$ with the ordered layered structure were formed along with water during the grinding of $LiOH{\cdot}H_2O/Co(OH)_2$ and $LiOH{\cdot}H_2O/\gamma$-FeOOH mixtures in agate milling jars in air [72,73]. After prolonged grinding, impurities of Co_3O_4 and $LiFe_5O_8$ were formed. These impurities also formed after prolonged grinding of α-$LiFeO_2$ and $LiCoO_2$ synthesized at high temperatures.

Here the results of the mechanochemical synthesis of $LiMO_2$ (M = Ti, Mn, Fe) from transition metals and metal oxides is reported. The series $Li_xMn_{1-x}O$ ($0<x<0.5$) was also prepared using the same method. All the materials prepared were found to have the α-$LiFeO_2$ structure. The effect of ball milling $LiCoO_2$ and $LiNiO_2$ powders was also studied. After prolonged milling these samples lost lithia and oxygen to form $Li_xM_{1-x}O$ ($0.25\leq x\leq 0.5$). Like α-$LiFeO_2$, cathodes of the resulting materials were found to have poor electrochemical performance in lithium cells.

4.4.1 Sample Preparation and Measurement

Ball milling was carried out with a SPEX 8000D mixer mill in 64ml vials containing two 0.5" ball bearings. Both vial and balls were of hardened steel. The vials were charged and sealed in an argon atmosphere with 3.3g of sample powder to give a ball to powder weight ratio of 5:1.

$LiTiO_2$, $LiFeO_2$ and $Li_xMn_{1-x}O$ ($0.50\leq x\leq 0.05$) were prepared from the following reactions:

$$1/2\ Li_2O + 3/4\ TiO_2 + 1/4\ Ti \rightarrow LiTiO_2 \qquad (4.1)$$

$$Li_2O + Fe_2O_3 \rightarrow 2LiFeO_2 \quad (4.2)$$

$$x/2\ Li_2O + (1/2\text{-}x/4)\ MnO_2 + (1/2\text{-}3x/4)\ Mn \rightarrow Li_xMn_{1-x}O \quad (4.3)$$

Li_2O (97%) and Mn powder (99+%) were obtained from Aldrich. Anhydrous Fe_2O_3 and TiO_2 powders were obtained from Fisher. Electrolytic MnO_2 (Mitsui TAD II grade) was heated in a furnace at 300°C overnight prior to use to remove water. Battery grade $LiCoO_2$ and $LiNiO_2$ powders obtained from Moli Energy (1990) Ltd. and the FMC Corporation respectively were ball milled as received.

After ball milling the oxide powders an overpressure, partial vacuum or some powder which had been blown out of the vial's o-ring was often observed. Similar observations have been made during the ball milling of hematite which loses oxygen and transforms to magnetite [74]. A study of the oxygen loss of $LiMO_2$ samples during ball milling should be the subject of future work. $LiMO_2$ composite cathodes were prepared by the Bellcore method as described in Chapter 2 and were cycled under thermostatic conditions at 30°C between 2 V and 4.3 V at a C/20 rate.

4.4.2 Effect of Ball Milling on $LiCoO_2$ and $LiNiO_2$

Figures 4.11 and 4.12 show the x-ray spectra of $LiCoO_2$ and $LiNiO_2$ powders respectively which were ball-milled directly for different milling times. As the milling time increases the superlattice peaks decrease in intensity, indicating that the cations are becoming more and more disordered as milling progresses. Concurrently the structure is converting from hexagonal to cubic symmetry. After 64 hours of milling the cations are completely disordered and only x-ray peaks that can be indexed with a cubic cell remain, indicating that the $LiCoO_2$ and $LiNiO_2$ have transformed into a disordered rocksalt phase during milling. As the milling time increases the x-ray peaks also shift to progressively

lower angles. This means that the lattice constants become larger with increasing milling time.

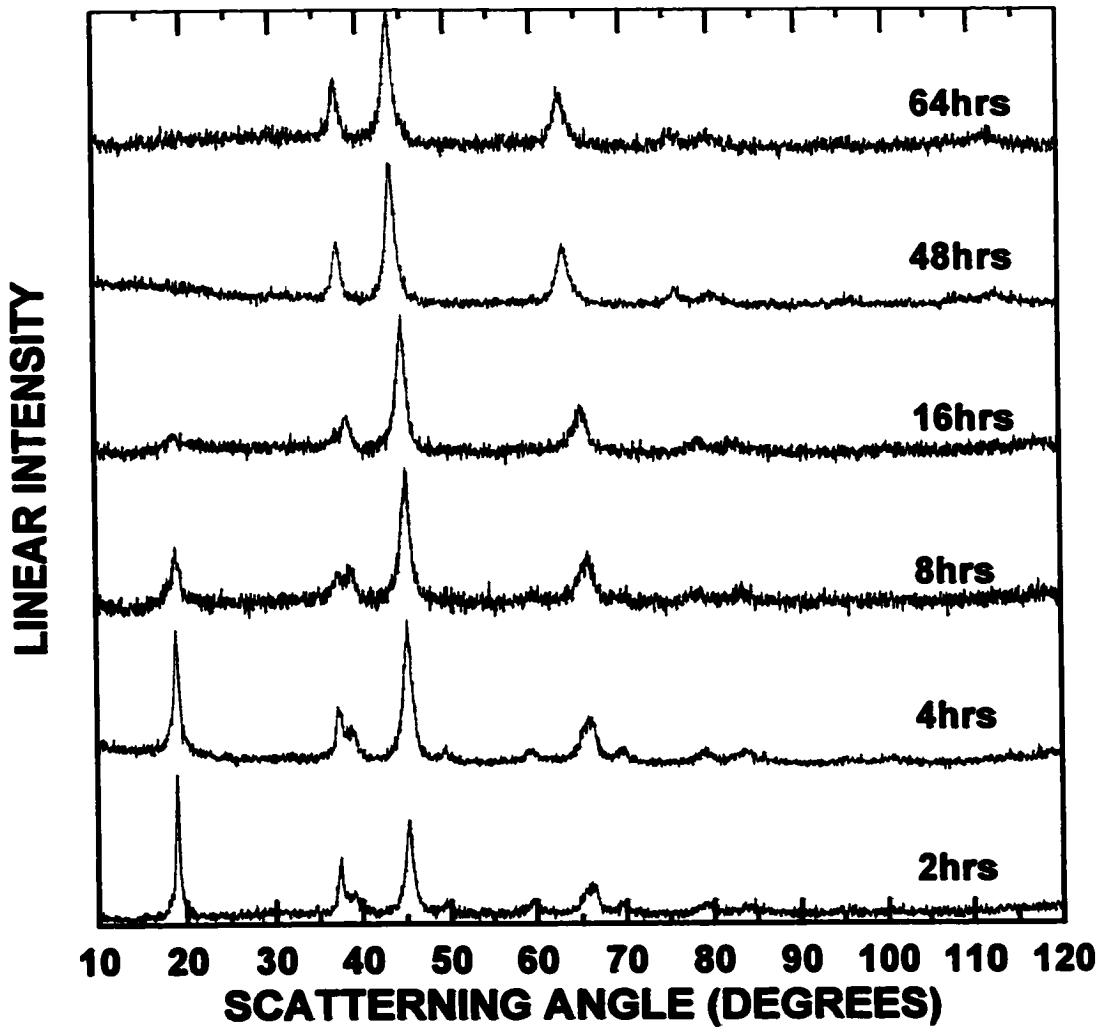

Figure 4.11 X-ray powder diffraction patterns of $LiCoO_2$ powders prepared at high temperature after subsequent exposure to different milling times.

These results are different than those obtained by Fernandez-Rodriguez et al. [72] who observed the formation of Co_3O_4 upon grinding $LiCoO_2$ in air whereas we observed no Co_3O_4 peaks in the x-ray powder diffraction spectra of our samples. The results of Ferandez-Rodriguez et al. may be due to the availability of oxygen from the air to their samples during milling. Also less energetic milling conditions were probably used which

would mean their samples were exposed to smaller pressures and temperatures upon impact with the grinding media.

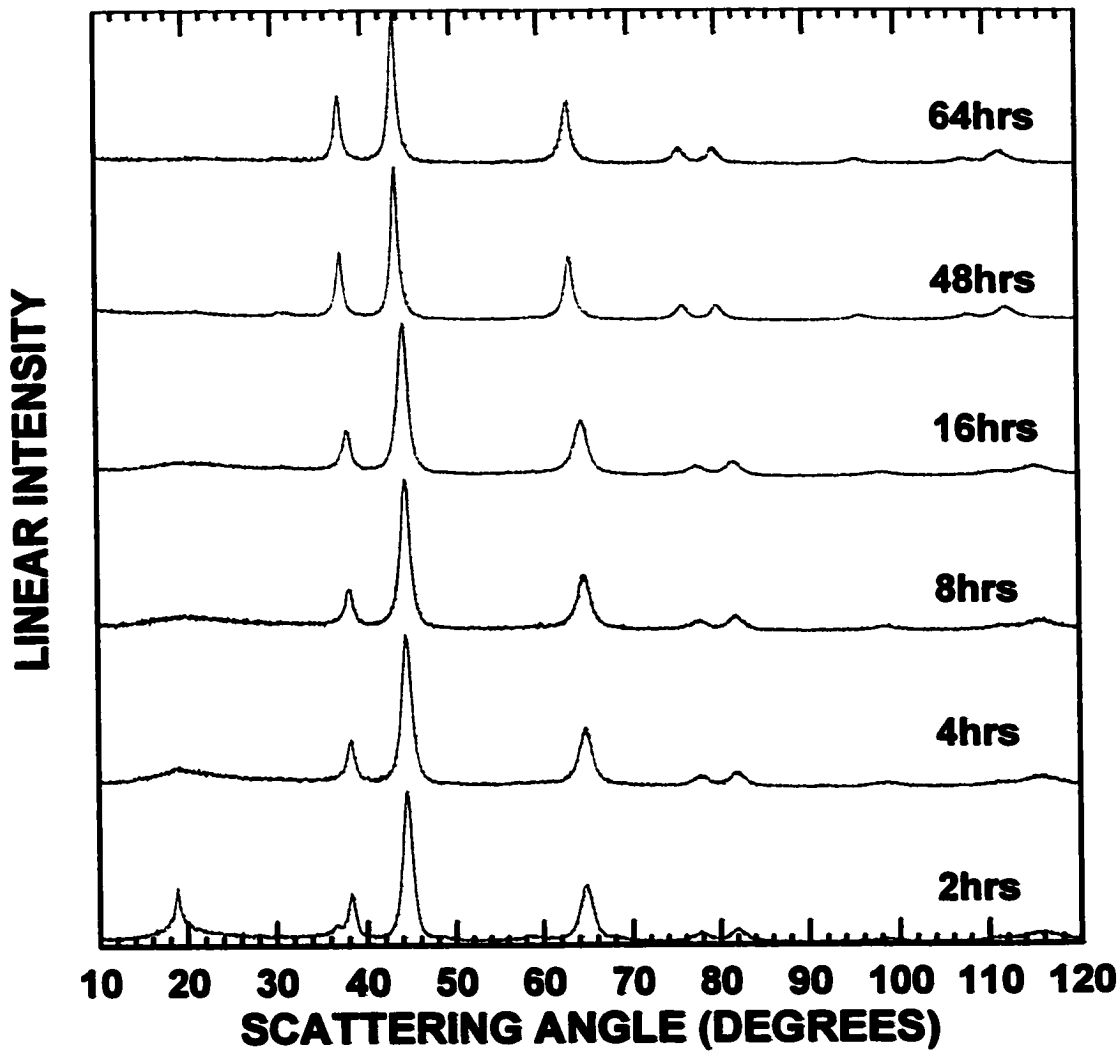

Figure 4.12 X-ray powder diffraction patterns of $LiNiO_2$ powders prepared at high temperature after subsequent exposure to different milling times.

It is well known that the high temperature phases of $Li_xM_{1-x}O$ ($x < 0.5$; M = Co, Ni) have the disordered rocksalt structure [75-77]. Furthermore the lattice constant of $Li_xM_{1-x}O$ increases as x is decreased. Thus the behaviour in figures 4.11 and 4.12 may be explained by the formation of $Li_xM_{1-x}O$ during milling according to the reaction:

$$(1\text{-}x)LiMO_2 \rightarrow Li_xM_{1-x}O + (1\text{-}2x)/2\ Li_2O + (1\text{-}2x)/4\ O_2 \qquad (4.4)$$

where the Li_2O formed may exist as very small particles or may be amorphous and thus be difficult to detect by x-ray diffraction.

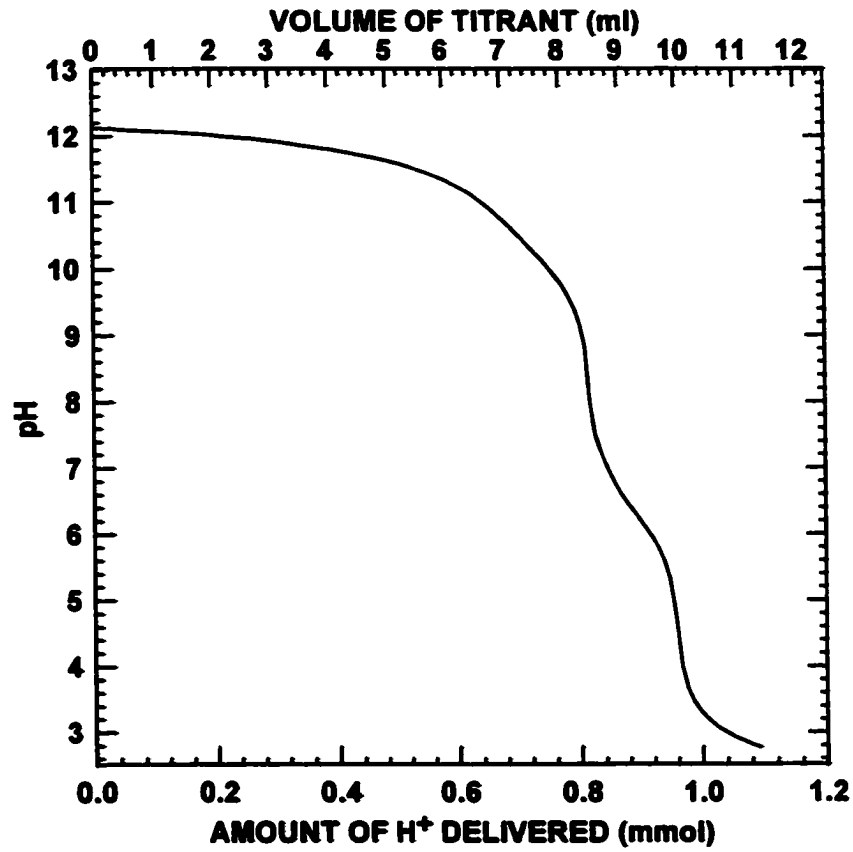

Figure 4.13 Titration curve of supernatant solution separated from a mixture of water and $LiCoO_2$ milled for 48 hours. The three plateaus at pH 12, 10 and 6 corresponding to the neutralization of lithium hydroxide and lithium carbonate respectively are clearly visable.

To verify equation (4.4), the Li_2O content of the $LiCoO_2$ samples was determined by titration as follows: 300 mg of $LiCoO_2$ was stirred with 50 ml of distilled water in a covered beaker for 1½ hours. The mixture was then centrifuged and 40 ml of the supernatant solution was titrated to a pH of 2.8 with a 0.0436 M H_2SO_4 solution using a Mettler DL21 autotitrator. A typical titration curve is shown in figure 4.13. There are 3

distinct plateaus in the figure. The first plateau at about pH 12 is due to the neutralization of hydroxide ion which is formed from the reaction of water with Li_2O. The second and third plateaus at pH 10 and 6 correspond to the neutralization of the carbonate ion. The presence of the carbonate ion is most probably due to the exposure of the samples to air after milling, since Li_2O reacts spontaneously with CO_2 in air to give Li_2CO_3. Thus the total amount of Li_2O formed during milling was calculated from the total concentration of lithium hydroxide and lithium carbonate as determined by titration.

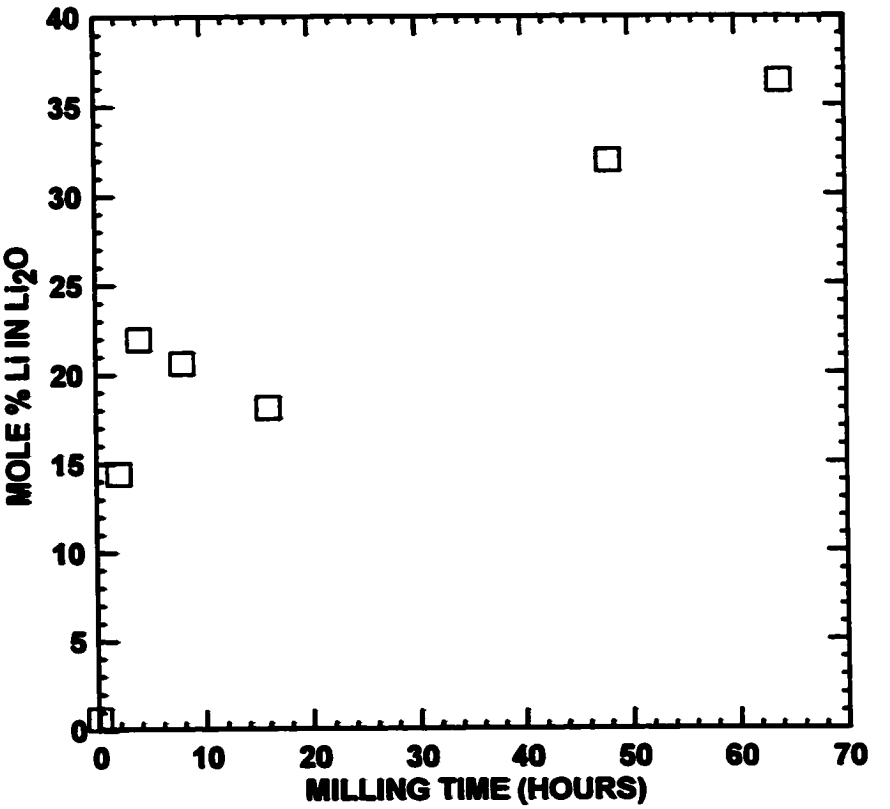

Figure 4.14 Mole percent of lithium lost in the form of lithia from the $LiCoO_2$ samples during milling as determined by titration.

Figure 4.14 shows the mole percent of lithium lost from $LiCoO_2$ to form Li_2O as determined by titration. As the milling time increases, the amount of lithium lost from

$LiCoO_2$ increases to almost 40%. The scatter in the plot may be due to differences in the seal of the milling containers between samples, which would cause the oxygen partial pressure in the containers to vary.

To determine the structural lithium content in $LiCoO_2$ and $LiNiO_2$ samples exposed to different milling times a Rietveld analysis of the x-ray diffraction patterns was performed. The analysis proceeded as follows. In all the refinements ionic scattering factors were used with Co and Ni having a valence of +3. Also, the superlattice peak was not included in any of the refinements. For those samples with hexagonal symmetry, the structure of stoichiometric $LiCoO_2$ and $LiNiO_2$ was assumed. This structure is based on the $R\bar{3}M$ space group with the oxygen atoms in the 6c sites forming cubic close packed layers and the lithium and transition metal atoms occupying the 3a and 3b sites respectively. In these refinements the oxygen occupation was set equal to one, while the cation occupations were set according to Li_xM_{1-x}, keeping the total cation occupation equal to one. Cation mixing was allowed on the 3a and 3b sites. The possibility of oxygen vacancies was not taken in to account in the refinements.

When no hexagonal peaks were present in the x-ray spectra this gave large errors for the lattice constants since fewer Bragg peaks were included in the refinement. In these cases a cubic cell with the rocksalt structure was used with the Li^+ and M^{3+} ions occupying the cation sites randomly. Here the oxygen occupation number and the total cation occupation number were fixed at one, but the relative amounts of the Li^+ and M^{3+} ions were allowed to vary. As with the above procedure no accounting for oxygen vacancies was taken in the refinements.

The results of the $LiCoO_2$ and $LiNiO_2$ refinements are listed in tables 4.1 and 4.2

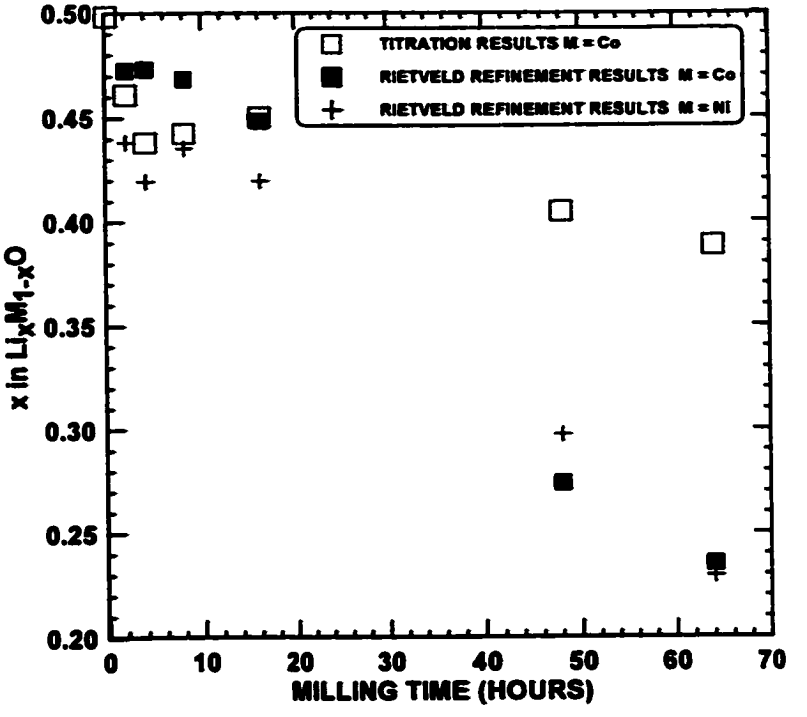

Figure 4.15 Composition of the $LiCoO_2$ and $LiNiO_2$ samples after different milling times as determined by titration and Rietveld refinement

Table 4.1 Results of Rietveld refinements of x-ray data from ball milled $LiCoO_2$ samples.

Milling Time (hours)	Structure	X_{Li}	a (Å)	c (Å)	$\sqrt{24}a/c$	χ^2	R_B
2	hex	0.47(1)	2.822(2)	14.09(1)	0.981(1)	1.02	0.85
4	hex	0.473(8)	2.823(2)	14.07(1)	0.983(1)	1.11	1.69
8	hex	0.47(1)	2.838(4)	14.05(3)	0.989(2)	1.00	0.69
16	hex	0.45(2)	2.849(4)	14.07(3)	0.992(2)	1.11	0.71
48	cub	0.27(1)	4.143(2)	-	1	1.03	1.00
64	cub	0.24(2)	4.164(3)	-	1	1.08	0.80

Table 4.2 Results of Rietveld refinements of x-ray data from ball milled $LiNiO_2$ samples.

Milling Time (hours)	Structure	X_{Li}	a (Å)	c (Å)	$\sqrt{24}a/c$	χ^2	R_B
2	hex	0.438(4)	2.879(1)	14.11(1)	0.9992(8)	1.41	2.05
4	cub	0.419(4)	4.074(1)	-	1	1.49	1.30
8	cub	0.435(4)	4.075(1)	-	1	1.47	1.13
16	cub	0.420(3)	4.0861(9)	-	1	2.09	0.89
32	cub	0.361(8)	4.130(2)	-	1	1.14	1.81
48	cub	0.298(4)	4.1517(5)	-	1	1.59	1.03
64	cub	0.230(6)	4.1675(7)	-	1	1.18	1.11

respectively. Figure 4.15 shows the value of x as calculated by the Rietveld refinements for the $LiCoO_2$ and $LiNiO_2$ samples and the value of x calculated from the titration results of $LiCoO_2$. The $LiNiO_2$ Rietveld refinement results are nearly the same as those for the $LiCoO_2$ samples. The values of x calculated from the titration results are close to the Rietveld results for $LiCoO_2$ for short milling times, but they are larger than the Rietveld results for milling times greater than 16 hours. According to the Rietveld results up to about 70% of the lithium originally in these samples is lost during milling. Some of this lithium, presumably in the form of Li_2O may be trapped within particles or absorbed on the milling container walls, thus being unavailable for titration.

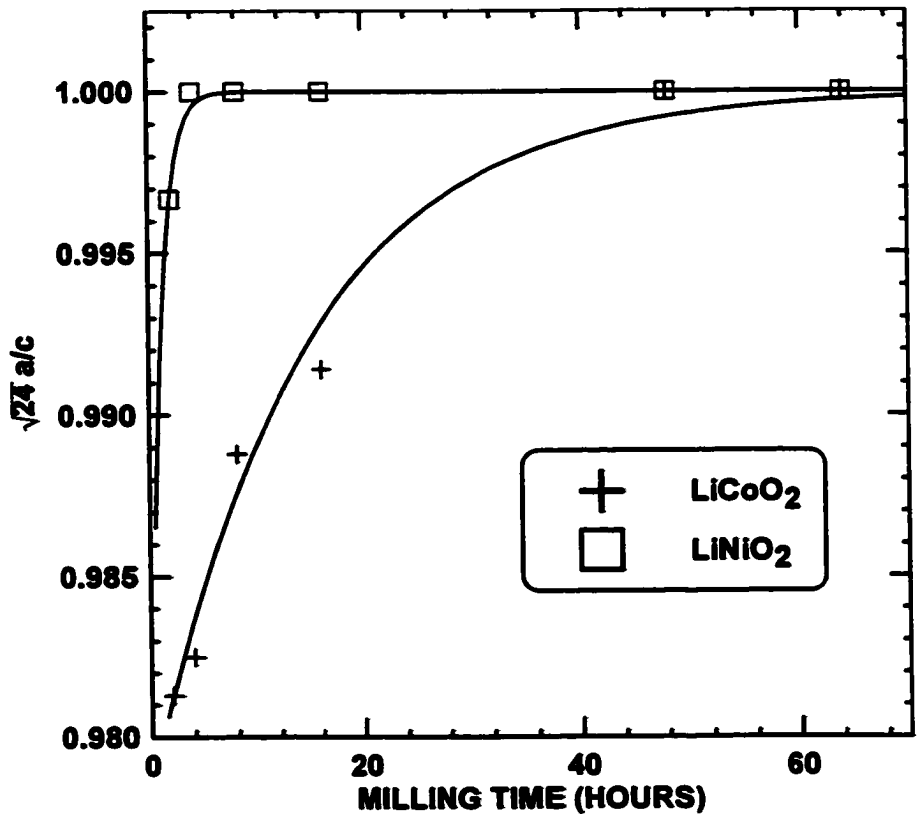

Figure 4.16 The cell constant ratio $\sqrt{24}a/c$ plotted as a function of milling time for $LiCoO_2$ and $LiNiO_2$ samples showing how their structures are transformed to cubic symmetry ($\sqrt{24}a/c = 1$) as the milling progresses.

In order to follow the hexagonal to cubic transformation in the samples of $LiCoO_2$ and $LiNiO_2$ exposed to different milling times, the ratio $\sqrt{24}a/c$ is also listed in tables 4.1 and 4.2 and is equal to one for an ideal cubic-close-packed oxygen lattice. In $LiCoO_2$ and $LiNiO_2$ prepared at high temperature, the cations are ordered in alternate lithium and cobalt layers which breaks the 3m symmetry, making the ratio non-ideal. Since the samples indexed with a cubic cell all gave good fits, $\sqrt{24}a/c$ was assumed equal to 1 for these samples. Figure 4.16 shows $\sqrt{24}a/c$ versus milling time for the $LiNiO_2$ and $LiCoO_2$ samples where the solid lines have been added as a guide to the eye. $LiNiO_2$ is transformed to the cubic structure only after about 2-4 hours of milling, while $LiCoO_2$ transforms gradually to the cubic structure over about 50 hours of milling.

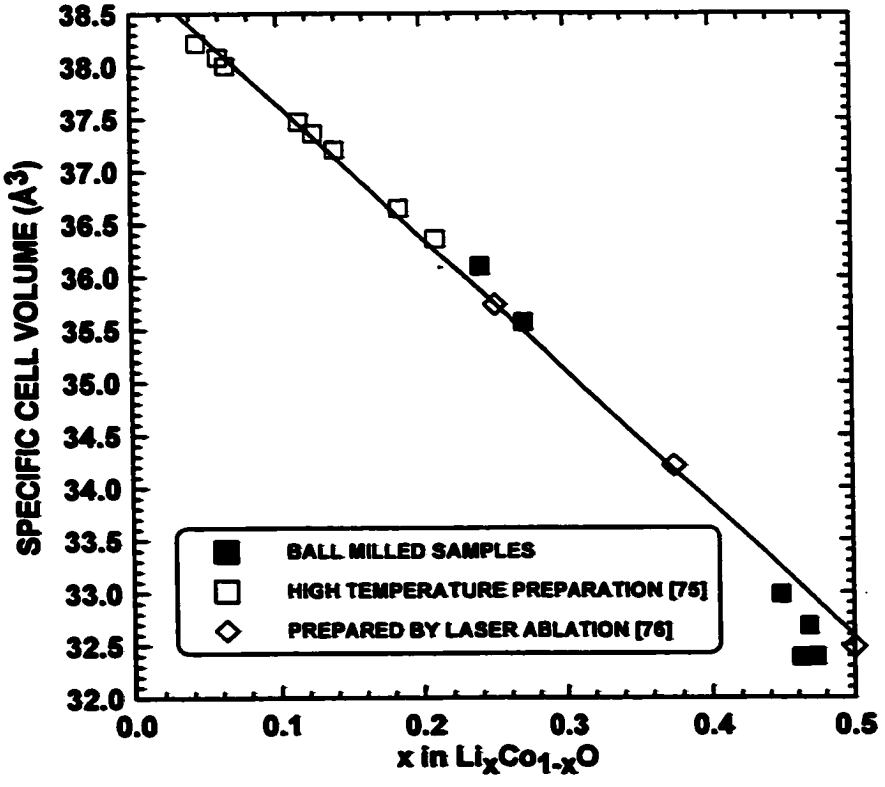

Figure 4.17 The specific cell volume of the $Li_xCo_{1-x}O$ samples prepared by ball milling compared to results from earlier studies.

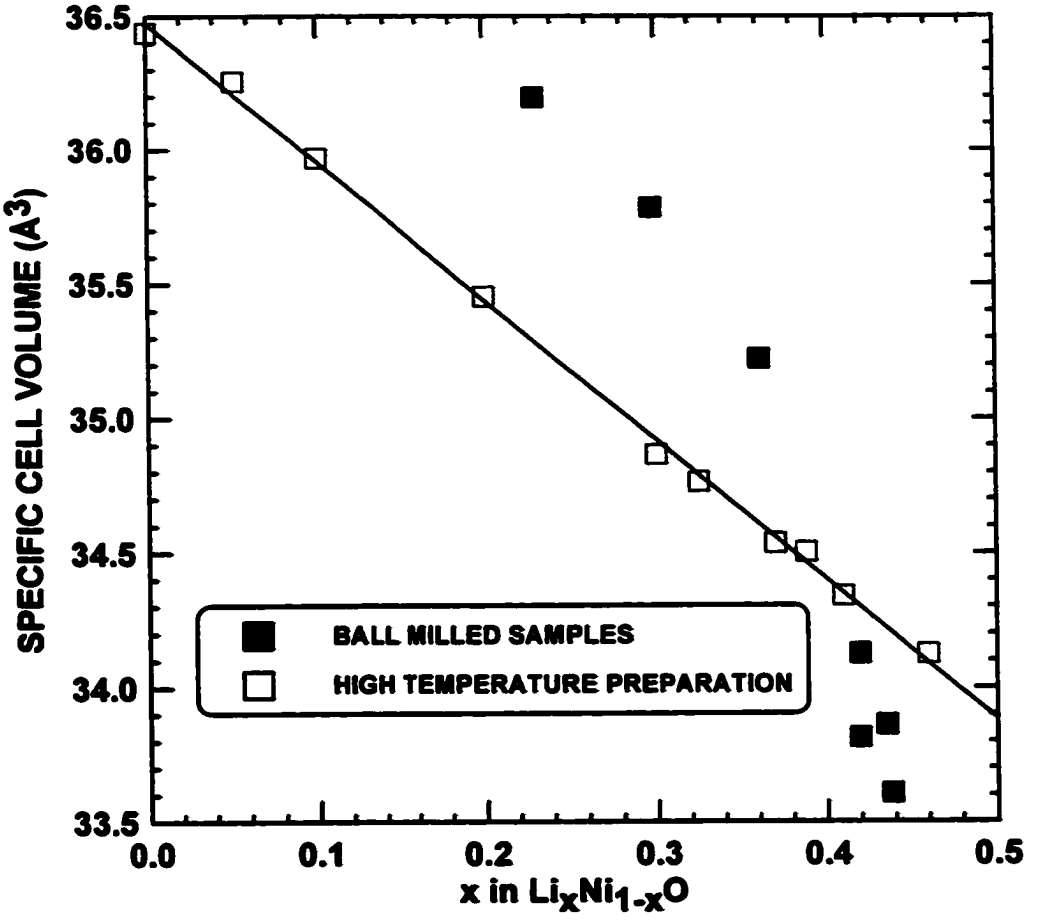

Figure 4.18 The specific cell volume of the $Li_xNi_{1-x}O$ samples prepared by ball milling compared to samples prepared at high temperature [77].

Figures 4.17 and 4.18 compare the specific cell volumes of the milled $LiCoO_2$ and $LiNiO_2$ samples as a function of x with those of rocksalt $Li_xCo_{1-x}O$ and $Li_xNi_{1-x}O$ from other studies [75-77]. There is good agreement between the cell volumes of the $Li_xCo_{1-x}O$ samples with earlier results. Agreement is less good between the milled $LiNiO_2$ samples and $Li_xNi_{1-x}O$ samples prepared at high temperatures in figure 4.19. For samples with small values of x (long milling times) the cell volume is larger than those prepared at high temperatures. This may be due to oxygen loss from the $Li_xNi_{1-x}O$ structure during milling. The discrepancy might also be caused by the substitution of

iron in the structure, since for Cu-Kα radiation iron has a smaller scattering factor than nickel this would cause the Rietveld program to underestimate the amount of transition metal in the material, overestimating the value of x. A Mössbauer study of these materials is needed to reveal if any iron has been incorporated in the structure.

4.4.3 Mechanochemical Synthesis of $LiTiO_2$, $LiFeO_2$ and $LiMnO_2$

Figure 4.19 shows the powder x-ray diffraction spectra of mechano-synthesized $LiMnO_2$ after different milling times. After 2 hours of milling the MnO_2 and Mn peaks from the starting materials are clearly visible, but no Li_2O peaks can be seen in the spectrum. Peaks from the final product are also visible after only 2 hours of milling. After 16 hours of milling none of the peaks from the starting materials are present. The product after 48 hours of milling has the NaCl structure, but there is a broad superlattice peak indicating some short range order exists among the cations.

Figures 4.20 and 4.21 show the powder x-ray diffraction spectra of $LiTiO_2$ and $LiFeO_2$ products respectively after 32 hours and 48 hours of milling. Both spectra correspond to the disordered rocksalt structure. However, in the case of the $LiTiO_2$ samples, the peaks with odd hkl are very weak making the x-ray spectra look like that of a simple cubic structure. If Li^+ and Ti^{3+} are arranged randomly on the cation lattice, then the scattering power of the cation lattice is roughly proportional to the average number of electrons in Li^+ and Ti^{3+} (ie, 10.5). This is nearly equal to the number of electrons in O^{2-}. Thus the scattering power of the cation and anion lattices are nearly the same. This has the effect of making $LiTiO_2$ appear to have the x-ray spectrum of a simple cubic lattice. Rietveld analysis of the spectra in figures 4.19, 4.20 and 4.21 gave poor fits unless a second elemental iron phase was included in the refinements, otherwise the refinement

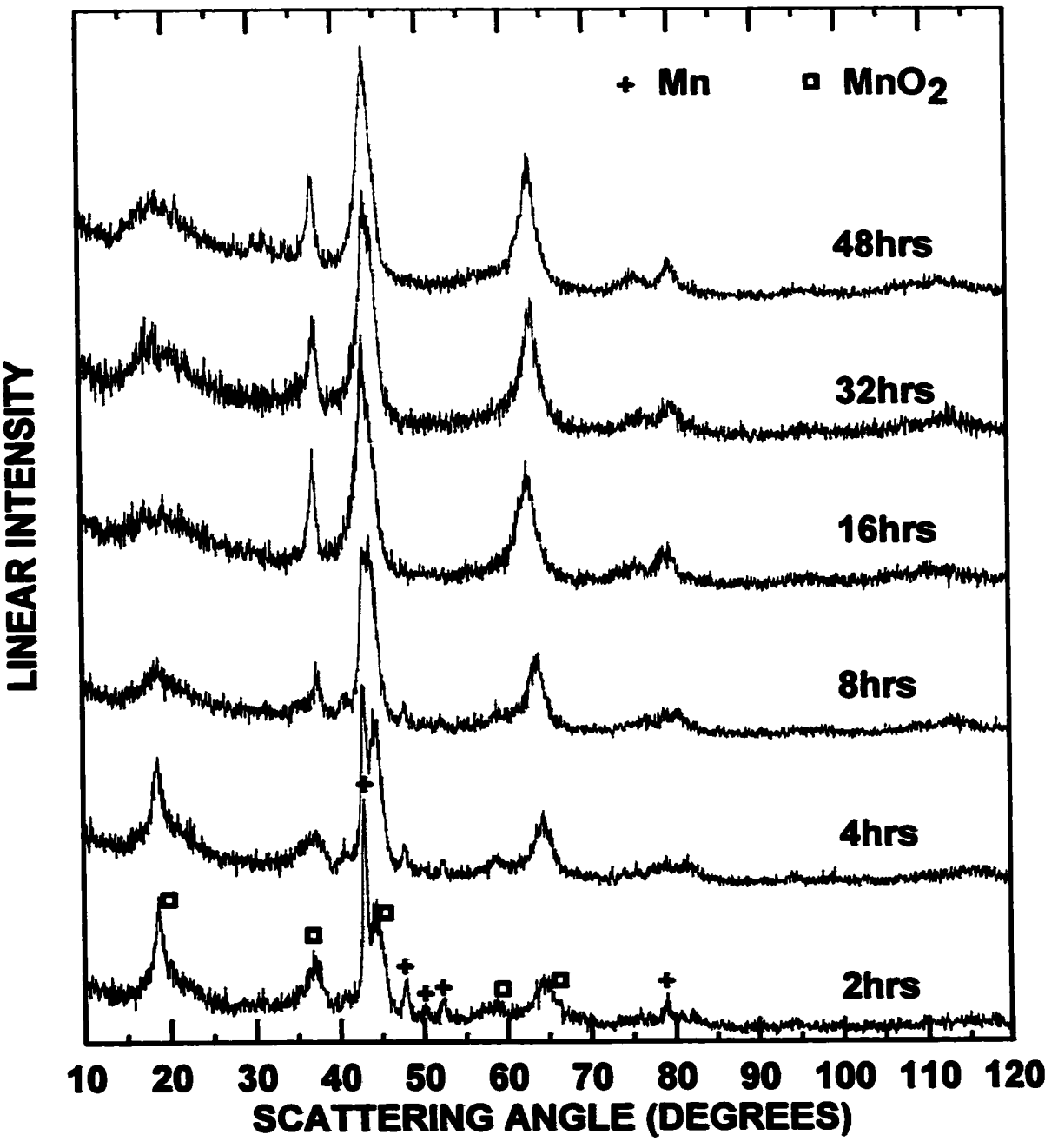

Figure 4.19 X-ray powder diffraction patterns of $LiMnO_2$ prepared at different milling times. The peaks in some of the spectra at about 22° and 32° are probably due to the formation of lithium carbonate after exposure of the samples to air

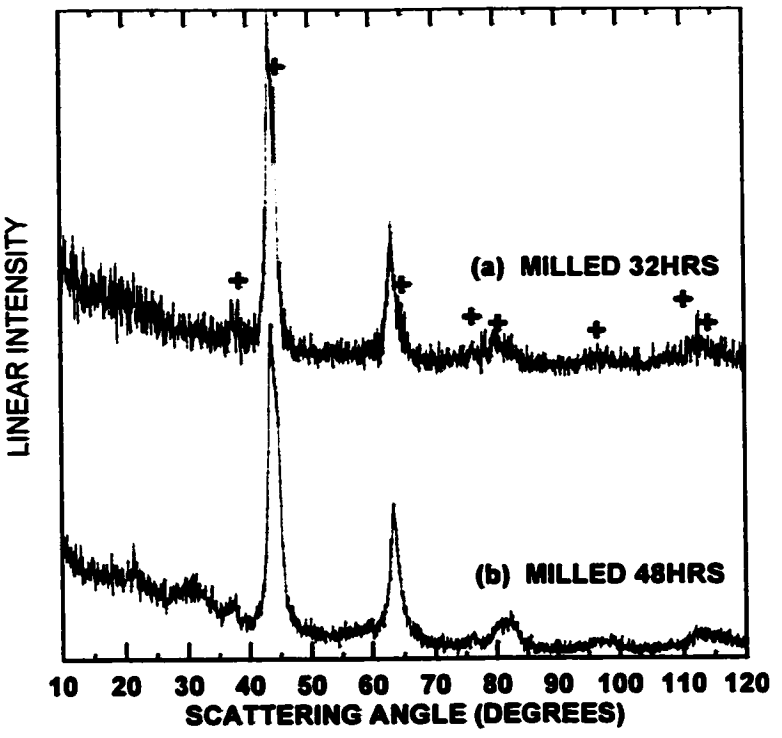

Figure 4.20 X-ray powder diffraction patterns of $LiTiO_2$ prepared by ball milling for (a) 32 and (b) 48 hours. The indicated peaks are due to the aluminum sample holder.

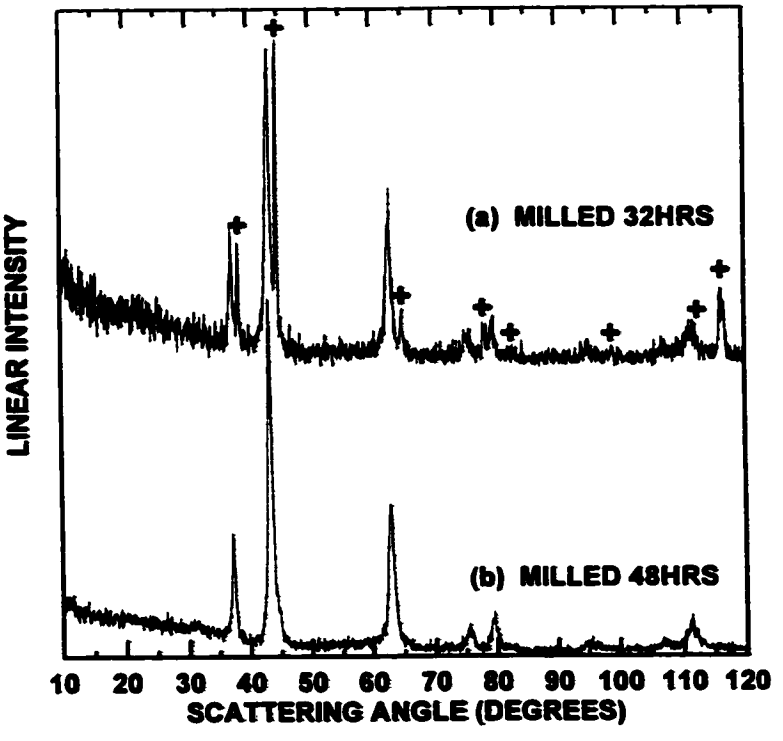

Figure 4.21 X-ray powder diffraction patterns of $LiFeO_2$ prepared by ball milling for (a) 32 and (b) 48 hours. The indicated peaks are due to the aluminium sample holder.

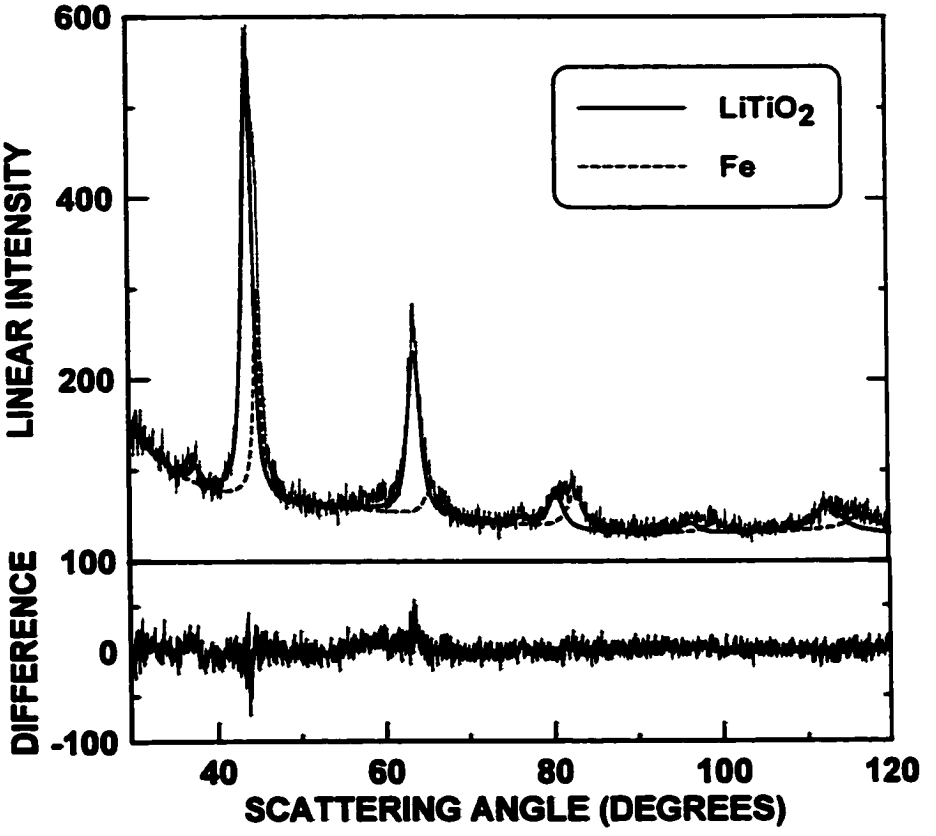

Figure 4.22 Rietveld refinement of $LiTiO_2$ spectrum showing the contributions from the $LiTiO_2$ and the Fe phases used in the fit. The difference between the observed and calculated patterns is shown in the bottom panel.

procedure was the same as for the cubic $LiCoO_2$ and $LiNiO_2$ samples above. Only the scale factor and the peak shape functions were allowed to vary in the iron phase. Figure 4.22 shows the contributions of the two phases in the refinement of $LiTiO_2$ after 48 hours of milling. There is a significant amount of elemental iron in this sample. Presumably the iron impurities came from the milling media. Table 4.3 lists the results of the refinements. Good fits were obtained ($R_B \leq 4$), except in the case of $LiMnO_2$, which nevertheless gave accurate values of the lattice constants. If an orthorhombic cell was used for this sample a similar R_B was obtained. Because of the iron impurity it is difficult to assign definitely either a cubic or orthorhombic cell to this sample. The values of the

lithium fraction in these samples is also questionable. This may be due to effects of the iron impurity in the refinements. In contrast to the $LiNiO_2$ and $LiCoO_2$ samples, there is only a small difference (<1.5%) in the specific cell volume of the milled $LiTiO_2$, $LiFeO_2$ and $LiMnO_2$ samples and those prepared at high temperature [69]. Further studies are needed to determine whether $Li_xM_{1-x}O$ (M=Fe, Ti, Mn) can be obtained from $LiMO_2$ samples by ball milling for extended periods.

Table 4.3 Rietveld refinement data of $LiMO_2$ (M=Ti, Mn, Fe) samples prepared by ball milling.

Sample	*a (Å)*	X_{Li}	χ^2	R_B
$LiTiO_2$	*4.149(1)*	*0.60(1)*	*1.24*	*2.87*
$LiMnO_2$	*4.179(4)*	*0.42(1)*	*1.65*	*5.05*
$LiFeO_2$	*4.175(4)*	*0.406(7)*	*1.22*	*4.62*

4.4.4 Mechanochemical Synthesis of $Li_xMn_{1-x}O$

Substituted manganese oxides, $Li_xMn_{1-x}O$ ($0.35 \leq x \leq 0.05$) were prepared by the following reaction:

$$x/2\ Li_2O + (1/2-x/4)\ MnO_2 + (1/2-3x/4)\ Mn \rightarrow Li_xMn_{1-x}O \qquad (4.5)$$

The spectra of the samples after milling 48 hours are shown in figure 4.23. These oxides were found to have the disordered rocksalt structure which is also formed in high temperature preparations of $Li_xMn_{1-x}O$ ($0.35 \leq x \leq 0.0$) [78]. The peaks at about $2\theta = 44.7°$ correspond to an iron metal impurity, presumably from the milling media.

The Rietveld refinements of the x-ray spectra using the same method as for the $LiTiO_2$, $LiMnO_2$ and $LiFeO_2$ samples above gave poor results (sometimes negative) for the lithium occupation number, possibly due to interference in the refinement from the

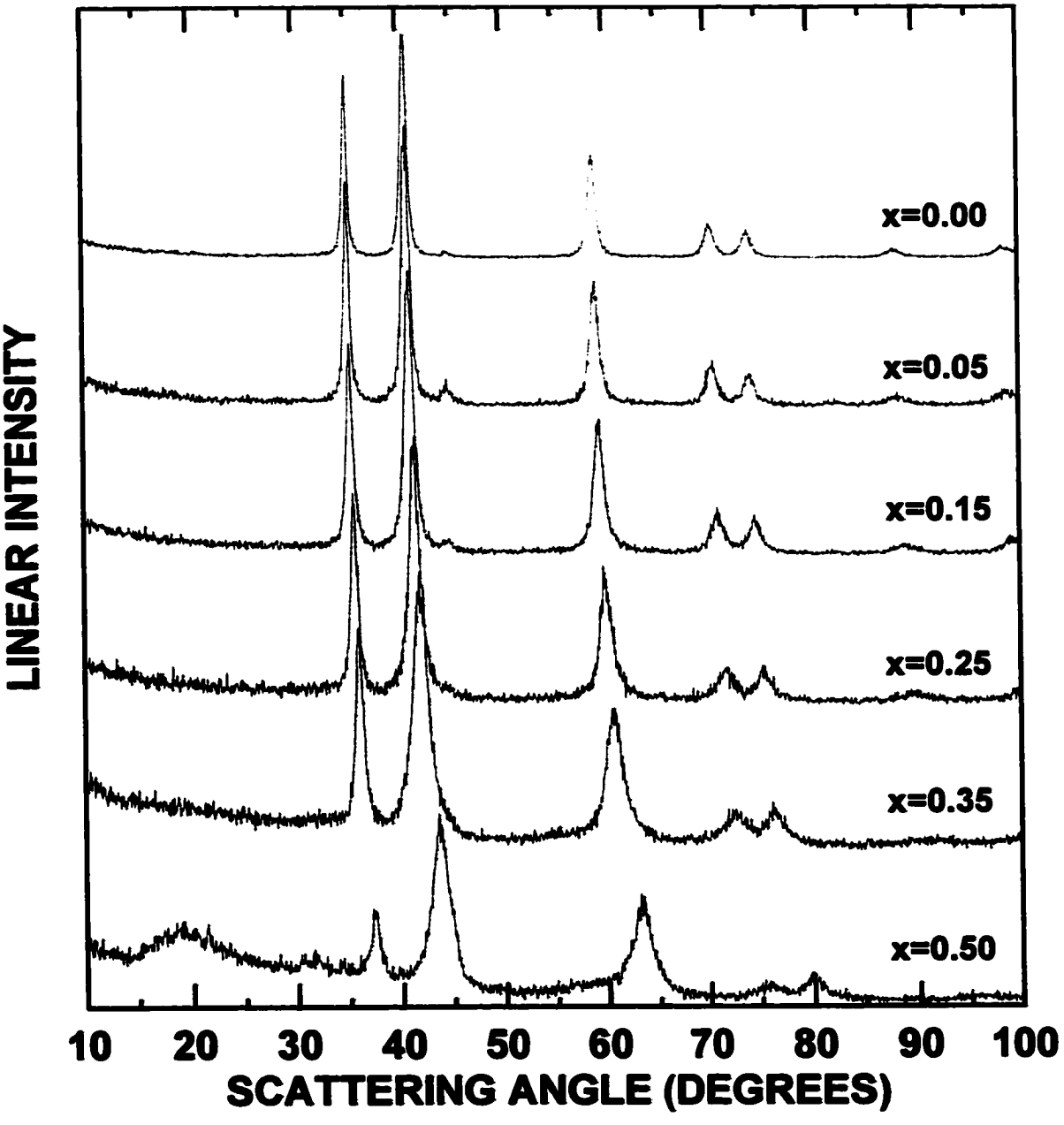

Figure 4.23 X-ray powder diffraction patterns of $Li_xMn_{1-x}O$ prepared by ball milling for 48 hours.

iron impurity. However accurate values of the cation stoichiometry according to equation (4.5) and letting the oxygen occupation vary. A second iron phase was included as above and atomic form factors were used in the refinements. Results of the Reitveld refinements of the $Li_xMn_{1-x}O$ ($0.35 \leq x \leq 0.0$) series of compounds are listed in table 4.4.

The fits have a Bragg R factor (R_B) of less than 3%. The specific volume of these samples is compared with those prepared at high temperature [78] in figure 4.24. There is good agreement between the specific volumes of the samples prepared by the two different methods indicating that after 48 hours of milling the composition of the samples differs little from that set by the initial stoichiometry of the starting materials.

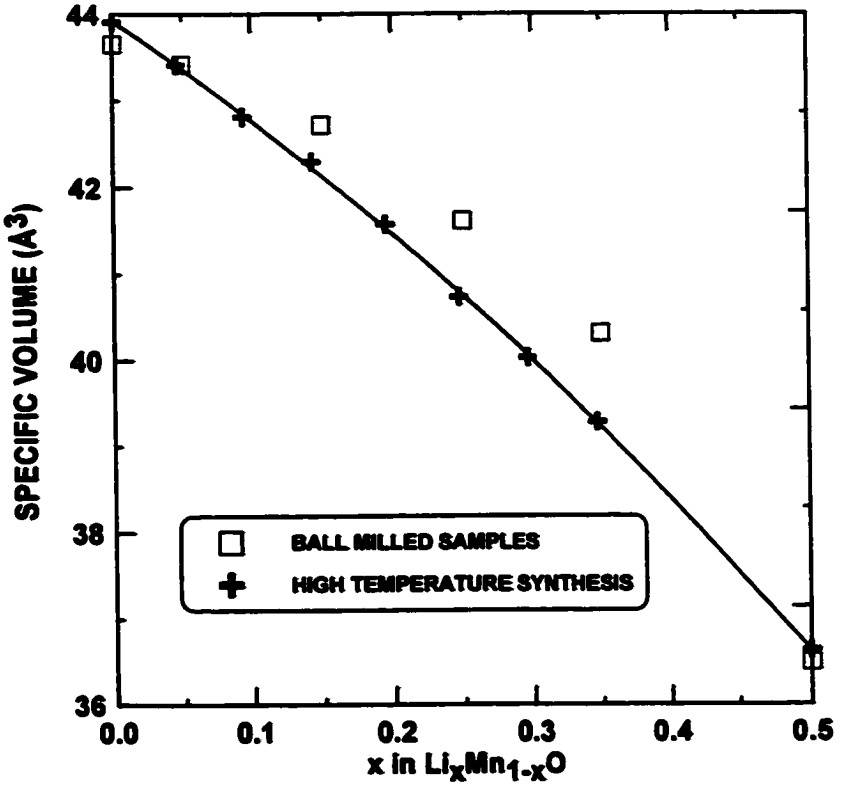

Figure 4.24 The specific volume of $Li_xMn_{1-x}O$ powders prepared by ball milling compared to samples prepared at high temperatures [75] as a function of composition.

Table 4.4 Lattice constants of $Li_xMn_{1-x}O$ samples calculated by Rietveld refinement.

x	a (Å)	χ^2	R_B
0.00	4.4364(6)	1.32	1.16
0.05	4.428(1)	1.15	2.26
0.15	4.405(1)	1.29	1.73
0.25	4.366(2)	1.18	2.53
0.35	4.320(2)	1.54	2.81
0.50	4.179(4)	1.65	5.05

4.4.5 Electrochemical Studies of $LiMO_2$ Oxides

Figures 4.25 and 4.26 show the voltage curves of $LiCoO_2$ and $LiNiO_2$ samples exposed to different milling times. As the milling time increases the reversible capacity decreases and the polarization increases for both compounds. The decrease in capacity is much less than can be taken into account by the loss of lithia from the samples during milling. Furthermore, above 3-volts, the milled samples have large irreversible capacities. The low capacity of these materials may be due to poor lithium diffusion in the disordered lattice. Decomposition of the cathode during charge may also account for the low capacities observed.

Figure 4.27 shows the voltage curves of $LiMnO_2$, $LiFeO_2$ and $LiTiO_2$ prepared by ball milling for 48 hours. The $LiFeO_2$ and $LiTiO_2$ samples have very little reversible capacity between 2V and 4.5V. The larger reversible capacity of the $LiMnO_2$ sample may be due to the short-range cation order still present even after extended milling.

4.4.6 Summary of Results

It was shown in this section that mechanical alloying can be used to synthesize $LiMO_2$ (M = Ti, Fe) and $Li_xMn_{1-x}O$ ($0.5 \leq x \leq 0.0$) at room temperature. In each case the grain size of the resulting products was small (about 25Å according to the Scherrer equation), however all of the compounds synthesized had the disordered rocksalt structure, excepting $LiMnO_2$ which had some short-range cation order. Extended mechanical alloying of $LiCoO_2$ and $LiNiO_2$ prepared at high temperature also resulted in small grain sized materials (about 50Å), but this was also accompanied by degradation of the structure to the rocksalt phase and the formation of $Li_xM_{1-x}O$ accompanied by Li_2O

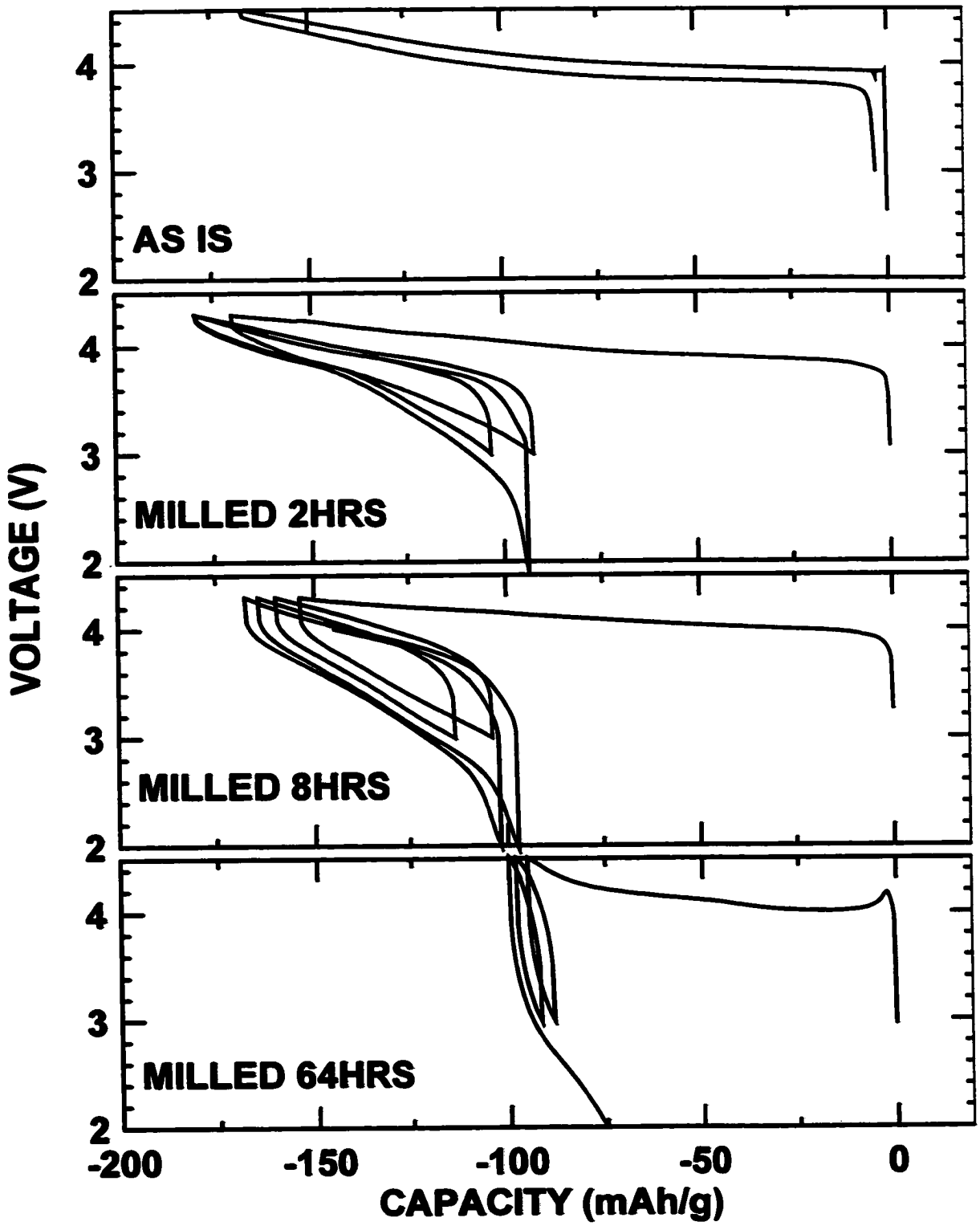

Figure 4.25 Voltage profiles of cathodes prepared from $LiCoO_2$ samples exposed to different milling times.

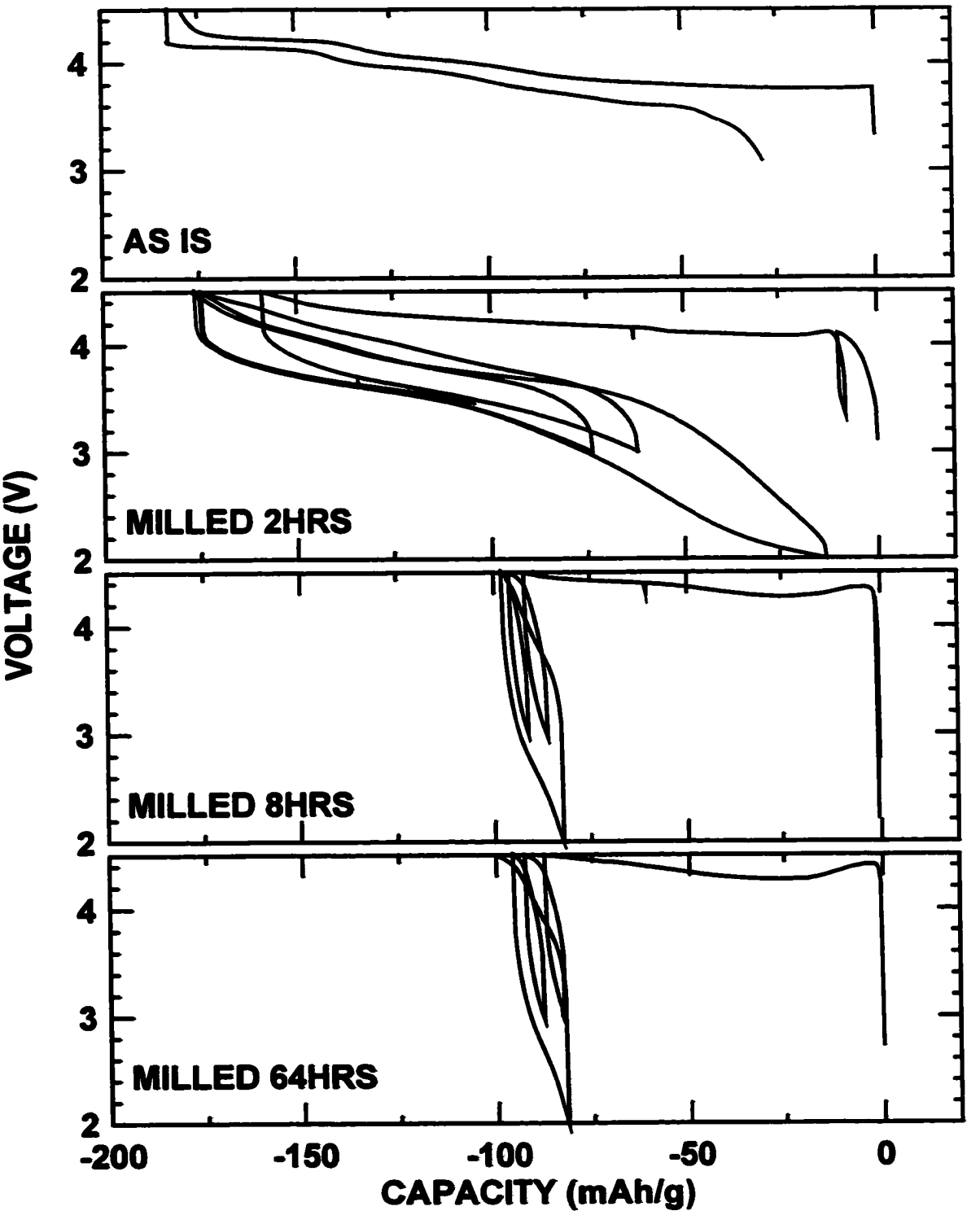

Figure 4.26 Voltage profiles of cathodes prepared from $LiNiO_2$ samples exposed to different milling times.

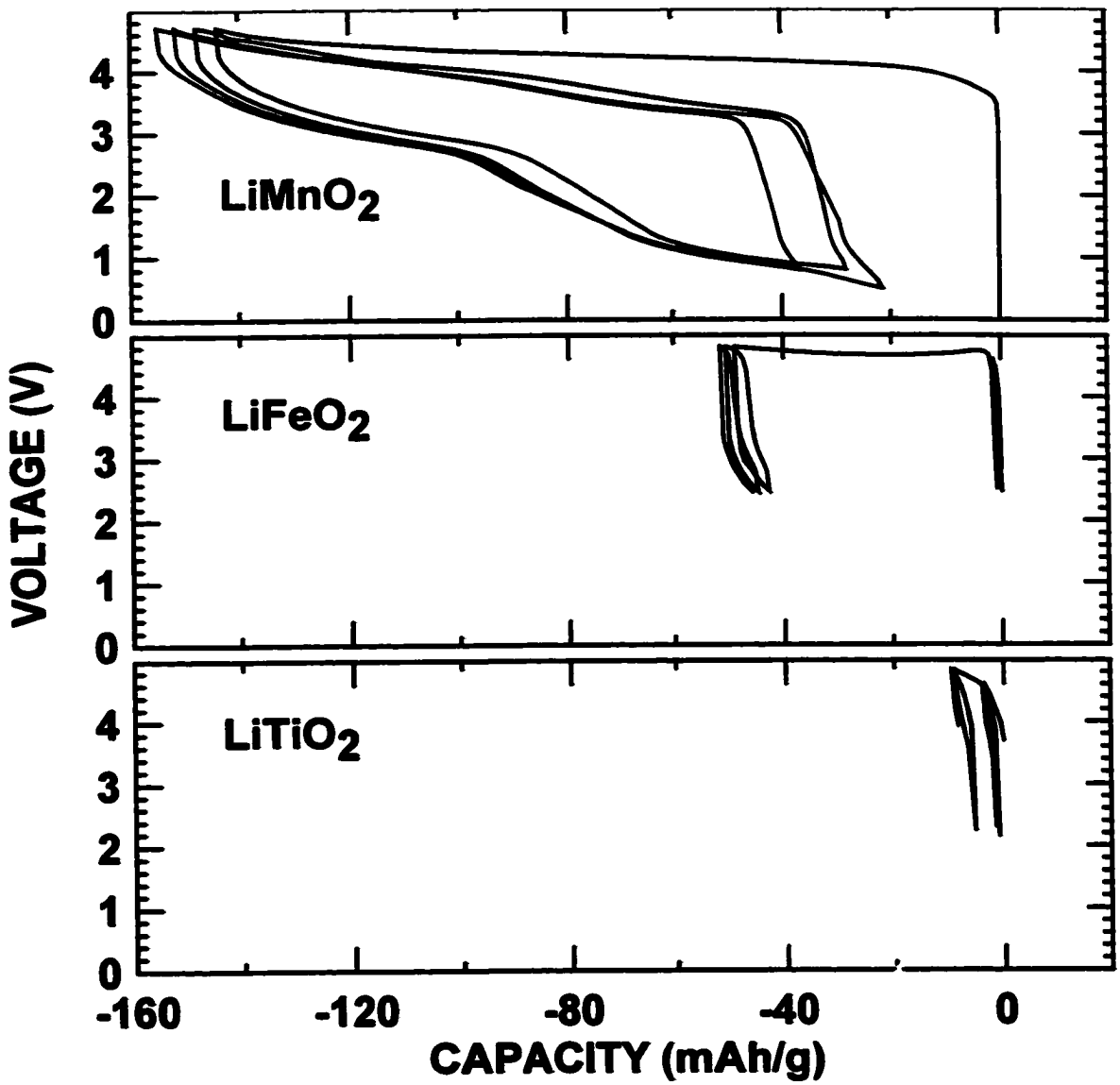

Figure 4.27 Voltage profiles of cathodes prepared from $LiMnO_2$, $LiFeO_2$ and $LiMnO_2$ samples milled for 48 hours.

and oxygen release. Nevertheless, ball milling may be a convenient way to prepare bulk quantities of lithium substituted monoxides, especially in the case of $Li_xCo_{1-x}O$, which is otherwise difficult to prepare in bulk quantities [76]. Further studies are required to determine if $Li_xM_{1-x}O$ can be prepared by extended milling of $LiMO_2$ for M = Ti, Fe and Mn.

The milled materials were shown to have poor electrochemical performance as cathodes in lithium batteries. However subsequent annealing of the mechanically alloyed material may produce electrochemically active phases and should be the topic of further study. In this way mechanical alloying could be a useful and easy method of preparing precursors for cathode materials with compositions difficult to prepare by other methods (see, for example, the synthesis of Li_5FeO_4 described in section 5.2). The materials could then be subsequently annealed to make them electrochemically active. Nanograined materials could not be made in this way, however, since the annealing step would cause grain growth.

4.5 SOLUTION-BASED SYNTHESIS AND ELECTROCHEMISTRY OF NANOGRAINED LITHIUM MANGANES OXIDE

As demonstrated in section 4.3 there is a conflict between making nanograined $LiMn_2O_4$ spinel and the high synthesis temperatures required to make this material. Thus in order to make nanograined $LiMn_2O_4$ the material has to be either confined in a matrix, as was attempted in section 4.3 or the material must be formed metastably at low temperatures. This was the approach of the mechanochemical syntheses in the last section, however that method was found to induce cation mixing as well as oxygen and lithia loss, resulting in rocksalt phases with poor electrochemical performance.

Another method has been described in a paper by Strobel et al [79]. They describe a room temperature solution-based synthesis of $Li_{1-x}Mn_2O_{4-\delta}$ ($x \sim 0.3$, $\delta \sim 0.01$). Although the material was claimed to be the spinel phase, no structural characterization was undertaken. Furthermore, electrochemical measurements were only made on the 3 V plateau while the 4 V pleatau is useful for lithium ion batteries. A study of the

microstructure of this material was also not presented. This section describes the synthesis, structure, morphology and electrochemistry of nanograin Li-Mn-oxide prepared in a similar way as described by Strobel [79]. As was found by Strobel et al., the material was found to be lithium rich. However here it is shown that the material is probably not a spinel phase as made, but rather converts to spinel during cycling. The very interesting microstructure of this material, consisting of a strange arrangement of self-assembled grains, will also be discussed.

4.5.1 Synthesis of Nanograin Lithium Manganese Oxide in Aqueous Solution

A typical synthesis of Li-Mn-oxide in aqueous solution, modified slightly from the synthesis used by Strobel [79], was as follows. 45 g of $LiOH \cdot H_2O$ (Aldrich) were dissolved in 225 ml of distilled water in a glass beaker. In a separate beaker 13.5 g of $Mn(NO_3)_2 \cdot 4H_2O$ were dissolved in 45 ml of distilled water and then added drop wise to the lithium hydroxide solution while stirring. This produced a rose coloured precipitate. Oxygen gas was then bubbled vigorously in the solution while stirring for 30 minutes, causing the precipitate to turn black. The solution was then filtered and washed with concentrated ammonium hydroxide solution. Ammonium hydroxide was used since it evaporates with no residue, it solubilizes lithium hydroxide and operating at a high pH would tend to avoid ion exchange of hydrogen for lithium in the spinel structure. After washing the recovered powder was dried in air overnight at 110°C.

4.5.2 Chemical Characterization of Nanograin Lithium Manganese Oxide

Samples of nanograin Li-Mn-oxide were sent to Chemetals for chemical analysis. The results of the analysis are listed in table 4.5. The lithium content was determined by

atomic absorption spectroscopy. Water content was determined by weight loss during heating at 110°C and 300°C. The total manganese content of the sample was determined by first dissolving the sample in concentrated HCl, which reduces all the manganese to Mn^{2+}. Then the total manganese concentration is determined by a potentiometric titration with $KMnO_4$ [80].

Table 4.5 Results of the chemical analysis of a lithium manganese oxide sample prepared in aqueous solution and dried at 110°C. The % O was derived both by the method of charge balance and by assuming all of the weight not accounted for by lithium, manganese and water is due to oxygen.

From Chemical Analysis		*Derived Quantities*	
% Mn	*51.7*	*Mn valence*	*3.82*
% MnO_2	*74.46*	*% O by weight*	*36.1*
% Li	*6.15*	*% O charge balance*	*35.8*
% H_2O	*6.09*		

The $\%MnO_2$ number has historic backgrounds and requires some explanation. The number comes from chemical analyses specified by the International Battery Material Association [80]. These analyses were originally designed for MnO_2, which is an electrode material in alkaline cells. A common method to determine the $\%MnO_2$ number is to dissolve the sample in an acidic solution containing an excess of $FeSO_4$ [80]. The manganese in the sample with a valence greater than two will be reduced by the Fe^{2+} ions in the solution. The Mn^{4+} and Mn^{3+} ions are reduced according to the following reactions.

$$MnO_2 + 2Fe^{2+} + 4H^+ \rightarrow Mn^{2+} + 2Fe^{3+} + 2H_2O. \quad (4.6)$$

$$1/2Mn_2O_3 + Fe^{2+} + 3H^+ \rightarrow Mn^{2+} + Fe^{3+} + 3/2H_2O. \quad (4.7)$$

The amount of Fe^{2+} which is remaining in solution (and thereby the amount consumed in

the reaction) is then determined by titrating with a standard $KMnO_4$ solution. Since every mole of Mn^{3+} consumes half as much Fe^{2+} as does a mole of Mn^{4+}, the $\%MnO_2$ number for an oxide with A moles of Mn^{4+} and B moles of Mn^{3+} and molecular weight W is given by:

$$\%MnO_2 = \frac{(A + B/2)W_{MnO_2}}{W} \times 100\%, \tag{4.8}$$

where W_{MnO_2} is the molecular weight of MnO_2. Thus from equation (4.8) MnO_2 would have A=1, B=0 giving $\%MnO_2$ = 100%; Mn_2O_3 would have A=0, B=1 giving $\%MnO_2$ = 27.5%; and $LiMn_2O_4$ would have A=1, B=1 giving $\%MnO_2$=72.1%.

The $\%MnO_2$ number is useful since it gives valence information for the manganese in the sample as will be shown here. For a sample containing only Mn^{3+} and Mn^{4+}, the total manganese content is given by:

$$\%Mn = \frac{(A + B)W_{Mn}}{W} \times 100\% \tag{4.9}$$

where W_{Mn} is the molecular weight of Mn. Solving the set of simultaneous equations (4.8) and (4.9) gives:

$$A = \frac{W}{100}\left[\frac{2(\%MnO_2)}{W_{MnO_2}} - \frac{(\%Mn)}{W_{Mn}}\right] \tag{4.10}$$

and

$$B = \frac{2W}{100}\left[\frac{(\%Mn)}{W_{Mn}} - \frac{(\%MnO_2)}{W_{MnO_2}}\right]. \tag{4.11}$$

Substituting %Mn = 60.8% and $\%MnO_2$ = 72% for $LiMn_2O_4$ gives A = 1 and B = 1, which indicates that $LiMn_2O_4$ has one each of Mn^{4+} and Mn^{3+}. Also the average valence would be given by:

$$avg.\,valence = \frac{4A+3B}{A+B}. \qquad (4.12)$$

Substituting A=1 and B=1 for stoichiometric spinel gives the average valence of 3.5. The average valence of manganese determined by this method is also listed in table 4.5.

The oxygen content in the sample remains to be determined. This was done by two methods: by assuming that the rest of the sample not accounted for in the weight percents of the other elements must be from oxygen, and by calculating the amount of oxygen required to counterbalance the charges of the positive ions in the sample. The results of both these methods are listed in the table and are in close agreement.

From all the above results a chemical formula for the Li-Mn-oxide can be derived to be $Li_{1.57}Mn^{4+}_{1.36}Mn^{3+}_{0.30}O_4 \cdot 0.60H_2O$. Such results must be taken with caution, however. For instance the observed weight-loss used to determine the amount of H_2O may have also been caused by some oxygen loss. Furthermore the determination of the lithium content is difficult and is, at best, qualitative. Nevertheless the results of the analysis are not compatible if the AB_2O_4 spinel structure is assumed since there are more cations present than cation sites in spinel. However the cations may be arranged slightly differently than in spinel, such as in $Li_2Mn_2O_4$ or the sample may have the layered $LiNiO_2$ structure. On the other hand the sample could be oxygen deficient or, more likely, contain some Li_2MnO_3. Also to be taken into consideration is that there could be some lithium hydroxide present from inadequate washing of the sample after synthesis. A manifestation of this can be seen in figure 4.28 as small Li_2CO_3 peaks are present. This was often observed in these samples. Nevertheless, from the large value determined for the average valence of manganese it can be at least said with relative certainty that the Li-Mn-oxides made in aqueous solution are lithium rich.

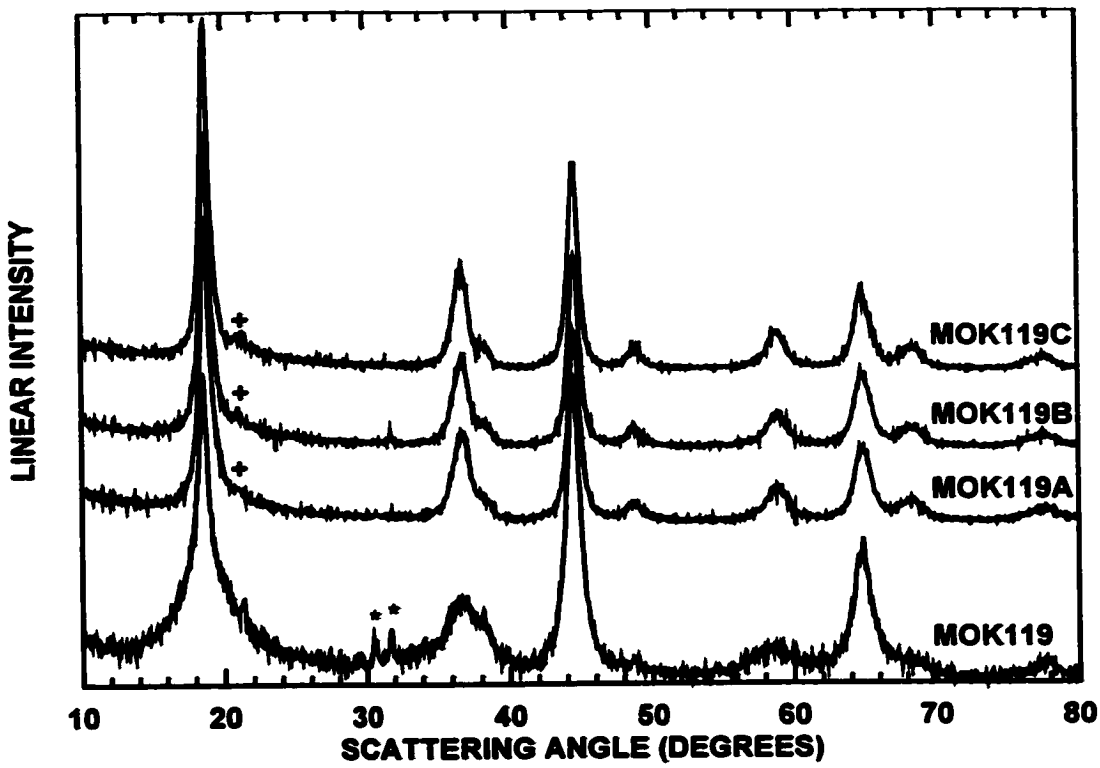

Figure 4.28 XRD patterns of nanograin lithium manganese oxides made from aqueous solution. MOK119: 110°C 24 hours, MOK119A: 500°C 0.5 hours, MOK119B 500°C 1 hour, MOK009C: 500°C 4 hours. All samples were heated in air. + peaks indexed to Li_2MnO_3 ; peaks indexed to Li_2CO_3 .*

4.5.3 Morphology of Nanograin Lithium Manganese Oxide

The morphology of the Li-Mn-oxides were studied at a nanoscopic level using a TEM. Details of the TEM measurement are described in section 2.4.2. To prepare TEM samples a few particles of Li-Mn-oxide were added to about 10ml of acetone. The mixture was then ultrasonicated for two minutes. After this a drop of the resulting suspension was placed on a copper TEM sample grid by means of a glass capillary.

Figure 4.29(a) shows a TEM image of a sample of Li-Mn-oxide sample MOK119. This sample was prepared as described in section 4.4.1 and was subsequently dried for 24 hours at 110°C. At this scale the sample appears to be made up of squares or cubes with dark edges. This image is in stark contrast to the TEM image of the commercial

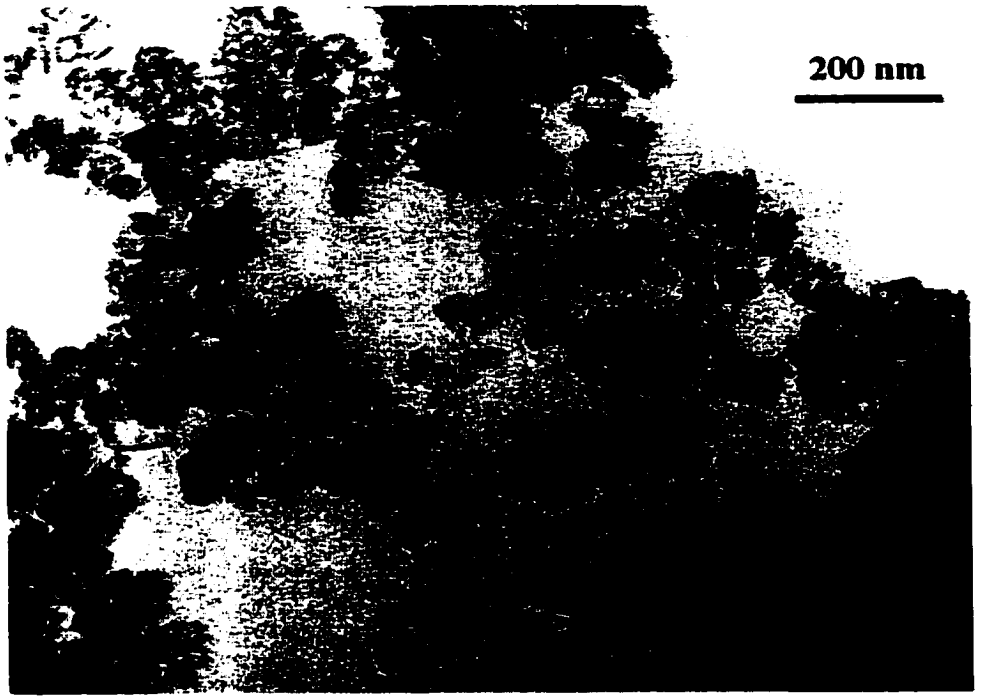

Figure 4.29(a)

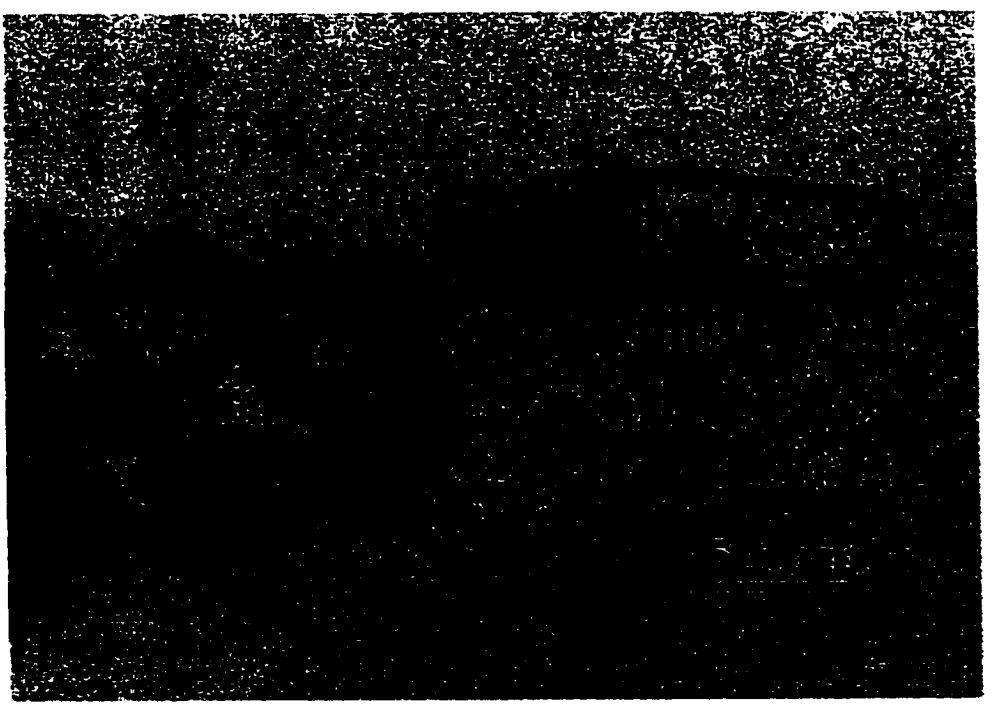

Figure 4.29(b)

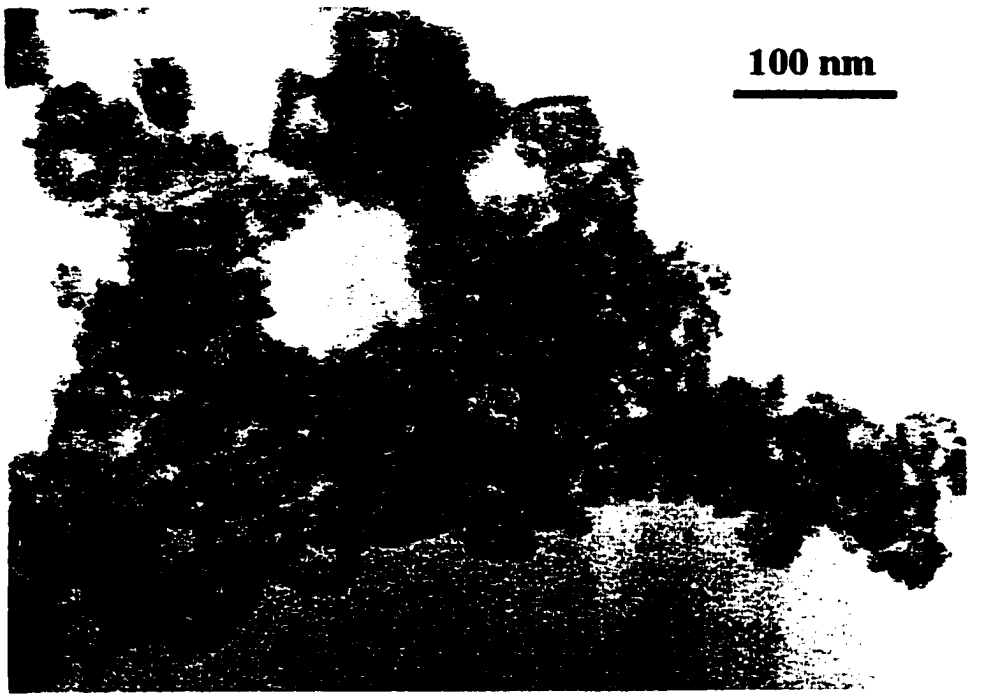

Figure 4.29(c)

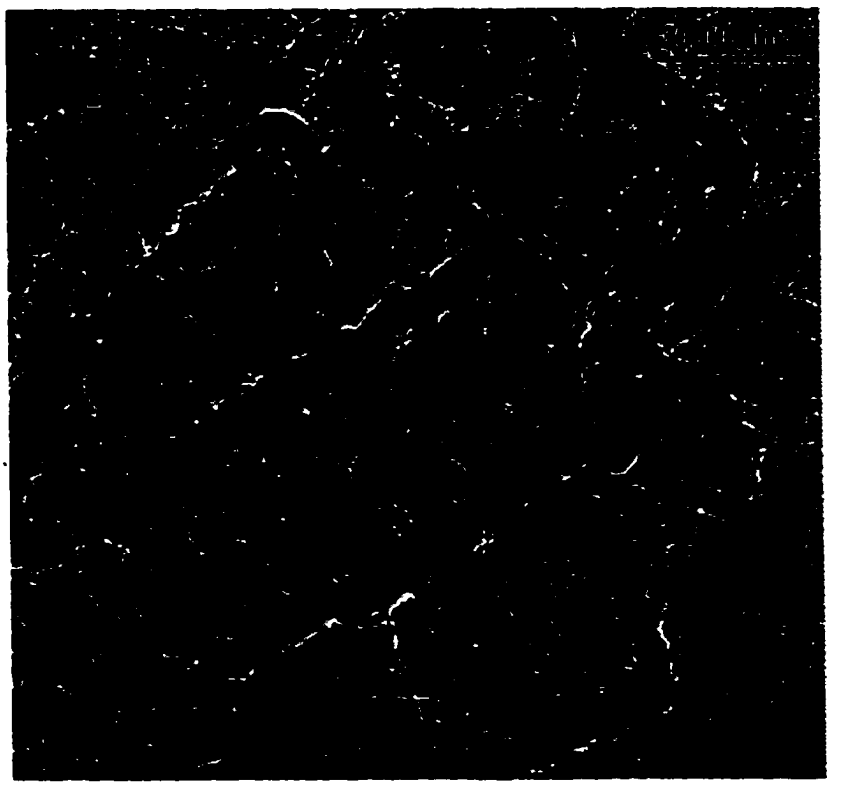

Figure 4.29(d)

Figure 4.29(e)

Figure 4.29 A series of TEM images of sample MOK119, a lithium manganese oxide prepared in aqueous solution and subsequently dried at 110°C for 24 hours.

$LiMn_2O_4$ sample shown in figure 4.3. At a higher magnification, shown in figures 4.29(b) and 4.29(c), the sample appears to be made up of two dimensional rectangles and squares with an average dimension of about 50 nm. Some of these rectangles are filled and some are partially filled with material. Figures 4.29(d) and 4.29(e) show images of sample MOK119 at still higher magnifications. The images show that the squares and rectangles are made up of single 7 nm grains. The grains have apparently self-assembled into the squares and rectangles. Some of these rectangles are empty while some are partially filled with non-assembled grains. Moiré patterns from the interference between the fringes of different grains can be clearly seen in figure 4.29(e).

Figure 4.30(a) shows a TEM image of sample MOK119B which was made by heating sample MOK119 at 500°C in air for one hour. Apparently the self-assembled

Figure 4.30(a)

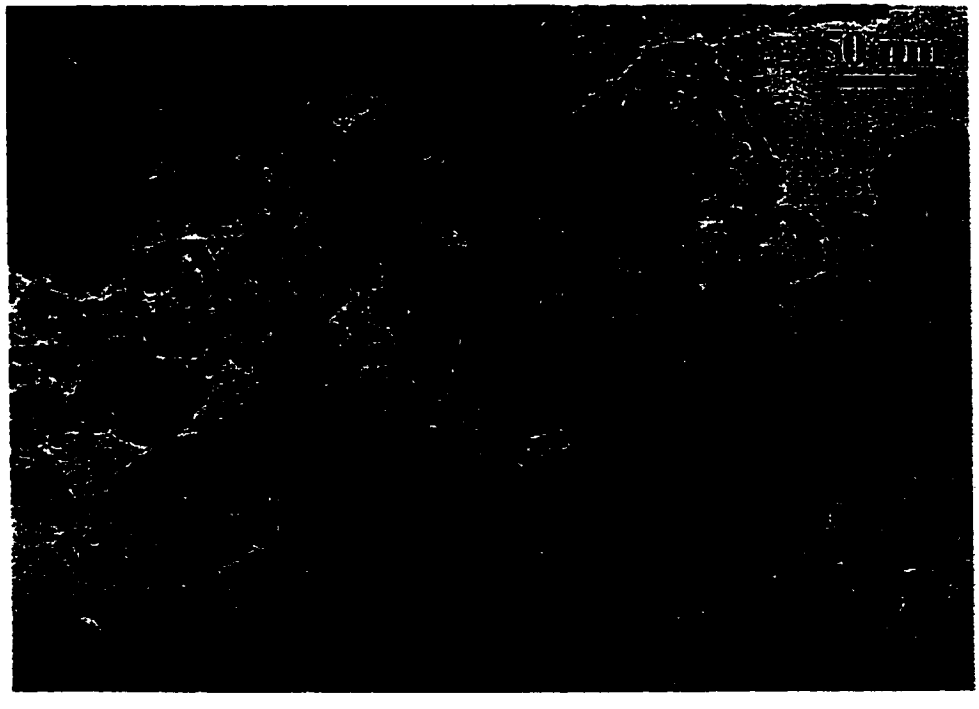

Figure 4.30(b)

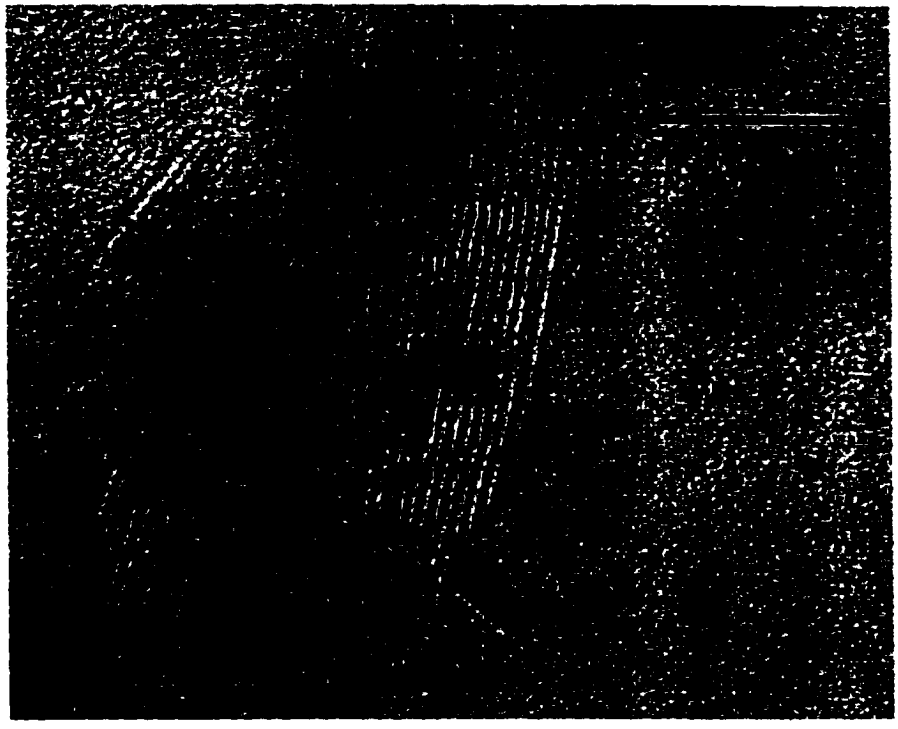

Figure 4.30(c)

Figure 4.30 A series of TEM images of sample MOK119B, a lithium manganese oxide prepared in aqueous solution and subsequently dried at 110°C for 24 hours and then heated at 500°C in air for 0.5 hours.

rectangles are stable at this temperature. At higher magnification, shown in figure 4.30(b), it appears that many of the grains on the edge of the rectangles have sintered together to form a solid border. Figure 4.30(c) shows a high resolution TEM image of the sample. Diffraction fringes from individual grains can clearly be seen in the figure. The average line spacing between the fringes was measured to be 4.677Å. As will be shown in the next section, this corresponds to precisely the 111 cubic plane spacing (or 001 if hexagonal indices are used) in this material as measured by XRD.

4.5.4 XRD Analysis of Nanograin Lithium Manganese Oxides

Figure 4.28 shows the XRD patterns of samples MOK119, MOK119A-C.

Sample MOK119 was prepared as described in section 4.4.1 and subsequently dried at 110°C for 24 hours. Samples MOK119A-C were made by heating sample MOK119 for 0.5 hours, one hour and four hours at 500°C in air respectively. Peaks identified to be from Li_2CO_3 and Li_2MnO_3 are labelled in the figure. The figure shows that after the first half-hour of heating at 500°C the XRD pattern of the sample remains essentially unchanged upon further heat treatment at this temperature. Figures 4.31(a) and 4.31(b) show the results of two fits obtained by Rietveld refinement for sample MOK119B. For the refinements a spinel $LiMn_2O_4$ structure and to a layered $LiNiO_2$ structure were used respectively. For the fit to the spinel structure in figure 4.31(a) the occupation of lithium in the 8a sites was fixed to a value of one and the number of oxygen atoms in the 32e sites was also fixed to four. A variable number of lithium or manganese atoms was allowed on the 16d sites with the restriction that the total site occupation equal two. For the fit in figure 4.31(b) to the $LiNiO_2$ structure a similar scheme was used. Here the occupation numbers of lithium atoms in the 3a sites and oxygen atoms in the 6c sites were fixed at one and two respectively, while the number of lithium and manganese atoms in the 3b sites were allowed to vary, with the restriction that the total occupation be equal to one.

Details of the fits are given in table 4.6. The refinements were hampered by the presence of the Li_2MnO_3 phase, which was not crystalline and therefore hard to include in the refinements. As a result of this the χ^2 parameter for both fits was rather high. The values of χ^2 for both fits are also similar to each other, making it difficult to tell which phase fits the diffraction pattern best. Thus from this data it is not possible to distinguish if the Li-Mn-oxide is the $LiMn_2O_4$ spinel phase or the layered $LiNiO_2$ phase. For both

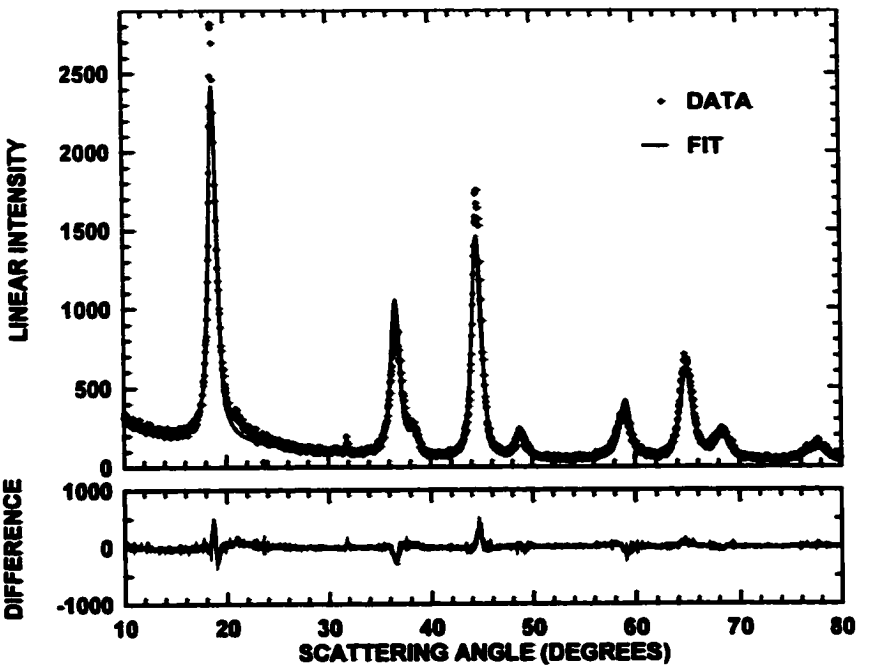

(a)

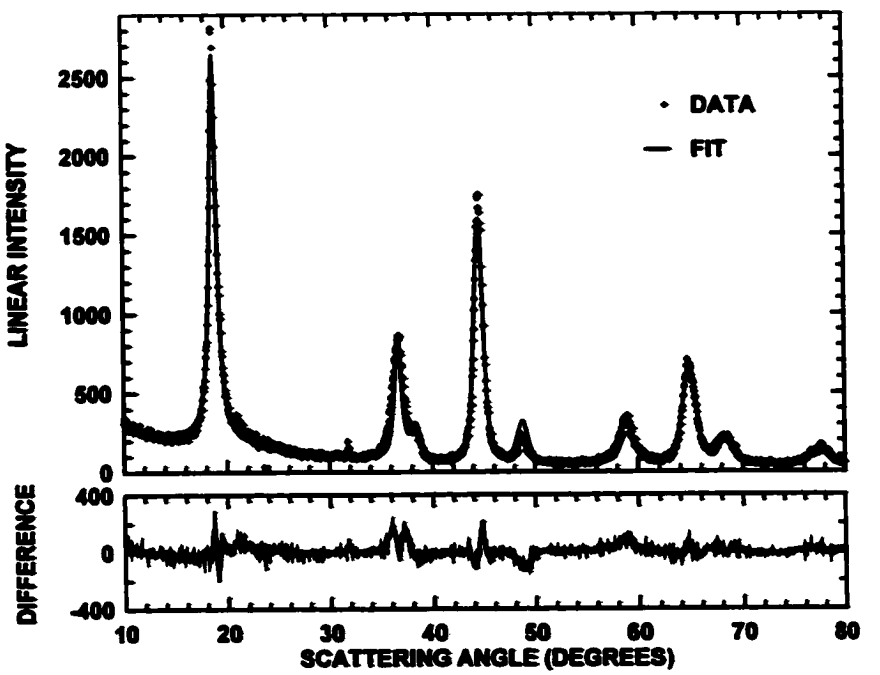

(b)

Figure 4.31 Reitveld refinements of sample MOK119B using (a) the $LiMn_2O_4$ structure and (b) the layered $LiNiO_2$ structure.

Table 4.6 Results of Rietveld refinements of nanograin lithium manganese oxide sample MOK119B. The refinements assumed either a $LiMn_2O_4$ spinel structure or a layered $LiNiO_2$ structure.

Structure	*$LiMn_2O_4$ spinel*	*layered $LiNiO_2$*
Space Group	$Fd\bar{3}m$	$R\bar{3}m$
Lattice constants	*a = 8.115 Å*	*a = 2.866; b = 14.101*
x in $Li_{1+x}Mn_{2-x}O_4$ or y in $Li[Li_yMn_{1-y}]O_2$	*x = 0.40*	*y = 0.110.*
χ^2	*4.956*	*6.227*

fits the peak width was not a simple function of theta and was hard to model. This may be due to the Li_2MnO_3 impurity, some strain or grain shape anisotropy in the sample or perhaps because the sample composition is non-homogenous. From the Scherrer equation the grain size varied from between 100 Å - 800 Å, depending on the peak used in the calculation. Clearly an accurate measure of the grain size of this sample could not be made by this method. Nevertheless the refinements did give accurate values of the lattice constant of this material. They are listed in table 4.6 for both the cubic and hexagonal phases. The small lattice constant for the cubic refinement corresponds to an extremely lithium rich lithium manganese spinel sample. This agrees with the results of the chemical analysis.

4.5.5 Electrochemical Characterization of Nanograin Lithium Manganese Oxide

Figure 4.32 shows the voltage curves of the samples MOK119, MOK119A and MOK119C that were prepared as described in section 4.4.1 and then heated in air at 110°C for 12 hours. Samples MOK119A and MOK119C were additionally heated in air at 500°C for 0.5 hours and for 5 hours respectively. All of the voltage curves are very

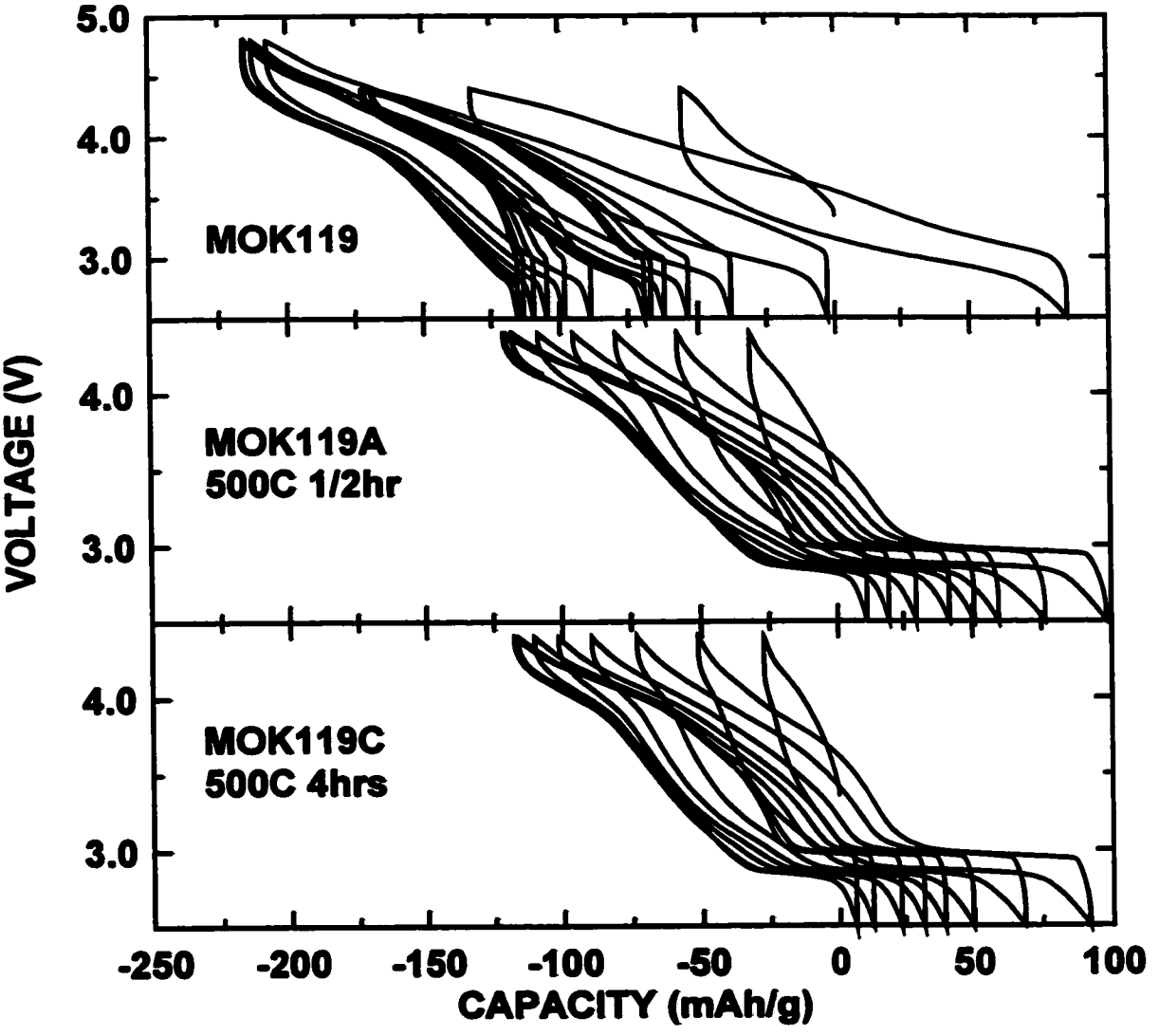

Figure 4.32 Voltage curves of nanograin lithium manganese oxide prepared in aqueous solution with the indicated heat treatment temperatures in air.

different than that of stoichiometric $LiMn_2O_4$, shown in figure 4.5. The first charge cycle of all the samples has little capacity. For sample MOK119 the first charge is followed by a long sloping discharge and then a huge (~200 mAh/g) charge cycle. Subsequent cycles show reduced capacity and become similar to the voltage curve of spinel as cycling progresses. It was found that more capacity is available in this sample when the upper cut-off voltage was increased to 4.8 V. After a very small first charge cycle, samples

MOK119A and MOK119C have a long spinel-like 3 V plateau on their first discharge. During subsequent cycling a 4 V plateau also begins to develop, making the voltage curves look more like $LiMn_2O_4$ spinel. At the same time the 3 V plateau fades rapidly, as is observed also for spinel.

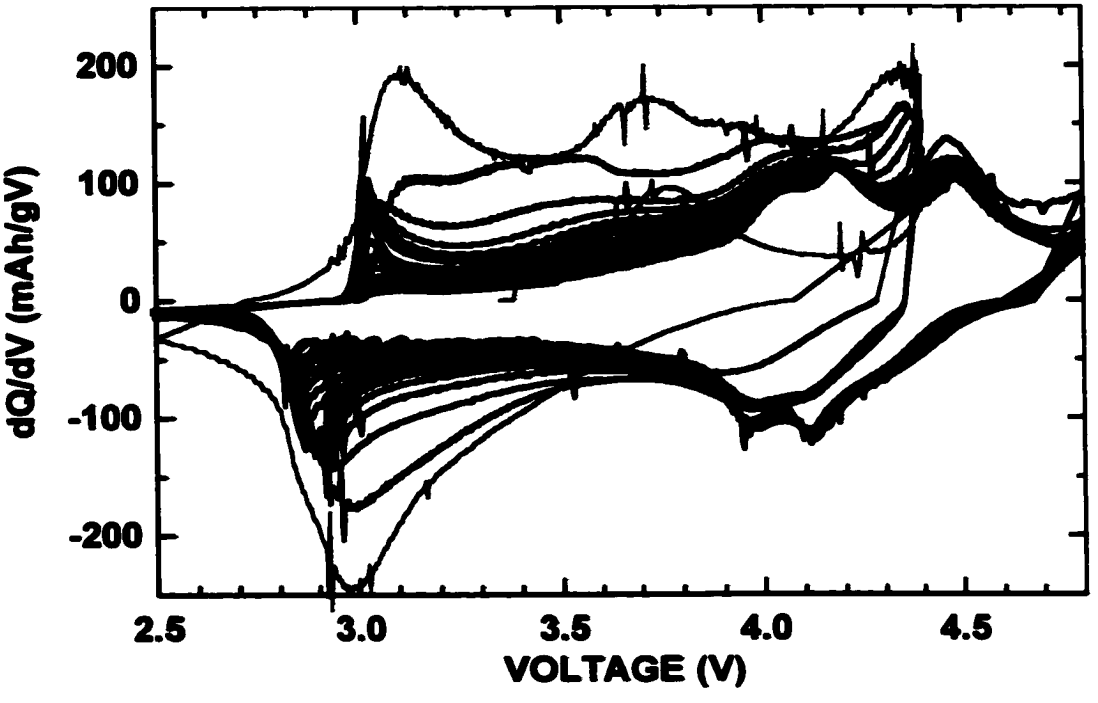

Figure 4.33 Differential capacity curve of sample MOK119. The first 1.0 cycles (1st charge, 1st discharge and 2nd charge) have been highlighted in red for clarity.

Figure 4.33 shows the differential capacity curve for sample MOK119. The first 1.0 cycles (1st charge, 1st discharge and 2nd charge) have been highlighted in red for clarity. The first two charge cycles have a peak at about 3.75 V, which is not present in the rest of the cycles. This peak may be caused by the oxidation of the bound water in this sample. As cycling progresses the differential capacity curve becomes similar to that of a $LiMn_2O_4$ spinel with a large 4.5 V and 3.3 V plateau. The most striking feature of figure 4.33 is the significant capacity between 3.3 V and 3.8 V. This is dissimilar to the differential capacity curve for spinel shown in figure 4.9. Figure 4.34 shows the

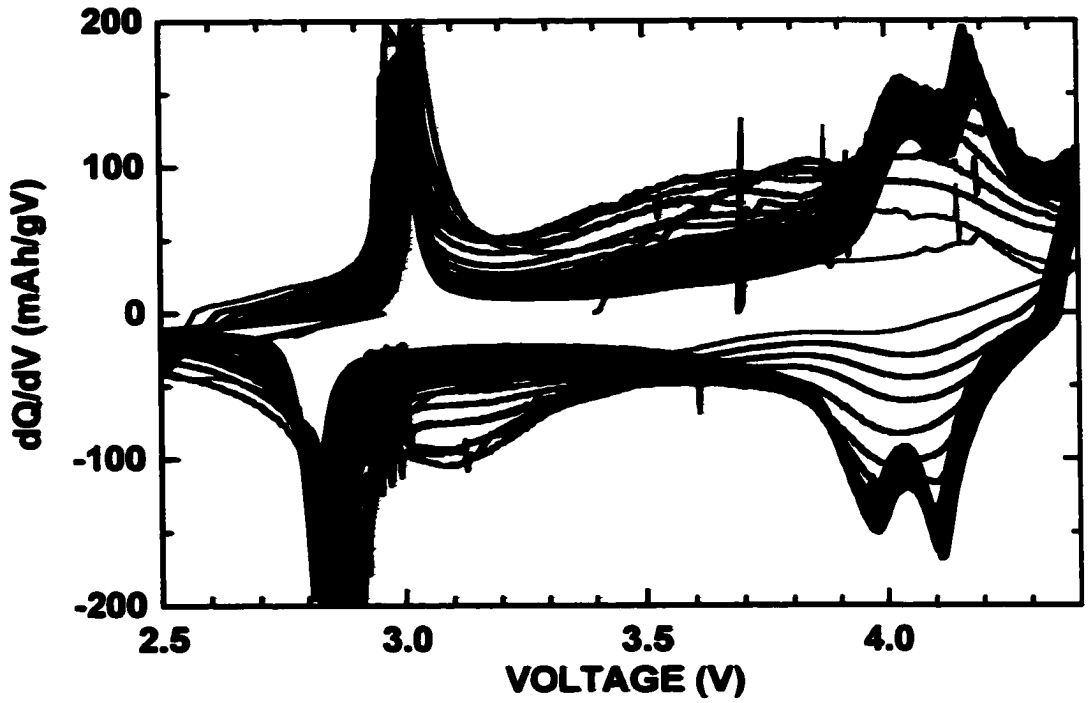

Figure 4.34 Differential capacity curve of sample MOK119A. The first 1.0 cycles have been highlighted in red for clarity.

differential capacity curve for sample MOK119A. The first charge is almost featureless. This is followed by number of cycles that have broad features between 3.0 V and 4.5 V. After a few cycles the curve becomes very similar to $LiMn_2O_4$ spinel, with the exception that there is a significant amount of capacity between 3.3 V and 3.8 V, as was also observed for sample MOK119.

4.5.6 Summary of Results

In this section the synthesis in aqueous solution of Li-Mn-oxide was explored. This method of synthesis produced nano-grained samples with an unusual microstructure. The sample grains are about 7 nm and apparently self assemble into two-dimensional ~50 nm squares and rectangles. Chemical analysis of the samples showed that they were

lithium rich and contained large quantities of water as made. XRD analysis of the samples could not distinguish if the samples had the $LiMn_2O_4$ spinel structure or the $LiNiO_2$ layered structure. It is fairly obvious from the electrochemical results, however, that the samples are converting to the spinel phase during cycling. The fact that there is not much capacity on the first charge in these materials compared to subsequent cycles may indicate that the samples have a large amount of disorder, which is somehow corrected by cycling on the 3 V plateau. Even after converting to spinel, the samples have significant capacity between 3.3 V and 3.8 V. This may be due to the capacity of the surface sites of the nano-sized sample grains as was predicted in the last chapter. On the other hand the capacity may be due to defect sites in the sample as a consequence of the low preparation temperature. In-situ XRD measurements are needed to determine what processes are occurring during cycling between 3.3 V and 3.8 V. If this capacity is a surface effect, then the lattice constant of the material should not change much in this region. On the other hand if the extra capacity is due to the filling of defect sites in the structure, this also might not be detectable by in-situ XRD. Manipulation of the sample grain size ought to effect the capacity in this region significantly if it is due to a surface effect. This is most easily accomplished by thermal treatment of the sample. However this would also reduce the number of defect sites. Thus, elucidating the origin of the 3.3 V - 3.8 V capacity in these materials might not be an easy task.

4.6 CONCLUSIONS

In the previous chapter theoretical predictions for the voltage behaviour of nano-grained lithium was presented. Here the attempted synthesis of actual nano-grained lithium intercalation materials to compare with the theory of the previous chapter is

discussed. Specifically it was attempted to synthesize nano-grained lithium transition metal oxides. This proved a difficult task using simple laboratory techniques. In section 4.3 it was found that the high temperatures required to synthesize $LiMn_2O_4$ spinel caused grain growth, even when the spinel was present in a low concentration in a matrix of Mn_2O_3. This method may have more success if the matrix used is Li_2MnO_3. To circumvent grain growth at high temperatures, metastable synthesis of nano-grained lithium transition metal oxides was attempted by high-energy ball milling. Although lithium transition metal oxides were produced by this method, they had the rocksalt phase and were lithia and oxygen deficient. As a result their electrochemical performance was poor.

In the final section Li-Mn-oxide was synthesized at room temperature from an aqueous solution. This material was electrochemically active and showed similar behaviour to that of bulk lithium manganese oxide spinel, excepting that there was significant capacity between 3.3 V and 3.8 V. This may be due to surface capacity on the nanograins, or to defect sites in the bulk material. Further studies are needed to explain this effect. However, this may not be an easy task, considering that the control of both the grain size and the defect concentration is achieved by thermal treatment.

Chapter 5

Electrochemical Displacement Reactions of Lithium with Metal Oxides

5.1 INTRODUCTION

So far in this thesis only nanocrystalline intercalation electrodes for lithium batteries have been considered. Although intercalation electrodes are exclusively used in commercially available lithium ion batteries today there is an increasing interest in non-intercalation electrodes. Among these are metal oxide electrodes that do not intercalate lithium, but do react with lithium at lower voltages. As will be shown in this chapter, the result of this reaction is a nano-dispersed composite of reduced metal and lithium oxide.

In this way a nanostructured electrode is made in-situ during cell discharge. The discussion of nanostructured electrode materials is thus continued in this chapter for the case of non-intercalating metal oxides.

At high temperatures, the reactivity of lithium with non-intercalating metal oxides has been well studied. In this case the displacement reactions with lithium progress through distinct phases which are in thermodynamic equilibrium [81]. This is unlikely to occur at room temperature. Indeed, many room temperature studies have reported an uptake of lithium greater than that predicted from a simple reduction of the metal [82,83,84], which has created an impetus for further studies. Overall, the results of earlier room temperature studies have been less satisfying than those at high temperature. This is exacerbated by the apparent insistence to study complex oxides rather than simple ones. Nevertheless, strikingly similar voltage profiles versus lithium were found, regardless of the starting oxide, and are typified by those shown in figure 5.1. The first discharge proceeds with a low-voltage, high-capacity plateau, followed by a charging plateau, typically at 1.5-2 V with less capacity. The second discharge always occurs at a higher voltage than the first, suggesting a different mechanism than the first discharge, but it still has large polarization compared to the charge profile. There is little change in the voltage profile for subsequent cycles, except from capacity loss. Although far from conclusive, past studies seem to agree on the mechanism of reaction. Until recently, the current understanding can be summarized as follows [82,83,84]:

i) The first discharge proceeds with the insertion of lithium into vacant sites in the metal oxide and is accompanied by the complete amorphization of the electrode.

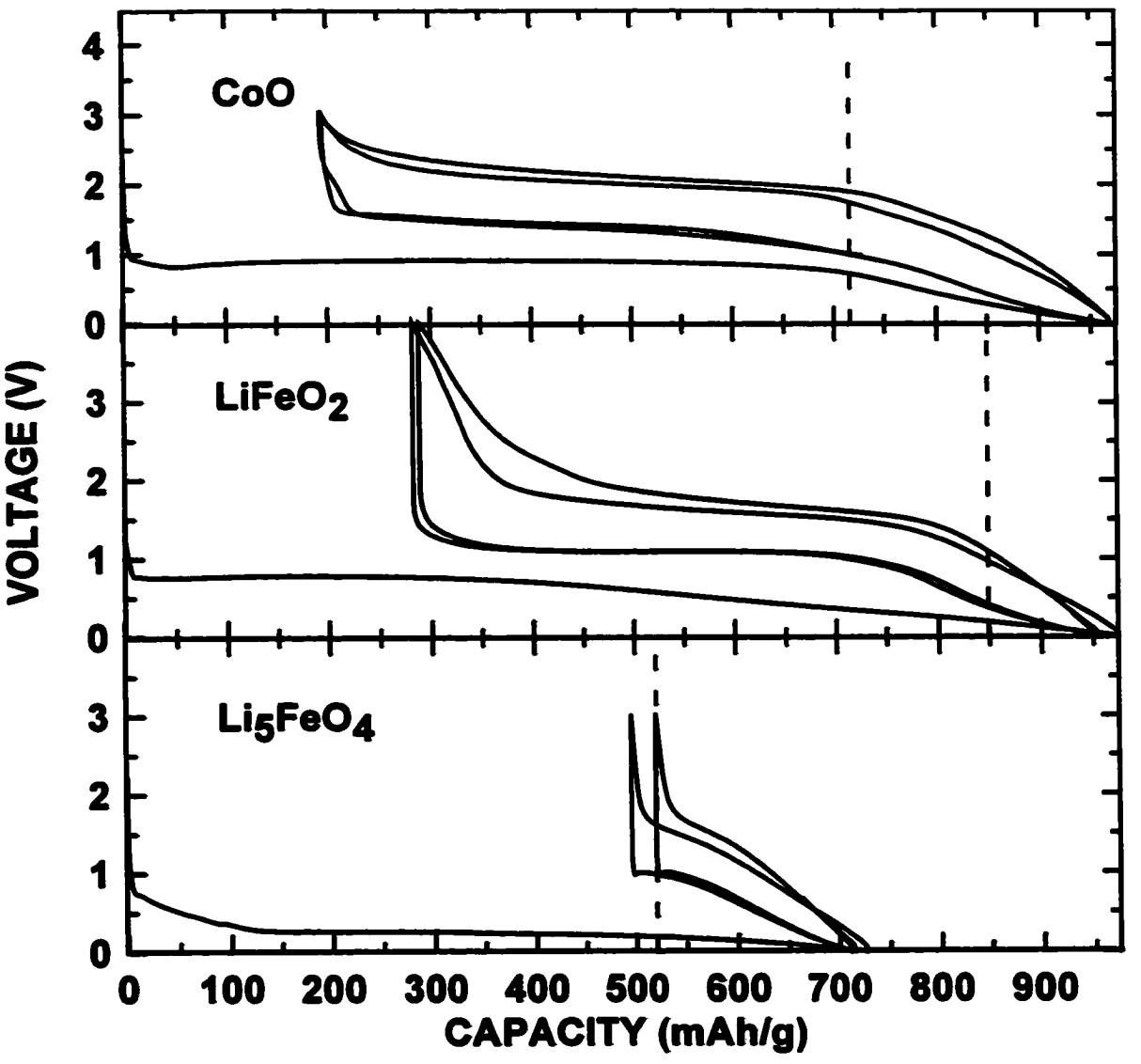

Figure 5.1 The voltage profiles of the α-CoO, $LiFeO_2$ and Li_5FeO_4 samples prepared in this study. Dashed lines indicate theoretical capacities based on equation (5.1).

ii) The discharge products contain more lithium than can be predicted by simple charge counting. (e.g. $Li_{7.8}MoO_{3-y}$ [82], Li_7InVO_4 [83], $Li_{6.6}Fe_2O_3$ [84]).

iii) Once formed, the discharge phase remains amorphous and cycles reversibly thereafter with no further phase changes.

From a simple chemical point of view all three of the above mechanisms seem

unlikely. Indeed, here it will be conclusively shown that they are incorrect. This study focuses on the electrochemical reaction of lithium with three simple oxides: α-$LiFeO_2$, β-Li_5FeO_4 and CoO. The high temperature phase of CoO (which will henceforth be called α-CoO here) and α-$LiFeO_2$ have the simple rocksalt structure [85,86] while β-Li_5FeO_4 has all the cations in tetrahedral sites and has a similar oxygen lattice to Li_2O [87]. This chapter describes a detailed in-situ x-ray diffraction (XRD) and in-situ Mössbauer study of these materials. From this study the following mechanism is suggested:

i) The first discharge proceeds via a displacement reaction with the immediate decomposition of the starting material. This decomposition reaction occurs through an intermediate surface phase and results in the formation of the reduced metal and lithium oxide as follows:

$$(2y-x)Li + Li_xMO_y \rightarrow yLi_2O + M \qquad (5.1)$$

The resulting discharge products are not amorphous, but are of nanometer scale.

ii) Excess capacity observed during the first discharge than predicted by (5.1) is most likely due to catalytic electrolyte decomposition reactions involving lithium on the high surface area decomposition products of the first discharge reaction.

iii) During the subsequent charge cycle the reduced metal is oxidized by a displacement reaction where the metal displaces the lithium in lithium oxide. In this reaction the original oxygen lattice of lithium oxide is preserved. Further cycling proceeds in a reversible three-phase region between this metal oxide, the reduced metal and lithia according to the reaction:

$$yLi_2O + M \rightleftharpoons Li_\alpha MO_\beta + (y-\beta)Li_2O + (2\beta-\alpha)Li. \quad (5.2)$$

For cobalt $\alpha=0$ and $\beta=1$ and the oxide formed is the low-temperature form of CoO which has the zinc blende structure [88,89] (which will be called β-CoO here). In the case of iron, the metal oxide formed during charge is a new phase of iron (III) oxide with α and β yet to be determined.

A recent study of the electrochemical reaction of lithium with CoO suggests that nano-grained cobalt metal is produced during the first discharge, supporting the first premise above [90]. However the study also suggests that amorphous metal oxide is formed at the top of charge and that a "continuous distribution of redox states" occurs during cycling. Here it will be shown that a nanocrystalline oxide is formed during charge, and that cycling after the first discharge occurs in a three-phase region via the simple displacement reaction (5.2) described above.

5.2 SAMPLE PREPARATION AND MEASUREMENT

α-$LiFeO_2$ was made by a solid state reaction [86]. Stoichiometric amounts of Li_2CO_3 (FMC) and Fe_2O_3 (Aldrich) were ground, pressed into pellets and heated in air at 900°C for 24 hours. The pellets were then quenched in liquid nitrogen, ground and re-heated at 900°C for a further 24 hours and then quenched again to give single phase material.

Single phase β-Li_5FeO_4 proved difficult to make by a solid state reaction similar to that used for $LiFeO_2$. Instead, under an argon atmosphere, stoichiometric amounts of Li_2O and Fe_2O_3 were placed in a 64 ml ball-milling container with two 0.5" ball bearings.

Both the vial and balls were of hardened steel. In total 3.3 g of reactants were added to each vial to give a ball-to-powder ratio of 5:1. The vials were milled for 32 hours with a SPEX 8000D mixer-mill. The resulting powder was then heated to 900°C for 24 hours in air to make a crystalline sample and immediately transferred to a helium-filled glovebox, as this material is moisture-sensitive.

$LiFeO_2$ composite electrodes were made by the Bellcore method as described in section 2.1. Composite electrodes of Li_5FeO_4 and CoO (Aldrich) were prepared by the method used to make air sensitive electrodes also described in section 2.1. XRD measurements of these materials were performed in a helium atmosphere using the air sensitive XRD sample stage described in section 2.2.3. Details of the in-situ XRD, in-situ Mössbauer and low temperature Mössbauer techniques can also be found in Chapter 2. The Mössbauer spectra were fitted with Lorentzian singlets, doublets and sextets or a Gaussian distribution of the former (to reflect a distribution of iron environments as in the α-$LiFeO_2$ structure) using a least-squares fitting routine. The component of the Mössbauer spectrum from iron impurities in the Be window was assumed to be small compared to that of the sample since the iron content in the samples was high. In fact, the spectrum of the Be window was near zero or even rejected by the least-squares fitting program when the attempt was made to include it in the fits.

5.3 EXPERIMENTAL RESULTS

5.3.1 Characterisation of Starting Materials

Figures 5.2(a), (b) and (c) show the x-ray diffraction patterns of the $LiFeO_2$ and Li_5FeO_4 (after and before heating) samples respectively. The spectra are in good

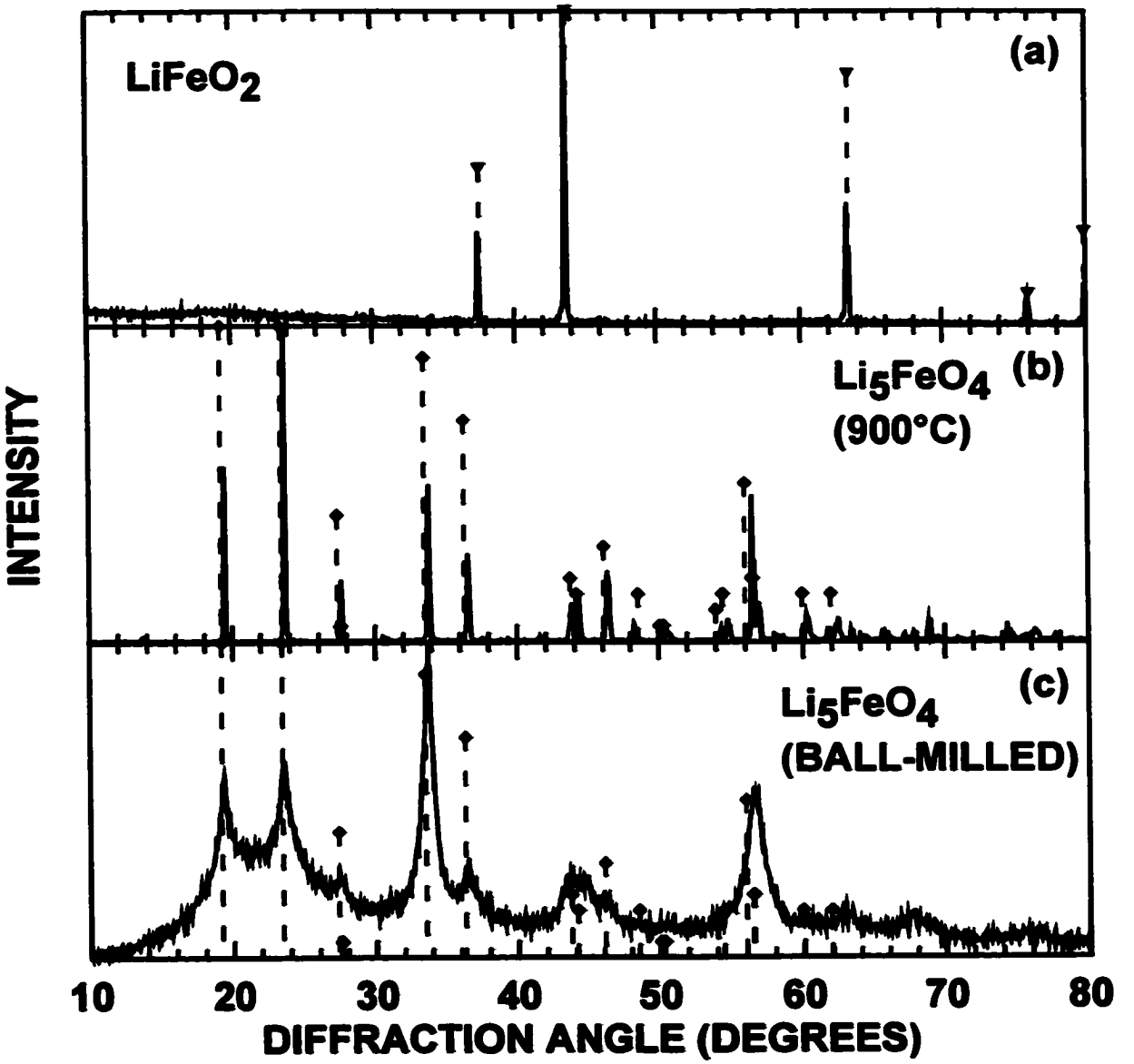

Figure 5.2 XRD spectra of the samples prepared in this study: (a) $LiFeO_2$, (b) Li_5FeO_4 prepared by ball-milling then heated at 900°C and (c) Li_5FeO_4 prepared by ball-milling. The dashed lines indicate values of the peak positions and intensities from the literature: ▼ α-$LiFeO_2$, Ref. [85]; ♦ β-Li_5FeO_4, Ref. [87].

agreement with previous spectra found in the literature [86,87]. Apparently single-phase β-Li_5FeO_4 is produced directly by ball milling. The width of the XRD peaks in the spectrum of this material correspond to an approximate grain size of 100Å according to the Scherrer equation [91]. After heating this material becomes crystalline. This

demonstrates the usefulness of ball-milling as a preparation step [71].

5.3.2 Electrochemical Studies

Figure 5.1 shows the voltage profiles of $LiFeO_2$, Li_5FeO_4 and α-CoO. The theoretical capacities of these materials according to equation (5.1) are indicated in the figure by dashed lines. The voltage profiles of all three oxides are very similar, suggesting that a similar reaction is occurring for all of them. In each case a low-voltage first discharge is observed which is about 15-20% larger in capacity than predicted by equation (5.1) (this corresponds to about 0.5-0.6 additional formula units of Li). The first discharge is then followed by a charge cycle with considerably higher voltage and a large irreversible capacity. The second discharge still shows considerable polarization compared to the charge cycle, but is higher in voltage than the first discharge. This suggests that different processes are occurring during the second and first discharges. There is little change in the voltage behaviour of subsequent cycles except for significant capacity fading. Electrochemical cells of other oxides versus lithium show similar voltage profiles as described above when discharged to zero volts. There are many examples in the literature as well [82,83,84].

5.3.3 In-situ Mössbauer Studies of $LiFeO_2$

Figure 5.3(a) shows the Mössbauer spectra of the as-made $LiFeO_2$ starting material at 298K. The spectrum is a symmetric doublet and was fit with a Gaussian distribution of Lorentzian doublets to reflect the number of different iron environments in the disordered rocksalt α-$LiFeO_2$ structure. The fitting parameters are listed in table 5.1. There is good agreement between the fit and earlier measurements listed in the table.

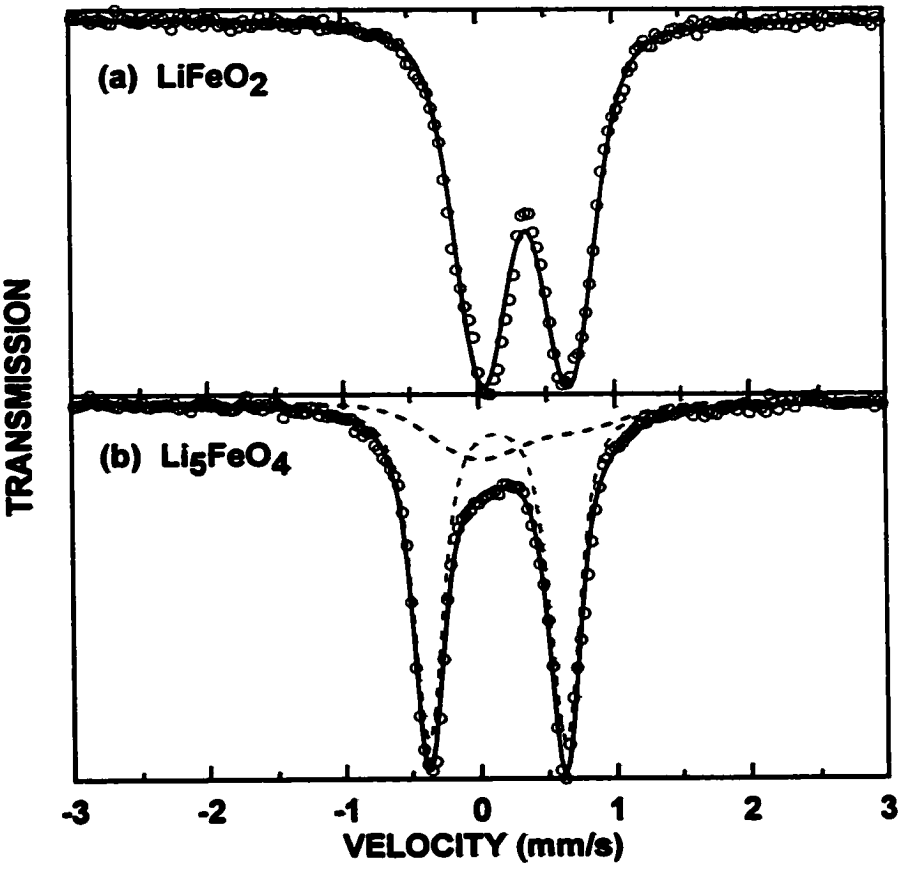

Figure 5.3 Mössbauer spectra of (a) $LiFeO_2$ and (b) Li_5FeO_4 prepared in this study. (Mössbauer Data: open circles, Fit Components: dashed lines, Total Fit: solid lines)

Figure 5.4 shows the voltage versus scan number of the $LiFeO_2$ in-situ Mössbauer cell. Some of the Mössbauer spectra taken during the first discharge are shown in figure 5.5. Since the least squares fitting program would not allow a mixture of pure Lorentzian lineshapes and lineshapes with a Gaussian distribution of Lorentzians, only pure Lorentzians were used in the fittings. This still provided a satisfactory fit for $LiFeO_2$ by allowing the peak width to vary to compensate for the distribution of iron environments. The pure Lorentzian fitting parameters for $LiFeO_2$ are also listed in table 5.1. Scan 27 (bottom of discharge) was fit with a combination of a singlet with zero centre shift and a symmetric doublet. This spectrum is consistent with iron with such a small grain size

Table 5.1 Fitting parameters from the Mössbauer spectra of the as prepared $LiFeO_2$ sample and from the $LiFeO_2$ Mössbauer in-situ cell. The $LiFeO_2$ spectrum was fit with a Gaussian distribution of Lorentzian functions. This spectrum was fit with a single Lorentzian function as well. All other lineshapes were fit with single Lorentzians. The singlet and quadrupole split components of the iron spectra are labeled $Fe^{(bulk)}$ and $Fe^{(surface)}$, respectively. The parameters for D-phase and C-phase refer to the majority component of the spectra measured at the bottom of discharge and top of charge, respectively. (δ: mean centre shift, Δ: mean quadruple splitting, Γ: peak HWHM, σ: Gaussian width (standard deviation) of the centre shift)*

Sample	δ (mm/s)	Δ (mm/s)	Γ (mm/s)	σ (mm/s)
$LiFeO_2$ (this study)	0.379	0.616	0.150	0.263
$LiFeO_2$* (this study)	0.380	0.608	0.230	—
$LiFeO_2$ (Ref. [86])	0.35	0.56	0.250	—
$Fe^{(bulk)}$	0	0	0.249	—
$Fe^{(surface)}$	0.055	0.647	0.233	—
D-Phase	0.168	0.973	0.227	—
C-Phase	0.265	0.871	0.301	—

that the hyperfine field is effectively zero due to thermal excitation, giving rise to super-paramagnetic behaviour. Because the grains are so small, much of the iron is in the region of grain boundaries. This iron would reside in a nonisotropic environment, giving rise to the observed quadrupole-split doublet. The iron atoms in the grain cores account for the paramagnetic iron singlet. This behaviour has been observed before for small grained iron particles produced at the bottom of discharge in the Sn_2Fe system [28]. For clarity, the iron giving rise to the singlet portion and quadruple split portion of the iron spectra will be referred to as $Fe^{(bulk)}$ and $Fe^{(surface)}$, respectively.

A simple linear combination of the lineshapes obtained at the bottom and top of discharge was used to fit the scans between scan 0 and 27. However this proved

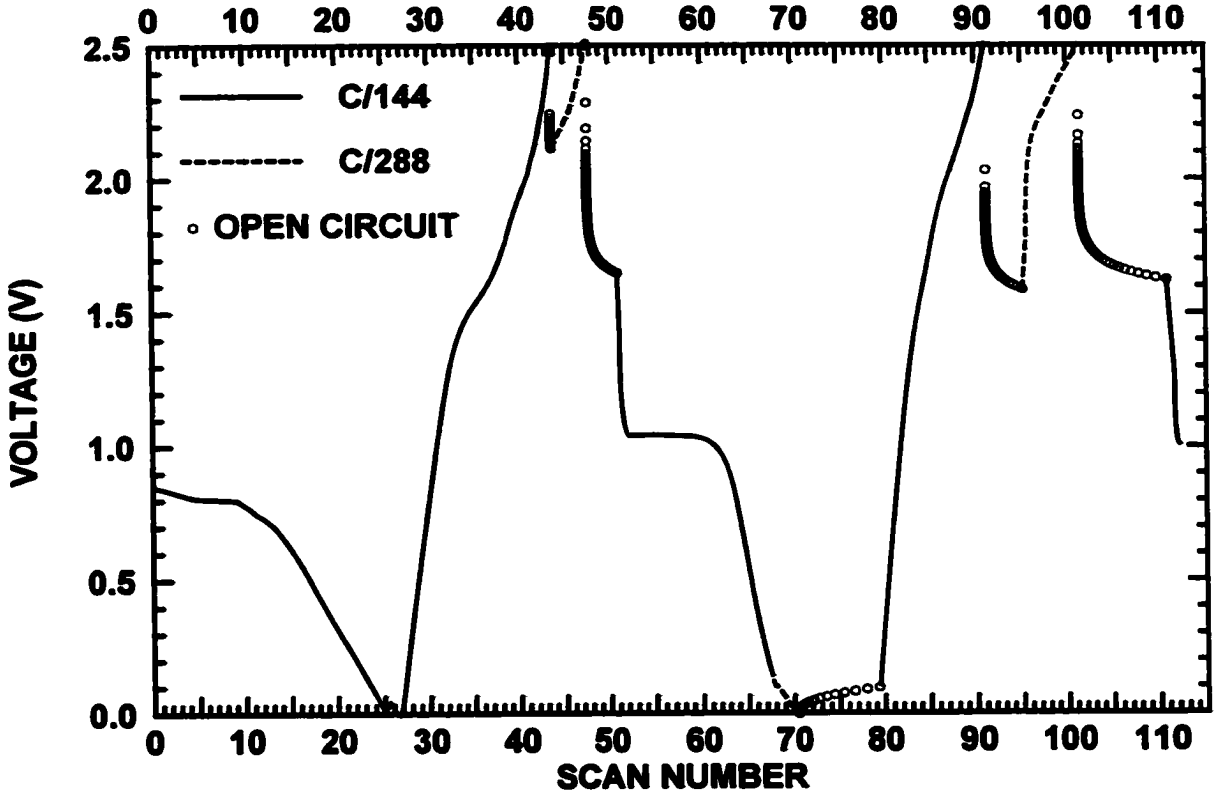

Figure 5.4 Voltage versus scan number for the $LiFeO_2$ in-situ Mössbauer study.

unsatisfactory. Instead, to fit these scans a new symmetric doublet with a large quadrupole splitting was added to the fit, which can be most easily seen in scans 10 and 21 in figure 5.5. This new doublet could represent either a new phase or iron atoms in anisotropic sites on the surface of $LiFeO_2$ as it is being decomposed during the discharge. This new phase will be referred to here as D-phase. To fit scans 0-27 only the areas of the iron, $LiFeO_2$ and D-phase peaks were allowed to vary. All other parameters were held constant. The parameters of the peaks used for fitting are listed in table 5.1.

Some of the Mössbauer spectra taken during the first charge are shown in figure 5.6. As the cell is charged the iron peaks become smaller and a new doublet emerges. This new phase will be called C-phase here. The C-phase doublet was fit at the top of charge by allowing only the areas of the iron peaks to vary while all of the parameters of

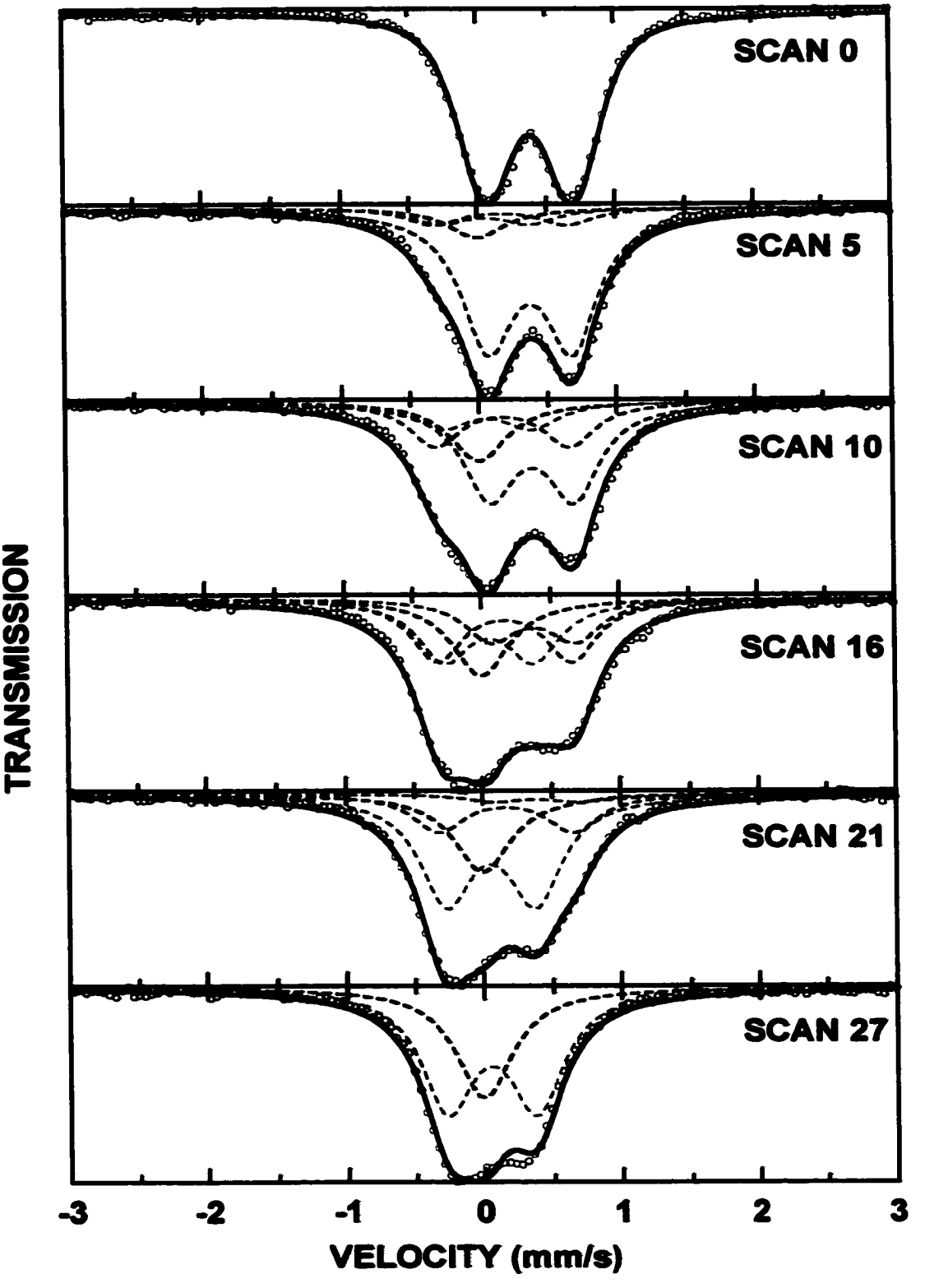

Figure 5.5 Some of the Mössbauer spectra taken during the first discharge of the $LiFeO_2$ in-situ Mössbauer cell. (Mössbauer Data: open circles, Fit Components: dashed lines, Total Fit: solid lines)

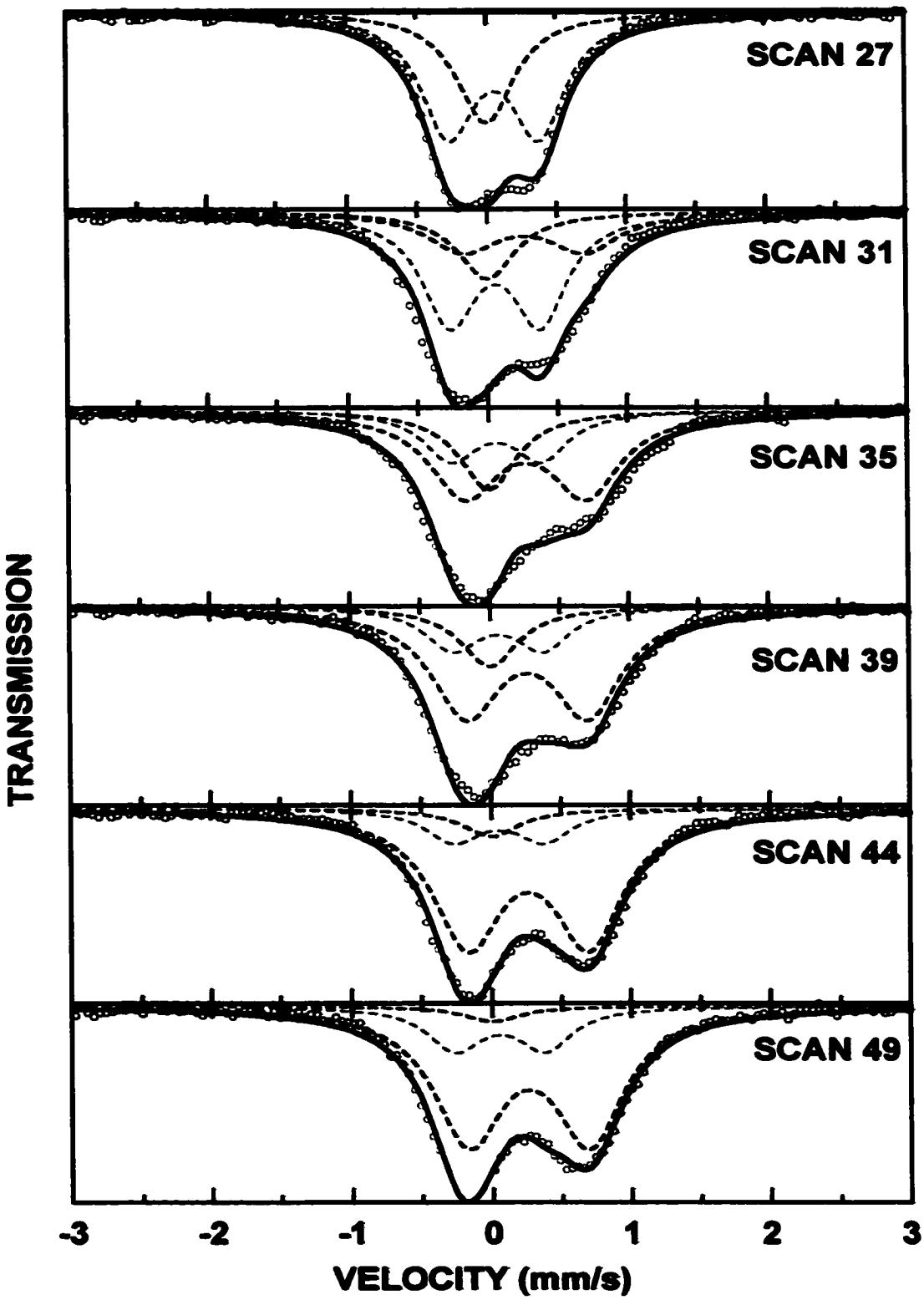

Figure 5.6 Some of the Mössbauer spectra taken during the first charge of the $LiFeO_2$ in-situ Mössbauer cell. (Mössbauer Data: open circles, Fit Components: dashed lines, Total Fit: solid lines)

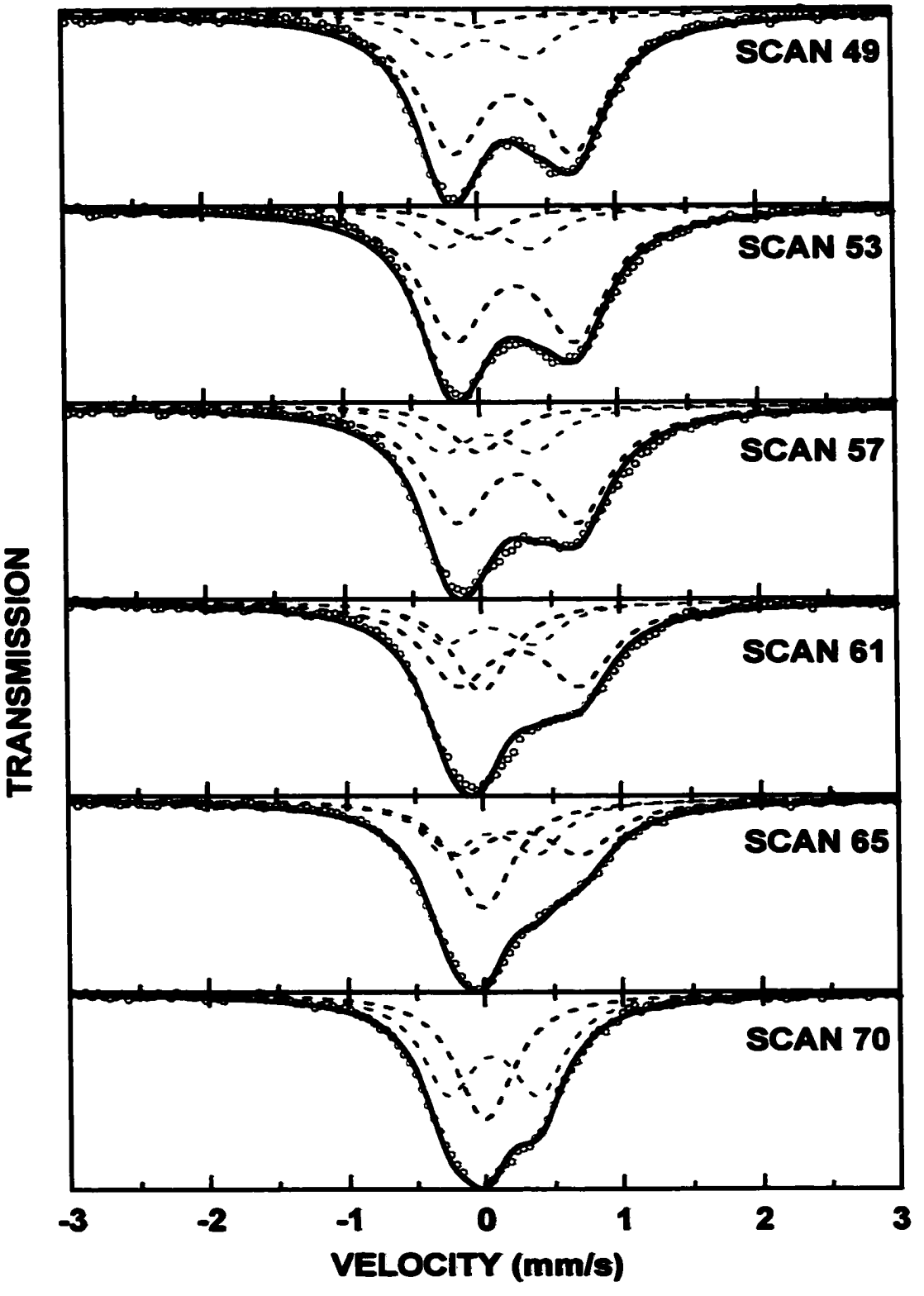

Figure 5.7 Some of the Mössbauer spectra taken during the second discharge of the $LiFeO_2$ in-situ Mössbauer cell. (Mössbauer Data: open circles, Fit Components: dashed lines, Total Fit: solid lines)

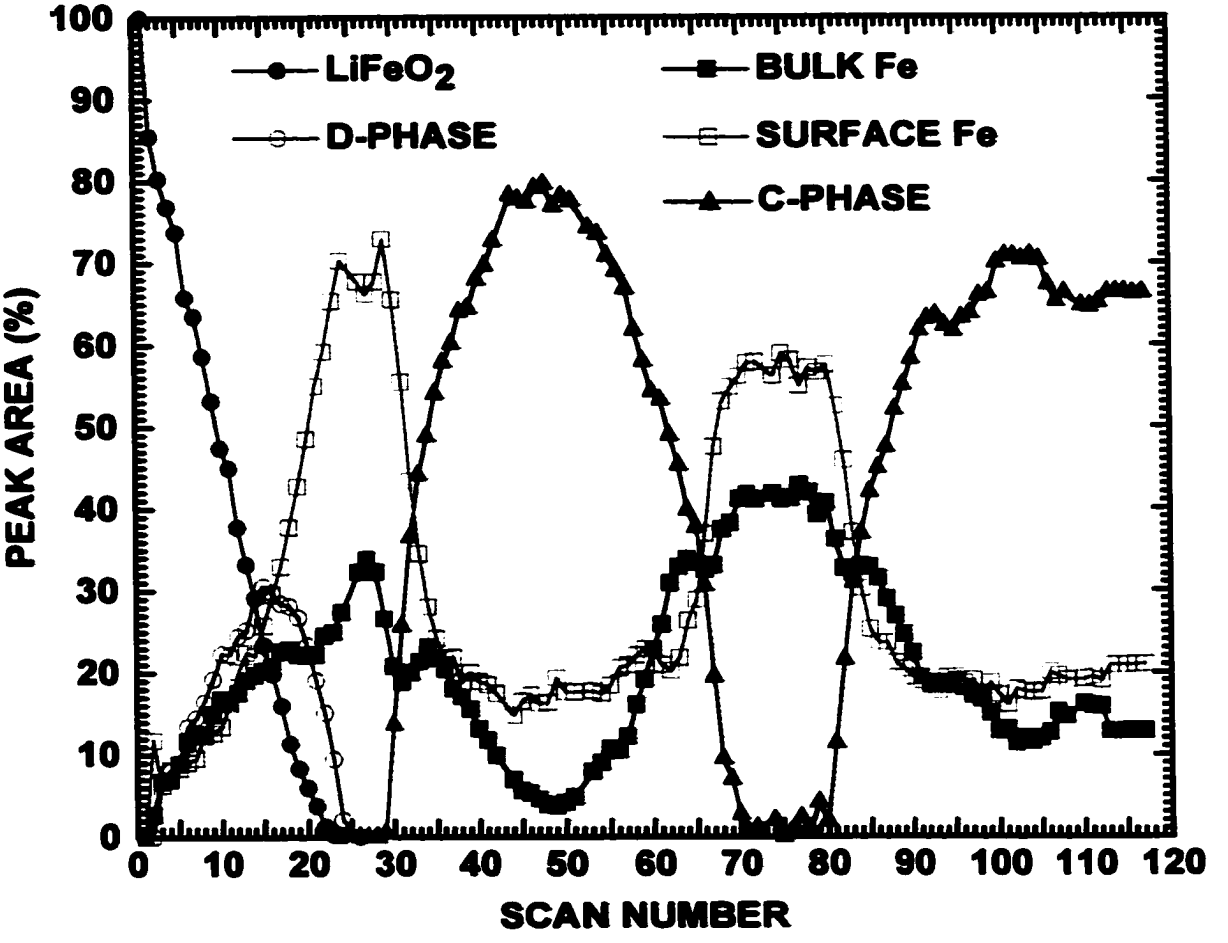

Figure 5.8 The spectral composition of the fits to the $LiFeO_2$ in-situ Mössbauer experiment scans.

a new symmetric doublet were varied. For all the other scans fits were obtained by combining the lineshapes obtained for iron and C-phase. Only the areas of these peaks were allowed to vary in the fits. Although the parameters of C-phase, D-phase and, to a lesser extent, even Li_5FeO_4 (table 5.2) are similar at room temperature, they are not at low temperature, as will be discussed later.

All other scans after the first discharge were fit with a combination of only the iron and C-phase peaks. Figure 5.7 shows the fits for the second discharge. As the discharge proceeds the C-phase doublet becomes smaller and the iron peaks grow in

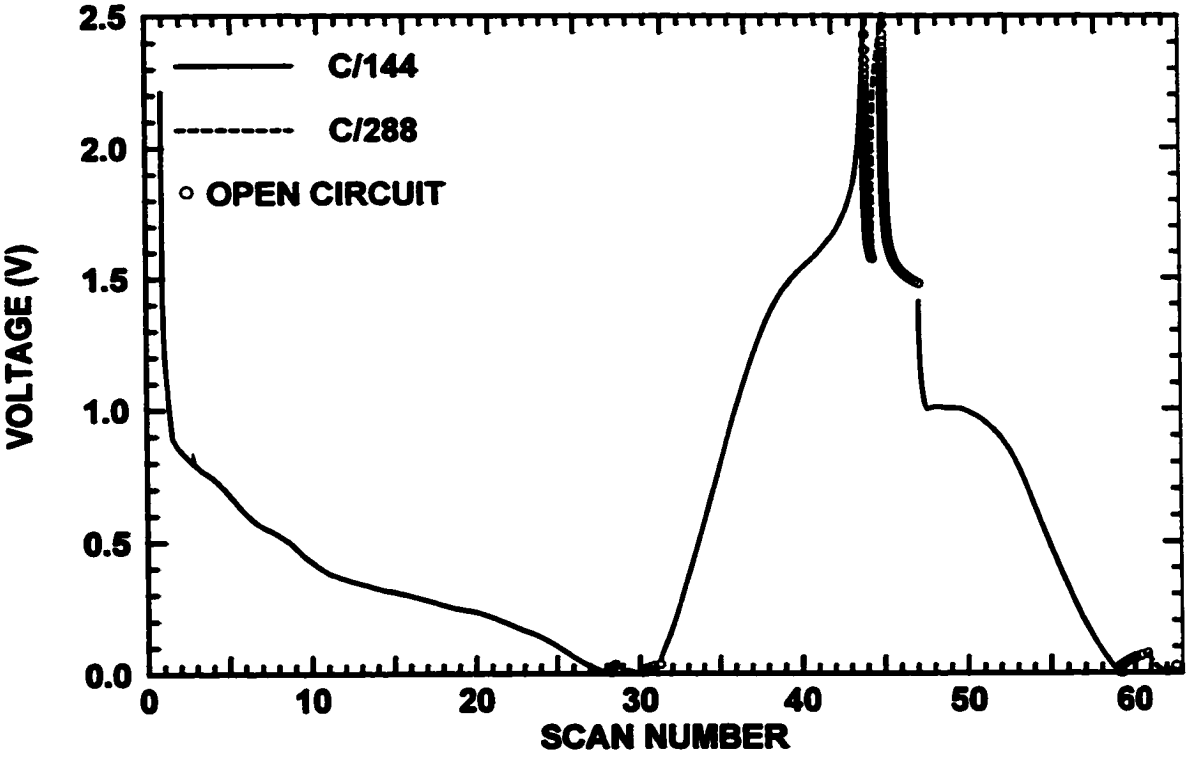

Figure 5.9 Voltage versus scan number for the Li_5FeO_4 in-situ Mössbauer study.

intensity until scan 70 where the spectrum is nearly entirely from the iron peaks. In the subsequent charge this process is reversed and the C-phase displaces the iron. This is illustrated in figure 5.8, which summarises the data from all the fits.

5.3.4 In-situ Mössbauer Studies of Li_5FeO_4

Figure 5.4(b) shows the room-temperature Mössbauer spectra of the Li_5FeO_4 sample, which was prepared by heating at 900°C. Previous measurements of this material report a symmetric doublet [92]. However, to obtain a good fit for our sample a small impurity peak, possibly due to some iron oxide hydroxide formed from air-exposure, had to be added to the spectrum. This impurity did not appear in the x-ray diffraction pattern (figure 5.3(b)). Despite the impurity, the symmetric doublet obtained

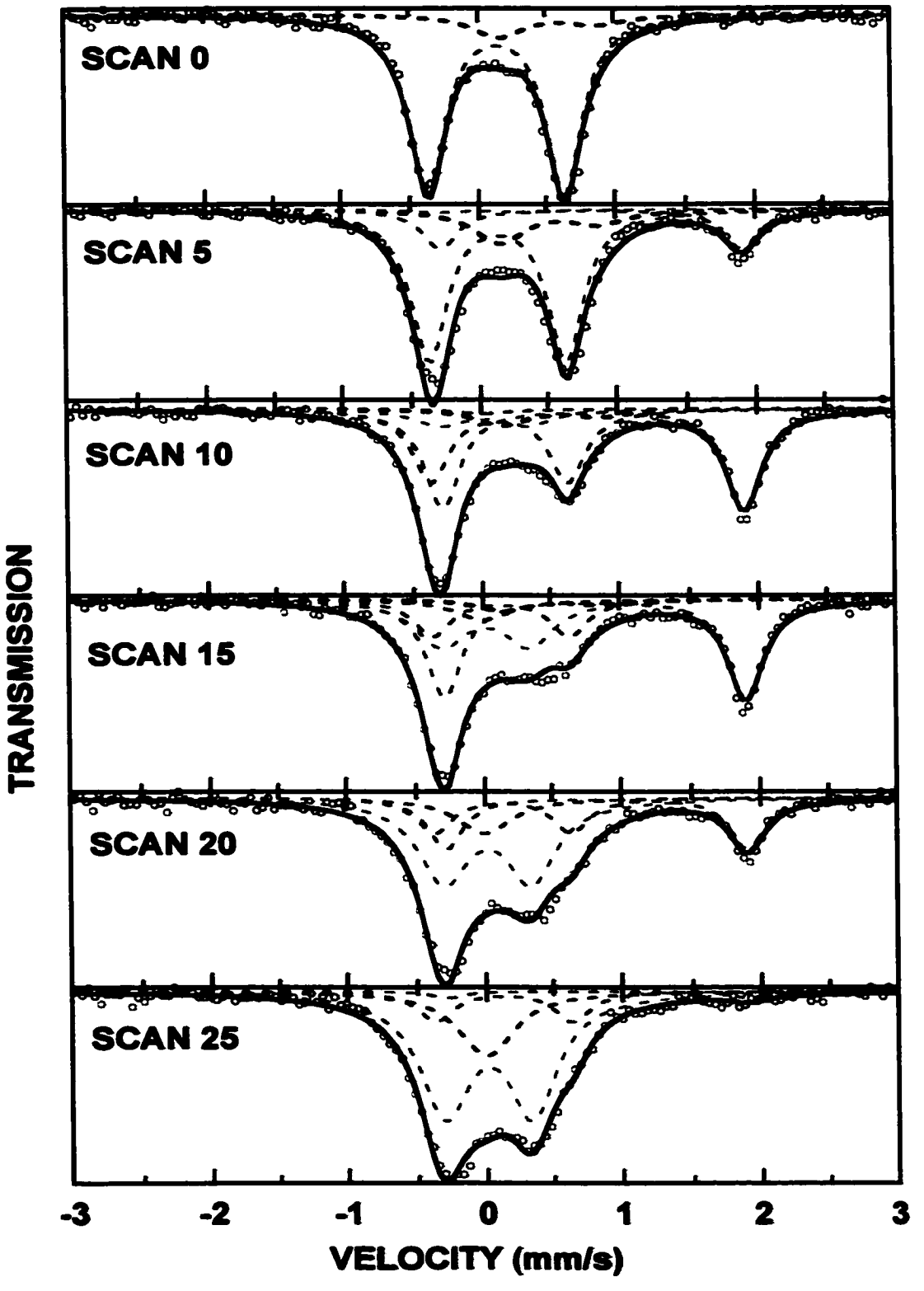

Figure 5.10 Some of the Mössbauer spectra taken during the first discharge of the Li_5FeO_4 in-situ Mössbauer cell. (Mössbauer Data: open circles, Fit Components: dashed lines, Total Fit: solid lines)

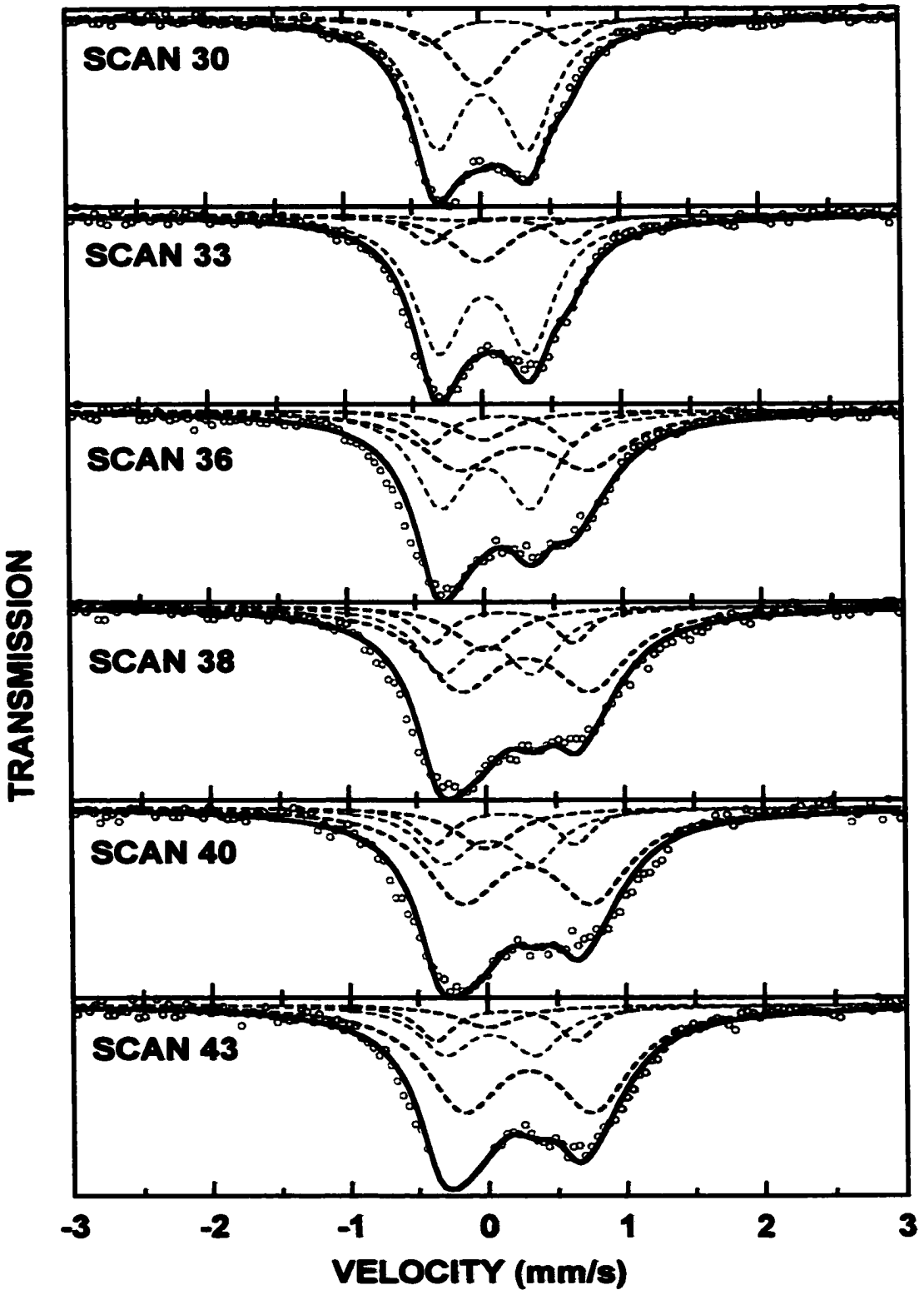

Figure 5.11 Some of the Mössbauer spectra taken during the first charge of the Li_5FeO_4 in-situ Mössbauer cell. (Mössbauer Data: open circles, Fit Components: dashed lines, Total Fit: solid lines)

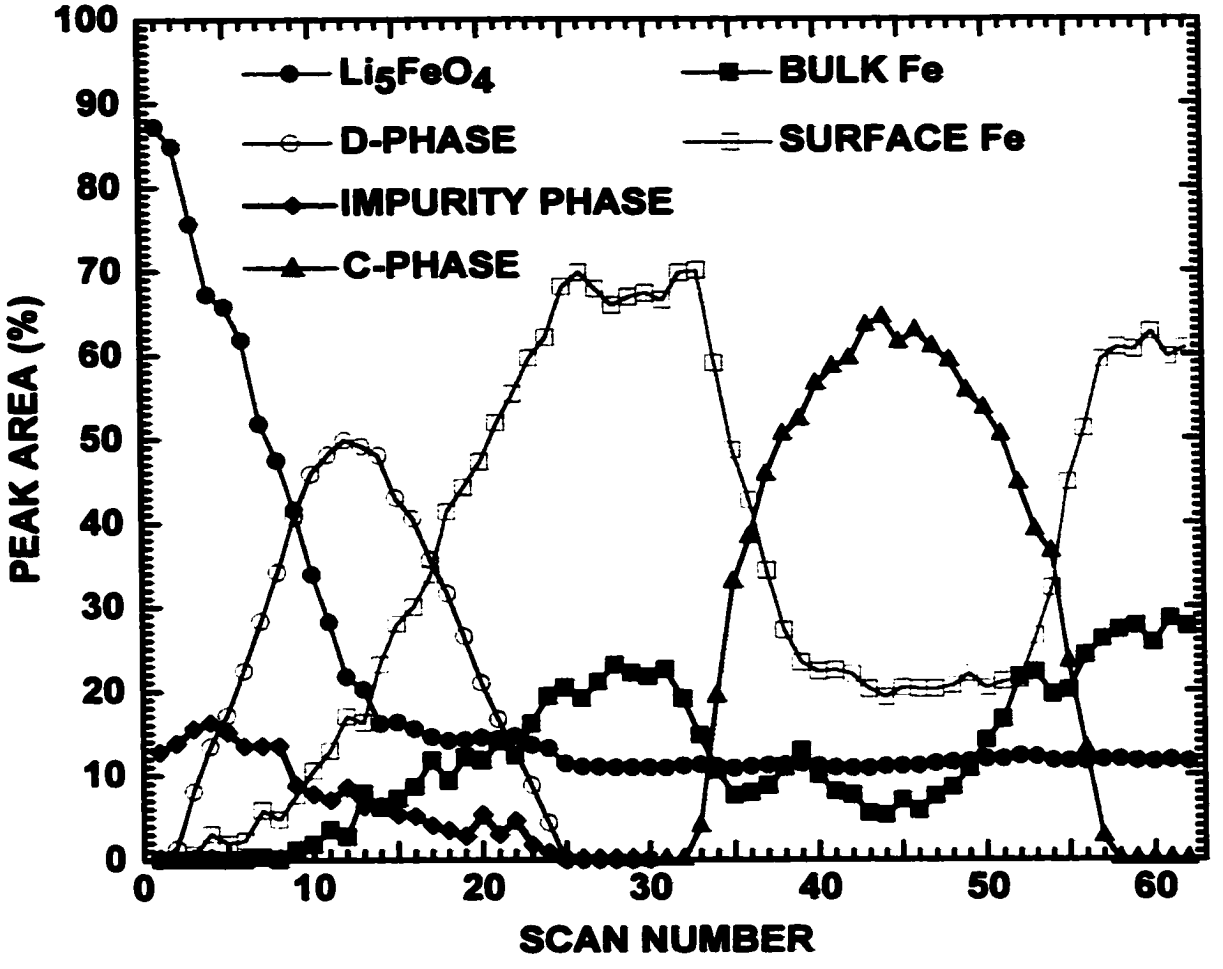

Figure 5.12 The spectral composition of the fits to the Li_5FeO_4 in-situ Mössbauer experiment scans.

from fitting the majority phase was in good agreement with the literature values [92]. The fitting parameters are listed in table 5.2.

Figure 5.9 shows the voltage versus scan number of the Li_5FeO_4 in-situ Mössbauer cell. The behaviour of Li_5FeO_4 is very similar to that of $LiFeO_2$ and the Mössbauer peaks were fit analogously. Figure 5.10 shows some of the Mössbauer scans taken during the first discharge. Like $LiFeO_2$, paramagnetic iron and a new phase (or perhaps surface iron in Li_5FeO_4) is formed during discharge while the peaks for the starting material disappear. This time, however, the "D-phase" has a large centre shift

Table 5.2 Fitting parameters from the Mössbauer spectra of the Li_5FeO_4 sample prepared at 900°C and from the Li_5FeO_4 Mössbauer in-situ cell. The Li_5FeO_4 spectrum was fit with a combination of a symmetric doublet for the main phase and a small asymmetric doublet representing an impurity phase or phases. The asymmetric doublet was added to account for the absorption from the impurities without attempting to interpret the physical significance of the parameters. The impurity doublet accounted for 16% of the total area of the fit. The singlet and quadrupole split components of the iron spectra are labeled $Fe^{(bulk)}$ and $Fe^{(surface)}$ respectively. The parameters for D-phase and C-phase refer to the majority component of the spectra measured at the bottom of discharge and top of charge, respectively. (δ: centre shift, Δ: quadruple splitting, Γ: peak HWHM, of the centre shift, A/A_+: ratio of the spectral areas of the low energy peak to the high energy peak)

Sample	δ *(mm/s)*	Δ *(mm/s)*	Γ *(mm/s)*	A/A_+ *(mm/s)*
Li_5FeO_4 (this study)	*0.122*	*0.985*	*0.137*	*1*
Li_5FeO_4 (Ref. [92])	*0.13*	*1.00*	*0.18*	*1*
Impurity Phase	*0.423*	*0.730*	*0.141*	*2.529*
$Fe^{(bulk)}$	*0*	*0*	*0.251*	*1*
$Fe^{(surface)}$	*0.018*	*0.645*	*0.222*	*1*
D-Phase	*0.809*	*2.188*	*0.155*	*1*
C-Phase	*0.293*	*0.928*	*0.332*	*1*

and also a very large quadrupole splitting of about 2.2 mm/s. This doublet can be easily seen in scans 5-20 in figure 5.10. Unlike the $LiFeO_2$ cell not all the Li_5FeO_4 was consumed at the bottom of discharge. This could be because the Li_5FeO_4 pressed electrode was quite brittle and some portions of the electrode became disconnected during cell assembly. After the first discharge the peak area of the unreacted Li_5FeO_4 varied substantially if it was allowed to vary. Thus for subsequent scans the Li_5FeO_4 peak area was fixed at its value at the bottom of the first discharge.

Figure 5.11 shows some of the Mössbauer scans taken during the first charge.

The first charge proceeds in the same way as for $LiFeO_2$, with the iron being displaced by a new doublet with a centre shift and quadrupole splitting very close to that for the C-phase formed from $LiFeO_2$. During the next discharge the C-phase is displaced once again with iron. These results are summarized in table 5.2 and figure 5.12.

5.3.5 Low Temperature Mössbauer Studies

Figures 5.13 shows the Mössbauer spectra taken at 298 K, 80 K, 39.8 K and 15 K of a $LiFeO_2$ cell at the bottom of discharge. At 15 K the spectrum is that of iron (see Fe-foil spectrum in the figure for comparison) confirming that iron is formed at the bottom of discharge. The spectrum at 15 K was fit with a sextet as well as a symmetric doublet. Apparently at this temperature some of the iron is still super-paramagnetic. The parameters of the fit are listed in table 5.3 with those of iron for comparison. The temperature at which small-grained iron magnetically orders can be related to the grain size [27]. This temperature is referred to as the blocking temperature and occurs when the area of the sextet is equal to the area of the paramagnetic peaks in the iron spectrum. From figure 5.13 this occurs between 15 K and 40 K corresponding to 3.5-4.5 nm iron grains [28].

Figure 5.14 (a), (b) and (c) show the low temperature Mössbauer spectra of the $LiFeO_2$ starting material, $LiFeO_2$ cells half-way through the first discharge and at the top of the first charge respectively. The parameters of the fits for these spectra are listed in table 5.3. At low temperatures $LiFeO_2$ magnetically orders giving a sextet with a hyperfine field of 489 kOe. This is in good agreement with reference [86], which reports a hyperfine field of 495 kOe. The fit obtained from this sextet plus the fit from the iron spectrum in figure 5.13(d) was used (varying only the intensity of the components) to fit

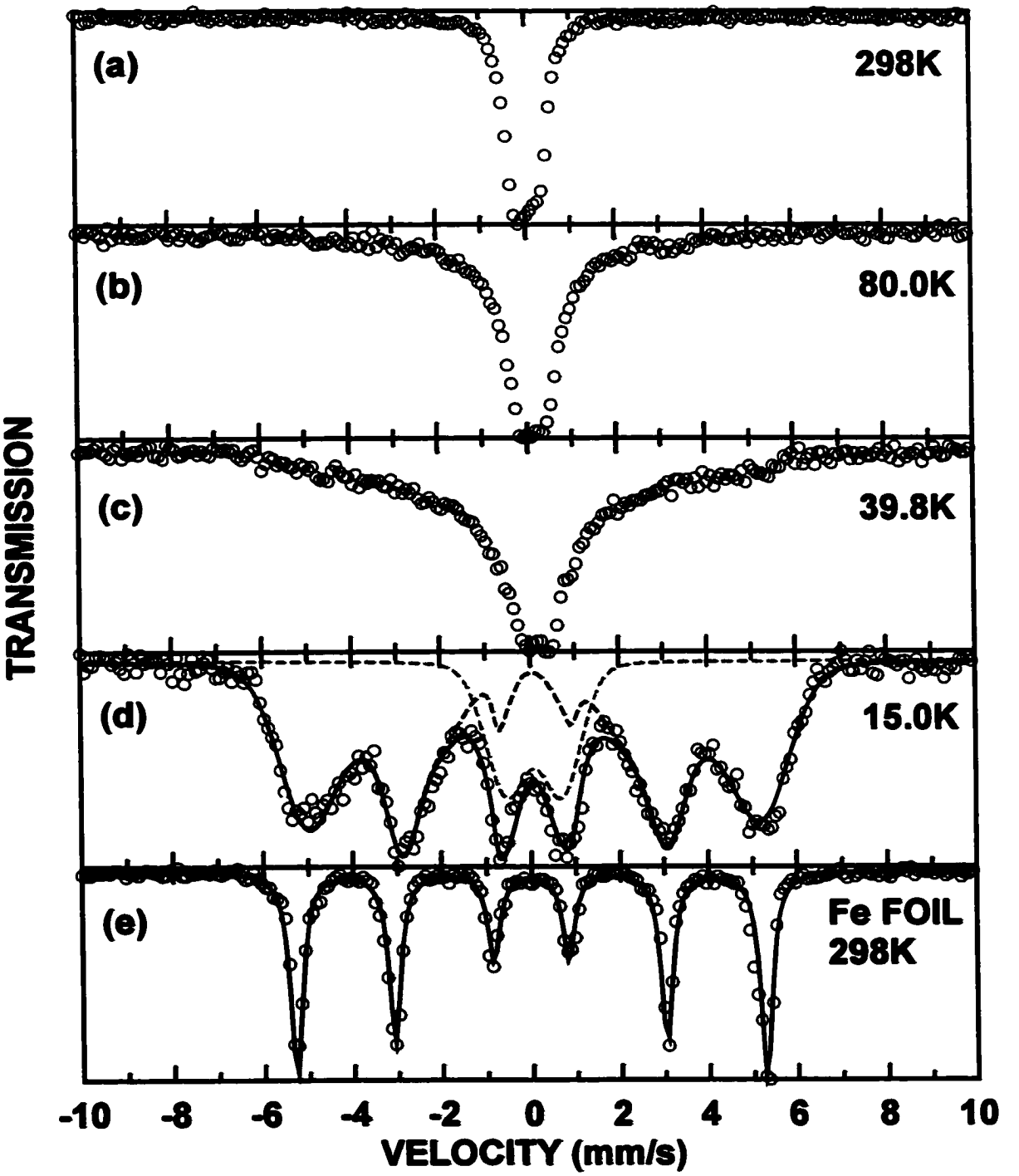

Figure 5.13 Mössbauer spectra taken at different temperatures of a $LiFeO_2$ cell at the bottom of the first discharge. The bottom panel shows a room temperature spectrum of iron foil for comparison. (Mössbauer Data: open circles, Fit Components: dashed lines, Total Fit: solid lines)

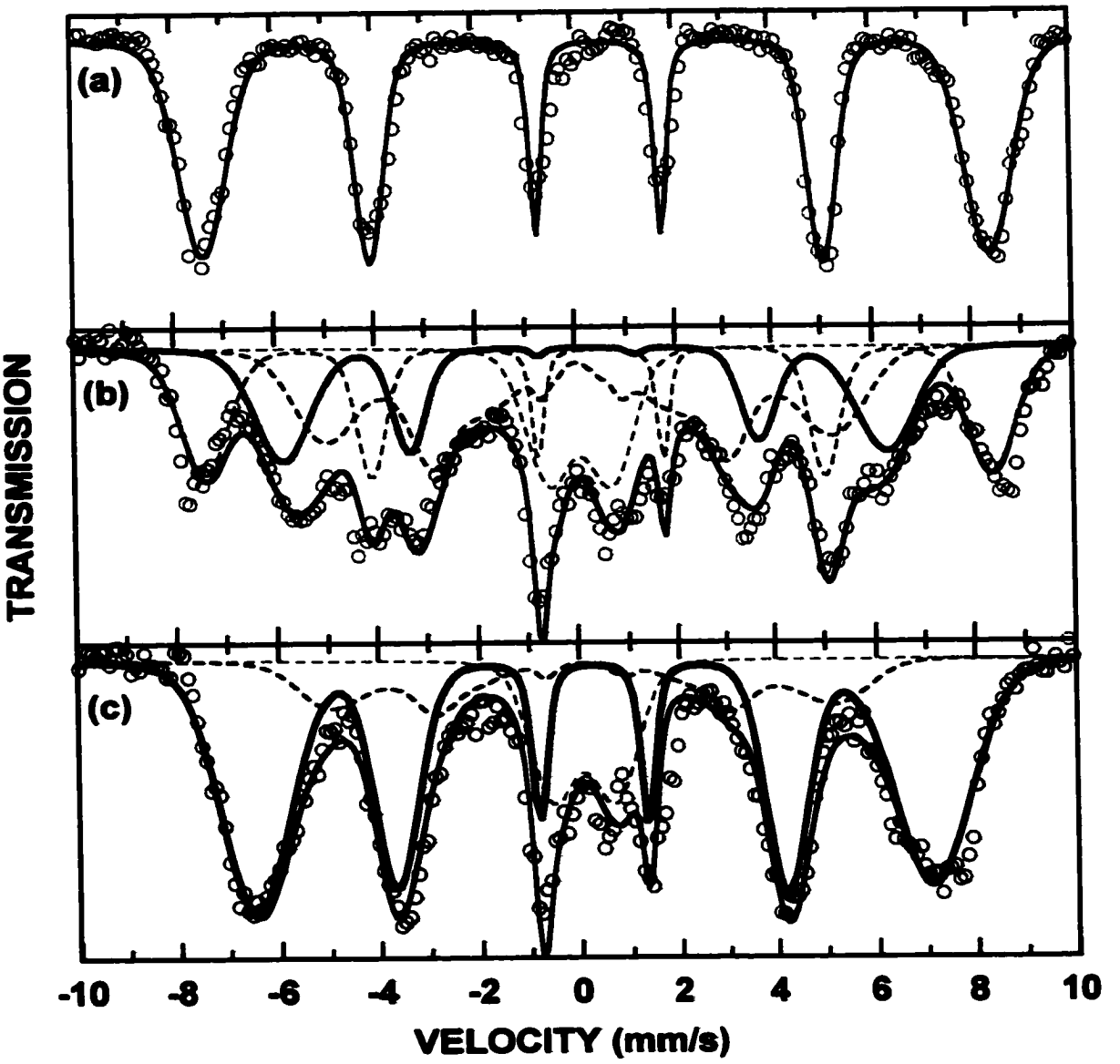

Figure 5.14 Mössbauer spectra taken at 15K of (a) the as-made $LiFeO_2$ sample (b) a $LiFeO_2$ cell half-way through the first discharge and (c) a $LiFeO_2$ cell at the top of the first charge. (Mössbauer Data: open circles, Fit Components: dashed lines, Total Fit: solid lines, D-phase: heavy solid line in panel (b), C-phase: heavy solid line in panel (c))

the spectrum in figure 5.14(b). However an additional sextet (shown with a heavy solid line in the figure) had to be added to the spectrum to obtain a good fit. This spectrum was attributed to magnetically ordered D-phase.

To fit the low-temperature spectrum of the $LiFeO_2$ at the top of the first charge

(figure 5.14(c)) the fit obtained from the iron spectrum in figure 5.13(d) was used (varying only the intensity of the components) plus a new sextet was added (shown with a heavy solid line in the figure) whose parameters are listed in table 5.3. This sextet is different than the low temperature spectrum of D-phase and of Li_5FeO_4 (which did not magnetically order above 15K) and was attributed to magnetically ordered C-phase. The C-phase component of the spectrum accounts for about 69% of the total area of the spectrum. Although this figure is comparable to what was obtained at room temperature it is probably more accurate since the peaks of iron and C-phase are less similar at low temperature.

Table 5.3 Fitting parameters from the Mössbauer spectra of the as prepared $LiFeO_2$ sample and from $LiFeO_2$ Mössbauer in-situ cells at low temperature. Except for the spectrum of iron foil, which was fitted with a single Lorentzian sextet, the spectra were fitted with Gaussian distributions of Lorentzian lineshapes. Only the average values of parameters are listed. The super-paramagnetic and hyperfine-split iron spectra are designated by S.P. Fe and H.S. Fe respectively. ($\langle\delta\rangle$: mean centre shift, $\langle|\Delta|\rangle$: mean quadruple splitting, $\langle\varepsilon\rangle$: the mean quadruple shift, $\langle H_m\rangle$: the mean hyperfine magnetic field)

Sample	*Figure in Text*	*Temp. (K)*	*Spectral Composition*	$\langle\delta\rangle$ *(mm/s)*	$\langle\|\Delta\|\rangle$ *(mm/s)*	$\langle\varepsilon\rangle$ *(mm/s)*	$\langle\|H_m\|\rangle$ *(kOe)*
$LiFeO_2$	*15(a)*	*20.0*	*100% $LiFeO_2$*	*0.495*	—	*0*	*489*
Fe foil	*14(e)*	*298*	*100% Fe foil*	*0*	—	*0*	*330*
S.P. Fe	*14(d)*	*15.0*	*19.7% S.P. Fe 80.3% H.S. Fe*	*0.072*	*1.28*	—	—
H.S. Fe	*14(d)*	*15.0*	*19.7% S.P. Fe 80.3% H.S. Fe*	*0.082*	—	*0*	*276*
C-Phase	*15(c)*	*15.0*	*14.6% S.P. Fe 16.0% H.S. Fe 69.4% C-Phase*	*0.302*	—	*0.019*	*421*
D-Phase	*15(b)*	*15.5*	*15.7% S.P. Fe 37.1% H.S. Fe 26.7% $LiFeO_2$ 20.5% D-Phase*	*0.202*	—	*0*	*377*

It is interesting that there is a larger contribution of super-paramagnetic iron in the iron components of the spectrum in figure 5.14(b) and especially figure 5.14(c) than in the spectrum of iron at the bottom of discharge (figure 5.13(d)). This suggests that the iron particles are smaller during their initial formation during discharge and also when they have been consumed by the reaction at the top of charge, than at the bottom of discharge, as expected. It is difficult to infer this from comparison of the areas of the super-paramagnetic and paramagnetic peaks of iron in figures 5.5-5.7, 5.10, 5.11 since there is probably some error in the relative magnitudes of these peaks due to their similarity. This does not pose a problem at low temperature.

5.3.6 Quasi In-situ XRD Studies of $LiFeO_2$

Figure 5.15 shows the voltage profile of the $LiFeO_2$ in-situ cell with the scan numbers indicated. This cell was cycled differently than other in-situ XRD cells. During XRD data collection which lasted 12 hours the cell was maintained at open circuit. After this the cell was discharged for 12 hours at a C/60 rate with no XRD data collection. The process was then repeated. This method will be referred to as the quasi in-situ XRD method. The initial scan (scan 0) for the cell is shown in figure 5.16 with peaks from $LiFeO_2$, Be and BeO identified. All the other small peaks in the spectrum are believed to be due to the cell parts. Figure 5.17 shows the XRD spectra of all the scans. It is not surprising that earlier studies reported amorphous materials after the first discharge [82,83], considering the poor statistics in figure 5.17, even for such a long scanning time. As the cell is discharged (scans 1-7) broad peaks appear at about 33.1°, 44° and 55.3° and increase in intensity. These peaks were identified with the (111) Li_2O, (110) α-Fe and the (220) Li_2O reflections. The literature values of the positions of these peaks are

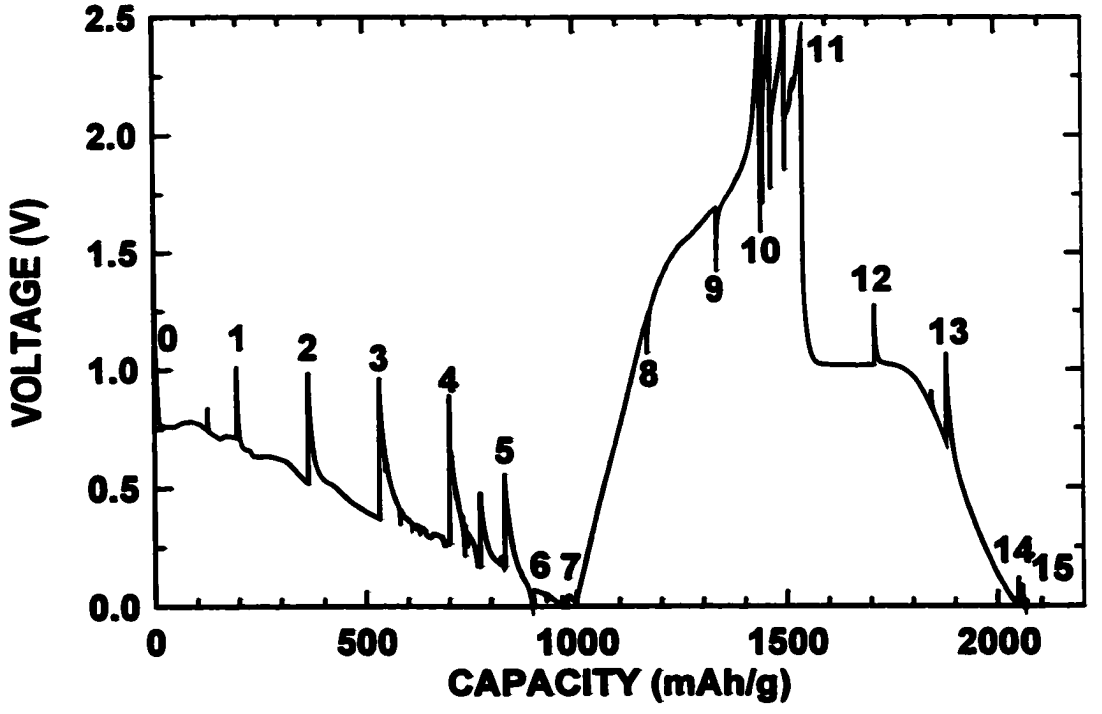

Figure 5.15 The voltage profile of the $LiFeO_2$ quasi in-situ XRD cell. At each scan number the cell was placed at open circuit while a twelve-hour XRD measurement was taken.

indicated in the figure. Although it is difficult to see from the figure the $LiFeO_2$ peaks decrease in intensity and finally disappear during the first discharge.

The most striking feature of figure 5.17 is the behaviour of the Li_2O peaks. During discharge they are at an angle 0.5° smaller than in crystalline Li_2O [85]. When the cell is charged (scans 8-11) the Li_2O (111) and (220) appear to shift to higher angle. This is quite unexpected for an alkali oxide. Furthermore the peak intensity remains constant, suggesting that it is not consumed during the charge. Also during charge, the Fe (110) reflection shifts to the left and becomes less broad. This peak decreases its intensity during the charge, but is not fully consumed as is suggested by the Mössbauer measurements. This could be attributed to the lower charge capacity of this cell compared to the in-situ Mössbauer cell. During the second discharge the process is

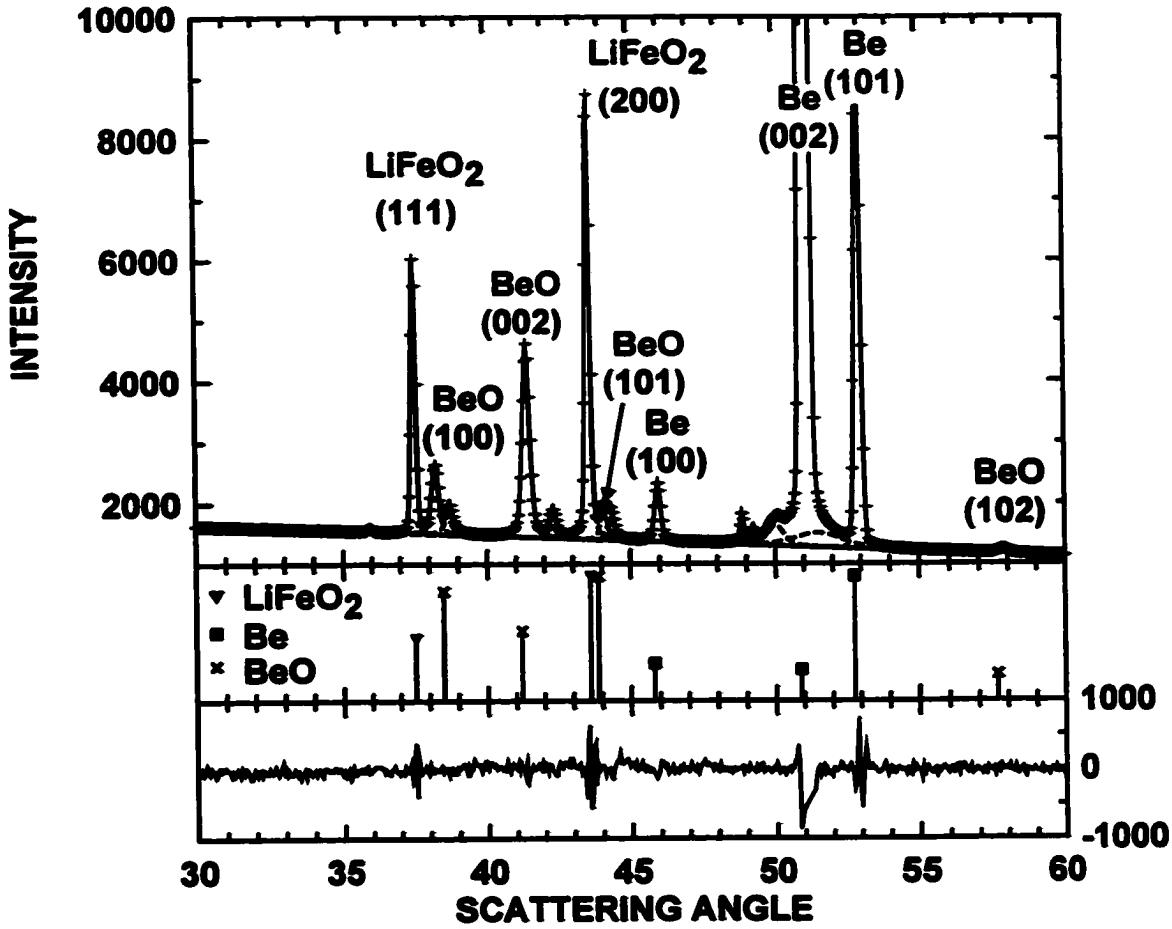

Figure 5.16 The XRD spectrum of the initial scan (scan 0) of the $LiFeO_2$ quasi in-situ XRD cell. Peak positions and intensities from the literature are indicated in the figure for α-$LiFeO_2$, Be and BeO [85]. The bottom panel shows the difference between the observed intensity and the fit to the scan. (XRD Data: crosses, Fit Components: dashed lines, Total Fit: solid line)

reversed and scan 15 is almost identical to scan 7 as is shown in figure 5.18. As will be discussed later, these observations are most likely caused by the formation of a new phase (namely C-phase) and not due to a change in the lattice constant of Li_2O from an intercalation process as the figure suggests.

To quantify the changes that occur during the in-situ experiment, each peak was fit individually using a pseudo-Voigt function. A linear background was used for the

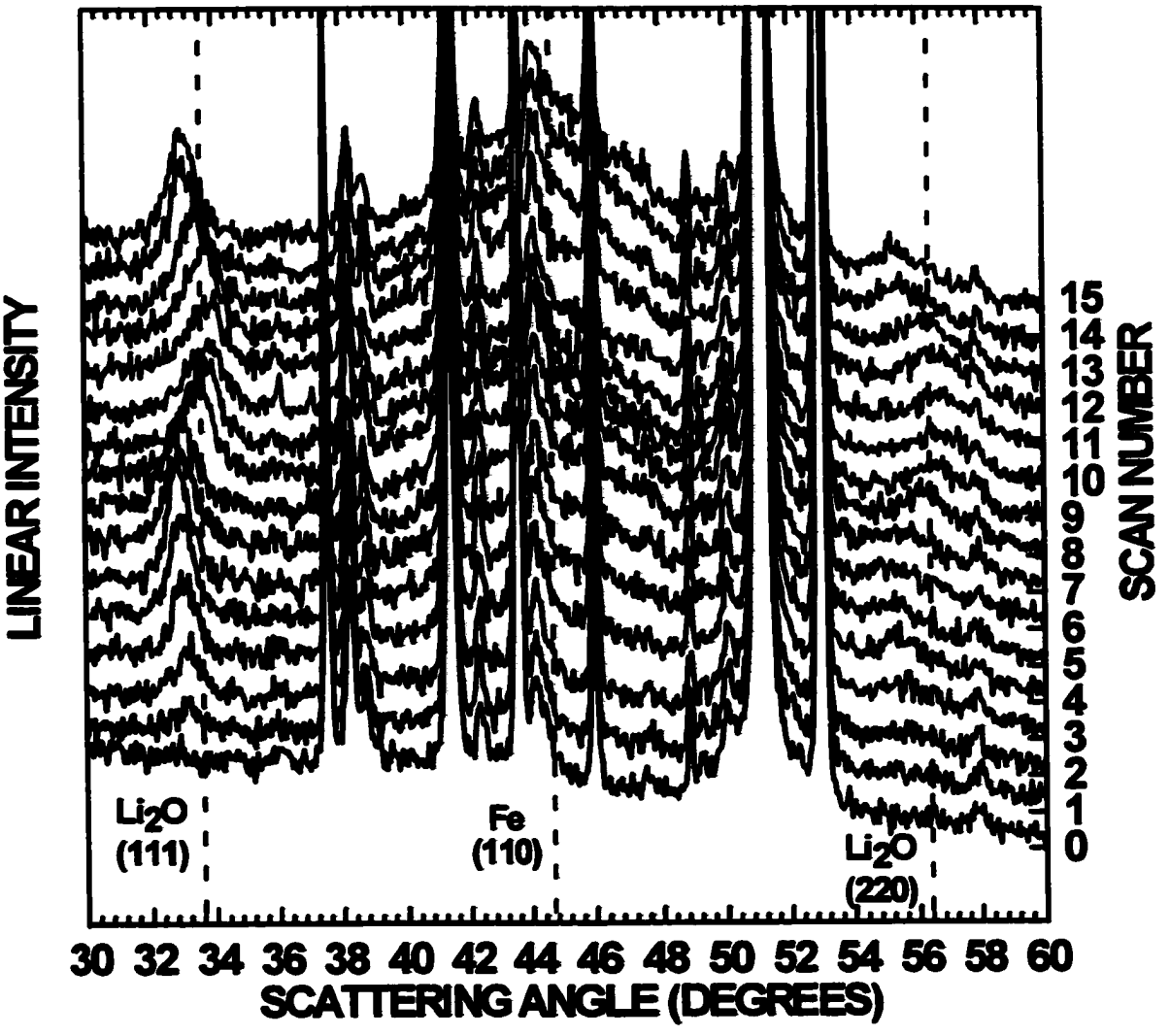

Figure 5.17 The XRD spectra from the $LiFeO_2$ quasi in-situ cell. The spectra are shifted on the vertical axis by an amount proportional to the scan number for clarity. Peak positions for crystalline Li_2O, and α-Fe are indicated in the figure by dashed lines [85].

entire spectrum. The peaks due to the beryllium window and the in-situ cell parts were fit from the initial scan (figure 5.16). Only the intensities of these peaks were allowed to vary for subsequent scans. For simplicity the (111) Li_2O, (110) Fe and (220) Li_2O reflections were each fitted with single peaks, instead of trying to fit the spectra with multiple phases. These peaks will always be referred to as the (111) Li_2O, (110) Fe, and (220) Li_2O reflections. The fits for these peaks were allowed to vary in size, position and

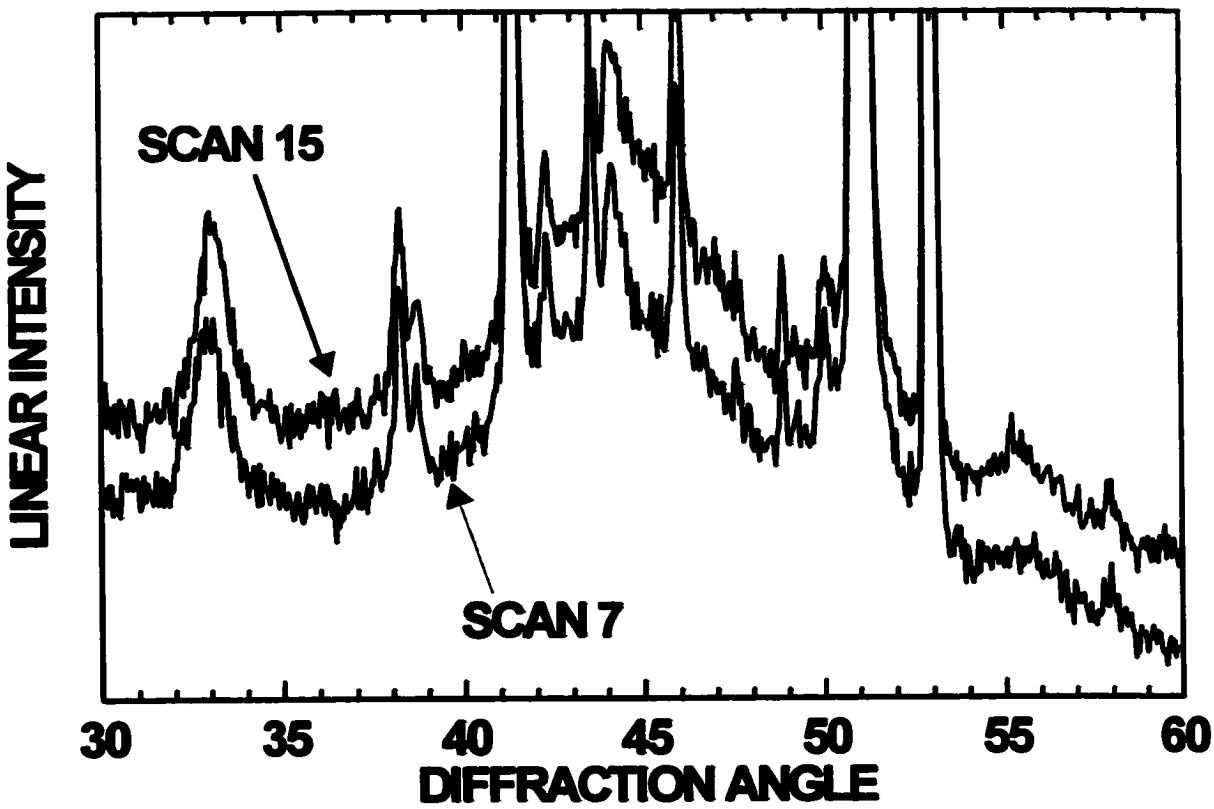

Figure 5.18 A comparison between the XRD patterns of the $LiFeO_2$ quasi in-situ cell at the bottom of the first (scan 7) and second (scan 15) discharges.

width. Since the Li_2O (220) and Fe (110) peaks mixed to a large extent their peak shape was restricted to Gaussian functions, while the peak shape of the Li_2O (111) was allowed to vary. Figure 5.19 shows the fit to the spectrum taken at the bottom of the first discharge (scan 7).

Figures 5.20 and 5.21 show the fitting results for the Li_2O (111) and (220) peaks. During the first discharge the peaks' positions remain constant while their intensity increases. The positions of the peaks are at a smaller angle than expected for crystalline Li_2O and are both consistent with a lattice constant of about 4.7 Å while crystalline Li_2O has a lattice constant of 4.6114 Å [85]. This effect could not be caused by an off-axis shift due to poor alignment of the sample in the x-ray diffractometer, since the peaks of

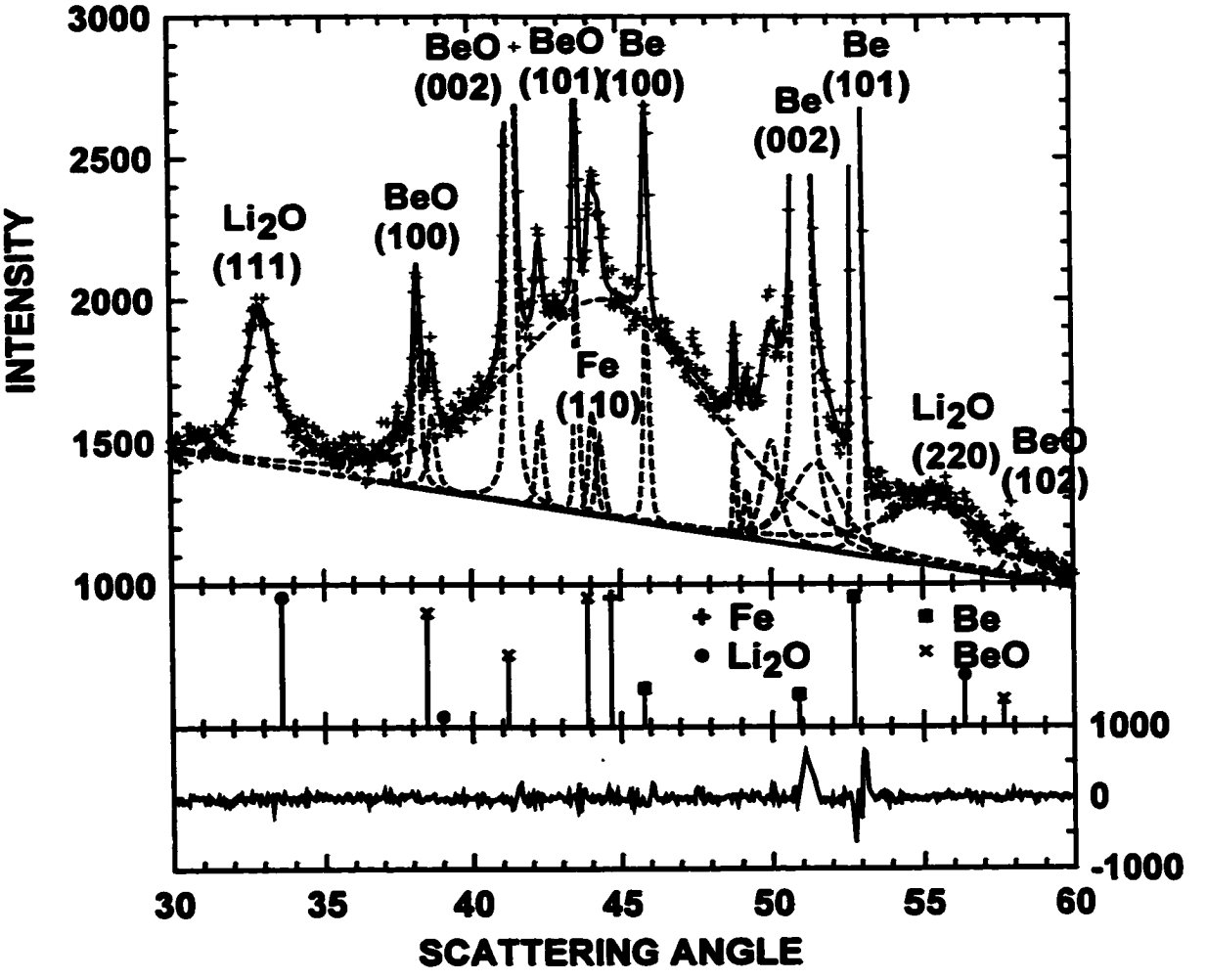

Figure 5.19 The XRD spectrum of the of the $LiFeO_2$ quasi in-situ XRD cell at the bottom of the first discharge (scan 7). Peak positions and intensities from the literature are indicated in the figure for Li_2O, α-Fe, Be and BeO [85]. The bottom panel shows the difference between the observed intensity and the fit to the scan. (XRD Data: crosses, Fit Components: dashed lines, Total Fit: solid line)

$LiFeO_2$ in the initial scans did not show any signs of an off-axis shift. During charge the peaks appear to markedly shift to higher angles. If this were due to a lattice contraction of Li_2O, the peak positions at the top of charge would correspond to a lattice constant of 4.6 Å. During the second discharge the peaks shift back to their initial position. However after the first discharge the intensities of the Li_2O peaks do not substantially

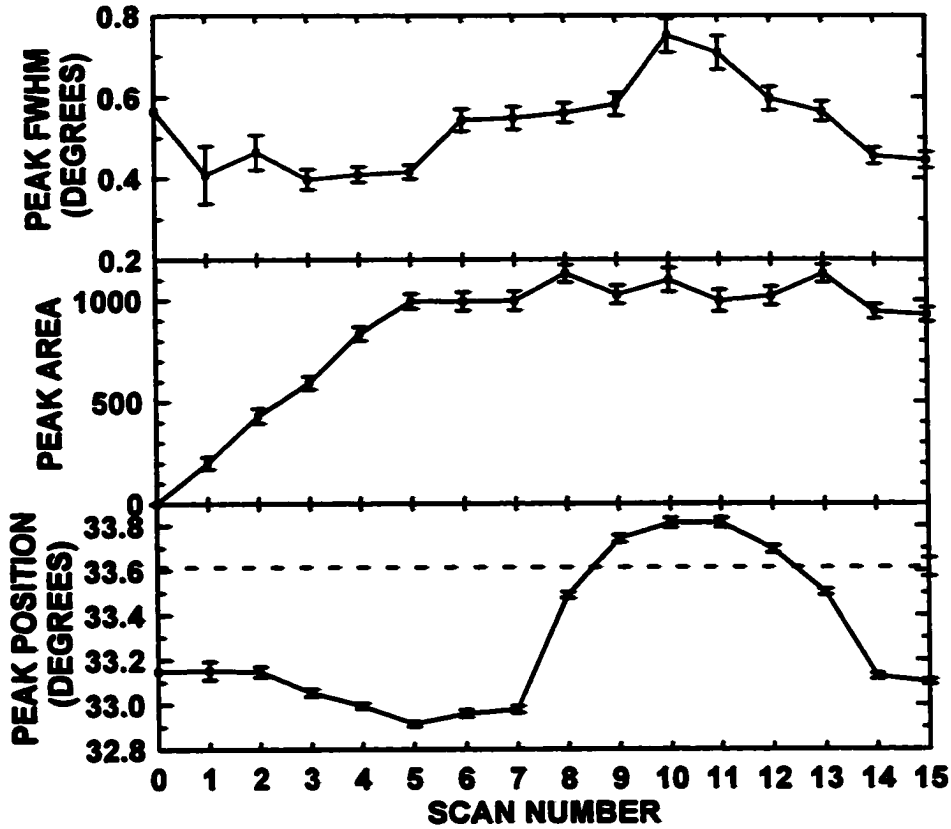

Figure 5.20 The fitting parameters obtained for the Li_2O (111) peak from the $LiFeO_2$ quasi in-situ XRD cell experiment. The position of this peak for crystalline Li_2O is indicated in the bottom panel by a dashed line [85].

change.

The behaviour of the Fe (110) is shown in figure 5.22. Because other peaks in the spectra affected the position of this peak during the fit, there is probably more error in its position and area than indicated by the error bars. This may be the reason for the apparent shift in the position of this peak as seen in the figure. Like the Li_2O peaks the iron is formed during the discharge. As expected from the Mössbauer results the area of the Fe (110) peak decreases during charge, then increases again during the next discharge. However the decrease in area is slight (only 30% of the original area) whereas about 80% of the iron was consumed during the charge of the in-situ Mössbauer cell.

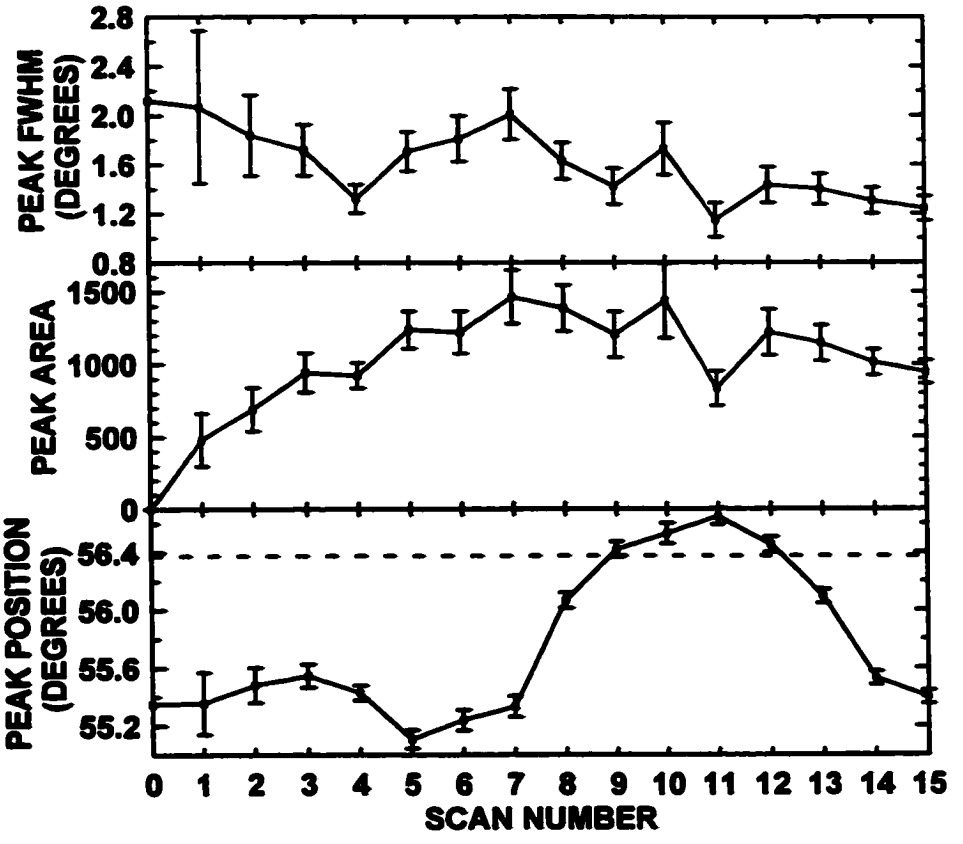

Figure 5.21 The fitting parameters obtained for the Li_2O (220) peak from the $LiFeO_2$ quasi in-situ XRD cell experiment. The position of this peak for crystalline Li_2O is indicated in the bottom panel by a dashed line [85].

The reasons for this are not entirely clear, however it could be partially due to the lower reversible capacity (about 25% lower) of the in-situ XRD cell compared to the in-situ Mössbauer cell. Also the first discharge of the in-situ XRD cell is somewhat irregular, but the cell seems to have recovered after this. Nevertheless problems with the in-situ XRD cell, such as perhaps some of the cathode becoming disconnected, may explain why less iron is oxidized in this cell than in the in-situ Mössbauer cell.

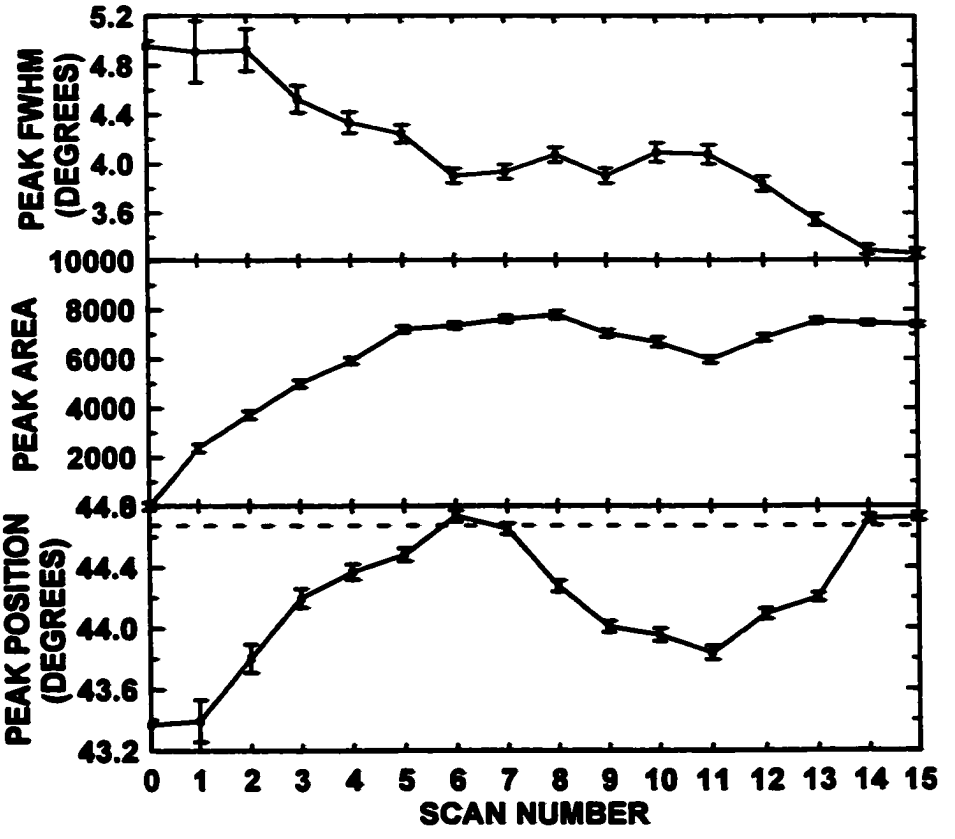

Figure 5.22 The fitting parameters obtained for the iron (110) peak from the $LiFeO_2$ quasi in-situ XRD cell experiment. The position of this peak for crystalline α-Fe is indicated in the bottom panel by a dashed line [85].

5.3.7 In-situ XRD Studies of α-CoO

Figure 5.23 shows the voltage profile of the CoO in-situ cell with the scan numbers indicated. This cell was cycled continuously at a C/60 rate while XRD data was collected. Each scan took six hours to collect. The data from the scans was then binned together in pairs to give better statistics. The initial scan (scan 0) is shown in figure 5.24 with the peaks from α-CoO, Be, and BeO identified. Figure 5.25 shows the averaged XRD spectra. Because of the many broad and overlapping peaks in the spectrum, a quantitative fitting procedure like that done for the $LiFeO_2$ in-situ cell proved difficult.

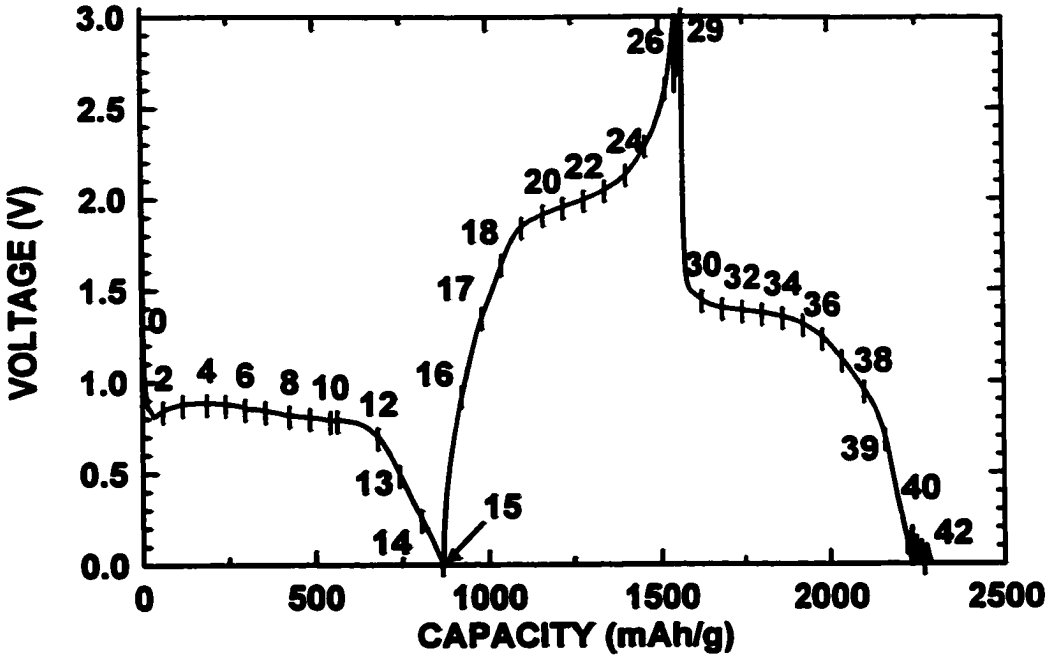

Figure 5.23 The voltage profile of the α-CoO in-situ XRD cell. The start of each six-hour scan is indicated in the figure.

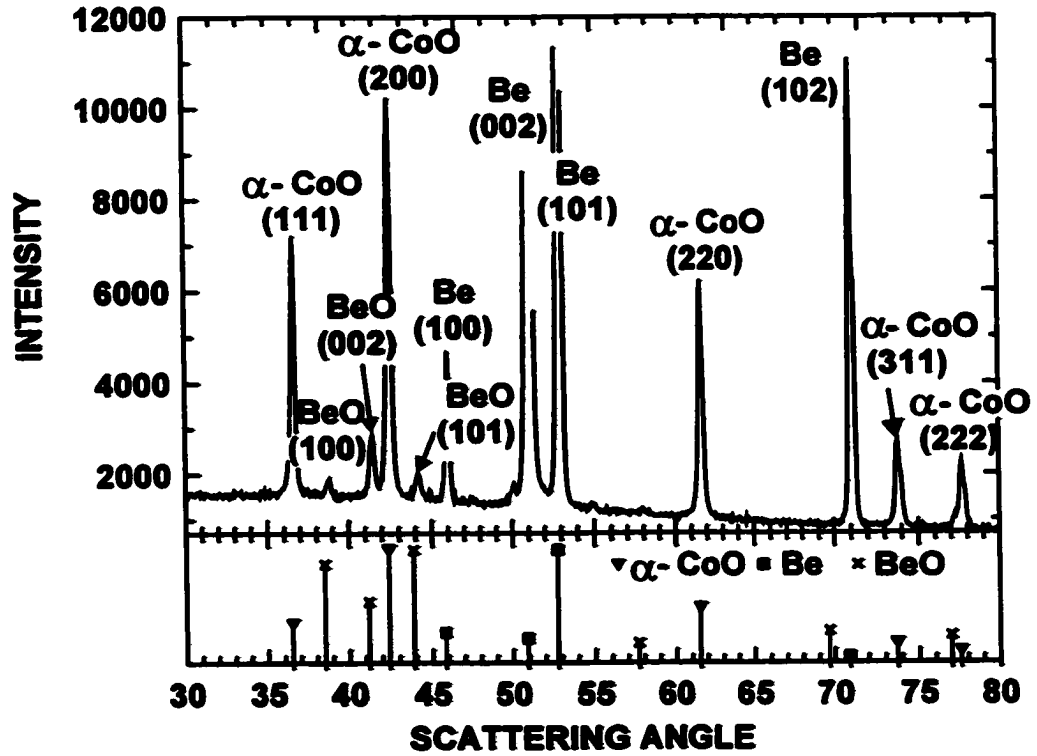

Figure 5.24 The XRD spectrum of the initial scan (scan 0) of the α-CoO in-situ XRD cell. Peak positions and intensities from the literature are indicated in the figure for α-CoO, Be and BeO [85].

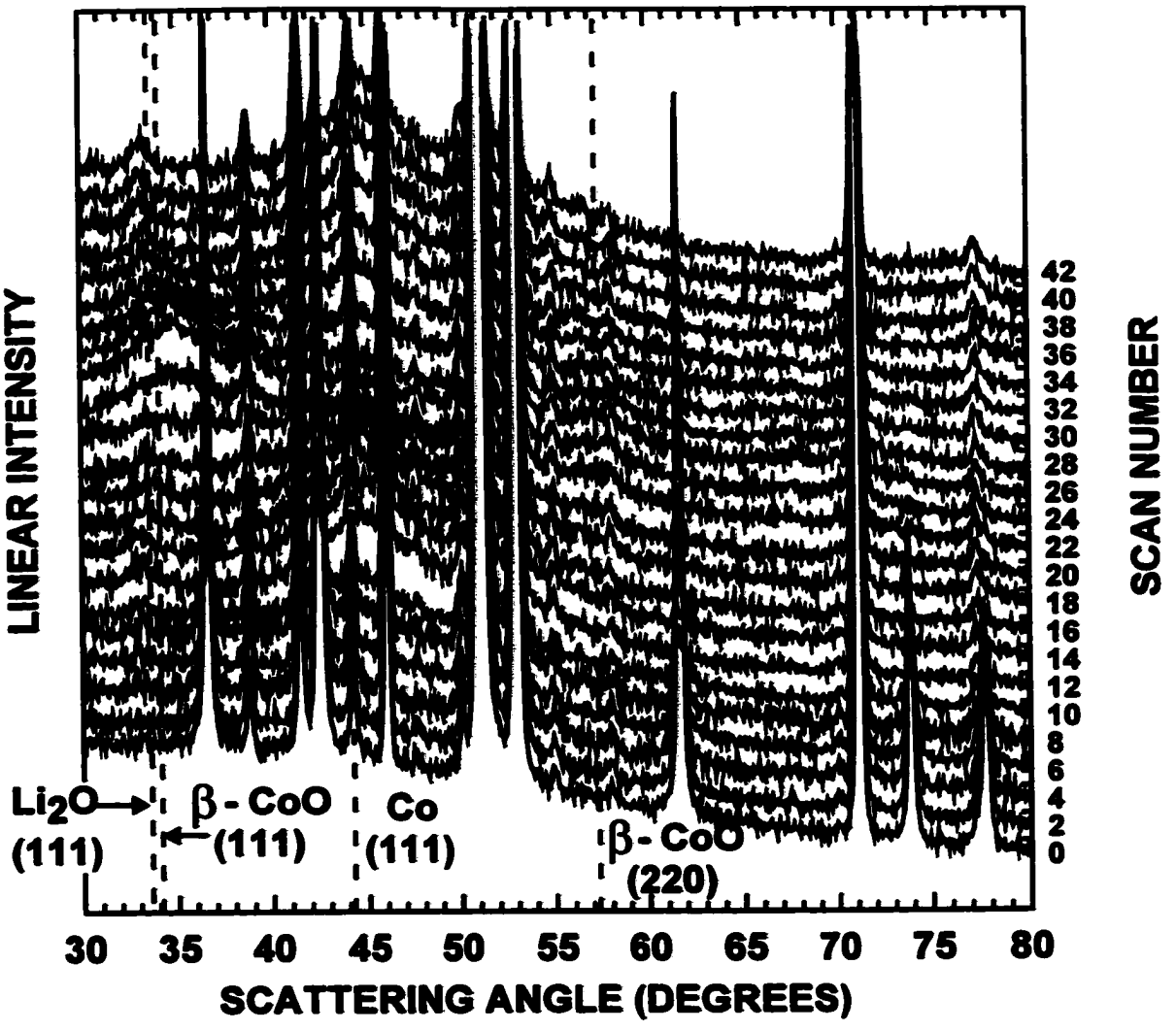

Figure 5.25 The XRD spectra from the α-CoO quasi in-situ cell. The spectra are averaged in pairs and shifted on the vertical axis by an amount proportional to the scan number for clarity. The strongest peak positions for crystalline Li_2O, β-CoO and Co are indicated in the figure by dashed lines [85].

Nevertheless the large changes in the XRD spectra that occur as the cell cycles leads to a straightforward interpretation of the spectra. In figure 5.25 the major peaks of Li_2O, β-CoO and Co are indicated by dashed lines. As the cell is discharged (scans 1-15) the behaviour is very similar to that of $LiFeO_2$. Broad peaks appear during the discharge at about 33°, 44° and 55°, which were identified as the (111) Li_2O, the (111) Co and the

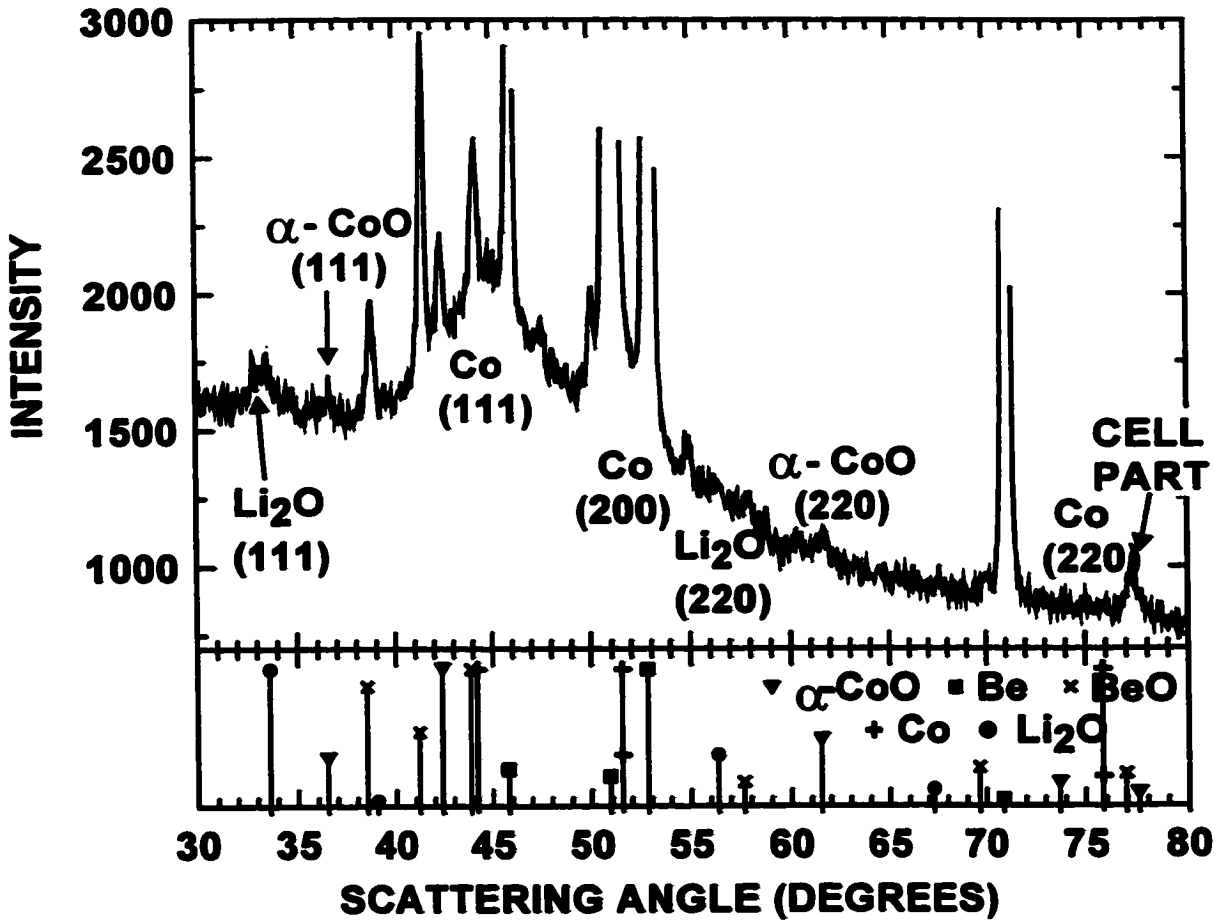

Figure 5.26 The XRD spectrum of the of the α-CoO in-situ XRD cell at the bottom of the first discharge (scan 15). Peak positions and intensities from the literature are indicated in the figure for Li_2O, α-CoO, Co, Be and BeO [85].

(220) Li_2O reflections as indicated in the figure. The positions of the Li_2O peaks are again at a slightly smaller angle than expected for crystalline Li_2O. Also during the discharge the intensity of the CoO peaks become smaller and nearly disappear by scan 15. This can be seen in figure 5.26, which shows the average of scans 14 and 15. The Li_2O and the Co peaks are also clearly visible in the figure, although they are quite broad. This spectrum is very similar to that of $LiFeO_2$ at the bottom of discharge as shown in figure 5.18. The small peak at about 77.5° in figure 5.26 is present in all of the scans and is thought to be due to a cell part.

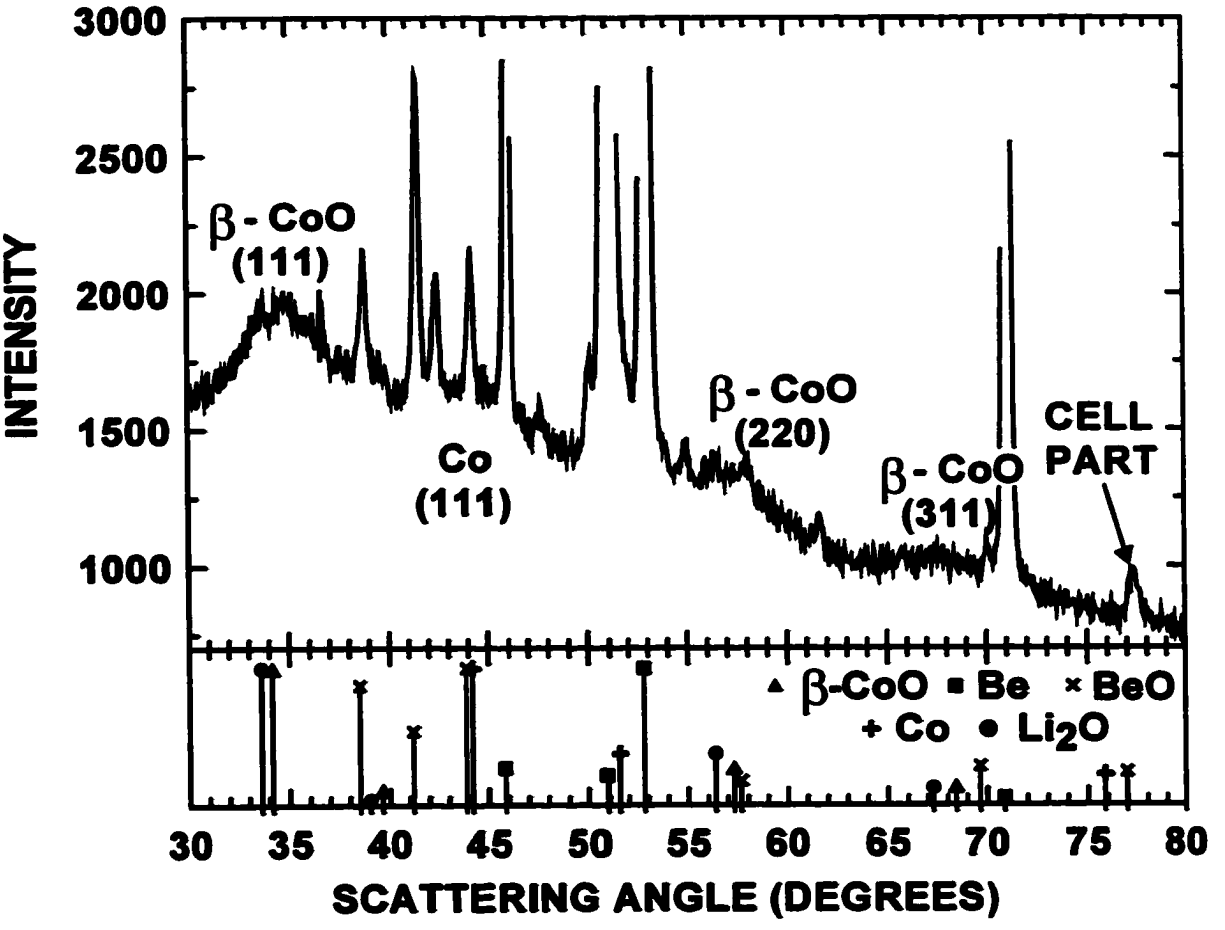

Figure 5.27 The XRD spectrum of the of the α-CoO in-situ XRD cell at the top of charge (scan 29). Peak positions and intensities from the literature are indicated in the figure for Li_2O, β-CoO, Co, Be and BeO [85].

The behaviour of the CoO cell at the beginning of charge (scans 16-20 in figure 5.25) is also similar to the $LiFeO_2$ cell in that the Li_2O peaks shift slightly to higher angle. However as the charge progresses (scans 20-29) the intensity of the Li_2O peaks increases dramatically. Also the Co peaks are nearly gone by the top of charge. This suggests that the Co is oxidized during charge to form β-CoO, which has a very similar XRD spectrum to Li_2O. This can be seen in figure 5.27, which shows the average of scans 28 and 29 at the top of charge.

During discharge (scans 30-42) the β-CoO peaks disappear and the Co and Li_2O

peaks form once again. At the bottom of discharge the spectrum consists entirely of Li_2O and Co and the scans of the first and second discharge are nearly identical as is shown in figure 5.28.

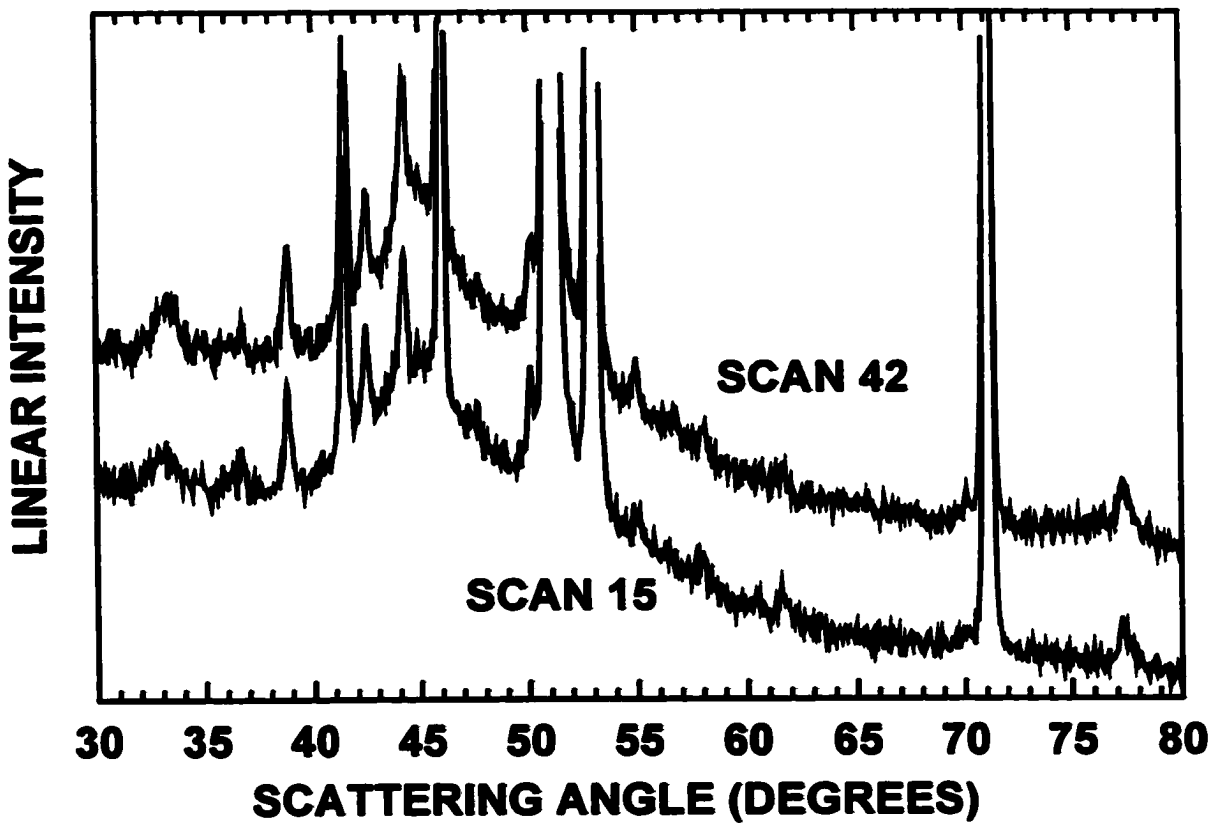

Figure 5.28 A comparison showing the similarity of the cathode material at the bottom of the first (scan 15) and second (scan 29) discharges of the α-CoO in-situ cell.

5.4 DISCUSSION OF EXPERIMENTAL RESULTS

In order to get an understanding of the displacement reaction of lithium with metal oxides consideration of all the above results is necessary. Starting from the initial moment of discharge it is clear from XRD and Mössbauer measurements that lithium oxide and the reduced metal in the form of small grains are immediately produced. At the same time Mössbauer measurements of the iron oxides show that some iron is in a different environment than the starting material or the reduced iron metal. This phase

was called D-phase iron. However there is no evidence for this phase in the XRD measurements, meaning it is either amorphous or very small grained. It is also interesting that the D-phases formed from $LiFeO_2$ and Li_5FeO_4 are different. The large quadrupole centre shift of the D-phase formed from Li_5FeO_4 is typical of Fe^{2+} compounds while the smaller centre shift of the D-phase formed from $LiFeO_2$ is typical of compounds containing Fe^{3+} [93]. The D-phase may represent the metal in the grain boundaries of the metal oxides, or in an intermediate phase of the reduction process. Actually, either interpretation is probably equivalent.

The other interesting thing about the discharge is its excess capacity compared to that predicted by a simple reduction reaction as is shown in figure 5.1. This could be caused simply from catalytically-activated electrolyte decomposition reactions with lithium on the newly formed small-grained materials, which may have large exposed surface areas. Another possible explanation is that a non-stoichiometric lithium oxide, i.e. $Li_{2+x}O$, is forming during discharge. This would also explain the large lattice constant of the lithium oxide that is formed for both the $LiFeO_2$ and CoO cells, although this effect may just be due to its small grain size.

For the charging process the Mössbauer measurements of the iron oxides show that a new phase is formed, which was called C-phase. This phase is the same for both the $LiFeO_2$ and Li_5FeO_4 cells. This is not surprising, since at the bottom of discharge, both cathodes are composed of only iron and lithia. Flat, horizontal plateaus in the voltage profiles during charge also support the presence of a three-phase region, especially for $LiFeO_2$. The centre shift of the C-phase material is consistent with iron (III), however it is rather small. This suggests short Fe-O bonds or that the iron is in

tetrahedral sites (Li_5FeO_4, an oxide with iron (III) in tetrahedral sites and a low centre shift, is a good example of this effect). The rather large quadrupole splitting of C-phase would also be a product of the non-isotropic field generated by an asymmetric arrangement of ions around the iron atom (as is also the case for Li_5FeO_4) or perhaps due to a distorted octahedral site. That iron (III) is being formed is also suggested from the electrochemical results. For the $LiFeO_2$ cell the observed charge capacity was 652mAh/g. Mössbauer studies suggest that 80% of the iron was oxidized to iron (III) during charge (figure 5.8). This corresponds to 676 mAh/g, which is very close to the observed capacity. Similarly, for the Li_5FeO_4 cell, Mössbauer studies suggest that 62% of the starting material was eventually oxidized back to iron (III) during charge (figure 5.12). This corresponds to a capacity of 323 mAh/g, which is also close to the observed capacity of 280mAh/g.

The identity of the C-phase is difficult to elucidate from the in-situ XRD measurements of the $LiFeO_2$ cell. However in the CoO in-situ experiment β-CoO is clearly formed at the top of charge while the Co and Li_2O peaks disappear. The reverse happens during the next discharge. This leads to the following reaction scheme:

$$\text{First discharge: } \alpha\text{-CoO} + 2\text{Li} \rightarrow \text{Co} + \text{Li}_2\text{O} \qquad (5.3)$$

$$\text{Further cycling: } \text{Co} + \text{Li}_2\text{O} \rightleftharpoons \beta\text{-CoO} + 2\text{Li} \qquad (5.4)$$

Electrochemical displacement reactions like the above are apparently quite rare. No similar examples could be found in the literature. The reason for the electrochemical activity of Li_2O and β-CoO in this case may be due to the similarity of these two

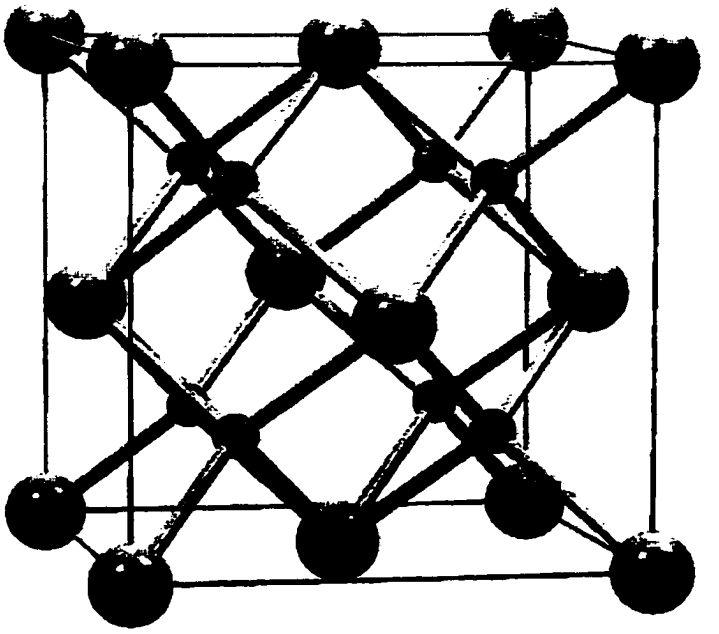

(a)

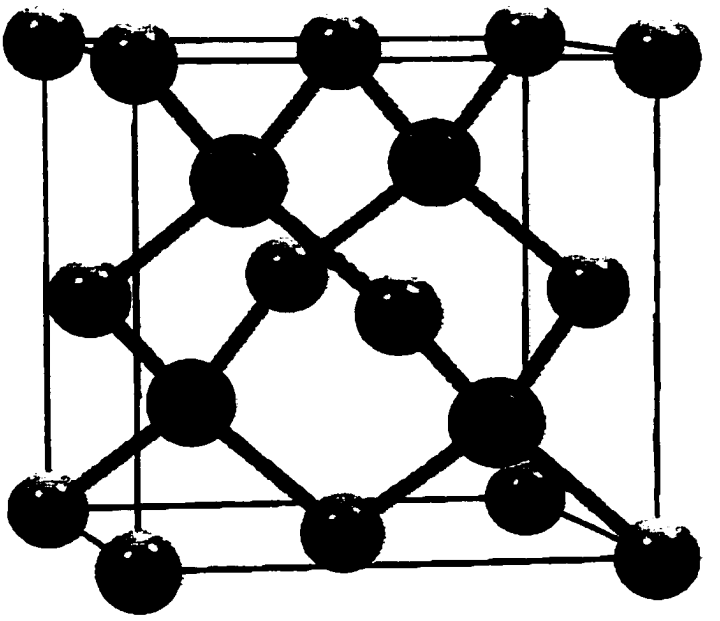

(b)

Figure 5.29 The structures of (a) Li_2O and (b) β-CoO showing the similarity in their oxygen lattice, cation positions and lattice constants. O: grey spheres, Li: small black spheres, Co: large black spheres

structures. Figure 5.29 shows the structures of Li_2O and β-CoO. Li_2O has the antifluorite structure while β-CoO has a zinc blende type lattice. In both structures the oxygen lattices are the same with β-CoO having a slightly smaller (4.544Å) lattice constant than Li_2O (4.619Å). Furthermore, the cations of both lattices are located in the tetrahedral sites of the oxygen lattice; Li_2O having all the tetrahedral sites filled and β-CoO having half the tetrahedral sites filled. Thus reaction (5.4) resembles an ion-exchange process where the Co^{2+} ions replace the Li^+ ions in the Li_2O lattice. How this ion-exchange process might work is illustrated in figure 5.30. At the bottom of discharge a mixture of nanograined Li_2O and Co is formed. It is supposed here that the two phases are formed such that they are in intimate contact as shown in figure 5.30(a). During charge the only species that can be oxidized is the cobalt metal. When this happens, as shown in figure 5.30(b), the Co^{2+} ion produced by the oxidation is in a position to ion exchange with two lithium ions in Li_2O. The resulting material from the ion exchange will be β-CoO as shown in figure 5.30(c). This reaction scheme may explain why the reaction occurs even though Li_2O is an insulator, since no electron transfer occurs during the ion exchange process.

A similar reaction may be happening during charge in the case of $LiFeO_2$ (and Li_5FeO_4). Here the charged species may also have a zinc blende type lattice with iron (III) in the tetrahedral sites (as suggested by the Mössbauer results). For instance one can envisage C-phase as a zinc blende form of $LiFeO_2$ with both the Li^+ and Fe^{3+} ions being located in the tetrahedral sites. The XRD spectrum of this material would be identical to that of Li_2O and β-CoO, save differences in lattice constants. This could explain why no new peaks were formed in the $LiFeO_2$ in-situ XRD cell during charge and the apparent

shift towards higher angles observed in the Li_2O peaks.

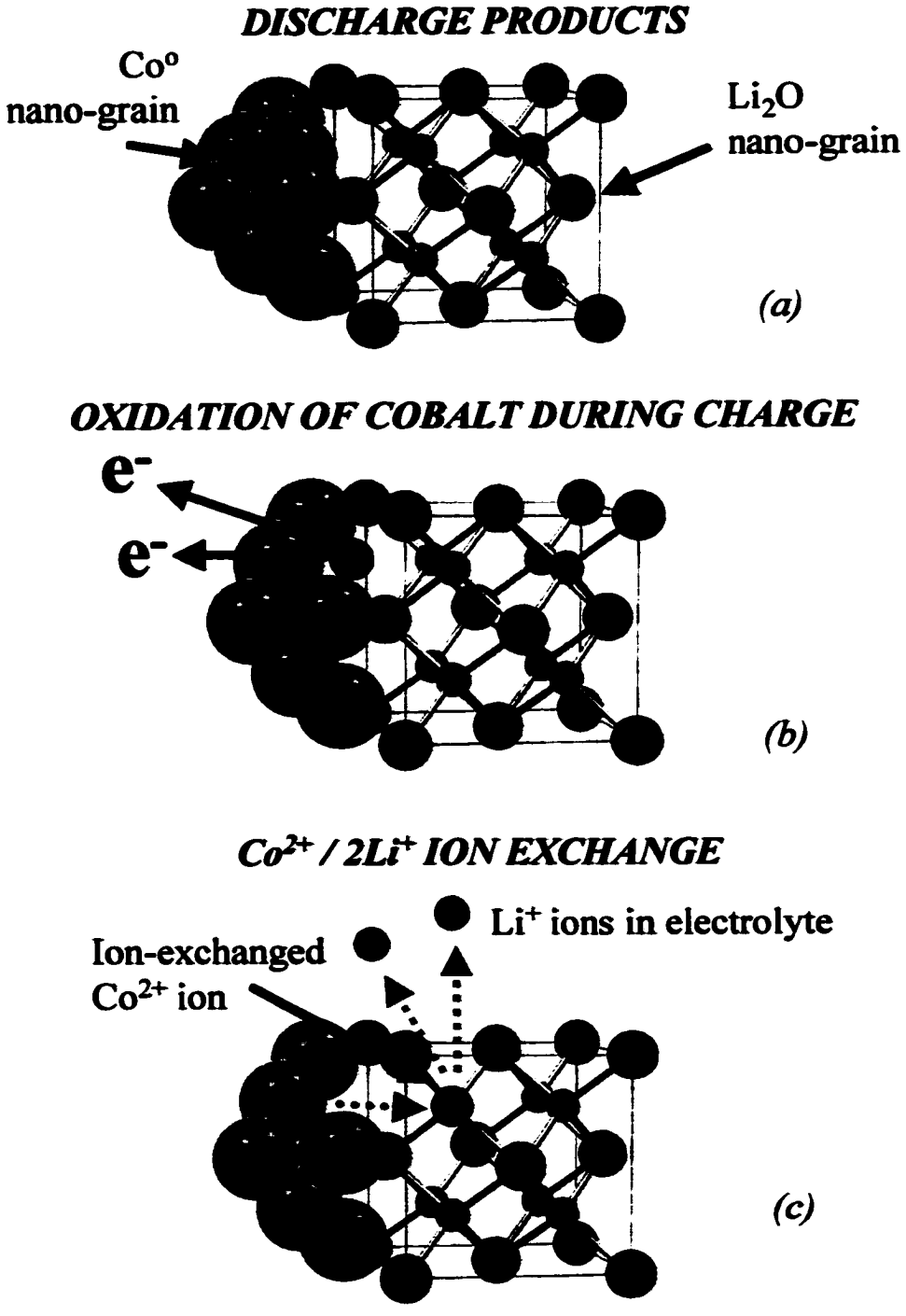

Figure 5.30 Illustration of the electrochemical ion-exchange process proposed in the text.

Chapter 6

Electrochemical Displacement Electrodes Containing Active Lithium

6.1 INTRODUCTION

In the last chapter lithium was found to undergo a reversible electrochemical displacement reaction with transition metal oxides. For a generic transition metal oxide the reaction may be written as follows:

$$\text{First discharge: } M_aO_b + 2bLi \rightarrow aM + bLi_2O \quad (6.1)$$

$$\text{Further cycling: } a'M + b'Li_2O \rightleftharpoons M_{a'}O_{b'} + 2b'Li. \quad (6.2)$$

Here reaction (6.1) may be regarded as a displacement reaction where the metal oxide reacts with lithium to make nanograined reduced metal and lithium oxide. The second

reaction (6.2) was found to possibly be an ion-exchange type process where the lithium ions reversibly exchange with metal ions in the oxygen lattice. Here a' and b' reflect that a structurally and even a stoichiometrically different metal oxide may be taking part in reaction (6.2) than the starting metal oxide in (6.1). Although it was found that such metal oxide electrodes have extremely large capacities, such electrodes, used as cathodes, are incompatible with lithium ion technology since the first step of the reaction (6.1) requires a lithium metal anode.

The obvious question that arises is if it is possible for the end products of reaction (6.1) to be synthesized outside of the cell. That is, if one starts with a composite of nanograined transition metal and lithium oxide, would it be possible to by-pass equation (6.1) and start on the left-hand side of equation (6.2)? Such a material would be a source of lithium ions in a lithium cell and thus would be a cathode material compatible with lithium ion technology. At this stage of the development of displacement electrodes, this idea may be wishful thinking, based on the poor cycling characteristics (ie, large polarisation and irreversible capacity) shown by these electrodes. Nevertheless, considering the huge capacity of displacement electrodes, even at their current stage, such composite electrodes may find an immediate use as a source of lithium in conventional cells which suffer from irreversible capacity losses.

In this chapter the possibility of lithium-containing displacement reaction electrodes will be explored. It will be shown that a material made of a composite of lithia and a transition metal is indeed electrochemically active. This is the first example of electrochemical displacement electrodes that contain active lithium as made.

6.2 SYNTHESIS OF LITHIUM CONTAINING DISPLACEMENT REACTION ELECTRODES

Lithia-transition metal composites were synthesized by ball-milling. The ball milling was carried out with a SPEX 8000D mixer mill in 64ml vials containing two 0.5" ball bearings. Both vial and balls were of hardened steel. The vials were charged and sealed in a helium atmosphere with 3.3 g of Li_2O (97%, Aldrich) and either Fe (chip, 99.98%, Aldrich) or Co (-100 mesh, 99.9+%, Aldrich) in a 1:1 molar ratio. The samples were then milled continuously for 16 hours. Electrodes were made in a helium filled glovebox using the method employed to make air-sensitive electrodes described in section 2.1. Curiously, all electrodes made in this manner with ball-milled Li_2O caused electrode slurry to instantly gel, forming a jelly-like mass. This may be due to highly reactive sites on the freshly milled Li_2O. Powder XRD of the samples was also performed under a helium atmosphere using the gas-tight sample stage described in section 2.3.1.

6.3 EXPERIMENTAL RESULTS

6.3.1 XRD Studies of the Li_2O/Co and Li_2O/Fe Composites

Figures 6.1 and 6.2 show the XRD patterns and the Rietveld refinements to the Li_2O/Fe composite and the Li_2O/Co composite respectively. The results of the fits are given in tables 6.1 and 6.2. The Li_2O/Fe composite XRD pattern was in excellent agreement with the refinement that assumed a mixture Li_2O and α-Fe. The Li_2O lattice constant was allowed to vary, but its refined value is not significantly different than the literature values. From the peak widths in the XRD pattern the average grain size for the

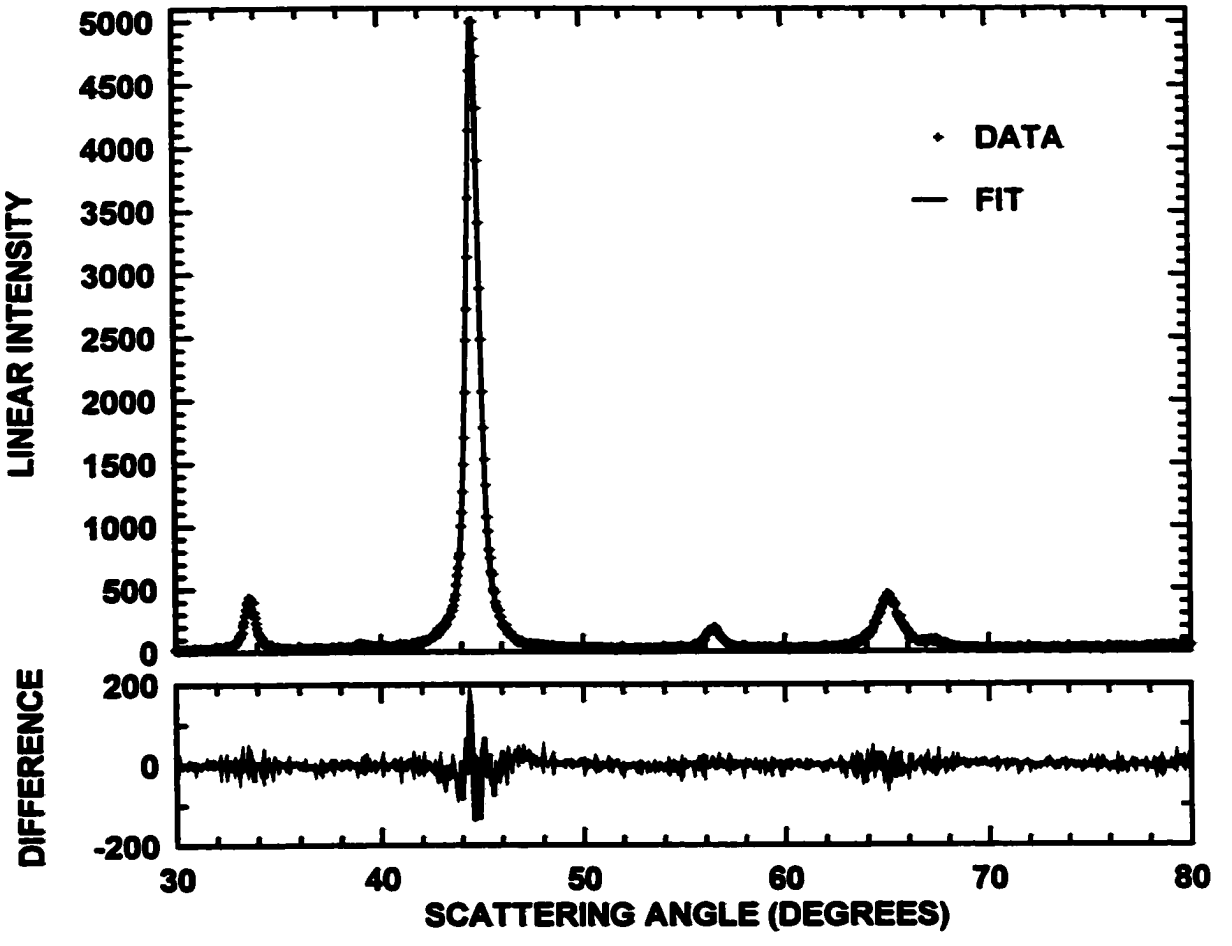

Figure 6.1 Rietveld refinement to the XRD pattern of the a 1:1 molar mixture of Li_2O and Fe which was ball milled for 16 hours.

Table 6.1 Results of the Rietveld refinement for the ball milled Li_2O/Fe sample. Overall χ^2 for the fit was 2.739.

phase	*symmetry*	*Z*	*refined lattice parameter (Å)*	*lattice parameter (Ref. [94]) (Å)*	*Bragg R*
Li_2O	$Fm\bar{3}m$	*2*	*4.615*	*4.619*	*2.86*
α-Fe	$Im\bar{3}m$	*2*	*2.869*	*2.8665*	*1.11*

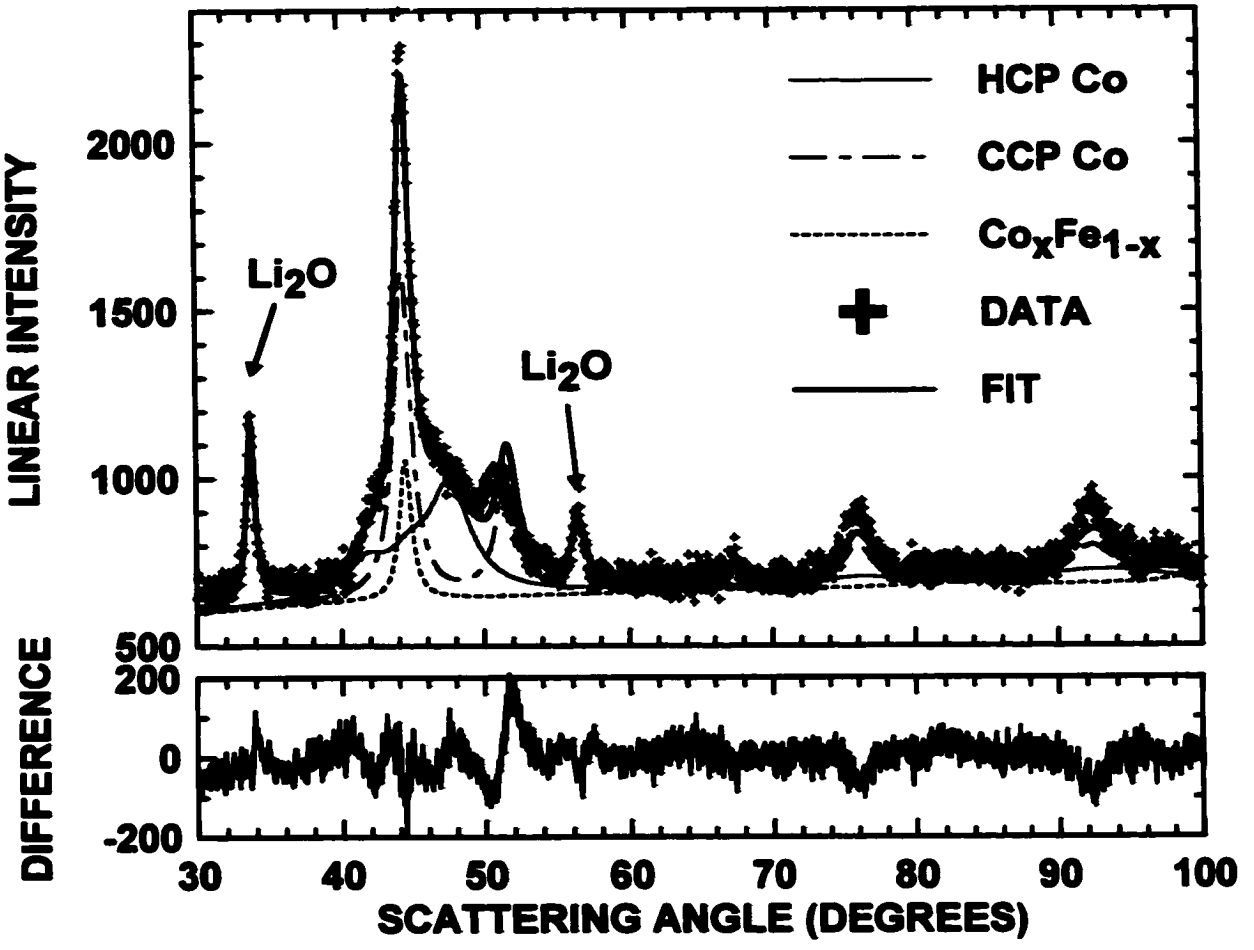

Figure 6.2 Rietveld refinement to the XRD pattern of the 1:1 molar Li_2O/Co composite which was ball milled for 16 hours. Shown also in the graph are the contributions from individual phases that were used to obtain the fit. The only visible features from Li_2O in the graph are the Li_2O (111) and Li_2O (022) peaks, which are indicated in the figure.

Table 6.2 Results of the Rietveld refinement for the ball milled Li_2O/Co sample. Overall χ^2 for the fit was 1.98.

phase	symmetry	Z	refined lattice parameters (Å)	lattice parameter (literature [94]) (Å)	Bragg R
Li_2O	$Fm\bar{3}m$	2	4.615	4.619	0.49
ccp-Co	$Fm\bar{3}m$	4	not refined	3.548	2.12
hcp-Co	$P6_3/mmc$	2	not refined	a = 2.505 c = 4.060	0.59
Co_xFe_{1-x}	$Im\bar{3}m$	2	2.885	2.84 - 2.86	1.90

Li_2O and α-Fe in the sample is 110 Å and 144 Å respectively.

The refinement of the Co/Li_2O composite, shown in figure 6.2, was complicated by an iron impurity in the sample that came from the milling media. To further complicate matters two phases of cobalt (an hcp and a ccp phase) normally coexist at room temperature. Also cobalt and iron can easily form bcc Co_xFe_{1-x} alloys [94]. The XRD patterns were refined by a combination of Li_2O, ccp- Co, hcp-Co and Co_xFe_{1-x} phases. The lattice constants of Li_2O and Co_xFe_{1-x} were allowed to vary. The details of the fit are given in table 6.2. The lattice constant of Li_2O is not significantly different than the literature value. The lattice constant of the Co_xFe_{1-x} phase is larger than the values for the composition range of the alloy and is even larger than that of pure α-Fe (2.8665 Å). There is probably considerable error in the lattice constant of this phase, since only one peak has a significant intensity in the pattern. Also the peak is rather small and there are a number of overlapping peaks in the region. It is difficult to tell whether this phase is from pure α-Fe or if a Co_xFe_{1-x} has been formed during milling. Although the fit gave a reasonable value of χ^2, some aspects of the fit, for instance, the poor treatment of the peak at 52° are unsatisfactory. This may be due to internal strain in the sample caused by milling. Application of the Scherrer equation to the 111 Li_2O, the 111 ccp-Co, the 010 hcp-Co and the 110 Co_xFe_{1-x} peaks gave a grain size of about 131Å for Li_2O, 59 Å for ccp-Co, 23 Å for hcp-Co and 103 Å for the Co_xFe_{1-x} phase.

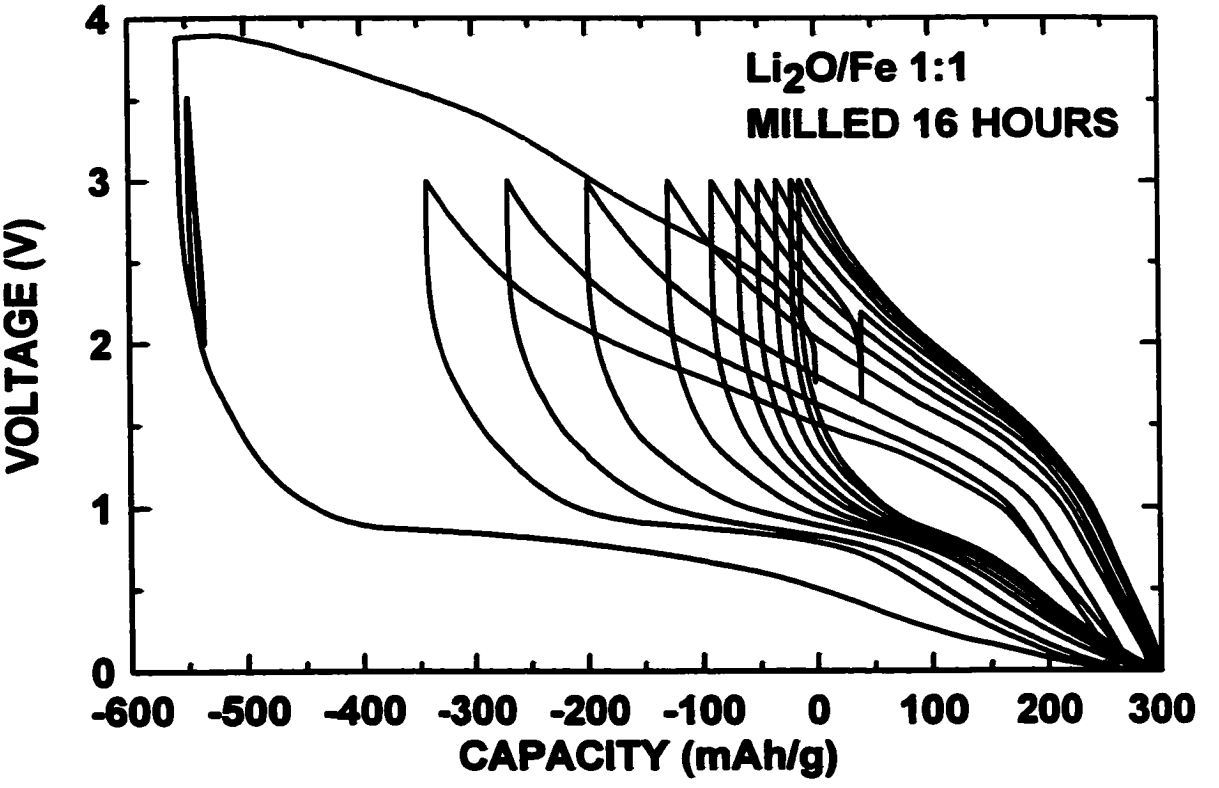

Figure 6.3 Voltage curve of the Li_2O/Fe electrode. The curve starts on the charge cycle from 0 mAh/g.

6.3.2 ELECTROCHEMICAL RESULTS

Figure 6.3 shows the voltage curve of the Li_2O/Fe composite electrode. The cycling of the cell starts on charge at 0 mAh/g on the graph. Theoretically, assuming the iron is oxidized to Fe^{3+}, one would expect a theoretical capacity of 625 mAh/g for this electrode. However the cell was switched to discharge after 550 mAh/g out of fear of iron dissolution, since the electrode has excess iron than is needed to react with the Li_2O. This is still an enormous charge capacity. The first discharge has a much greater capacity (800 mAh/g) than the first charge. This may be due to electrolyte decomposition reactions during the first discharge as was observed for the transition metal oxides in the last chapter. However, as will be shown below, this may not be the

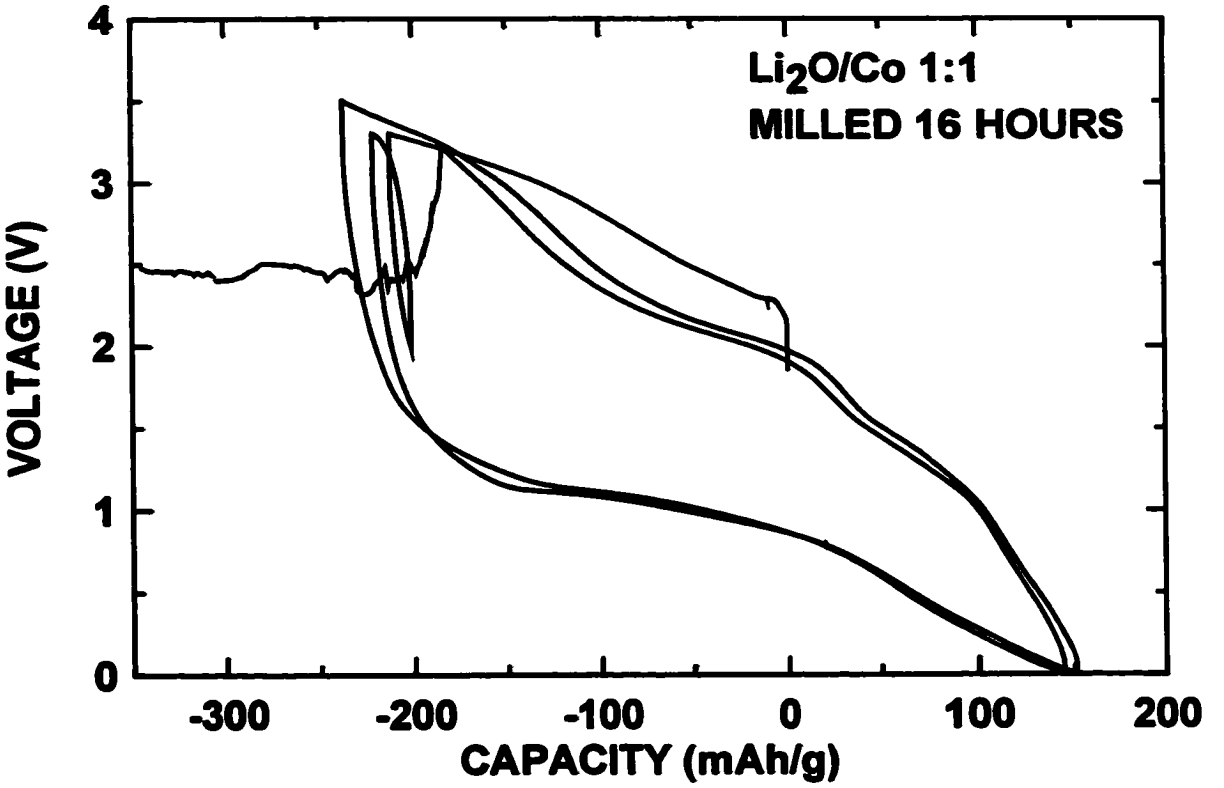

Figure 6.4 Voltage curve of the Li_2O/Co electrode. The curve starts on the charge cycle from 0 mAh/g.

case. After the first cycle the upper voltage limit was lowered to 3 V. The subsequent cycles resemble that of the transition metal oxides in the previous chapter, but show rapid capacity loss.

Figure 6.4 shows the voltage curve of the product obtained from milling Li_2O and cobalt metal. Again, cycling starts on charge at 0 mAh/g on the graph. The cycling was limited to 3.5 V to reduce the possibility of Co or iron dissolution, since because of the large iron impurity, there is also an excess of transition metal than is needed to react with the Li_2O. This gave a capacity on the first charge of 250 mAh/g. Theoretically the capacity of a Li_2O/Co composite is 603.5 mAh/g, assuming all the cobalt is oxidized to Co^{2+}. Perhaps this capacity could be obtained at higher voltages.

Like the Li_2O/Fe composite more capacity was observed on the first discharge than on the first charge. However for the Li_2O/Co milled product all of the extra capacity was recovered on the second charge. If the extra capacity on the first discharge were due to electrolyte decomposition reactions, then this would not be the case. It could also be argued that the extra capacity on discharge could be caused by a CoO impurity in the electrode (from an oxygen leak during milling, say). However from the last chapter it was shown that CoO has a large irreversible capacity. Here the cell has no irreversible capacity whatsoever.

One possible explanation of the above mystery may be found in the recently observed low voltage capacity in nanograined metals that do not alloy with lithium [96]. It was discovered that significant amounts of lithium reside in the grain boundaries of a nanograined $SnMn_3C$ electrode prepared by ball-milling. Thus perhaps during discharge of the Li_2O/Co electrode, after all of the metal has been reduced, lithium can insert in the grain-boundaries of the material, giving an extra 150 mAh/g during the discharge. Upon charge this extra lithium can apparently be removed. This may be the cause of the feature in the voltage curve at a capacity near 0 mAh/g in figure 6.4. It may also help to explain the extra capacity observed on discharge of the metal oxides in figure 5.1. Indeed a similar feature on the first charge of the CoO cell can be seen near the cell's theoretical capacity, which is indicated by the dashed line in the figure.

After two cycles with no capacity loss the Li_2O/Co cell's voltage suddenly dropped during its third charge. The voltage then became erratic. This effect seems to be common with this type of electrode. In fact an identical cell to that in figure 6.4 did not cycle at all, but the voltage showed the same erratic behaviour immediately on the first

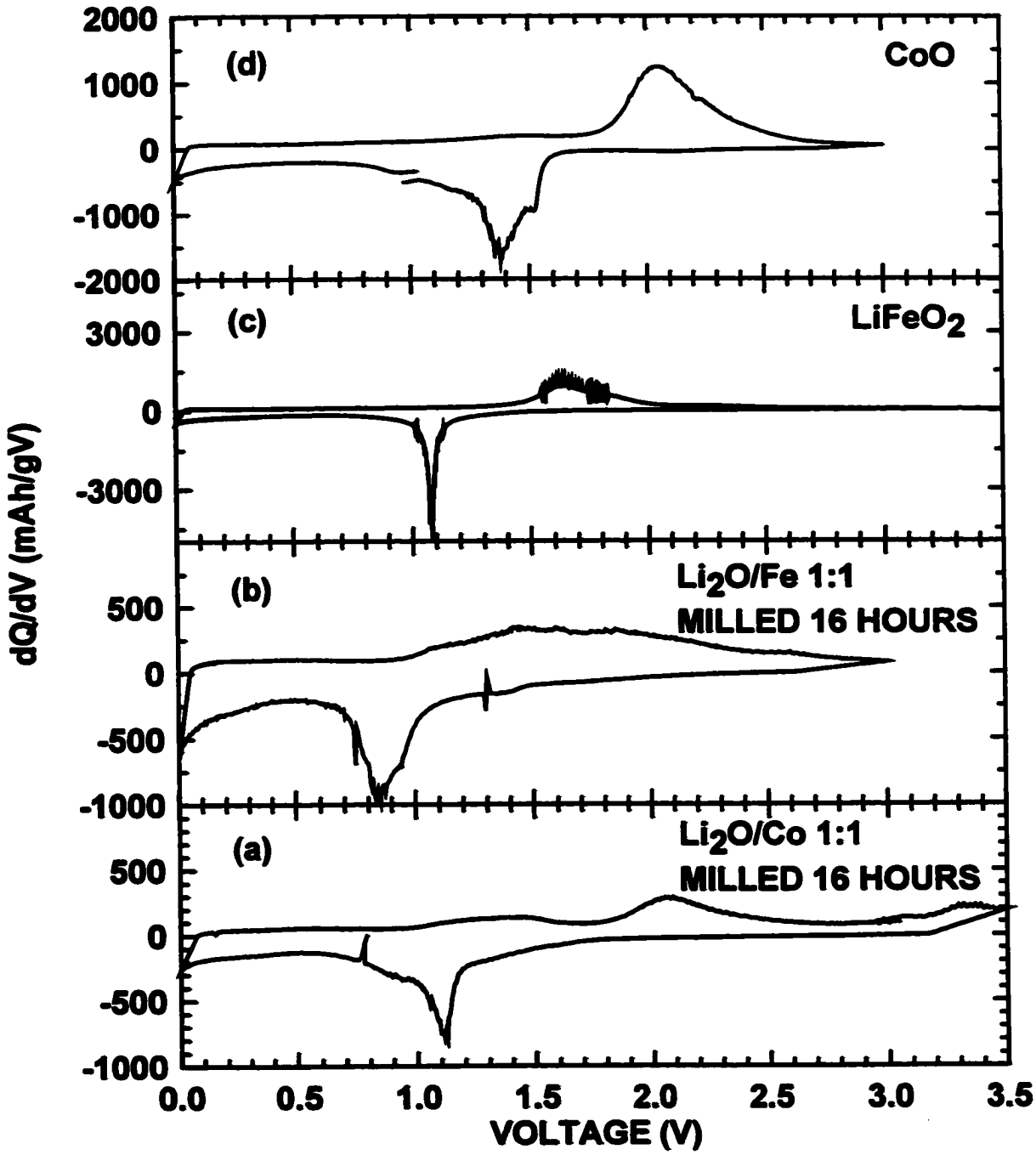

Figure 6.5 Differential capacity curves of displacement electrodes with (a),(b) and without (c),(d) active lithium. The data for (c) and (d) were taken from the voltage curves of CoO and $LiFeO_2$ shown in figure 5.1.

charge. This could be due to the dissolution of exposed metal in the composite at high voltages. Considering that iron or cobalt metal will oxidize to Fe^{2+} or Co^{2+} at voltage of 2.6 V and 2.7 V versus lithium respectively, it is rather amazing that such composite electrodes cycle at all. The complete encapsulation of the metal in Li_2O may be key to the cycling of the Li_2O/Fe and Li_2O/Co electrodes, which do not show signs of metal dissolution (for the first few cycles at least, in the case of Li_2O/Co).

Figure 6.5 shows the differential capacity curves of the second cycle of the Li_2O/Co, Li_2O/Fe cells and the $LiFeO_2$ and CoO cells of the previous chapter. The Li_2O/Fe cell shown in figure 6.5(b) has very broad features compared to the $LiFeO_2$ cell's differential capacities in figure 6.5(c). Also it is obvious that the discharge peak is at different voltages in both cells. Similarly it is difficult to make any comparisons between the Li_2O/Co cell and the CoO cell in figures 6.5(a) and 6.5(d), respectively. Perhaps different processes are occurring in the composite electrodes than the metal oxide electrodes or the differences in the voltage curves may be due to hampered lithium diffusion in the composite electrodes which cause a larger polarization in these cells compared to the metal oxide cells.

6.4 CONCLUSIONS

In this chapter it was shown that a composite of transition metal and lithium oxide can be used as an electrode material which contains active lithium as made. These electrode materials were produced by mechanical alloying of Li_2O and transition metals. This produced composites with grain sizes of about 100 Å. These electrodes possess an enormous first charge capacity which may make them immediately attractive as a source of lithium in cells which suffer from irreversible capacity losses. On the other hand the

cycling characteristics of the Li_2O/metal composites themselves are poor. The Li_2O/Fe cell showed significant capacity fading during cycling, while the Li_2O/Co cell's voltage became erratic after the second cycle, possibly because of the dissolution of the metal in the composite during charge. Interestingly, however, the Li_2O/Co cell did not have any irreversible capacity during cycling. This brings into question the nature of the extra capacity observed during the first discharge of the metal oxide electrodes in the last chapter. One possibility is that this capacity is due to the reversible insertion of lithium into grain boundaries, as has been previously observed in nanostructured alloys [96].

From comparing the differential capacity curves of the Li_2O/metal composites with the metal oxides from the last chapter, it is difficult to tell whether both electrodes follow the same mechanism. An in-situ XRD and Mössbauer study such as the one presented in the last chapter, should be undertaken to understand more fully the reactions that are taking place. More work also is needed to solve the poor cycling characteristics of these composites if they are to have industrial relevance as electrode materials. For instance it was mentioned that total encapsulation of the metal in Li_2O may be important to the functioning of these electrodes. A way to ensure this might be to use sputtering to deposit multilayers of Li_2O and metal, say, on an electrode substrate. Also, inorganic lithium compounds other than Li_2O should also be tried. For instance it was shown in chapter 1 that NiF_2 can be used as a high capacity electrode material versus a lithium metal anode. In this cell the lithium anode is used as the source of lithium for the cell. In a lithium ion cell the cathode must be the source of lithium when the cell is made. Thus a NiF_2 cathode is not compatible with lithium ion technology. However a composite of 2LiF/Ni would be a source of lithium as made and thus would be a cathode compatible

with lithium ion technology. Furthermore, as shown in figure 1.3, such an electrode theoretically would have an enormous advantage in energy density over today's intercalation technology. Composites of materials with large anions, for instance, a Li_2CO_3/metal composite would also be interesting, as the delocalized charge in these anions may improve ion conduction during cycling. Composites with mixed anions might also achieve this by introducing defects. This may improve the electrical conductivity of the electrode as well. Clearly the opportunities for research here are huge.

Chapter 7

The Reactivity of Binary Lithium Compounds with Transition Metal Ions in Solution

7.1 BACKGROUND

Many solid-state materials are made via exchange (or metathesis) reactions. These reactions can be of the single displacement (AB + C → A + BC) or double displacement (AB + CD → AC + BD) type. Common examples of such reactions are, for example, the synthesis of transition metal nitrides [97]:

$$MX_n + n/3Li_3N \rightarrow MN + nLiX + (n/3 - 1)/2\ N_2 \qquad (7.1)$$

or the carbothermic route to metal formation:

$$MO_{2x} + xC \rightarrow M + xCO_2. \quad (7.2)$$

Both of the above reactions must be carried out at very high temperatures (>1000°C) in order to overcome the large diffusion barriers in the solid phase. Solution based exchange reactions are also known in which metal halides react with alkali compounds to form chalcogenides and pnictides [98,99]:

$$TiCl_4 + Li_2S \rightarrow TiS_2 + 4LiCl \text{ (in THF, PC or AN)} \quad (7.3)$$

$$GaCl_3 + Na_3P \rightarrow GaP + 3NaCl \text{ (in diglyme)} \quad (7.4)$$

where THF = tetrahydrofuran and AN = acetonitrile. Such reactions can occur quickly at room temperature or under reflux conditions. Reaction 7.3 was also found to proceed readily for chlorides of Zr, Hf or V giving the analogous chacogenides. The products of these reactions were reported to be amorphous and often formed a suspension [98]. Thus far such reactions have not been observed for transition metal oxides. However in chapter 5 it was suggested that such exchange reactions might be the mechanism for the observed capacity in lithium versus transition metal oxide cells. To give further credibility to this argument, the possibility that transition metal oxides may be formed by exchange reactions with lithia in nonaqueous solvents is explored in this chapter. This possibility is firstly evaluated on a purely theoretical basis in section 7.2. Other binary compounds that might be formed by such reactions are also theorised in this section. In section 7.3 the results of some exchange reactions between Li_2O and iron and cobalt salts in nonaqueous solvents are presented.

7.2 THEORETICAL CONSIDERATIONS FOR EXCHANGE REACTIONS

To calculate the free energy of an exchange reaction in solution such as equation (7.3) or (7.4), a convenient reference free energy state is the standard state of the ions in

solution. Since the anion (the sulfur in the case of equation (7.3)) always stays in the solid phase, it is useful here to define the free energy of formation of a binary material according to the reaction:

$$aM^{n+} + ane^- + \frac{b}{c}X_c \rightarrow M_aX_b. \tag{7.5}$$

where X_c is the anion in its standard neutral state and M^{n+} is the aqueous cation.* This free energy of formation will be referred to here as the electrolytic free energy of formation, or ΔG_{el} and is equal to:

$$\Delta G_{el} = \Delta G_f^o(M_aX_b) - a\,\Delta G_f^o\left(M^{n+}\right) - aRT\ln a_{M^{n+}} \tag{7.6}$$

where $a_{M^{n+}}$ is the activity of the M^{n+} ion in solution If it is assumed that the activity of the ions in solution is limited to be between 0.1 and 3, then the maximum absolute value of the last term in the above equation will be about $RT\ln(9)$ = 5.4 kJ/mol (although the activity coefficient of a single ion in solution is not a definable quantity, it is assumed that a suitable anion in solution exists). To a first approximation the last term will be ignored and ΔG_{el}^o will be defined as:

$$\Delta G_{el}^o = \Delta G_f^o(M_aX) - a\Delta G_f^o\left(M^{n+}\right). \tag{7.7}$$

This is equivalent to the free energy change of equation (7.5) at constant unit activity for all ions. This approximation will be even better when the differences between electrolytic free energies are taken to calculate the free energies for ion exchange

---

* Although non-aqueous solvents are used in this chapter the thermodynamic data for cations in various non-aqueous solvents is difficult to obtain. Thus aqueous ion thermodynamic data are used here as a first approximation.

*Table 7.1 The aqueous cation formation free energy, free energy of formation and electrolytic free energy of formation of a number of binary compounds. All values are in kJ/mol. $\Delta G_f(M^{n+})$ data derived from EMF data in ref. [100], $\Delta G_f(M_aX_b)$ from ref [101], except for * which was interpolated from the data in ref. [102].*

Compound	$\Delta G_f(M^{n+})$	$\Delta G_f(M_aX_b)$	$\Delta \overline{G}^o_{el}$
Li_2O	-293.3	-562.1	24.5
K_2O	-282.8	-322.1	121.7
Na_2O	-261.5	-379.1	71.9
Cu_2O	50.23	-147.9	-124.2
Ag_2O	77.1	-11.2	-82.8
CuO	66.0	-129.8	-97.9
NiO	-49.6	-211.9	-81.1
CoO	-54.0	-214.0	-80.0
FeO	-86.3	-245.3	-79.5
ZnO	-147.0	-318.5	-85.8
MnO	-228.7	-363.2	-67.2
TiO	-314.5	-495.3	-90.4
Mn_2O_3	103.2	-881.7	-181.4
Fe_2O_3	-10.7	-743.5	-120.4
Cr_2O_3	-215.4	-1053.1	-103.7
Al_2O_3	-481.1	-1673.4	-118.5
Li_2S	-293.3	-421.6	82.5
NiS	-49.6	-85.2	-17.8
FeS	-86.3	-156.2	-35.0
Li_3N	-293.3	-128.6	250.4
TiN	-314.5	-308.9	1.9
AlN	-481.1	-287.0	64.7
LiF	-293.3	-588.7	-295.3
CuF_2	66.0	-491.6	-278.8
MnF_2	-49.6	-752.8*	-351.6
CoF_2	-54.0	-656.6	-301.3
FeF_2	-86.3	-663.2	-288.5
NiF_2	-228.7	-610.6*	-191.0
FeF_3	-10.7	-972.3	-320.5
TiF_3	-481.1	-1361.9	-293.6

reactions.

Table 7.1 lists the values of $\Delta\overline{G}^{o}_{el}$, which is the eletrolytic free energy of formation per equivalent, for a number of binary compounds. The compounds are grouped according to anion with further subgroups according to cationic charge. Within the subgroups the compounds are listed in order of decreasing cation formation free energy. The most striking aspect of table 7.1 is that, with few exceptions, $\Delta\overline{G}^{o}_{el}$ is relatively constant within each subgroup of compounds. The reason for this is, as $\Delta G_f(M^{n+})$ decreases in going from top to bottom in a subgroup, this means that the electron affinity of the cation must also be increasing. It follows then that the binary compounds which are formed tend to be more stable and thus $\Delta G_f(M_aX_b)$ is also becoming more negative as one goes from the top to the bottom of a subgroup. These changes tend to cancel themselves in the difference in equation (7.7). Notable exceptions are Ag_2O and Cu_2O. In these compounds the bonding is more covalent and thus $\Delta G_f(M_aX_b)$ is more negative than one would expect if the interactions were chiefly ionic, as is the case for the alkali metal oxides. Thus (keeping in mind that one should be wary of comparing highly ionic compounds to covalent ones) binary compounds with like anions and with the same cation oxidation state tend to have the same values of $\Delta\overline{G}^{o}_{el}$. Another trend which can be seen from the table is that compounds with more electronegative anions tend to have more negative values of $\Delta\overline{G}^{o}_{el}$. This is simply because compounds with more electronegative anions tend to have more negative free energies of formation.

A table of $\Delta\overline{G}^{o}_{el}$ is useful since the difference between values of $\Delta\overline{G}^{o}_{el}$ for any two compounds with the same anion will give the free energy per equivalent for a cation exchange type reaction between the compounds. For instance subtraction of the value of $\Delta\overline{G}^{o}_{el}$ for CoO from that for Li_2O in table 7.1 gives a value of -104.5 kJ/mol·eq (or -209.0 kJ/mol) for the reaction:

$$Li_2O + Co^{2+}_{(aq)} \rightarrow 2Li^{+}_{(aq)} + CoO. \qquad (7.8)$$

This reaction is in fact exactly that suggested in chapter 5 to be occurring at the cathode of a Li/CoO cell during charge. From figure 5.1 the cell reaction for the Li/CoO couple occurs at an average voltage of about 1.75 V versus lithium or about -337.7 kJ/mol. From this it is possible to determine the free energy of the reaction at the cathode as follows:

$Li_2O + Co \rightarrow \beta\text{-}CoO + Li$	385.9 kJ/mol	(7.9)
$2Li \rightarrow 2e^- + 2Li^{+}_{(aq)}$	2 × (-293.3) kJ/mol	
$Co^{2+}_{(aq)} + 2e^- \rightarrow Co$	54 kJ/mol	
$Li_2O + Co^{2+}_{(aq)} \rightarrow \beta\text{-}CoO + 2Li^{+}_{(aq)}$	-194.9 kJ/mol.	

The value is very close to that calculated for equation (7.8) and provides further evidence that an exchange reaction might be occurring in these cells.

Other compounds may also be formed by exchange reactions. According to table 7.1, all exchange reactions between Li_2O, Li_3N and Li_2S and the transition metal ions listed in the table are energetically favourable. Such reactions will not be favourable, or not very favourable, for displacement reactions involving LiF. Of course kinetic factors

must also be considered. For reaction (7.8) to take place both the lithium and cobalt ions

Table 7.2 A list of the ionic crystalline radii for a number of cations. From ref [100].

Ion	*Charge*	*Radius (Å)*
Al	*+3*	*0.51*
Cr	*+3*	*0.63*
Cu	*+2*	*0.72*
Fe	*+2*	*0.74*
Fe	*+3*	*0.64*
Li	*+1*	*0.68*
Ni	*+2*	*0.69*
Ti	*+2*	*0.94*
Ti	*+4*	*0.68*

must be mobile in the solid. Fortunately many binary lithium compounds have structures which exhibit rather high lithium ion conductivities. Li_2O and Li_2S are based on the antifluorite structure (its structure is shown in figure 5.30). Materials with the fluorite structure, in which the oxygen are arranged in the in the tetrahedral sites of a fcc cation lattice, such as ZrO_2 and ThO_2, are well known oxygen conductors [103]. In the antifluorite structure the cations are in the tetrahedral sites and have been shown to be cation conductors, such as Li_2O doped with trivalent metal ions [103]. This may explain the relative ease at which exchange reactions occur with Li_2S. The structure of Li_3N consists of layers of lithium sandwiched between Li_2N layers. This structure allows for a large degree of lithium ion mobility and gives Li_3N a high room temperature ion conductivity of 2.5×10^{-3} S/cm [103], which is similar to that of nonaqueous liquid electrolytes. Thus exchange reactions may also be possible with Li_3N. Besides ionic diffusion the size of the ions must also be considered. Again it is fortuitous that many

transition metal ions are about the same size or even smaller than Li^+, as listed in table 7.2. This makes the possibility for ion exchange for a number of compounds seem even more likely.

7.3 SOME REACTIONS OF LITHIA WITH TRANSITION METAL IONS IN POLAR NONAQUEOUS SOLVENTS

7.3.1 The Reaction of Li_2O with $CoCl_2$ and $FeCl_3$ in Anhydrous Methanol

An exchange reaction between Li_2O and $CoCl_2$ or $FeCl_3$ in anhydrous methanol was attempted. Li_2O (96.2%), $CoCl_2$ (97%), $FeCl_3$ (97%) and anhydrous methanol (99.8%) were all obtained from Aldrich. Methanol was chosen for the reaction since it is a good solvent for LiCl (42.36 g /ml [100]). Samples from the various reactions will be designated by their reactants, solvent and reaction temperature respectively, with the following notation: BM-Li_2O/$FeBr_3$/MeOH/25C. In this hypothetical example MeOH stands for methanol and 'BM' indicates that ball-milled Li_2O was used in the reaction. All reactions were carried out in an argon-filled glovebag. For each reaction 1 g of Li_2O was placed into a 125 ml Nalgene bottle, then 20 % excess transition metal salt was added according to the following stoichiometry:

$$Li_2O + CoCl_2 \rightarrow 2LiCl + CoO \tag{7.10}$$

$$Li_2O + \frac{2}{3}FeCl3 \rightarrow 2LiCl + \frac{1}{3}Fe_2O_3 \tag{7.11}$$

This corresponds to 5.214 g of $CoCl_2$ for reaction (7.10), and 4.342 g of $FeCl_3$ for reaction (7.11). 100 ml of anhydrous methanol was then added while stirring. In each reaction this produced a significant amount of heat, even causing the methanol to boil slightly. Both reactions occurred within a few seconds. For the reaction with $CoCl_2$ a

pink solid was formed, while the methanol remained clear, indicating that all the cobalt was in the solid. For the reaction with $FeCl_3$ an orange solid was formed while the methanol remained red, indicating that all the iron was not used in the reaction. The reactants were left overnight, with no noticeable change the next day. The solids were then isolated by centrifuge, washing repeatedly with methanol. The solids were then dried under vacuum for several hours at room temperature.

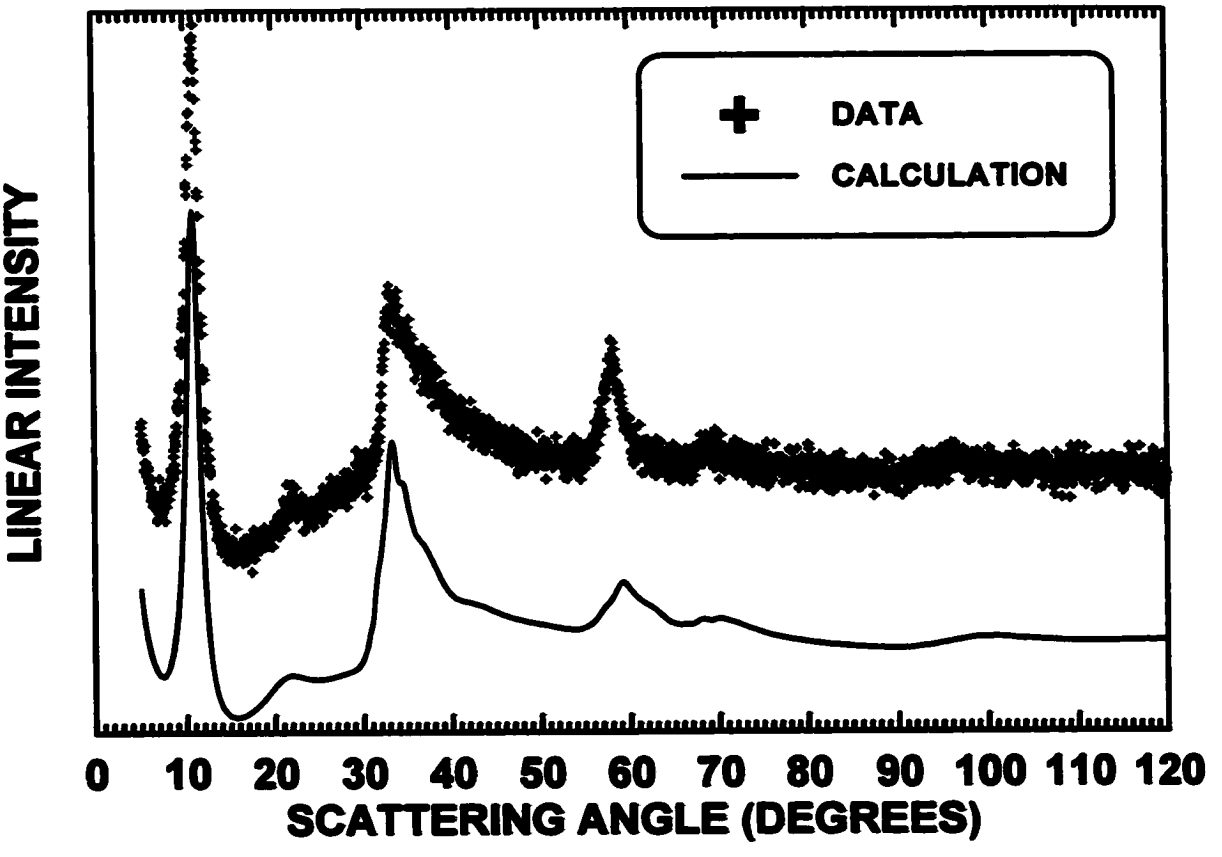

Figure 7.1 The XRD pattern of $Li_2O/CoBr_2/MeOH/25C$. Also shown is a calculation of the XRD pattern of a finite randomly stacked sequence of finite triangular lattices of cobalt atoms.

XRD spectra were taken with the air sensitive sample stage described in section 2.2.4. Figure 7.1 shows the XRD pattern of $Li_2O/CoBr_2/MeOH/25C$. This pattern could

not be matched to any of the known compounds in our PDF database [104]. The XRD pattern is very similar to that observed for turbostratically disordered carbons. A program developed in our lab by Hang Shui to model the XRD patterns of carbons with stacking faults was used to model the XRD pattern in figure 7.1 [20]. The program and the meaning of its various parameters are described in section 2.2.2. The program was modified slightly to fit the data here. Firstly the atomic form factor was changed from carbon to that of Co^{2+}. Secondly, it was found that a good fit was obtained if the in-plane structure factor was changed from that of a graphite lattice to a triangular lattice. A calculation of the XRD pattern of a random sequence of A, B and C layers of such planes is also shown in figure 7.1 and models the data quite well, yielding an overall goodness of fit of $\chi^2 = 2.28$. Parameters from the fit are listed in table 7.3. The fit suggests that most of the scattering in $Li_2O/CoBr_2/MeOH/25C$ is due to finite layers of Co atoms

*Table 7.3 Parameters used in the calculation of the XRD pattern of finite-sized randomly stacked layers of Co atoms arranged in a triangular lattice. *Fixed during the refinement.*

Parameter Description	*Value*
a, In plane Cell constant (Å)	*3.121 (6)*
002, Interlayer Spacing (Å)	*7.98 (1)*
L_a, Layer Extent (Å)	*46 (6)*
M, Total Number of Layers	*5.7 (7)*
σ_M, Width of M Distribution	*4.6 (1)*
ζ, In plane strain	*0.040 (9)*
$\sqrt{\langle\delta\rangle}$, Inter Plane Strain (Å)	*1.15 (1)*
P, Probability of Random Stacking	*0**
g, Fraction of Organized Layers,	*0**

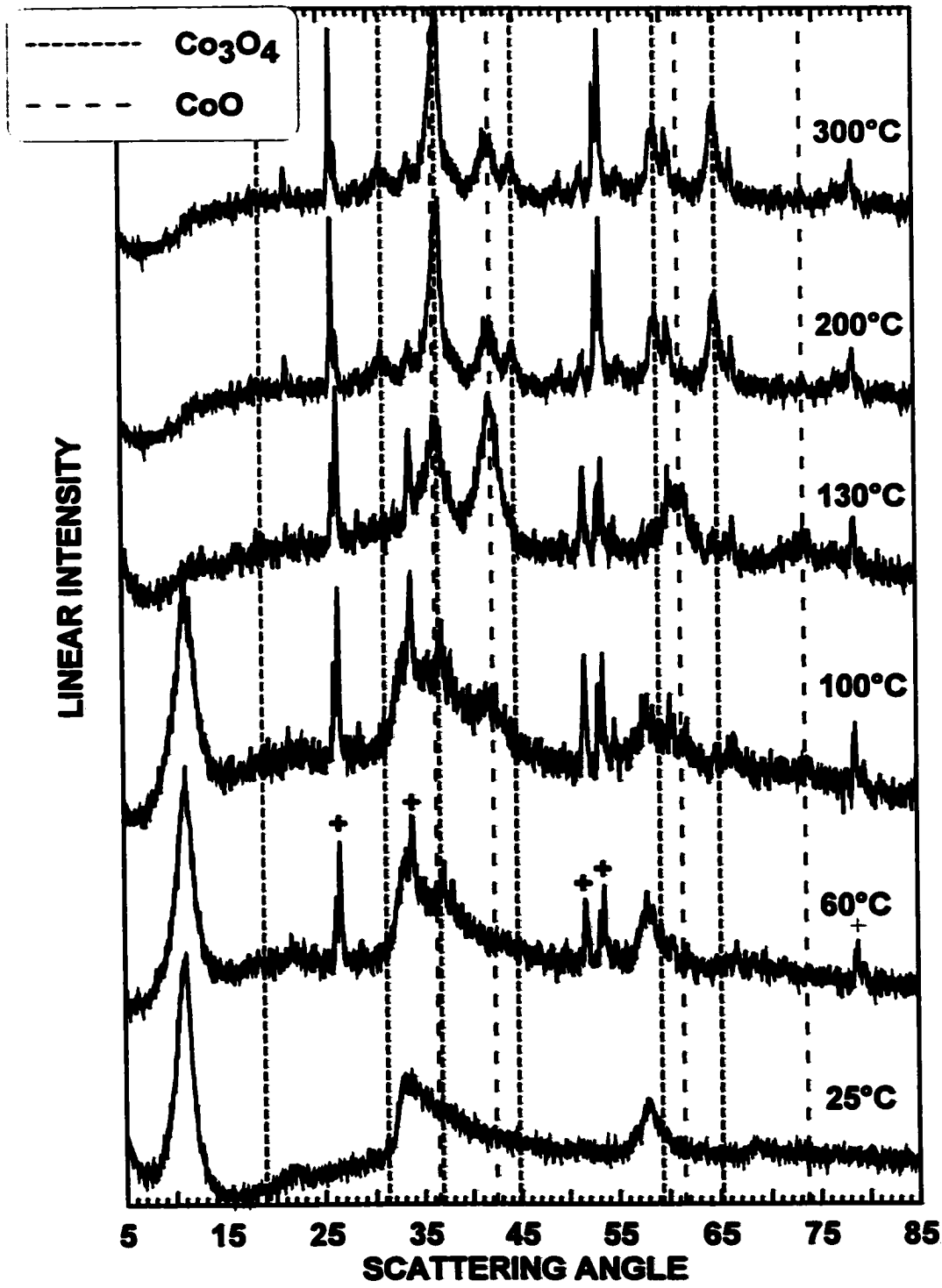

Figure 7.2 XRD patterns of $Li_2O/CoBr_2/MeOH/25C$ taken at different temperatures. Spectra measured above 25°C were measured with the high temperature sample stage described in section 2.2.4. + indicates peaks from the high temperature sample stage.

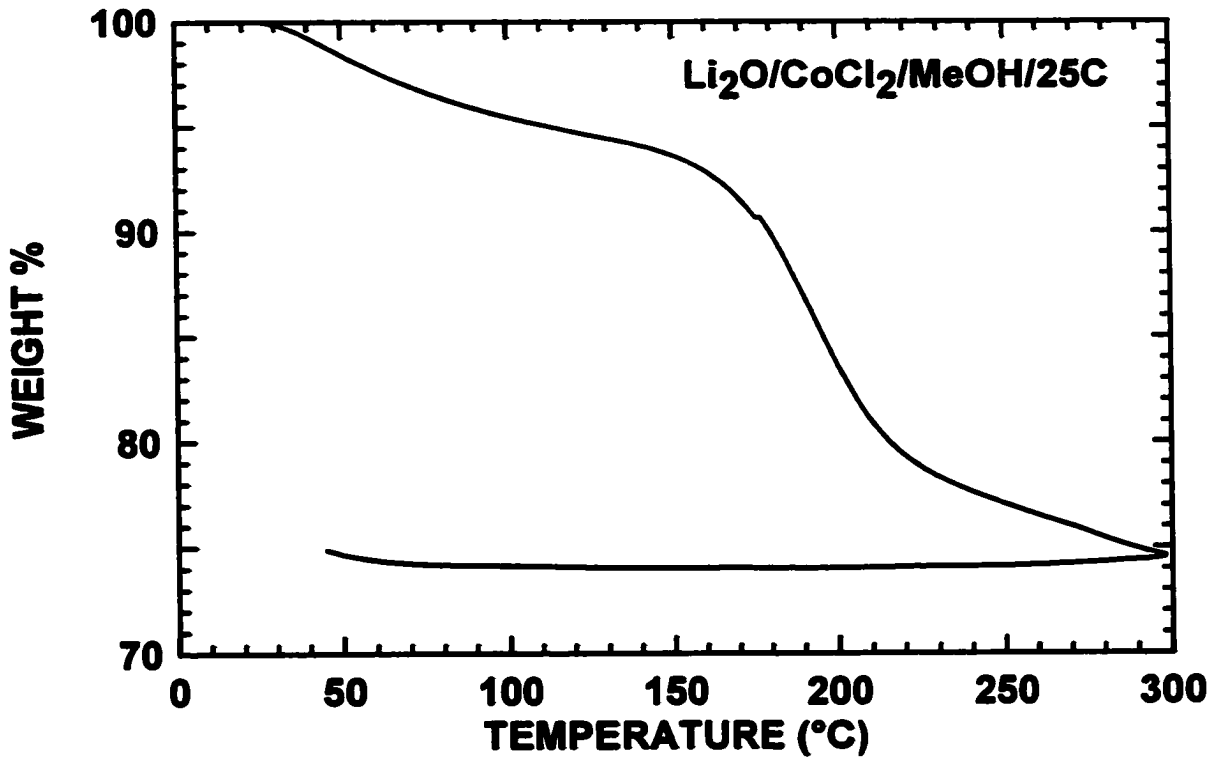

Figure 7.3 TGA weight loss curve in argon gas of $Li_2O/CoBr_2/MeOH/25C$.

arranged in a triangular lattice, randomly stacked with a large inter-layer spacing of about 8 Å.

Figure 7.2 shows XRD patterns of $Li_2O/CoBr_2/MeOH/25C$ taken at different temperatures in the high temperature XRD stage described in section 2.2.4. Starting immediately at 60°C peaks from α-CoO appear. At 130°C the superstructure peak suddenly disappears and the structure has completely converted to α-CoO. At higher temperatures the α-CoO converts to Co_3O_4, indicating that some oxygen is present in the sample stage. Figure 7.3 shows a TGA weight loss curve of $Li_2O/CoBr_2/MeOH/25C$ in argon gas. At about 150°C there is a large weight loss in the sample. This weight loss is close to the temperature at which the formation of α-CoO was observed by XRD.

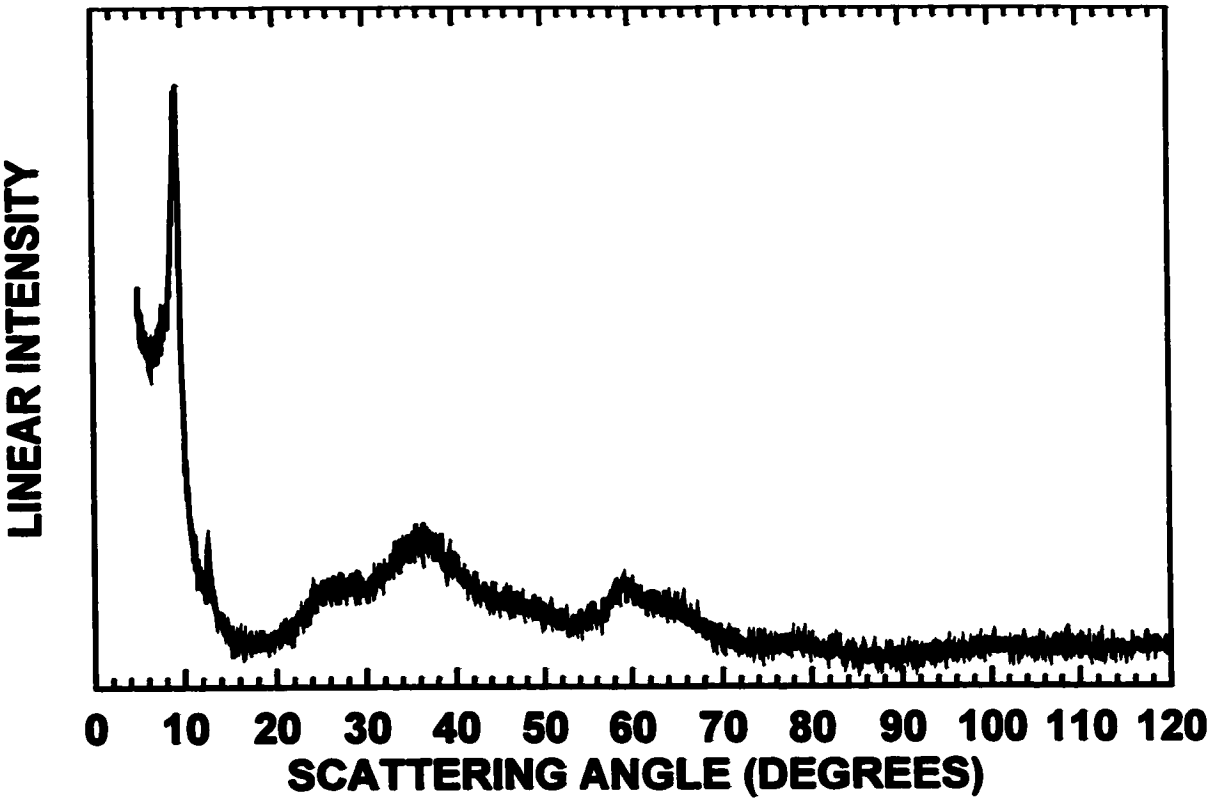

Figure 7.4 XRD pattern of $Li_2O/FeCl_3$/MeOH/25C.

Figure 7.4 shows the XRD pattern of $Li_2O/FeCl_3$/MeOH/25C. The pattern is similar to that for $Li_2O/CoBr_2$/MeOH/25C, except that the *002* peak is missing. This might happen if the structure were made up of widely spaced double layers of iron, however the structure of this material has not yet been elucidated. Figure 7.5 shows the XRD pattern of $Li_2O/FeCl_3$/MeOH/25C at different temperatures, as the sample was heated in the high-temperature XRD stage. As the sample is heated the low angle peak at about 8° becomes smaller and finally disappears at 200°C. At the same time the TGA weight loss curve for $Li_2O/FeCl_3$/MeOH/25C, which is shown in figure 7.6 shows a large (~70%) continual weight loss in the sample starting from the moment of heating to 275°C. At 300°C the structure starts to decompose and peaks from Fe_2O_3 form in the

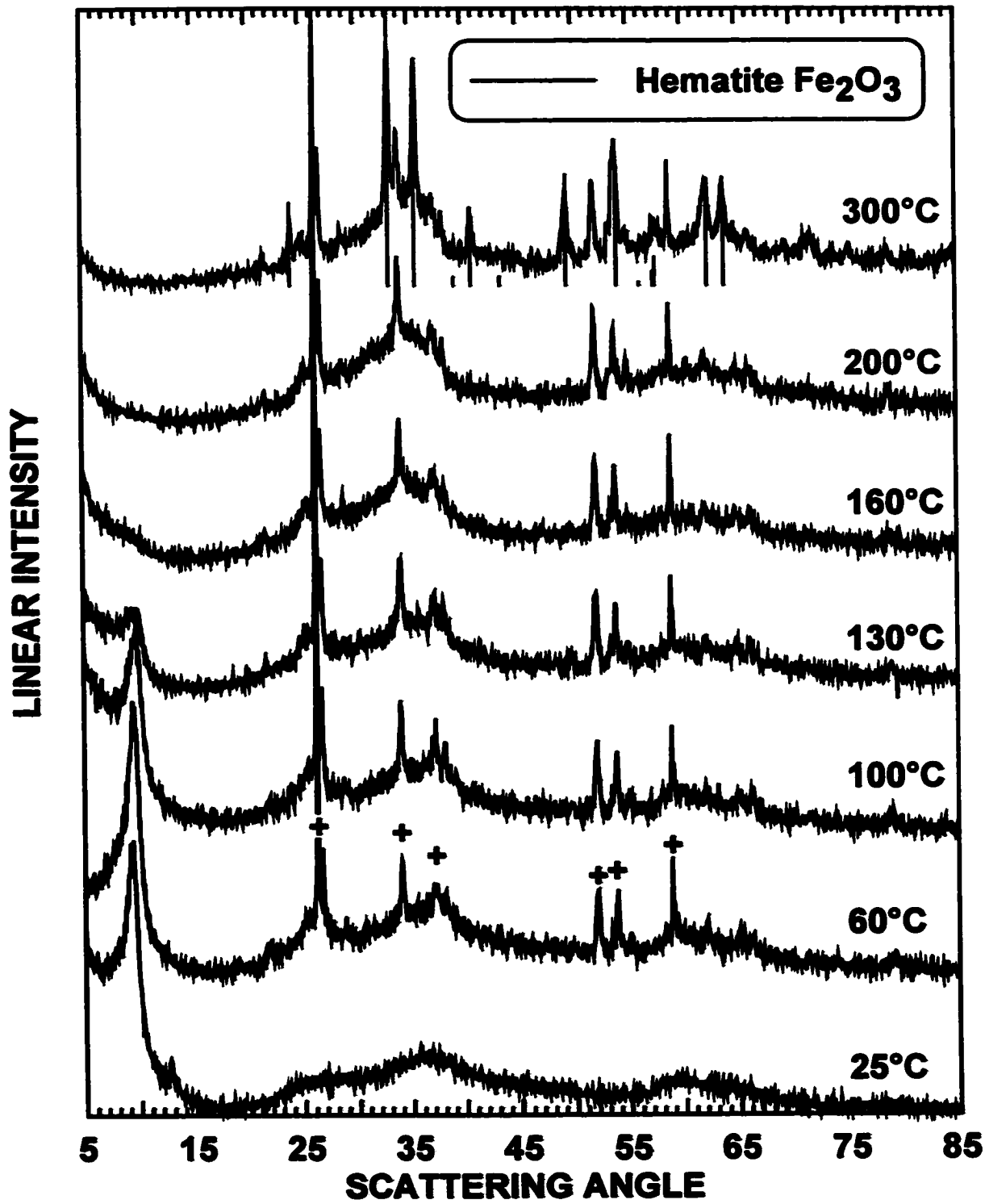

Figure 7.5 XRD patterns of Li_2O/$FeCl_3$/MeOH/25C taken at different temperatures. Spectra measured above 25°C were measured with the high temperature sample stage described in section 2.2.4. + indicates peaks from the high temperature sample stage.

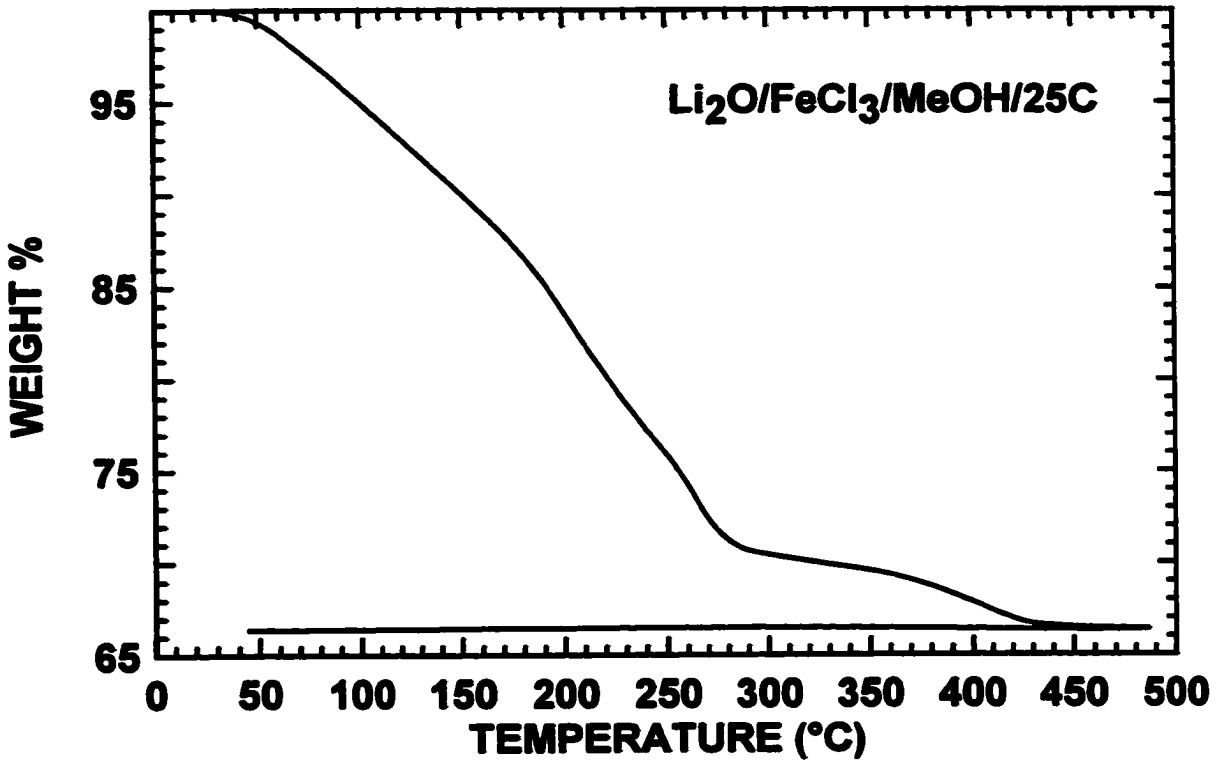

Figure 7.6 TGA weight loss curve in argon gas of $Li_2O/FeCl_3/MeOH/25C$.

XRD pattern.

After the above experiments it was noticed that a large amount of Li_2O (at least 5 g/100 ml) could dissolve in methanol. A 10 ml solution of 0.5 g Li_2O in 10 ml of methanol was left overnight in a glovebox antechamber, to remove the methanol. The XRD pattern of the recovered solids, shown in figure 7.7, match those of lithium methoxide. Alkoxide formation has been reported for reactions between alkali hydroxide and alcohols [105]:

$$M(OH) + ROH \rightleftharpoons M(OR) + nH_2O. \qquad (7.12)$$

It is not wholly surprising that lithium methoxide was formed. If there was even a trace amount of water present in the methanol it would react with Li_2O to make LiOH. This would then initiate reaction (7.12), which would then produce more water. Thus all the

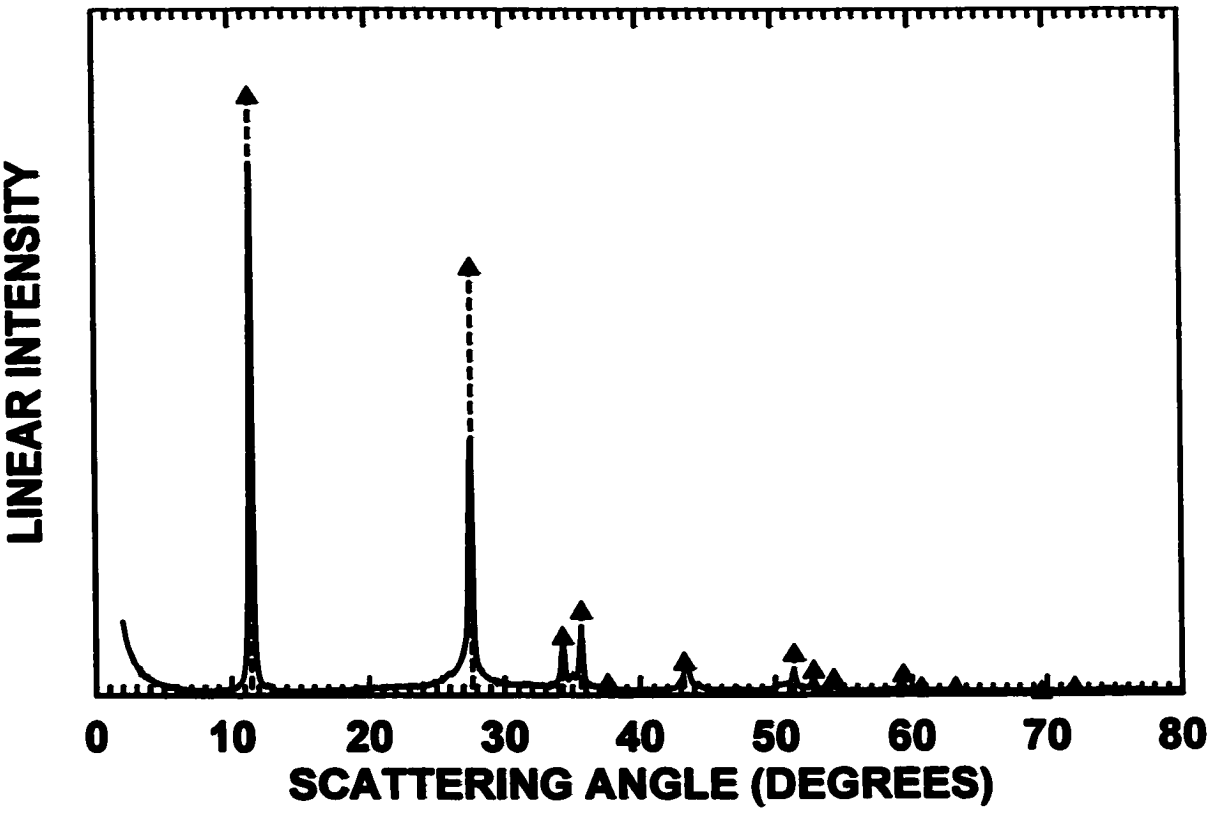

Figure 7.7 An XRD pattern of the solids recovered from a solution of Li_2O in methanol, after the methanol was evaporated. The identified peaks are those of lithium methoxide.

Li_2O could be consumed, as was observed, even if a small amount of water was present.

Reactions between transition metal halides and lithium alkoxides in their parent alcohol readily form transition metal halo-alkoxides which are often coordinated with methanol [105]. For example [106]:

$$4FeCl_3 + 6LiOMe + 4MeOH \rightarrow Fe_4Cl_6(OMe)_6 \cdot 4MeOH + 6LiCl, \qquad (7.13)$$

however the structure of these compounds has not yet been reported. It has been suggested that transition metal alkoxides do form structures made from infinite layers as suggested here [105]. These compounds also form metal oxides when thermally decomposed in an inert atmosphere [105]. It is most likely that the reactions described in this section produced metal halo-alkoxides and do not represent exchange reactions with

lithium oxide. For this reason the above reactions were repeated in aprotic solvents in which Li_2O is stable.

7.3.2 Reactions Involving Li_2O with Fe^{3+} and Co^{2+} Ions in Propylene Carbonate

Ion exchange type reactions with Li_2O in propylene carbonate (PC) (Aldrich anhydrous, 99.7%) were attempted. PC was used since it is an aprotic solvent in which Li_2O is stable. All reactions and sample handling were carried out in a helium-filled glovebox, to minimise water impurity. Since the solubility of LiCl is very small in PC, $FeBr_3$ (Alpha, anhydrous 98+%) and $CoBr_2$ (Alpha, anhydrous, 73.05% Br) were used for the transition metal salts. For each reaction 2.2 g of $CoBr_2$ (or 2.0 g of $FeBr_3$) was slowly added while stirring to a 125 ml pyrex beaker containing 60 ml of PC. After all of the metal salt was dissolved, 0.25 g of Li_2O were then added to the beaker. The amount of transition metal ions in the solution corresponds to 20 % excess than that required to react with the Li_2O according to equations (7.10) and (7.11) (substitute Br for Cl). The solution was then heated to 150°C, covered with a watch glass and stirred for six hours in the case of the reaction with $FeBr_3$ and 10 hours for the reaction with $CoBr_2$. The solid products were then separated by centrifuge, rinsing many times with PC until the rinse became colourless, indicating that the dissolved transition metals had been removed. The solids were rinsed once more with AN (Aldrich, anhydrous 99.8%) and then dried under vacuum in the glovebox antichamber for about 30 minutes. The recovered solids were in the form of a loose powder, dark olive in colour for the reaction with $FeBr_3$, and light violet for the reaction with $CoBr_2$.

XRD patterns of the reaction products were measured with the air-sensitive sample XRD stage described in section 2.2.4 and are shown in figure 7.8. The XRD

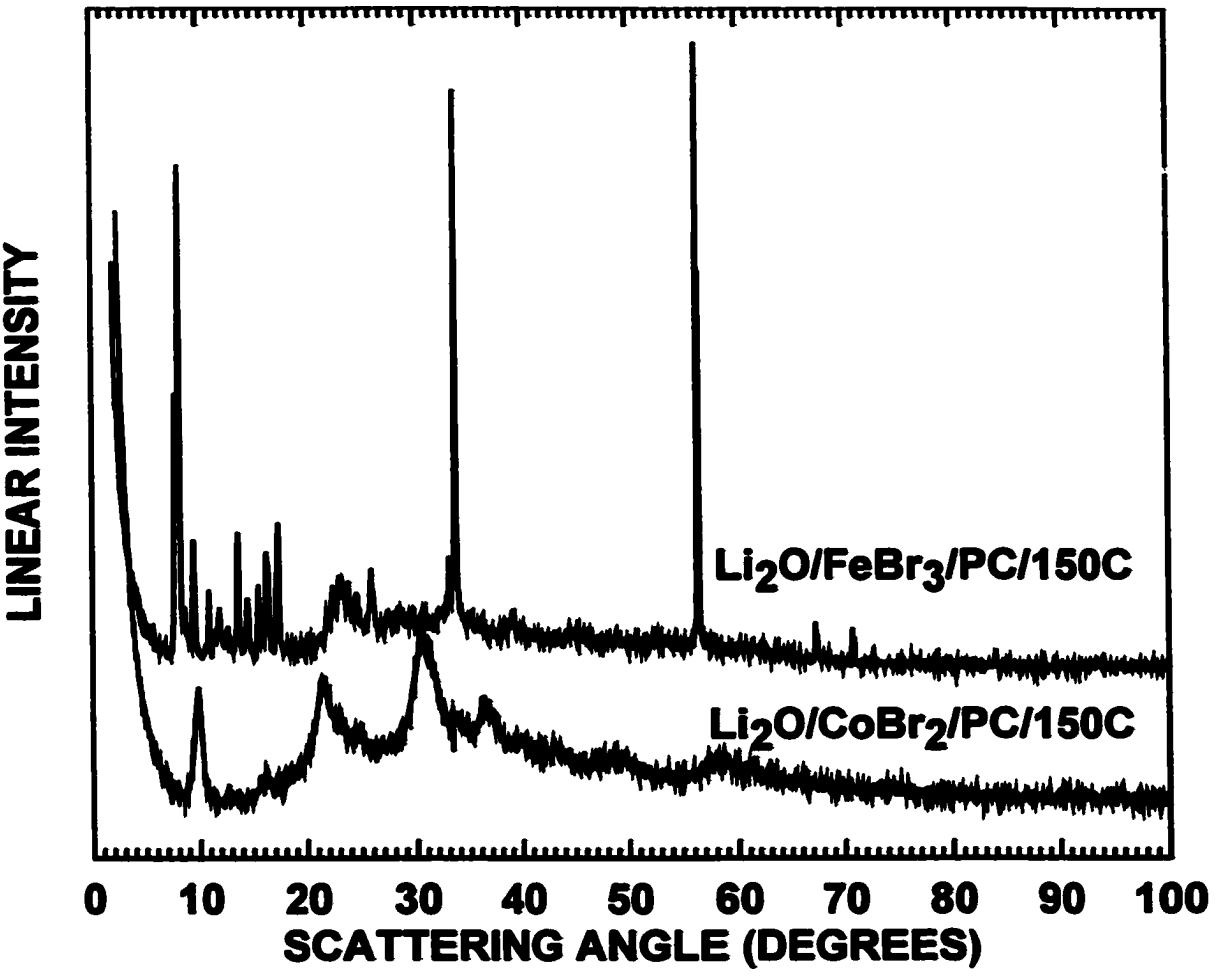

Figure 7.8 XRD patterns of the products from the exchange reactions between Li_2O and $FeBr_3$ or $CoBr_2$ in PC at 150°C.

pattern of $Li_2O/FeBr_3/PC/150C$ products has many sharp peaks. Most peaks could not be identified with any phase containing Li, Fe, O or Br. The peaks at about 33°, and 55° are near the Li_2O (111) and (110) reflections which may indicate that some of the Li_2O was unreacted. However it is likely that these peaks do not at least entirely come from Li_2O since the relative intensities of the peaks are wrong. The XRD pattern of $Li_2O/CoBr_2/PC/150C$ shows no Li_2O peaks. Curiously, the XRD pattern is similar to that of $Li_2O/CoCl_2/MeOH/25C$, which was thought to be a cobalt chloride methoxide. Perhaps PC is also taking part in this reaction at high temperature.

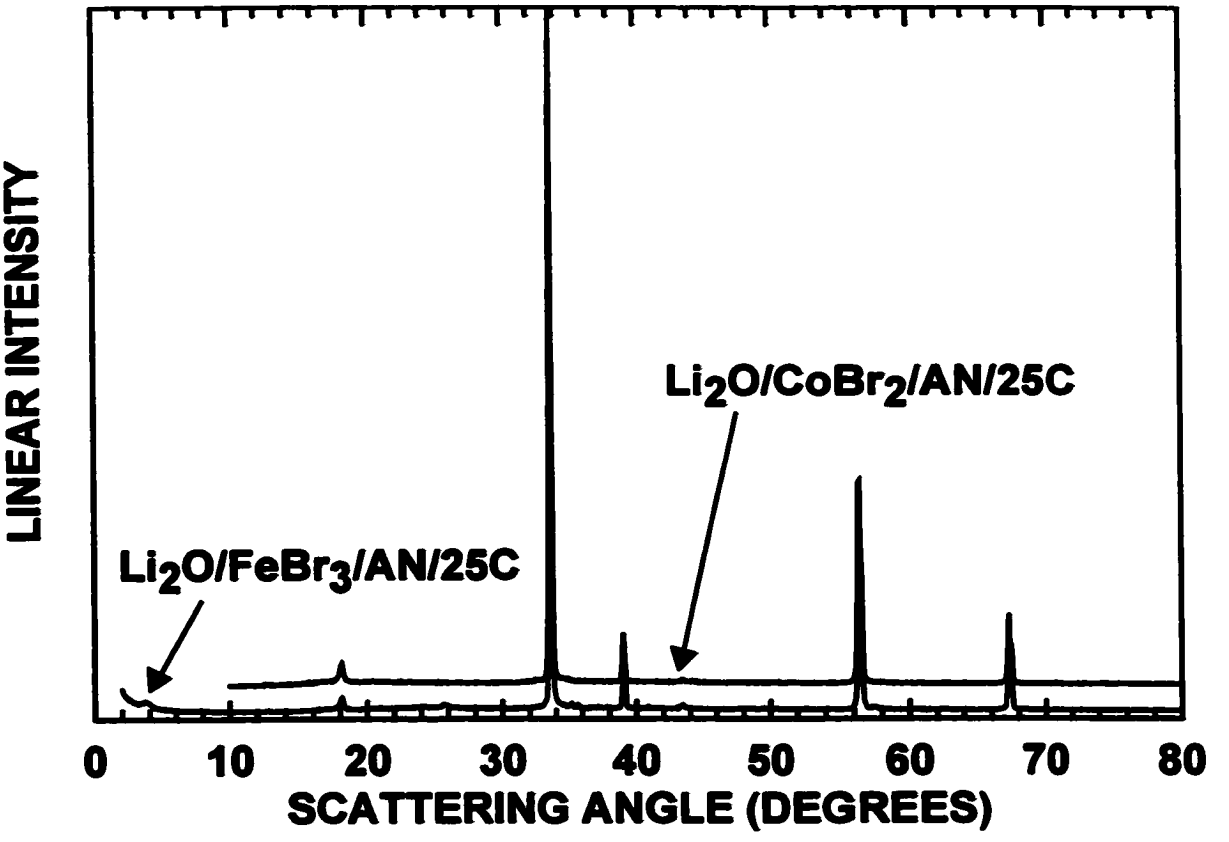

Figure 7.9 XRD patterns of $Li_2O/FeBr_3$/PC/25C and $Li_2O/CoBr_2$/PC/25C.

If the above reactions were repeated at room temperature with PC or AN solvents dark coloured products were also recovered after several weeks reaction time. However the XRD spectra of these samples showed only peaks from Li_2O, saving a small peak at 18°, as shown in figure 7.9. If $Li_2O/CoBr_2$/PC/25C was rinsed with water all the Li_2O peaks disappeared, but the peak at 18° remained. Since the scattering power of the transition metal ions are much greater than that of lithium, the amount of product represented by the peak at 18° must be minuscule and may be even due to impurities in the starting material. It was concluded that the reaction at room temperature must be very slow or not even proceed at all. However it was supposed in chapter 5 that such exchange reactions do occur at room temperature in lithium versus transition metal oxide

cells. In these cells the lithia produced at the bottom of discharge is nano-grained and probably has a high defect density. This may facilitate the reaction at room temperature. To simulate this, the above reaction was repeated with ball-milled Li_2O and is discussed in the next section.

7.3.3 The Reaction of Ball-Milled Li_2O with $FeBr_3$ and $CoBr_2$ in Acetonitrile

In order to increase the amount of product formed by the reaction of Li_2O with dissolved metal ions at room temperature, the surface area of the Li_2O was increased by ball-milling. The ball milling procedure has been described in detail in section 4.4.1. 2.0 g of Li_2O were added to the milling container in a helium-filled glovebox along with two 0.5" hardened steel bearings and then milled for 16 hours. The resulting ball-milled Li_2O was a grey powder, probably owing to some iron impurities from the milling media. In a helium filled glovebox, the milled Li_2O powder was placed in a glass vial containing about 50 ml of AN. To this was added either 2.0 g of $FeBr_3$ or 2.2 g of $CoBr_2$ The vials were covered and the contents were then stirred for ten days. The solids in the container were centrifuged, washed repeatedly with AN and were then dried in the glovebox antechamber under vacuum for one hour. This yielded a black powder for the reaction with $CoBr_2$ and a red powder for the reaction with $FeBr_3$.

XRD patterns of the reaction products were measured with the air-sensitive sample XRD stage described in section 2.2.4 and are shown in figure 7.10. Also shown in the figure is the XRD pattern of unreacted ball-milled Li_2O. All of the patterns were taken with the same counting time and are plotted on the same vertical scale except that the patterns of the ball-milled Li_2O and BM-Li_2O/$CoBr_2$/AN/25C have been shifted vertically for clarity. The peak width of the (111) peak of the ball-milled Li_2O sample is

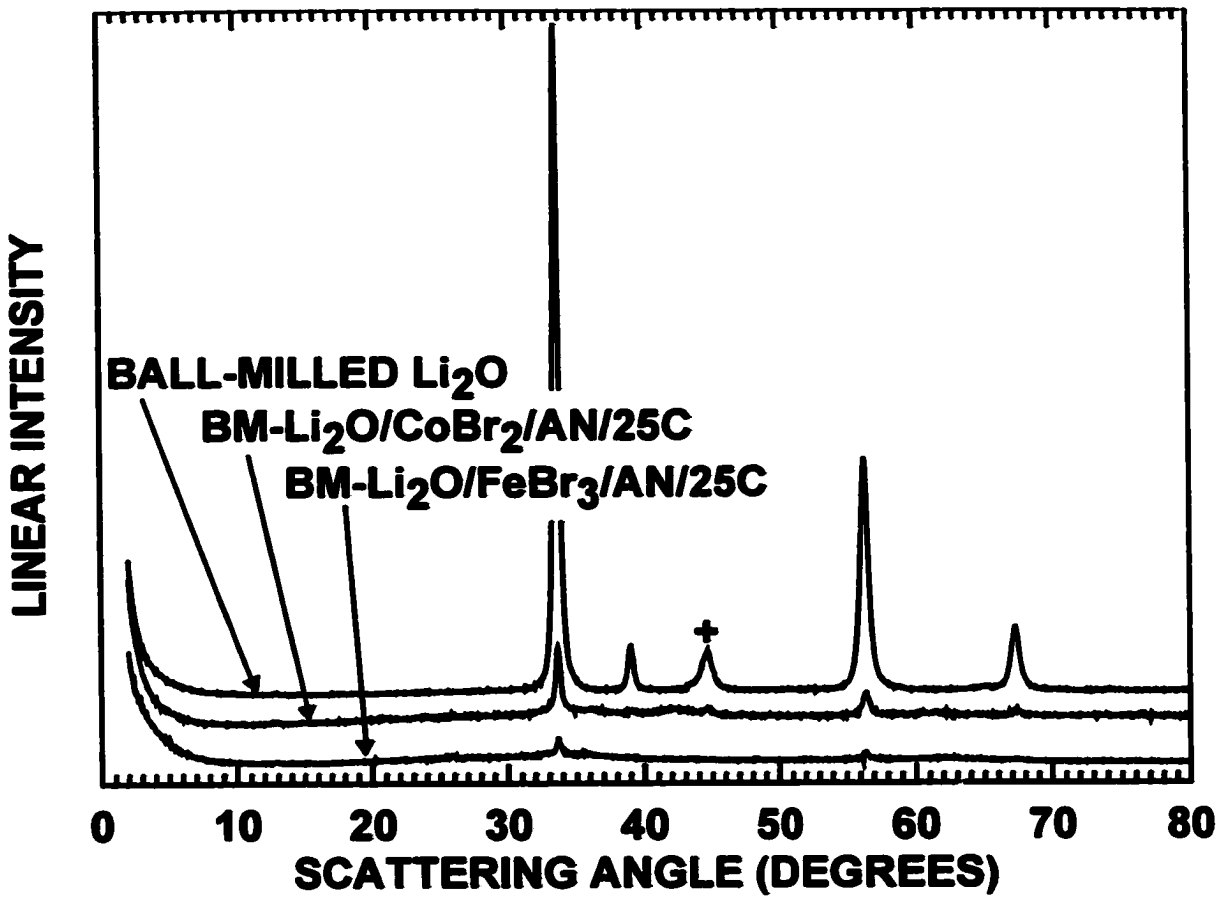

Figure 7.10 The XRD patterns of ball-milled Li_2O and of BM-Li_2O/$FeBr_3$/AN/25C amd BM-Li_2O/$CoBr_2$/AN/25C. All of the XRD patterns were taken with the same counting time and are plotted on the same vertical scale, except that the patterns of Li_2O and BM-Li_2O/$CoBr_2$/AN/25C have been shifted vertically for clarity. + indicates the position of the Fe (110) reflection.

about 0.6°. From this the grain size of this sample was estimated by the Scherrer equation to be about 144 Å. The sample also shows a peak at about 44°, which was identified as the iron (110) reflection. The iron undoubtedly came from the milling media. In the XRD pattern of BM-Li_2O/$FeBr_3$/AN/25C the Li_2O peaks have become very small and are even smaller in the XRD pattern of BM-Li_2O/$CoBr_2$/AN/25C. It is obvious that some reaction is taking place which is consuming the Li_2O. Also in the XRD pattern BM-Li_2O/$FeBr_3$/AN/25C the iron peak has become very small and for BM-

$Li_2O/CoBr_2/AN/25C$ it has disappeared all together. This may mean that either the iron metal has also been consumed in the reaction or perhaps that the reaction products are much stronger x-ray scatterers than Li_2O, and thus the small iron impurity is much harder to detect by XRD in these samples. It must be noted also that some amount of sample was found to be stuck to the magnetic stirrer used during the reaction. It is possible that the magnetic stirrer may have removed some of the iron impurity during synthesis.

Figure 7.11 shows the XRD pattern of BM-$Li_2O/CoBr_2/AN/25C$. Other than the Li_2O and iron peaks, broad peaks from α-CoO can be identified in the pattern. Also shown in the figure is the XRD pattern of BM-$Li_2O/CoBr_2/AN/25C$ which was repeatedly rinsed with distilled water and then centrifuged. The sample then was rinsed twice with acetone and dried under vacuum for 30 minutes before the XRD pattern was taken. It was found that 40% of the original sample could be recovered after rinsing. All the peaks in the XRD pattern were identified as being from either β-$Co(OH)_2$ or α-CoO. A small iron peak is also visible in the pattern. Figure 7.12 shows the XRD pattern of BM-$Li_2O/FeBr_3/AN/25C$ and also of the same sample rinsed in distilled water, as described above. It was found that 64% of this sample could be recovered after rinsing. All the peaks in the XRD pattern of BM-$Li_2O/FeBr_3/AN/25C$ could be identified as being from Li_2O and γ-Fe_2O_3 excepting a small peak at 26°, which could not be identified. After rinsing with distilled water the XRD pattern was entirely due to γ-Fe_2O_3. It is difficult to determine by XRD whether an iron impurity also exists in these samples because of the broad γ-Fe_2O_3 peak at about 43°, which is near the Fe (110) reflection at 44°.

A sample of ball-milled Li_2O was exchanged in AN using the same procedure as

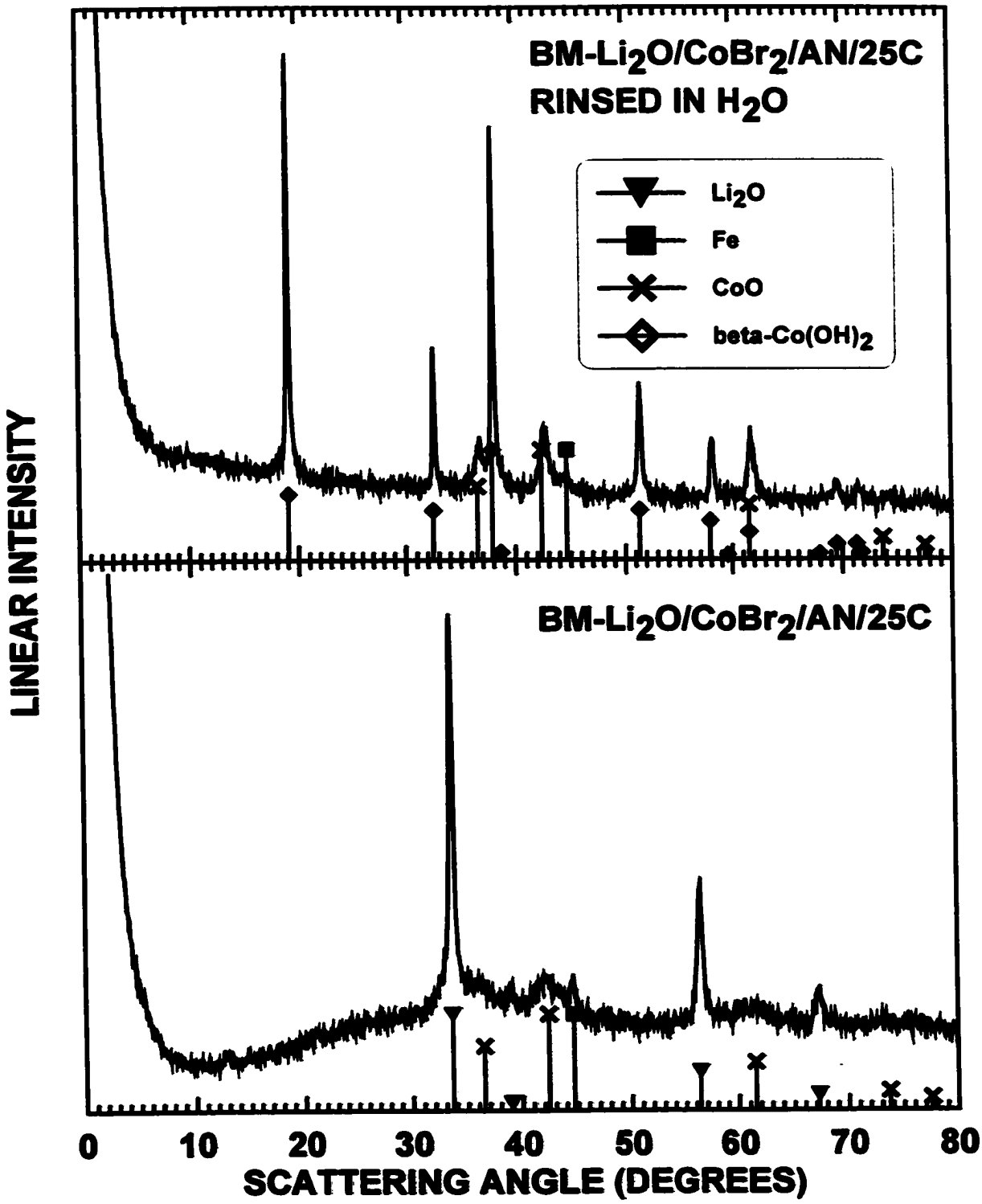

Figure 7.11 XRD patterns of BM-Li_2O/$CoBr_2$/AN/25C and of the same sample after rinsing with distilled water (top panel).

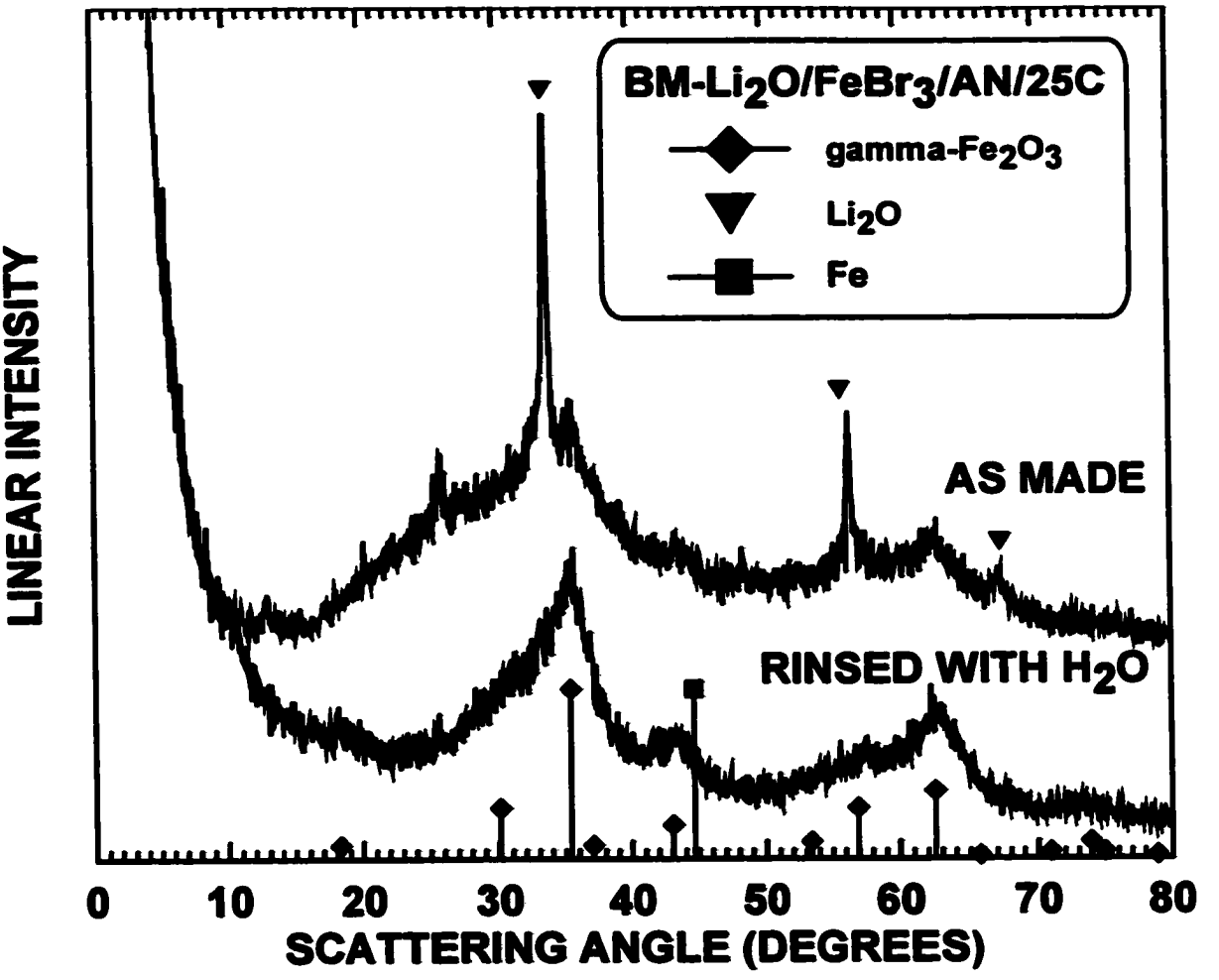

Figure 7.12 The XRD patterns of BM-Li_2O/$FeBr_3$/AN/25C and of the same sample after rinsing with distilled water.

for BM-Li_2O/$FeBr_3$/AN/25C, excepting that $FeCl_3$ was used instead of $FeBr_3$ and the solution was left to react for only two days. This sample was similar to BM-Li_2O/$FeBr_3$/AN/25C, excepting that the XRD peaks of unreacted Li_2O are much stronger, as shown in figure 7.13. The Fe impurity peak is also clearly seen in the XRD pattern. A small peak at about 18° in the pattern could not be identified. Figure 7.14 shows the XRD pattern of the BM-Li_2O/$FeCl_3$/AN/25C sample after rinsing with distilled water. Like BM-Li_2O/$FeBr_3$/AN/25C,the XRD pattern is now entirely due to γ-Fe_2O_3, excepting the Fe impurity peak.

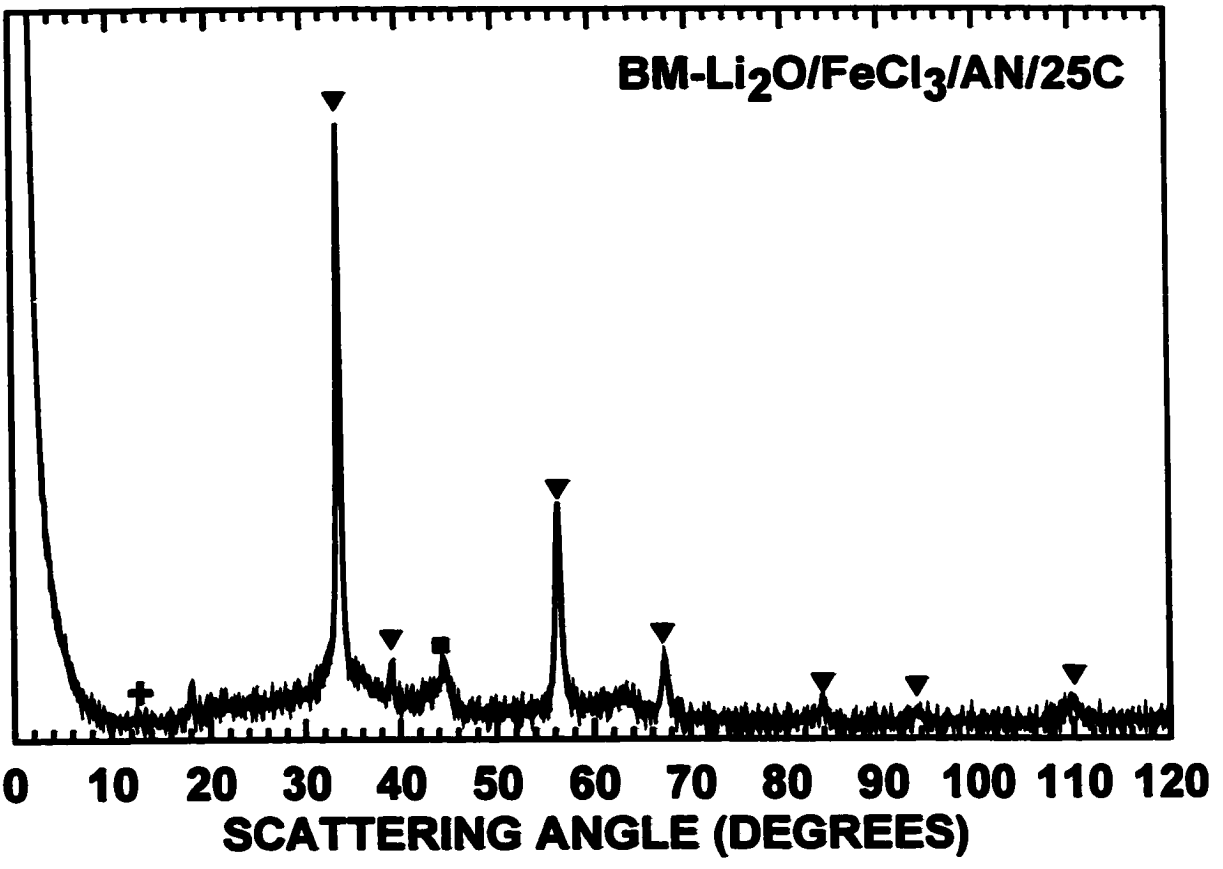

Figure 7.13 The XRD pattern of $Li_2O/FeCl_3/AN/25C$. ▼ Li_2O; ■ Fe; ✚ sample stage.

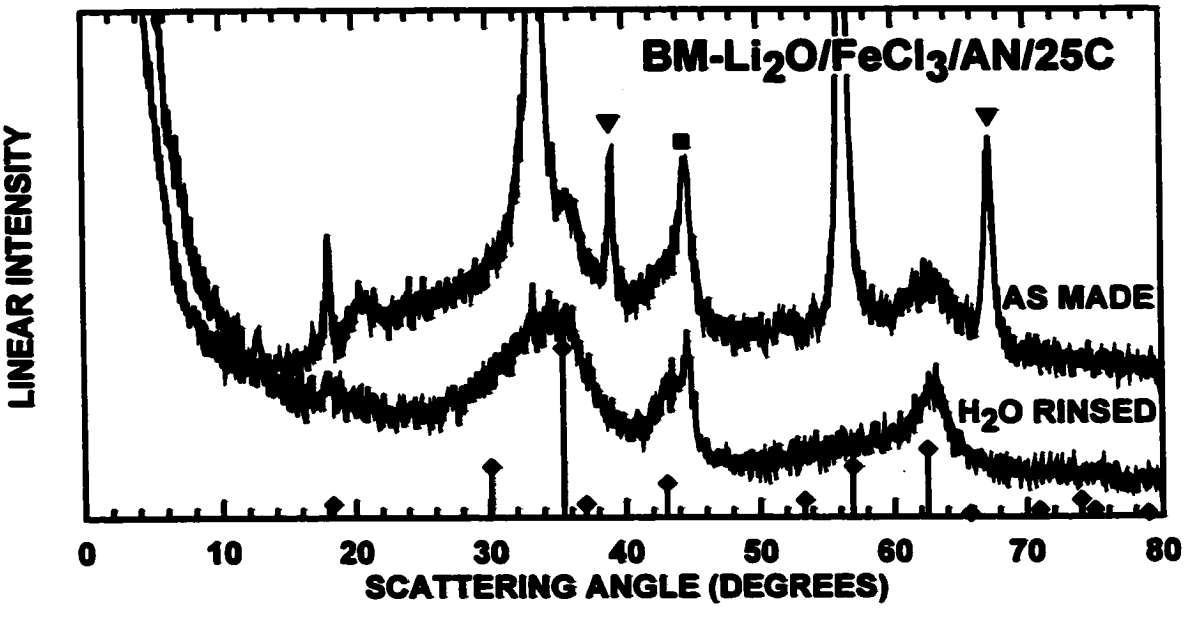

Figure 7.14 The XRD pattern of BM-$Li_2O/FeBr_3/AN/25C$ and of the same sample after rinsing in distilled water. ▼ Li_2O; ■ Fe; ◆ γ-Fe_2O_3

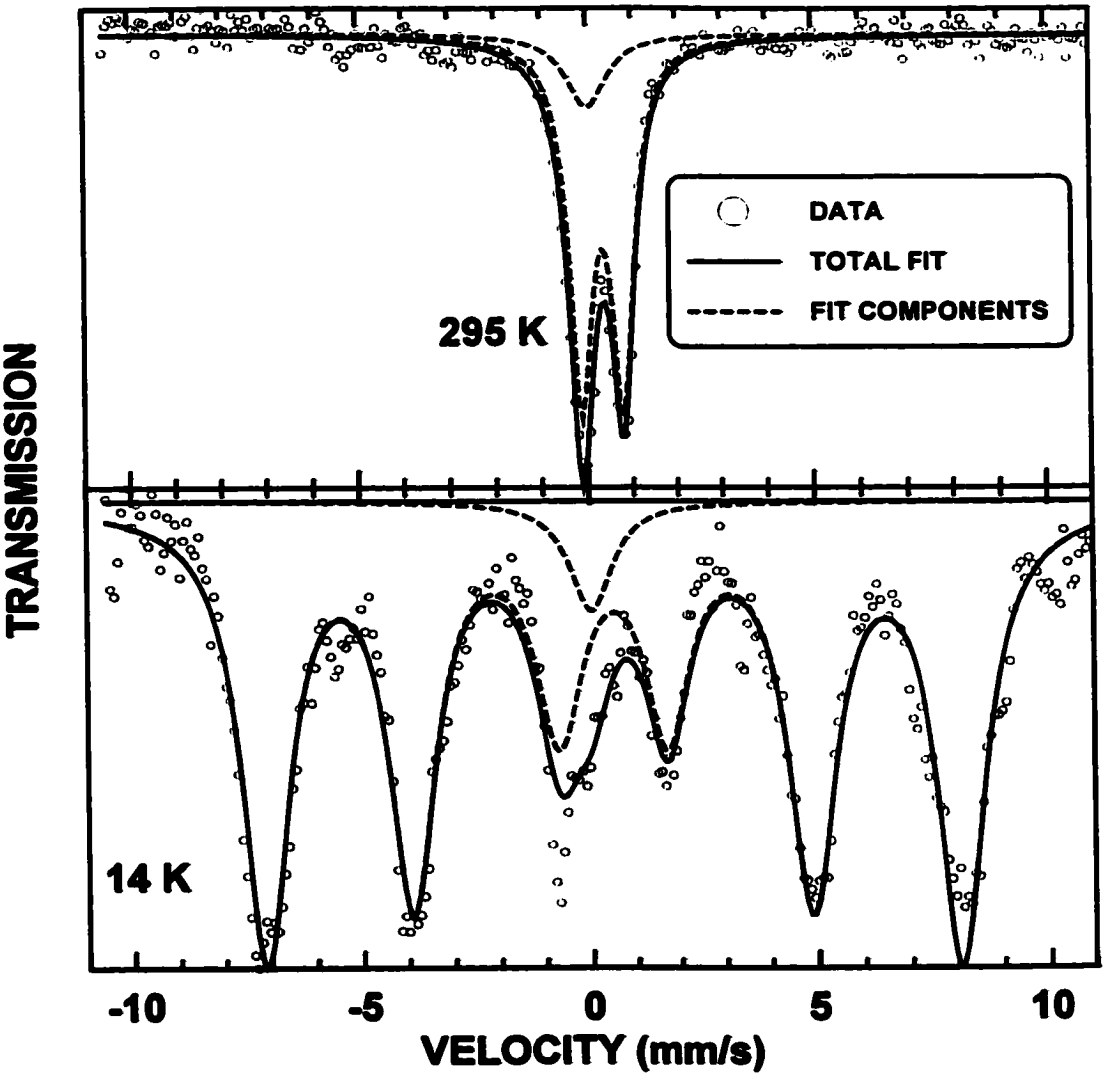

Figure 7.15 The room temperature and 14 K Mössbauer spectra of BM-Li_2O/$FeCl_3$/AN/25C.

Figure 7.15 shows the room temperature and 14 K Mössbauer spectra of BM-Li_2O/$FeCl_3$/AN/25C. Details of the Mössbauer experiment are given in section 2.3.2. At room temperature the Mössbauer spectra of bulk samples of γ-Fe_2O_3 are a hyperfine-split sextet. The hyperfine splitting has been observe to collapse to a doublet at room temperature for γ-Fe_2O_3 with nanometer grain sizes due to superparamagnetic relaxation, as is the case here. The spectra were fitted with a single Loretzian doublet and a single Loretzian sextet respectively. It was found that the fitting was improved if a

Table 7.4 Fitting parameters from the Mössbauer spectra of BM-$Li_2O/FeCl_3$/AN/25C. *These are compared with values for C-phase samples from chapter 5 and with bulk and nano-grain* γ-Fe_2O_3 *from the literature. (*$\langle\delta\rangle$*: mean centre shift,* $\langle|\Delta|\rangle$*: mean quadruple splitting,* $\langle\varepsilon\rangle$*: the mean quadruple shift,* $\langle H_m\rangle$*: the mean hyperfine magnetic field)*

Sample	Ref.	Characteristics	Temp. (K)	$\langle\delta\rangle$ (mm/s)	$\langle\|\Delta\|\rangle$ (mm/s)	$\langle\varepsilon\rangle$ (mm/s)	$\langle\|H_m\|\rangle$ (kOe)
BM-$Li_2O/FeCl_3$ /AN/25C	—	17 nm ball-milled Li_2O reacted with $FeCl_3$ in AN	RT	0.317	0.921	—	—
			14	0.488	—	0	471
C-Phase	—	charge product from $LiFeO_2$ / Li cell	RT	0.265	0.871	—	—
			15	0.302	—	0.019	421
C-Phase	—	charge product from Li_5FeO_4 / Li cell	RT	0.293	0.928	—	—
γ-Fe_2O_3	[107]	bulk sample	RT	0.34	—	—	500
γ-Fe_2O_3	[108]	prepared by spray pyrolysis; 170 nm hollow spheres with 6 nm grains	RT	0.32	0.97	—	—
			46	0.45	—	—	460

Lorentzian singlet component fixed at 0 mm/s isomer shift was also included. This singlet is presumably due to small superparamagnetic iron grains in the sample. The fitting parameters are listed in table 7.4 along with literature values for bulk γ-Fe_2O_3 and nanometer grain sized γ-Fe_2O_3. Because there is more than one iron site in these materials, the values in table 7.4 represent site averages. Also listed in the table are the fitting parameters for C-phase samples from chapter 5, which may also have been formed via Fe^{3+} ion-exchange with Li_2O. There is excellent agreement between the room

temperature spectrum of BM-$Li_2O/FeCl_3$/AN/25C and those observed for small grained γ-Fe_2O_3 and for the C-phase materials. There is also excellent agreement for the low temperature data, excepting for the C-phase material, which has slightly lower values of the isomer shift and hyperfine field. Nevertheless the agreement is still quite good considering the parameters for the C-phase material were derived from a multi-component spectrum.

7.3.4 Discussion of Experimental Results

Exchange reactions attempted between Li_2O and $FeCl_3$ or $CoCl_3$ in methanol are thought to have produced metal methoxides. This is because Li_2O was found to dissolve in methanol to form lithium methoxide. The lithium methoxide in methanol then reacts with the metal chlorides to produce transition metal methoxides and lithium chloride. Because of this, the exchange reactions were attempted in aprotic solvents. This produced no reaction for bulk Li_2O in either AN or PC solvents at room temperature. At 150°C a reaction did occur in PC, but the products could not be identified and it is difficult to tell if the solvent took part in the reaction, as in the case of methanol. Ball-milled Li_2O was found to react with Fe^{3+} or Co^{2+} ions in AN at room temperature to produce γ-Fe_2O_3 or α-CoO. This provides some evidence that an ion-exchange type reactioin may be occuring, since both structures have the same oxygen lattice as Li_2O. On the other hand, both materials could have also been formed if there was water present during the reaction. This would react with the Li_2O to from LiOH. The transition metal oxides would then precipitate from the basic solution. It is unlikely that a sizeable quantity of water was present since only Li_2O (and no LiOH) was detected in the XRD patterns of the reaction products. However even a trace amount of water might cause the

γ-Fe_2O_3 or α-CoO to form:

$$n/2Li_2O + n/2H_2O \rightarrow nLiOH \quad (7.14a)$$

$$MCl_n + nLiOH \rightarrow MO_{n/2} + n/2H_2O + nLiCl. \quad (7.14b)$$

In this reaction scheme the water acts as a catalyst and is not consumed by the reaction. Thus it is rather difficult to tell whether an exchange type reaction or a water catalysed reaction as suggested above is occurring.

During the charge of lithium cells with cobalt oxide displacement electrodes formed β-CoO on charge, whereas α-CoO was formed during the reaction between ball-milled Li_2O and $CoBr_2$. This provides further evidence that a different reaction is probably happening in the electrochemical cell than the exchange reactions attempted here with cobalt ions. The Mössbauer results of the products from the reaction between ball-milled Li_2O and $FeBr_3$ showed that nanograined γ-Fe_2O_3 is formed by this reaction, confirming the XRD measurements. On the other hand discharging and then charging lithium cells with $LiFeO_2$ electrodes produced an iron oxide phase called C-phase in chapter 5. From table 7.4, C-phase has a very similar Mössbauer spectrum as that of γ-Fe_2O_3. The XRD pattern of C-phase (scan 11 in figure 5.17), however, is not that of γ-Fe_2O_3, but is identical to that of Li_2O. As was pointed out in chapter 5, this XRD in-situ cell probably never reached a fully charged state. This experiment should be repeated to verify whether or not C-phase is actually γ-Fe_2O_3.

7.4 CONCLUSIONS

In this chapter theoretical predictions as to the possibility of exchange reactions between binary lithium compounds and transition metal ions in nonaqueous solution were

made. It was found that such exchange reactions were energetically favourable between transition metal ions and Li_3N, Li_2O and Li_2S. Furthermore since these materials possess structures which make ion conduction favourable, it was argued that the kinetics for such reactions may not be prohibitive. Indeed, earlier studies show that exchange reactions readily occur between Li_2S and transition metal ions [98].

Exchange reactions between Li_2O and Fe^{3+} or Co^{2+} ions in methanol were first attempted. This produced transition metal alkoxides. No reaction was observed between bulk Li_2O and Fe^{3+} or Co^{2+} ions in PC or AN. A reaction did occur at 150°C in PC, however the products could not be identified and it is thought that the PC might be taking part in the reaction. If nanograined ball-milled Li_2O was reacted with Fe^{3+} or Co^{2+} ions, a reaction was observed in AN at room temperature. This produced γ-Fe_2O_3 or α-CoO. It could not be determined if these products were formed via an exchange type reaction or a water catalysed reaction. Although not presented here, it was found that Li_2S and Li_3N both react quickly at room temperature with Fe^{3+} and Co^{2+} ions in both AN and PC solvents. This reaction can generate much heat and must be done with extreme caution, especially in the case of reactions with Li_3N. The products of these reactions were in the form of colloidal suspensions and were difficult to separate from the solution.

Although the above results to not conclusively show that an ion exchange reaction between transition metal ions and Li_2O is possible, they do show that if such a reaction does occur it must be a slow process. The reaction in electrochemical cells might not even involve solvated ionic species at all, but may proceed by ion migration in the solid phase, facilitated by the close contact between the components of the metal-Li_2O nanocomposite produced at the bottom of charge and by a large concentration of grain

boundaries in the product. Nevertheless, since Li_2S and Li_3N apparently react more readily than Li_2O with metal ions, metal sulfide or nitride displacement electrodes might be better candidates for displacement electrodes than oxides. Indeed FeS_2 electrodes can be cycled reversibly with lithium to zero volts with little hysteresis between the charge and discharge cycles [109]. The mechanism is slightly different than a simple exchange reaction because at low voltages FeS_2 can intercalate lithium to form Li_2FeS_2. Thus the Li_2S and Fe, which are formed at the bottom of discharge, form Li_2FeS_2 during the subsequent charge, instead of FeS_2 directly [109]. Recently lithium transition metal nitrides also have been demonstrated as anodes in lithium cells [110]. Up to 1.6 lithium per formula unit can be reversibly extracted from $Li_{2.6}Co_{0.4}N$, for example (this corresponds to 770 mAh/g) [110]. Upon discharging to zero volts an amorphous phase is produced and further cycling proceeds with about a 0.7 V hysteresis between the charge and discharge curves. It is not unlikely that an exchange reaction could be occurring during the cycling of these electrodes after the first discharge to 0 V. It would be interesting to see if a composite of Li_3N and Co metal would also be electrochemically active. Such anode materials are attractive, since they are compatible with high capacity cathodes that do not contain lithium, such as V_2O_5.

Further work on this topic to determine if transition metal oxides can be made via exchange reactions with Li_2O would be challenging. However the results could lead to new low temperature metal oxide phases and a better understanding of non-intercalating metal oxide electrodes. TEM studies are needed to examine the grain structure of the Li_2O starting material and the ion exchanged products. If the reaction is water-catalysed as suggested in equations (7.14) and (7.15), then one would expect a complete

reorganisation of the grain structure. If, on the other hand, the reaction were an exchange reaction the grain structure of the Li_2O starting material should be preserved. Another way of studying these reactions might also be to react Li_2O with molten salts containing transition metal ions. This would avoid the problem of water impurities, but the reaction might form high temperature phases that are not formed in electrochemical cells.

Chapter 8

Conclusions

8.1 SUMMARY OF RESULTS

This thesis focuses on two aspects of nanograined electrode materials for lithium batteries. Firstly, the properties of nanograined intercalation materials were investigated. Lattice gas model calculations showed that such materials may have quite different voltage-composition behaviour than their bulk counterparts, such as extra plateaus or sloping plateaus in their voltage curves. Even the voltages at which phase transitions occur in bulk were found to be modified by the grain size. It may be possible to take advantage of these effects to tailor the voltage curves of these materials by modification of the particle size or surface chemistry. Synthesis of nano-intercalation materials proved difficult by standard laboratory techniques. However it was found that a nanograined

lithium manganese oxide could be made from aqueous solution. XRD studies of this material could not determine if the structure was the $LiMn_2O_4$ spinel or the layered $LiNiO_2$ type. TEM studies showed that the material consisted of 7 nm grains which had self-assembled into 50 nm squares or rectangles. This material was electrochemically active and showed similar behaviour to that of bulk lithium manganese oxide spinel, excepting that there was significant capacity between 3.3 V and 3.8 V and the voltage plateaus were significantly sloped. It is unclear, however, if this behaviour is due to surface or size effect as predicted by the lattice gas theory or to defect sites in the bulk material. It would be very difficult to solve this problem since the control of both the grain size and the defect concentration is achieved by thermal treatment.

The second focus of the thesis examines the behaviour of non-intercalating transition metal oxide electrodes for lithium batteries. During the first discharge, these electrodes were found to form a mixture of nanograin Li_2O and the reduced transition metal. It was found that during the subsequent charge lithium could be removed from the material and a transition metal oxide was once again formed. In the case of CoO electrodes, the zinc blende form of β-CoO is formed on charge. For $LiFeO_2$ electrodes only Li_2O peaks could be detected from XRD scans at the top of charge, while Mössbauer spectra showed an Fe^{3+} compound had formed. From this evidence an electrochemical ion-exchange mechanism was suggested where the transition metal exchanges for the lithium ion in Li_2O during charge, leaving the oxygen lattice unchanged. The reverse mechanism was supposed to occur during discharge. This is the first reported electrochemical ion-exchange type reaction reported in the literature.

Assuming the above reaction scheme to be correct a nanocomposite of Li_2O and

transition metal ought to be able to serve as a cathode material in a lithium cell which could be charged on the first cycle. Such composites were prepared by ball-milling cobalt or iron metal with lithia and were indeed found to be electrochemically active and, moreover, have much larger capacities (~500 mAh/g) than conventional cathode materials (~150-200 mAh/g). These electrodes are the first reported displacement electrodes that contain active lithium as made. Such electrodes could have enormous advantages over conventional electrodes because of their large capacities. However voltage curves of such electrodes have a large polarization between the charge and discharge cycles. The polarizisation would have to be reduced if practical cells were to be made using such electrodes. Nevertheless, because of their enormous capacity, such materials might find immediate use as an additive that would provide an extra source of lithium for conventional anodes that suffer from irreversible capacity losses or for cathode materials, such as O2-type $Li_{2/3}[Ni_{1/3}Mn_{2/3}]O_2$, that can accommodate more lithium than they contain as made [111].

To provide further evidence that exchange type reactions are occurring in displacement electrodes, exchange reactions between transition metal ions and lithia in nonaqueous solvents were examined. Theoretically such exchange reactions between Li_2S, Li_2O, Li_2N and transition metal ions were found to be energetically favourable. Indeed examples of exchange reactions between transition metal ions and Li_2S in organic solvents already exist in the literature [98]. This reaction was reported to be very fast. Although the products have not been characterised similar exchange reactions with Li_2N were also found to occur within a couple of seconds at room temperature.

In contrast to the above reactions exchange reactions between Li_2O and Co^{2+} and

Fe^{3+} ions in nonaqueous solvents did not proceed at all. If ball-milled Li_2O was used as a starting material this was found to react at room temperature, forming α-CoO or γ-Fe_2O_3. This reaction was slow and after several days was still not complete. Unfortunetly it is not possible to tell if water was involved in the reaction or if an ion-exchange type reaction actually took place. Nevertheless the slow reaction rate of Li_2O perhaps indicates that oxides are not the materials of choice for displacement type electrodes, but that sulphides or nitrides might be better suited.

8.2 FUTURE WORK

Many areas of future work are suggested by this thesis. As new synthesis methods are being developed to produce nanocrystalline intercalation cathode materials, it may be possible to more carefully investigate the finite size effects, which were predicted from lattice gas calculations. A plethora of new research could be devoted to the area of displacement electrodes for lithium batteries. These electrodes are particularly exciting because they offer a quantum leap in energy density over the current technology. Such electrodes were formally not compatible with lithium ion technology, because they contained no active lithium, however it was shown in this thesis that displacement electrodes which do contain active lithium are possible. These electrodes were made from a nanocomposite of Li_2O and transition metal. Work needs to be done on reducing the polarisation voltage in these electrodes. This might simply be done by coating the composite particles with a conductive material. Also, doping the Li_2O with different anions or cations to increase the concentration of defects might aid ion and electronic conductivity. Different lithium compounds might also be tried like lithium sulphide, nitride, fluoride or even lithium carbonate or borate perhaps. More ordered

material such as a layered metal-Li_yX-metal nanocomposite might also be prepared by sputter deposition. Such an ordered arrangement might also improve ion and electron conduction thereby reducing the polarisation observed during cycling. The polarisation could also be lowered if nitrides or sulphides are used instead of oxides, as suggested in the previous chapter.

References

[1] David Linden, *Handbook of Batteries,* McGraw-Hill, New York (1995).

[2] Ian A. Courtney and J.R. Dahn, J. Electrochem. Soc., **144** (1997) 2045.

[3] Ian A. Courtney and J.R. Dahn, J. Electrochem. Soc., **146** (1999) 59.

[4] Ou Mao and J.R. Dahn, J. Electrochem. Soc., **146** (1999) 423.

[5] F. Leroux, G.R. Goward, W.P. Power and L.F. Nazar, Electrochem. Solid State Lett., **1** (1998) 255.

[6] S. Denis, E. Baudrin, M. Touboul and J-M. Tarascon, J. Electrochem. Soc., **144** (1997) 4099.

[7] S. Morzilli and B. Scrosati, Electrochim. Acta., **30** (1985) 1271.

[8] M.N. Obrovac, R.A. Dunlap, R.J. Sanderson and J.R. Dahn, submitted to J. Electrochem Soc., August 2000.

[9] N.A. Godshall, I.D. Raistrick and R.A. Huggins, J. Electrochem. Soc., **131** (1984) 543.

[10] E.J. Cairns and H. Shimotake, Science, **164** (1969) 1347.

[11] Raymond Jasinski, Electrochem. Thechnol., **6** (1968) 28.

[12] H.N. Seiger, A.E. Lyall and R.C. Shair, Power Sources **2:** Res. Develp. Non-Mech. Elec. Power Sources, Proc. Int. Symp., 6th 1968 (Pub. 1970), 267-87.

[13] R. Keller, J. Electrochem. Soc., **117** (1970).

[14] Antoni Godz, Caroline Scmutz, Jean-Marie Tarascon, Pall Warren, International Patent Application: PCT/US94/08772.

[15] B.E. Warren, *X-Ray Diffraction*, Dover Publications Inc. (1990).

[16] B.E. Warren, Phys. Rev., **59** (1941) 693.

[17] A Guinier, *X-ray Diffraction in Crystals, Imperfect Crystals, and Amorphous Bodies*, W.H. Freeman, San Francisco (1963).

[18] S. Hendricks and E Teller, J. Chem. Phys., **10** (1942) 147.

[19] V.A. Drits and C. Tchoubar, *X-ray Diffraction by Disordered Lamellar Structures*, Springer-Verlag, New York (1991).

[20] Hang Shi, J.N. Reimers and J.R. Dahn, J. Appl. Cryst., **26** (1993) 827.

[21] G.W. Brindley, J. Mering, Acta Cryst., **4** (1951) 441.

[22] H. M. Rietveld, Acta Crystallogr., **22** 151 (1967).

[23] H. M Rietveld, J. Appl. Crystallogr., **2** 65 (1969).

[24] Aaron Davis, MSc. Thesis, Dept. of Physics, Dalhousie University (2000).

[25] M.N. Richard, I. Koetschau and J.R. Dahn, J. Electrochem. Soc., **144** (1997) 554.

[26] *Mössbauer Spectroscopy*, N.N. Greenwood and T.C. Gibb, Chapman and Hall Ltd., London (1971).

[27] W. Kundig, H. Bommel, G. Constables and R.H. Lundquist, Phys. Rev., **142** (1966)
327.

[28] Ou Mao, R.A. Dunlap, I.A. Courtney and J.R. Dahn, J. Electrochem. Soc., **145** (1998) 4195.

[29] Ludwig Reimer, *Transmission Electron Microscopy*, Springer-Verlag, Berlin (1984).

[30] T. Zheng, W.R. McKinnon and J.R. Dahn, J. Electrochem. Soc., **143** (1996) 2137.

[31] O. Mao, R.L. Turner, I.A. Courtney, B.D. Fredericksen, M.I. Buckett, L.J. Krause and J.R. Dahn, Electrochem. Solid State Lett., **2** (1999) 3.

[32] D. Xiao, P.R. Strutt, M. Benaissa, H. Chen and B.H. Kear, NanoStruc. Mater., **10** (1998) 1051.

[33] David E. Reisner, Alvin J. Salkind, Peter R. Strutt and T. Danny Xiao, NanoStruc. J. Power Sources, **65** (1997) 231.

[34] J.-H. Choy, D.-H. Kim, C.-W. Kwon, S.-J. Hwang, Y.-I. Kim, J. Power Sources, **77** (1999) 1.

[35] M.E. Fisher, in *Proceedings of the 1970 Enrico Fermi Summer School on Ctritical Phenomena, Villa Monastero, Varenna sul Lago di Como, Italy*, Academic (1971).

[36] D.P. Landau, Phys. Rev. B, **13** (1976) 2997.

[37] Arthur E. Ferdinand and Micheal E. Fisher, Phys. Rev., **185** (1969) 185.

[38] H. Nakanishi and M. E. Fisher, J. Chem. Phys. **78** (1983) 3279.

[39] M.N. Obrovac and J.R. Dahn, Phys. Rev. B, **61** (2000) 6713.

[40] W.R. McKinnon and R.R. Haering, Mondern Aspects of Electrochemistry, **15** (1983) 235.

[41] Yuan Gao, K. Myrtle, M. Zhang, J.N. Reimers and J.R. Dahn, J. Electrochem. Soc., **144** (1997) 205.

[42] M.N. Obrovac, Yuan Gao and J.R. Dahn, Phys. Rev. B, **57** (1998) 5728.

[43] Tao Zheng and J.R. Dahn, Phys. Rev. B, **56** (1997) 3800.

[44] L. Onsager, Phys. Rev. **65**, (1944) 117.

[45] S.T. Coleman, W.R. McKinnon and J.R. Dahn, Phys. Rev. B., **29** (1984) 4147.

[46] J.R. Dahn and W.R. McKinnon, J. Phys. C., **17** (1984) 4231.

[47] Yuan Gao, J.N. Reimers and J.R. Dahn, Phys. Rev. B, **54** (1996) 3878.

[48] D.P. Landau, Phys. Rev. B **14**, (1976) 255.

[49] H.W. Diehl in *PhaseTransitions and Critical Phenomena Vol. 10*, edited by C. Domb and J.L. Lebowitz, (Academic, New York, 1986), p. 76.

[50] E.V. Albano, K. Binder, Dieter W. Heermann and W. Paul, Surf. Sci. **223**, (1989) 151.

[51] Micheal E. Fisher and Arthur E. Ferdinand, Phys. Rev. Lett. **19**, (1967) 169.

[52] Micheal E. Fisher and A. Nihat Berker, Phys. Rev. B **26**, (1982) 2507.

[53] Hisao Nakanishi and Micheal E. Fisher, Phys. Rev. Lett. **49**, (1982) 1565.

[54] M.F. Sykes and Micheal E. Fisher, Physica **28**, (1962) 919.

[55] Ole G. Mouritsen, *Computer Studies of Phase Transitions and Critical Phenomena*, Springer-Verlag, Berlin (1984).

[56] N. Metropolis, A.W. Rosenbluth, M.N. Rosenbluth, A.H. Teller and E. Teller, J. Chem. Phys. **21**, (1953) 1087.

[57] P. Papanek, M. Radosavljevic and J.E. Fischer, Chem. Mater. **8**, (1996) 1519.

[58] Craig R. Horne, 198th Electrochemical Society Meeting Abstracts, Oct. 22-27 2000, Phoenix Arizona.

[59] R.G. Wyckoff, *Crystal Structures*, 2nd ed., Krieger Malabar, FL, (1981), Vol. 3.

[60] J.M. Paulsen and J.R. Dahn, Chem. Mater., **11**, (1999) 3065.

[61] J.M. Tarascon, W.R. McKinnon, F. Coowar, T.N. Bowmer, G. Amatucci and D. Guyomard, J. Electrochem. Soc., **141** (1994) 1421.

[62] Yuan Gao, J.N. Reimers and J.R. Dahn, Phys. Rev. B, **54** (1996) 3878.

[63] M.M. Thackeray, W.I.F. David, P.G. Bruce and J.B. Goodenough, Mat. Res. Bull., **18** (1983) 461.

[64] S.H. Kang and J.B. Goodenough, J. Electrochem. Soc., **147** (2000) 3621.

[65] M. Doyle, J. Newman and J. Reimers, J. Power Sources, **52** (1994) 211.

[66] M.R. Palacin, Y. Chabre, L. Dupont, M. Hervieu, P. Strobel, G. rousse, C. Masquelier, M. Anne, G.G. Amatucci and J.M. Tarascon, J. Electrochem. Soc., **147** (2000) 845.

[67] Naichao Li, Charles J. Patrissi, Guangli Che and Charles R. Martin, J. Electrochem. Soc., **147** (2000) 2044.

[68] T. Tsumura, A. Shimizu and M. Inagaki, J. Mater. Chem., **3** (1993) 995.

[69] T.A. Hewston and B.L. Chamberland, J. Phys. Chem. Solids **48**, (1987) 97.

[70] See, for example, *Nonaqueous Electrochemistry*, Doron Aurbach ed., New York, Marcel Dekker pub., 1999.

[71] M.N. Obrovac, Ou Mao and J.R. Dahn, Solid State Ionics, **112** (1998) 9.

[72] J.M. Fernandez-Rodriguez, J. Morales and J.L Tirado, React. Solids **4** (1987) 163.

[73] J.M. Fernandez-Rodriguez, J. Morales and J.L Tirado, J. Mater. Sci. **23** (1998) 2971.

[74] S. Luinderoth, J.Z. Jiang and S. Mørup, Mater. Sci. Forum **235-238** (1997) 205.

[75] W.D. Johnston, R.R. Heikes and D. Sestrich, Phys. Chem. Solids, **7** (1958) 1.

[76] M. Anataya, K. Cearns, J.S. Preston, J.N. Reimers and J.R. Dahn, J. Appl. Phys., **76** (1994) 2799.

[77]. J.B. Goodenough, D.G. Wickham and W.J. Croft, J. Phys. Chem. Solids, 5 (1958) 107.

[78] W.D. Johnston and R.R. Heikes, J. Am. Chem. Soc., **78** (1956) 3255.

[79] P. Strobel, S. Robs and F. LeCras, J. Mat. Chem., **6** (1996) 1591.

[80] *Handbook of Manganese Dioxdes Battery Grade*, D. Glover, B. Schumm Jr. and A. Kozawa eds., the Int'l Battery Material Ass'n (IBA, Inc.) 1989.

[81] N.A. Godshall, I.D. Raistrick and R.A. Huggins, J. Electrochem. Soc., **131** (1984) 543.

[82] F. Leroux, G.R. Goward, W.P. Power and L.F. Nazar, Electrochem. Solid State Lett., **1** (1998) 255.

[83] S. Denis, E. Baudrin, M. Touboul and J-M. Tarascon, J. Electrochem. Soc., **144** (1997) 4099.

[84] S. Morzilli and B. Scrosati, Electrochim. Acta, **30** (1985) 1271.

[85] JCPDS CD-ROM Version 2.16, International Centre for Diffraction Data, Newtown, Pennsylvania, 1996. α-CoO: 43-1004, β-CoO: 42-1300, Co: 15-0806, Li_2O: 12-0254, Fe: 06-0696, α-$LiFeO_2$: 17-0938, α-Be: 22-0111, BeO: 43-1000.

[86] D.E. Cox, G. Shirane, P.A. Flinn, S.L. Ruby and W.J. Takei, Phys. Rev., **132** (1963) 1547.

[87] Von F. Stewner and R. Hoppe, Z. Allg. Chem., **381** (1971) 149.

[88] R. Grimes and A. J Fitch, J. Mater. Chem, **1** (1991) 461.

[89] M. J. Redman and E. G. Steward, Nature **193** (1962) 867.

[90] P. Poizot, S. Laruelle, S. Grugeon, L. Dupont, J-M Tarascon, Nature, **407** (2000) 496.

[91] H.P. Klug and L.E. Alexander, *X-Ray Diffraction Procedure for Polycrystalline and Amorphous Materials*, Wiley-Interscience Pub., New York (1974).

[92] Christian le Corre, Alain Malve, Charles Gleitzer and Jacques Foct, C.R. Acad. Sc. Paris, **274**(1972) 466.

[93] R. Ingalls, F. Van Der Woude and G.A. Sawatzky in *Mössbauer Isomer Shifts*, G.K. Shenoy and F.E. Wagner Eds., North-Holland Publishing Company, Amsterdam (1978).

[94] Ralph W.G. Wyckoff, *Crystal Structures*, Vol. 1, Robert E. Krieger pub., Malabar, Florida, (1982).

[95] Hofer, Peebles, J. Am. Chem. Soc., **69** (1947) 897.

[96] L.Y. Beaulieu, D. Larcher, R.A. Dunlap and J.R. Dahn, J. Electrochem. Soc., **147** (2000) 3206.

[97] E.G. Gillan and R.B. Kaner, Inorg. Chem., **33** (1994) 5701.

[98] Russell R. Chianelli and Martin B. Dines, Inorg. Chem., **17** (1978) 2758.

[99] S.S. Kher and R.L. Wells, Chem. Mater., **6** (1994) 2056.

[100] *CRC Handbook of Chemistry and Physics*, 70th edition, Robert C. Weast, David R. Lide, eds., CRC Press Inc., Boca Raton, Florida, 1989.

[101] *NIST-JANAF Thermochemical Tables*, 4th edition, Malcolm W. Chase, Jr., American Institute of Physics, Woodbury, NY, 1998.

[102] *Free Energy of Formation of Binary Compounds*, Thomas B. Reed, MIT Press, Cambridge, Mass., 1971.

[103] U.V. Alpen and M.F. Bell in *Fast Ion Transport in Solids*, Vashishta, Mundy, Shenoy, eds., Elsevier North Holland Inc., 1979.

[104] JCPDS CD-ROM Version 2.16, International Centre for Diffraction Data, Newtown, Pennsylvania, 1996.

[105] *Metal Alkoxides*, D.C. Bradley, R.C. Mehrotra and D.P. Gaur, Academic Press, London, 1978.

[106] G.A. Kakos and G. Winter, Australian J. Chem., **22** (1969) 300.

[107] M. Pernet and P. Strobel, Defect and Diffusion Forum, **127-128** (1995) 73.

[108] T. González-Carreño, M.P. Morales, M. Gracia and C.J. Serna, Materials Letters, **18** (1993) 151.

[109] Rosamaria Fong and J.R. Dahn, J. Electrochem. Soc., **136** (1989) 3206.

[110] Y. Takeda, M. Nishijima, M. Yamahata, K. Takeda, N. Imanishi and O. Yamamoto, Solid State Ionics, **130** (2000) 61.

[111] J.M. Paulsen and J.R. Dahn, J. Electrochem. Soc., **147** (2000) 2478.